DGK Veröffentlichungen der DGK

Ausschuss Geodäsie der Bayerischen Akademie der Wissenschaften

Reihe C | Dissertationen | Heft Nr. 910

Felix Johann

Magnetic Calibration and GNSS Processing in Strapdown Dynamic Gravimetry

München 2023

Bayerische Akademie der Wissenschaften

ISSN 0065-5325 ISBN 978-3-7696-5322-9

Diese Arbeit ist gleichzeitig veröffentlicht in:
Schriftenreihe Fachrichtung Geodäsie der Technischen Universität Darmstadt, ISBN 978-3-935631-49-5, Heft-Nr. 60 und
E-Publishing-Service der TU Darmstadt, http://tuprints.ulb.tu-darmstadt.de/24342, Darmstadt 2023

Veröffentlichungen der DGK

Ausschuss Geodäsie der Bayerischen Akademie der Wissenschaften

Reihe C | Dissertationen | Heft Nr. 910

Magnetic Calibration and GNSS Processing in Strapdown Dynamic Gravimetry

Fachbereich Bau- und Umweltingenieurwissenschaften

der Technischen Universität Darmstadt

zur Erlangung des Grades

Doktor-Ingenieur (Dr.-Ing.)

genehmigte Dissertation

von

Felix Johann, M.Sc.

aus Frankfurt am Main

München 2023

Bayerische Akademie der Wissenschaften

ISSN 0065-5325 | ISBN 978-3-7696-5322-9

Diese Arbeit ist gleichzeitig veröffentlicht in:
Schriftenreihe Fachrichtung Geodäsie der Technischen Universität Darmstadt, ISBN 978-3-935631-49-5, Heft-Nr. 60 und
E-Publishing-Service der TU Darmstadt, http://tuprints.ulb.tu-darmstadt.de/24342, Darmstadt 2023

Adresse der DGK:



Ausschuss Geodäsie der Bayerischen Akademie der Wissenschaften (DGK)

Alfons-Goppel-Straße 11 ● D – 80 539 München

Telefon +49 - 331 - 288 1685 ● E-Mail post@dgk.badw.de

http://www.dgk.badw.de

Prüfungskommission:

Vorsitzender: Prof. Dr.-Ing. habil. Boris Lehmann

Referent: Prof. Dr.-Ing. Matthias Becker

Korreferenten: Prof. Dr. René Forsberg
Prof. Dr.-Ing. Andreas Eichhorn

Tag der mündlichen Prüfung: 20.04.2023

© 2023 Bayerische Akademie der Wissenschaften, München

Alle Rechte vorbehalten. Ohne Genehmigung der Herausgeber ist es auch nicht gestattet,
die Veröffentlichung oder Teile daraus auf photomechanischem Wege (Photokopie, Mikrokopie) zu vervielfältigen

ISSN 0065-5325 ISBN 978-3-7696-5322-9

Acknowledgements

First, I would like to thank my supervisor *Prof. Dr.-Ing. Matthias Becker* for his trust and valuable support of my work over the past years. I am very grateful that he still was frequently apparent at the institute after his retirement and shared his profound experience. I would also like to thank *Dr.-Ing. Stefan Leinen* who excellently guided the chair of Physical and Satellite Geodesy through diverse projects without an active professor. He was always open for new ideas and provided important impulses to the GNSS processing. I would like to express my gratitude to *Dr.-Ing. David Becker* who introduced me to theoretical and practical aspects of the field of dynamic gravimetry and supported me in countless technical discussions. Thanks a lot also to my other colleagues at TU Darmstadt for the support and the very enjoyable working atmosphere.

Also many thanks to my co-supervisor *Prof. Dr. René Forsberg* and his team at DTU Space for the successful long-time cooperation in many projects and many fruitful discussions on the subject of airborne gravimetry. I also want to thank *Prof. Dr.-Ing. Andreas Eichhorn* for taking over the co-supervision.

I would like to thank *Dr.-Ing. Christoph Förste* and the other colleagues at the GFZ and the BKG for the thriving cooperation at the shipborne campaigns and many fruitful discussions. Thanks to the colleagues from TU Dresden and the AWI for cooperating in successful recent airborne projects.

I would like to express my gratitude to *Matthias Hoß*, *Dr. Alexander Löwer* and their colleagues at iMAR Navigation for the generous insights into our Inertial Measurement Unit and the access to the magnetic calibration facility.

The Malaysia airborne gravity campaigns were financed by the Department of Survey and Mapping, Malaysia (JUPEM) and were conducted in cooperation with the Technical University of Denmark (DTU Space). The Odenwald 2017 campaign was conducted by PSGD in cooperation with DTU Space, the Technical University of Dresden (TU Dresden) and the Technical University of Munich (TU Munich). The Odenwald 2018 campaign was conducted by iMAR Navigation in cooperation with DTU Space. The Denmark 2020 campaign was headed by DTU Space. The campaigns starting from Bremen and Chile were conducted by a cooperation of the Alfred Wegener Institue for Polar and Marine Research (AWI), TU Dresden and the University of Erlangen-Nuremberg. The Baltic Sea and North Sea campaigns have been carried out by the German Federal Agency for Cartography and Geodesy (BKG), the German Research Centre for Geosciences (GFZ Potsdam) and the German Federal Maritime and Hydrographic Agency (BSH). The Baltic Sea campaigns were part of subactivity 2.1 of the project “Finalising Surveys for the Baltic Motorways of the Sea” (FAMOS), co-financed by the European Union. The Lake Müritz campaign was headed by the GFZ. The Chekan-AM observations were processed by E. Sinem Ince, GFZ. Joachim Schwabe, BKG, adapted the GFZ Chekan-AM results of the Baltic Sea 2017 campaign. The financial support by the Deutsche Forschungsgemeinschaft (DFG) as a part of the project “Innovative calibration methods for strapdown airborne vector gravimetry aboard HALO” within the framework of SPP 1294 “Atmospheric and Earth System Research with the ‘High Altitude and Long Range Research Aircraft’ (HALO)” is gratefully acknowledged.

Abstract

Dynamic gravimetry means the determination of the gravity acceleration with observations conducted on a moving platform. In strapdown gravimetry, gravity is obtained as the difference between the kinematic acceleration due to vehicle movement and the specific force observed by the accelerometers of an Inertial Measurement Unit (IMU). This thesis analyses potential improvements in both summands. Strategies for kinematic acceleration determination using GNSS observations are reviewed, categorised and promising methods are implemented with slight adaptions. The methods are either based on the numerical differentiation of GNSS-derived position solutions or on GNSS phase range observations followed by least-squares estimation. In static and dynamic experiments, both approaches were found to be suited for dynamic gravimetry with accuracies being approximately on par. Recommendations for the selection of a method are made based on available data and tolerable processing delay due to waiting time for required precise satellite products. For Q-Flex QA-2000 accelerometers, reading errors of several mGal ($1\,\mathrm{mGal} = 10^{-5}\,\mathrm{m/s^2}$) were observed for a magnetic field intensity in the order of the Earth's field. A calibration based on the magnetic field is developed based on static experiments inside of a 3-D Helmholtz coil in addition to thermal calibration. The calibration functions were applied to several airborne and shipborne campaigns using the direct method of strapdown gravimetry. For almost all campaigns, the magnetic calibration resulted in precision improvements between 8 and 82 % depending on the observation region, the intersection angle between crossover point lines and the carrier vehicle type. The high number of campaigns allows for an evaluation of possible relations between the observation conditions and the obtained gravity precision. A line-wise upward continuation approach is introduced for comparing repeated lines of a shipborne and an airborne campaign. The strapdown gravimetry approach proved to reliably deliver a precision around the 1 mGal level. Based on crossover residual analysis, without any crossover adjustment, the best precision estimates obtained for airborne and shipborne campaigns were 0.50 and 0.27 mGal, respectively.

Zusammenfassung

Die Dynamische Gravimetrie bezeichnet die Bestimmung der Schwerebeschleunigung unter Verwendung von Beobachtungen, die auf einer bewegten Plattform erhalten wurden. In der Strapdown-Gravimetrie wird die Schwere als Differenz zwischen der Kinematischen Beschleunigung aufgrund der Bewegung des Fahrzeugs und der Spezifischen Kraft, die von den Beschleunigungssensoren einer Inertialen Messeinheit (IMU) beobachtet wird, erhalten. In der vorliegenden Arbeit wird Verbesserungspotenzial in beiden Bestandteilen analysiert. Zur Bestimmung der Kinematischen Beschleunigung werden verschiedene Strategien aus der Literatur vorgestellt und kategorisiert. Erfolgsversprechende Methoden werden mit leichten Anpassungen implementiert. Die Methoden basieren entweder auf der numerischen Differentiation von mittels GNSS bestimmten Positionslösungen oder von GNSS-Phasenbeobachtungen, in letzterem Fall gefolgt von einer Beschleunigungsschätzung nach der Methode der kleinsten Quadrate. In statischen und dynamischen Versuchen wurde festgestellt, dass beide Ansätze für die Anwendung in der Dynamischen Gravimetrie geeignet sind. Die Qualität von deren Ergebnissen ist ähnlich. Es werden Empfehlungen zur Auswahl einer Methode getroffen basierend auf den verfügbaren Daten und der maximal tolerierbaren Verzögerung aufgrund der Wartezeit auf benötigte präzise Satellitenprodukte. Für Beschleunigungssensoren des Typs Q-Flex QA-2000 wurden bei Einwirkung eines Magnetfelds in der Größenordnung des Erdmagnetfelds Sensorfehler von mehreren mGal ($1\,\mathrm{mGal} = 10^{-5}\,\mathrm{m/s^2}$) beobachtet. Auf Grundlage statischer Experimente in einer 3D-Helmholtzspule wurde, zusätzlich zu einer thermischen Kalibrierung, eine Kalibriermethode basierend auf einem äußeren Magnetfeld entwickelt. Die Kalibrierfunktionen für die Akzelerometer wurden auf verschiedene Flug- und Schiffskampagnen angewendet. Dabei wurde die Direkte Methode der Strapdown-Gravimetrie angewendet. Bei fast allen Kampagnen führte die Anwendung der magnetischen Kalibrierung zu einer Verbesserung der Präzision zwischen 8 und 82 %, abhängig von der Region, dem Schnittwinkel zwischen den Linien der Kreuzungspunkte und dem Fahrzeugtyp. Die hohe Anzahl an Kampagnen ermöglicht eine Analyse möglicher Korrelationen zwischen den Beobachtungsbedingungen und der Präzision der erhaltenen Schwere. Ein Ansatz zur linienweisen Schwerefortsetzung nach oben wurde eingeführt, um wiederholte Linien einer Schiffs- und einer Flugkampagne vergleichen zu können. Mithilfe der Strapdown-Gravimetrie wurde zuverlässig eine Präzision um 1 mGal erhalten. Basierend auf Kreuzungspunktanalysen ohne zugehörige Justierung wurden als beste Präzision 0.50 mGal für eine Flug- und 0.27 mGal für eine Schiffskampagne erreicht.

Contents

Acknowledgements iii

Abstract iv

Zusammenfassung v

List of symbols ix

1 Introduction 1

2 Strapdown dynamic gravimetry: Basics and state of the art 3
- 2.1 The Earth's gravity field . . . 3
- 2.2 Gravimetry . . . 6
  - 2.2.1 Satellite gravimetry . . . 8
  - 2.2.2 Airborne gravimetry . . . 10
  - 2.2.3 Shipborne gravimetry . . . 11
  - 2.2.4 Static terrestrial gravimetry . . . 12
- 2.3 Gravimeter types of dynamic gravimetry . . . 12
  - 2.3.1 Horizontally-stabilised gravimeters: Chekan-AM and LaCoste S-Type . . . 13
  - 2.3.2 Strapdown gravimeter: iMAR iNAV-RQH-1003 with iTempStab-AddOn . . . 14
- 2.4 Thermal IMU calibration . . . 18
  - 2.4.1 Possible approaches . . . 18
  - 2.4.2 Renewed warm-up calibration . . . 20
- 2.5 Coordinate frames . . . 23
- 2.6 Processing methods of strapdown gravimetry . . . 26
  - 2.6.1 Indirect method . . . 26
  - 2.6.2 Direct method . . . 27

3 Magnetic field influences on accelerometer readings 30
- 3.1 The Earth's magnetic field . . . 31
- 3.2 Static experiments in a 3-D Helmholtz coil . . . 33
  - 3.2.1 Homogeneity of the generated magnetic field . . . 33
  - 3.2.2 Methods . . . 34
  - 3.2.3 Results . . . 37
- 3.3 Calibration approach for the vertical accelerometer . . . 40

4 GNSS-based kinematic acceleration determination 43
- 4.1 State of the art . . . 43
- 4.2 Numerical differentiation methods . . . 46
- 4.3 Position differentiation approach (PosDif) . . . 47

4.4 Phase differentiation approach (PhaseDif) . . . 48
4.4.1 Derivation of the PhaseDif functional model . . . 48
4.4.2 Specifics of the PhaseDif-PPP functional model . . . 50
4.4.3 Specifics of the PhaseDif-POP functional model . . . 51
4.4.4 PhaseDif algorithm . . . 53
4.4.5 Specifics of the PhaseDif-PPP algorithm . . . 55
4.4.6 Specifics of the PhaseDif-POP algorithm . . . 55
4.4.7 Phase observation types . . . 56
4.4.8 Weighting . . . 56
4.4.9 Outlier test . . . 61
4.5 Static experiments in the IGS network . . . 63
4.5.1 Methods . . . 63
4.5.2 Results . . . 65
4.5.3 Conclusions . . . 70

5 Algorithmic design of the direct method 74
5.1 Basic GNSS/IMU pre-processing and integration . . . 74
5.2 Lever arm . . . 75
5.3 Gravity disturbance determination . . . 76
5.4 Bias and linear drift removal using base reading data . . . 77
5.5 Quality assessment . . . 77
5.5.1 Crossover analysis . . . 80
5.5.2 Repeated trajectory segments . . . 81
5.5.3 Comparison to external gravity data . . . 81

6 Airborne experiments 82
6.1 MY2014: Malaysia 2014 . . . 82
6.1.1 Campaign details . . . 82
6.1.2 Main results . . . 84
6.2 MY2022: Malaysia 2022 . . . 87
6.2.1 Campaign details . . . 87
6.2.2 Main results . . . 88
6.3 ODW2017/2018: Odenwald 2017/2018 . . . 92
6.3.1 Campaign details . . . 92
6.3.2 Main results . . . 94
6.4 DK2020: Denmark 2020 . . . 96
6.4.1 Campaign details . . . 96
6.4.2 Main results . . . 98
6.5 BRE2021: Bremen 2021 . . . 99
6.5.1 Campaign details . . . 99
6.5.2 Main results . . . 101
6.6 CL2021: Patagonia 2021 . . . 104
6.6.1 Campaign details . . . 104
6.6.2 Main results . . . 107

7 Shipborne experiments 108
7.1 BTS2017/2018: Baltic Sea 2017/2018 . . . 108
7.1.1 Campaign details . . . 108

7.1.2 Main results . . . 110
7.2 NTS2021/2022: North Sea 2021/2022 . . . 112
7.2.1 Campaign details . . . 112
7.2.2 Main results . . . 115
7.2.3 Influence of ocean tides . . . 119
7.3 MRZ2019: Lake Müritz 2019 . . . 120
7.3.1 Campaign details . . . 120
7.3.2 Main results . . . 120

8 Dynamic experiments result summary 124
8.1 Error sources of dynamic gravimetry . . . 124
8.2 Influence of measurement conditions . . . 124
8.3 Magnetic calibration . . . 126
8.4 Selection criteria for the kinematic acceleration approach . . . 127

9 Comparison of different approaches in dynamic gravimetry 129
9.1 Strapdown gravimeter model and processing method . . . 129
9.2 Gravimeter types: ”Classical“ and strapdown gravimeters . . . 131
9.2.1 Comparison at several shipborne campaigns . . . 131
9.2.2 Potential multi-instrument combinations . . . 132
9.3 Comparison of congruent line results at different observation heights . . . 135
9.3.1 Line-wise upward continuation . . . 135
9.3.2 Application to NTS2021/BRE2021 . . . 138

10 Conclusions and outlook 142
10.1 Conclusions . . . 142
10.2 Outlook . . . 143

Bibliography 145

Own publications 153

List of acronyms I

List of figures IV

List of tables VIII

List of symbols

Coordinate frames

a	Accelerometer sensor frame
b	Body frame
$\boldsymbol{C}_a^b$	Rotation matrix for the transformation from a coordinate frame a to a frame b
$\boldsymbol{c}^f$	Vectorial quantity c fiven in a frame f
c_i^f	Component of a quantity $\boldsymbol{c}$ in the axis i of the coordinate frame$f$
c_H	Horizontal component of a vectorial quantity $\boldsymbol{c}$
e	Earth frame
h	Ellipsoidal height
i	Inertial frame
n	(Local) navigation frame
R_E	Transverse radius of curvature
R_N	Meridian radius of curvature
r	Distance to the geocentre
X	First axis of the IMU frame
x_f	First axis of a cartesian right-hand frame f
Y	Second axis of the IMU frame
y_f	Second axis of a cartesian right-hand frame f
Z	Third axis of the IMU frame
z_f	Third axis of a cartesian right-hand frame f
β	Angle between the vehicle front axis x_b and the IMU front axis X
θ	Geocentric colatitude
θ_b	Pitch angle
θ_R	Earth Rotation Angle (ERA)
λ	Geodetic longitude
ϕ	Geodetic latitude
$\bar{\phi}$	Geocentric latitude
ϕ_b	Roll angle
ψ_b	Yaw angle

Scalars

a	Semi-major axis of the ellipsoid
a_i, b_i	Coefficients
B	Phase ambiguity and instrumental delay bias
b	Semi-minor axis of the ellipsoid
b_S	Vertical gravity disturbance for a specific disturbance wavelength
d	Combination of satellite acceleration and centrifugal term in the PhaseDif method

dt	Clock error
$\dot{dt}$	Clock drift
$\ddot{dt}$	Clock drift rate
C_{nm}	Coefficient linked to the cosine function in spherical harmonics of degree n and order m
c	Speed of light
c_a	Specific constant of type a
e_{Sat}	Satellite elevation angle
e'_{Sat}	Projected satellite elevation for soft elevation weighting method
e_{cut}	Cut-off elevation angle
e_0	Elevation coefficient
e_{el}	Primary eccentricity of the ellipsoid
f	Frequency
f_g	Disturbing signal frequency
g_n^m	Gauß coefficient linked to the cosine function in spherical harmonics of degree n and order m
G	Gravitational constant
GM	Gravitational parameter of the Earth
H	Orthometric height
H_f	Upper flight height (unspecific metrical height system)
H_m	Lower flight height or marine height (unspecified metrical height system)
h_n^m	Gauß coefficient linked to the sine function in spherical harmonics of degree n and order m
I	Ionospheric signal delay
k	Reference station (index)
M	Multipath effect
m	Rover (index)
n_a	Number of elements a
p	Satellite (index)
q	Crossover adjustment correction factor
R_0	Approximated mean Earth radius
S_{nm}	Coefficient linked to the sine function in spherical harmonics of degree n and order m
T	Tropospheric signal delay
T_i	Temperature observed by a sensor i
t	Epoch
V	Gravitational potential
V_{mag}	Geomagnetic potential
V_S	Gravitational disturbing potential
W	Gravity potential
w	Weight assigned to an observation
y	Function $y(t)$ depending on t
Z	Centrifugal potential
α	Angle between local magnetic North and the maximal susceptibility direction of a sensor
γ_0	Normal gravity on the ellipsoid
Δt	Time difference between two consecutive epochs
δ	Magnetic field declination
$\delta\phi_{\text{rel}}$	Relativistic phase range error
ε	Error or noise
κ	Angle between the front axis and the maximal susceptibility direction of a sensor
λ_g	Disturbing signal wavelength

μ	Magnetic permeability
ν	Accelerometer bias
ρ	Geometric range
ρ_{sea}	Sea water density
$\dot{\rho}$	Range velocity
$\ddot{\rho}$	Range acceleration
Σ_n	Amplitude of the gravitational potential for a degree n
σ_0^2	Variance factor
ϕ	Carrier-phase range
$\dot{\phi}$	Carrier-phase range velocity
$\ddot{\phi}$	Carrier-phase range acceleration
ω	Phase wind-up effect
ω_{ie}	Earth rotation rate
0	Master station (if index in PhaseDif-POP method)

Vectors

$\boldsymbol{B}$	Magnetic flux density (“magnetic field”)
$\boldsymbol{b}$	Gravitational acceleration
$\boldsymbol{e}_a^b$	Unit vector pointing from a to b
$\boldsymbol{f}$	Specific force
$\boldsymbol{g}$	Gravity
$\boldsymbol{H}$	Magnetic field strength
$\boldsymbol{L}$	(Linear) observation vector
$\boldsymbol{l}$	Lever arm (vector from IMU CoM to GNSS antenna phase centre)
$\boldsymbol{r}$	Position
$\dot{\boldsymbol{r}}$	Velocity
$\ddot{\boldsymbol{r}}$	Kinematic acceleration
$\boldsymbol{v}$	Observation residuals
$\boldsymbol{X}$	Unknown parameters
$\boldsymbol{x}$	Position vector
$\dot{\boldsymbol{x}}$	Velocity
$\ddot{\boldsymbol{x}}$	(Kinematic) acceleration
$\boldsymbol{x_a^b}$	Position difference $\boldsymbol{x}^b - \boldsymbol{x}_a$
$\boldsymbol{z}$	Centrifugal acceleration
$\boldsymbol{\varepsilon}$	Errors
$\boldsymbol{\gamma}$	Normal gravity at a specific height above the ellipsoid
$\boldsymbol{\delta g}$	Gravity disturbance
$\boldsymbol{\delta g}_{\text{eot},a}$	Rotating frames correction based on kinematic acceleration computation in the frame a
$\boldsymbol{\omega}_{ab}^c$	Angular rate of a frame b with respect to a frame a given in a frame c

Matrices

$\boldsymbol{A}$	Design matrix
$\boldsymbol{P}$	Weight matrix
$\boldsymbol{\Sigma}$	Variance covariance matrix

Mathematical notation

a_x	x component of a vector a
a_H	Horizontal component of a vector a
$\hat{a}$	Estimated parameter a
$\lvert\boldsymbol{a}\rvert$	Euclidean norm a of a vector $\boldsymbol{a}$
P_{nm}	Associated Legendre polynomial of degree n and order m
P_n^m	Schmidt-normed Legendre polynomial of degree n and order m
$\Delta y_{i,j}$	Difference $y_j - y_i$
$\boldsymbol{\Omega} = [\boldsymbol{\omega}\times]$	Skew-symmetric matrix of a angular rate vector $\boldsymbol{\omega}$
$\boldsymbol{a} \cdot \boldsymbol{b} = \boldsymbol{a}\,\boldsymbol{b}$	Scalar product (dot product) of two vectors $\boldsymbol{a}, \boldsymbol{b}$
$\boldsymbol{a} \times \boldsymbol{b}$	Cross product of two vectors $\boldsymbol{a}, \boldsymbol{b}$
$\boldsymbol{\nabla}(A)$	Gradient of a scalar field A
$\dot{a} = \frac{\delta a}{\delta t}, \ddot{a} = \frac{\delta^2 a}{\delta t^2}$	First and second time derivative of a function $a(t)$
σ_a	Standard deviation of a quantity a
$\boldsymbol{\varnothing}$	Matrix with all elements being 0
$\bar{a}$	Normalised quantity a

1 Introduction

The gravity field of the Earth needs to be determined precisely to establish physical height systems that are referenced to the sea level. Such height systems are required, for instance, to establish height-dependent infrastructure like water distribution networks. Furthermore, the measurement of gravity accelerations allows conclusions on the density of the material under the terrain surface, which is valuable information for geology and exploration. In climate research, gravity observations are used to monitor changes in the thickness of glaciers and in the sub-surface water storage.

In dynamic gravimetry, the Earth's gravity field is observed from moving platforms like aircraft or vessels allowing for measurements over specific regions. The observations are conducted much faster than in terrestrial gravimetry; the spatial resolution is higher than in satellite gravimetry. In the past, horizontally stabilised gravimeters have been primarily used for dynamic gravimetry. Recently, strapdown Inertial Measurement Units (IMUs) proved to be on par with "classical" gravimeters, especially after reducing temperature-dependent sensor drifts (Becker, 2016).

In strapdown gravimetry, gravity is basically obtained as the difference of the accelerometer measurements of the IMU and the kinematic acceleration obtained from Global Navigation Satellite Systems (GNSS) observations. According to the law of variance propagation, the gravity accuracy depends on the accuracy of both summands. In the scope of this thesis, potential areas of improvement will be identified for both parts.

While it is commonly known that reducing thermally induced errors is essential for high precision gravimetry, previous research has neglected to find evidence of magnetic fields influencing strapdown gravimetry. To the knowledge of the author, it will be shown for the first time that accelerometer errors for the analysed IMU can be significantly reduced by considering the magnetic field of the Earth.

The kinematic acceleration is examined by analysing existing strategies for its determination based on GNSS observations. Typically, standard GNSS processing methods are used for positioning. The position is numerically differentiated two times to obtain the acceleration. Other approaches are based on the direct use of the second derivative of the GNSS phase observable avoiding some slowly changing error sources. The latter approaches are seldom used since the acceleration determination based on GNSS observations is rarely required outside the field of gravimetry. Several GNSS processing methods will be implemented and slightly adapted.

Multiple airborne and shipborne campaigns using a wide range of vehicles and being subject to diverging observation conditions will be evaluated. The comparatively high number of campaigns will allow for an analysis of the correlation between campaign conditions and the obtained precision.

Section 2 will introduce the basics of gravimetry, the state of the art of airborne and shipborne gravimetry, thermal calibration, the definition of coordinate frames and processing methods of strapdown gravimetry. Furthermore, the used gravimeters will be presented. Section 3 starts with a brief introduction to the Earth's magnetic field. After that, several static experiments will be presented where an IMU is exposed to a known magnetic field. The results will be incorporated in a newly developed calibration approach. In Section 4, methods for kinematic acceleration determination will be evaluated. The derivation of methods based on phase differentiations will be discussed in detail. The algorithms of appropriate methods will be described and evaluated in two static experiments. Section 5 will present the algorithm of the direct method of strapdown

gravimetry, which was used in the scope of the thesis. This section might be especially helpful if a new dynamic gravimetry algorithm shall be implemented.

After the introduction to the methods and the evaluation in static experiments, a wide range of airborne and shipborne campaigns will be presented in Sections 6 and 7. For each campaign, the vehicle and trajectory set-up, the observation conditions and the main results will be discussed briefly. The overall main findings of the dynamic experiments will be summarised in Section 8. After naming the main error sources of dynamic gravimetry, the section focuses on the influence of the measurement conditions, the magnetic calibration and the kinematic acceleration determination methods. For the latter, guidelines will be developed helping to select a method. Based on the presented dynamic campaigns, results of different gravimeter types and processing methods of strapdown gravimetry will be compared in Section 9. Furthermore, an approach for line-by-line upward continuation will be developed. It can be used to compare the results of congruent measurement lines that were passed at different altitudes. The key findings of this work will be summarised in Section 10.

2 Strapdown dynamic gravimetry: Basics and state of the art

2.1 The Earth's gravity field

The Earth's gravitational potential V is the work that needs to be done by gravitation to move a unit mass from infinity to a specific position in this field (Torge and Müller, 2012). If the centrifugal potential Z is added, the gravity potential W is obtained. The gradient of this scalar field is the vectorial gravity field

$$\boldsymbol{g} = \boldsymbol{\nabla}(W) = \boldsymbol{\nabla}(V + Z) = \boldsymbol{b} + \boldsymbol{z}, \tag{2.1}$$

which in turn is the sum of two vectorial components: gravitational acceleration $\boldsymbol{b}$ (gravitation) and centrifugal acceleration $\boldsymbol{z}$. The Earth's gravity is the acceleration that acts on a body that is resting with respect to the Earth's surface.

- If the Earth was a homogenous sphere, *gravitation* would induce an acceleration pointing towards the Earth's centre of mass. The Euclidean norm of gravitation would be equal for all points on the surface of the sphere.
- The diurnal rotation of the Earth induces the *centrifugal acceleration* which is perpendicular to Earth's rotation axis and points towards space. It is proportional to the distance to the rotation axis. Hence, on a sphere around the geocentre, it is maximal on the equator and zero at the poles.

The Earth's gravity deviates from the model of a homogenous sphere for several reasons:

- Due to the centrifugal force induced by the diurnal rotation of the Earth, the Earth resembles a rotational ellipsoid rather than a sphere. The semi-major axis goes from the centre of mass to the equator and the semi-minor axis goes from the centre of mass to the poles. The latter axis coincides with the rotational axis.
- The topography of the Earth induces higher gravitation above high mountains and lower gravitation above ocean trenches.
- Furthermore, the density under the surface depends on rock types. High-density rocks induce higher gravitation.
- Global and local mass changes affect gravity, especially the global water cycle. Changes in ice mass, sea level and land water storage (instantaneous, seasonal or secular) directly reshape the gravity field.

The gravity field of the Earth provides an insight into the Earth's interior. Hence, determining the gravity field is of special interest when investigating the Earth's figure (geodesy, geophysics), its subsurface (geology) and changes in the Earth system due to the global warming (climate research).

Table 2.1: Main influencing factors on gravity observations at the Earth's surface (values taken from Torge (1989))

Influencing factor	Gravity change [mGal]
Flattening, centrifugal acceleration and height	up to 5000
Disturbing masses in crust and mantle	50...500
Ore and coal deposits	0.1...1
Tidal effects	up to 0.3
Groundwater level and soil moisture variation	up to 0.1
Non-tidal atmospheric variation over several days	up to 0.02

The magnitudes of the main factors influencing gravity on the Earth's surface are indicated in Table 2.1. In gravimetry, the unit $1\,\text{Gal} = 10^{-2}\,\frac{\text{m}}{\text{s}^2}$ in combination with prefixes ($1\,\text{mGal} = 1000\,\mu\text{Gal} = 10^{-5}\,\frac{\text{m}}{\text{s}^2}$) is commonly used for accelerations. Mean gravity at the Earth's surface is $g \approx 9.80\,\frac{\text{m}}{\text{s}^2} = 980\,000\,\text{mGal}$ (Torge, 1989). Figure 2.1 illustrates the spatial and temporal resolution which is required to monitor processes of the Earth system influencing the gravity field. Additional information on the observation techniques will be presented in Section 2.2.

If the Earth is approximated as a homogenous rotational ellipsoid, gravity can be exactly determined in this model and is called *normal gravity*. According to the conventions of the International Earth Rotation and Reference Systems Service (IERS) (Petit and Luzum, 2010), the Geodetic Reference System 1980 (GRS80) ellipsoid is recommended to be used in geodesy which is defined by the equatorial radius (semi-major axis), the geocentric gravitational constant, the dynamical form factor (excluding permanent tidal deformation) and the angular velocity of the Earth (Moritz, 1980). For a given geodetic latitude ϕ, the scalar normal gravity γ_0 at the ellipsoid is given by the series expansion

$$\gamma_0 \approx \gamma_a \cdot (1 + 0.0052790414\sin^2(\phi) + 0.0000232718\sin^4(\phi) + 0.0000001262\sin^6(\phi) + 0.0000000007\sin^8(\phi)) \tag{2.2}$$

using the normal gravity $\gamma_a = 9.7803267715\,\frac{\text{m}}{\text{s}^2}$ at the equator (Torge and Müller, 2012; Moritz, 1980) with an accuracy of $10^{-3}\,\frac{\mu\text{m}}{\text{s}^2} = 0.1\,\mu$Gal. In a local navigation frame (see Section 2.5) on the ellipsoid, normal gravity is perpendicular to the ellipsoid surface. Hence, the horizontal components are zero. For a given ellipsoidal height h in m, the downwards-pointing normal gravity γ_D of the vector $\boldsymbol{\gamma} = (\gamma_N\ \gamma_E\ \gamma_D)^T$ can be derived from γ_0 as (Torge and Müller, 2012)

$$\gamma_D \approx \gamma_0 - (3.0877 \cdot 10^{-6}\,\frac{1}{\text{s}^2} - 4.3 \cdot 10^{-9}\,\frac{1}{\text{s}^2} \cdot \sin^2(\phi)) \cdot h + 0.72 \cdot 10^{-12}\,\frac{1}{\text{s}^2\text{m}} \cdot h^2. \tag{2.3}$$

Since the normal plumb line is curved in Northern direction, the horizontal normal gravity for $h \neq 0$ is non-zero. The North component γ_N can be approximated as (Jensen, 2018; Torge and Müller, 2012)

$$\gamma_N \approx 8.2 \cdot 10^{-9}\,\frac{1}{\text{s}^2} \cdot h\sin(2\phi), \tag{2.4}$$

the East component γ_E is always zero due to symmetry reasons simplifying the normal gravity vector to

$$\boldsymbol{\gamma} = (\gamma_N\ 0\ \gamma_D)^{\text{T}}. \tag{2.5}$$

For many applications, the normal gravity field is a sufficient approximation of the actual gravity field. For high accuracy applications, e.g. precise physical height systems, geological research and exploration, gravimetric measurements (see Section 2.2) are required. Typically, the results are given as the deviation of gravity from normal gravity. Historically, normal gravity was computed at a reference surface with constant

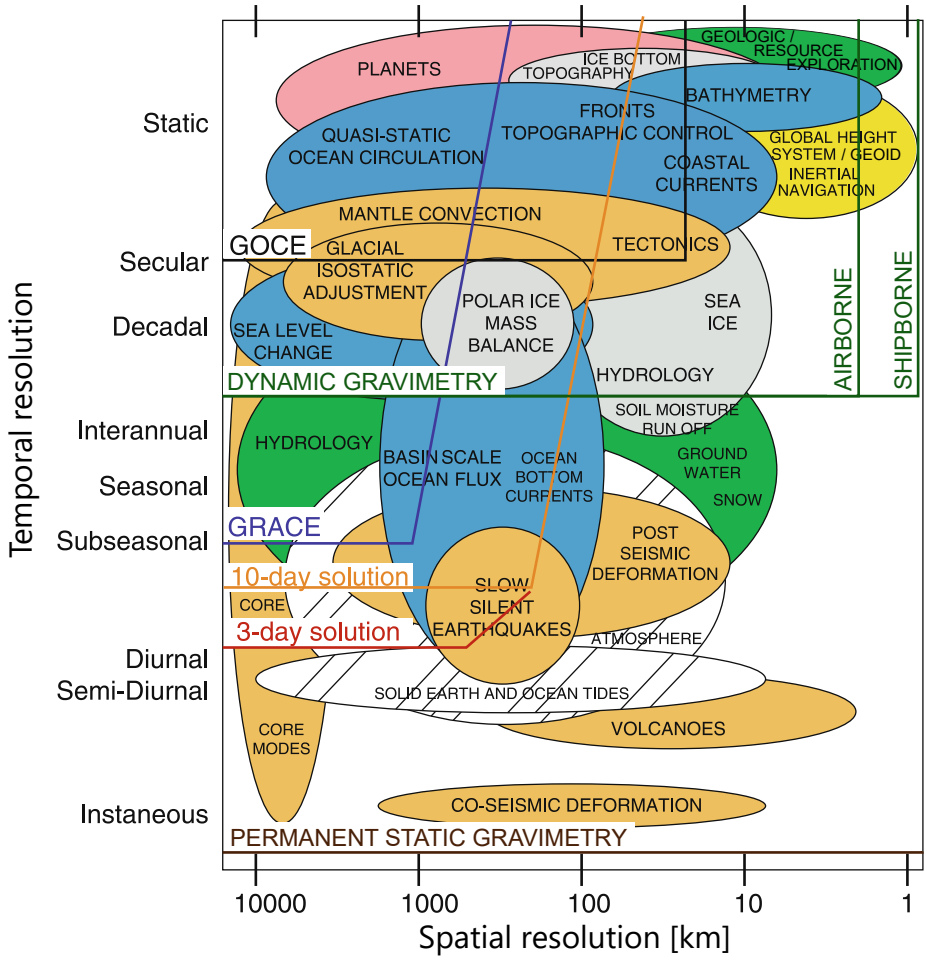


Figure 2.1: Spatial and temporal resolution of Earth system processes and gravimetric measurement methods (3-/10-day solutions are based on concepts for next generation gravity missions; reworked after Anselmi et al. (2019) and Bruton (2000))

gravity potential, i.e. the geoid. In geodesy, the corresponding difference between observed gravity and normal gravity at the reference surface is called *gravity anomaly*.

The advent of the GNSS enabled the precise observation of the ellipsoidal height at a measurement point. This allowed for the computation of normal gravity at the gravity observation point. The so-called *gravity disturbance*

$$\delta g = g - \gamma \tag{2.6}$$

is then computed as the difference of the observed gravity and normal gravity, both at the observation point. Since it is more straightforward than the gravity anomaly, the gravity disturbance is the standard result of dynamic gravimetry nowadays. However, several types of gravity anomalies are sometimes computed additionally for specific purposes like geologic research.

The gravitational potential of the Earth can be approximated using spherical harmonics. With the geocentric constant GM, the semi-major axis a of the ellipsoid, the associated Legendre polynomials P_{nm}, the geocentric colatitude θ, longitude λ and the distance r to the geocentre, the gravity potential is (Torge and Müller, 2012)

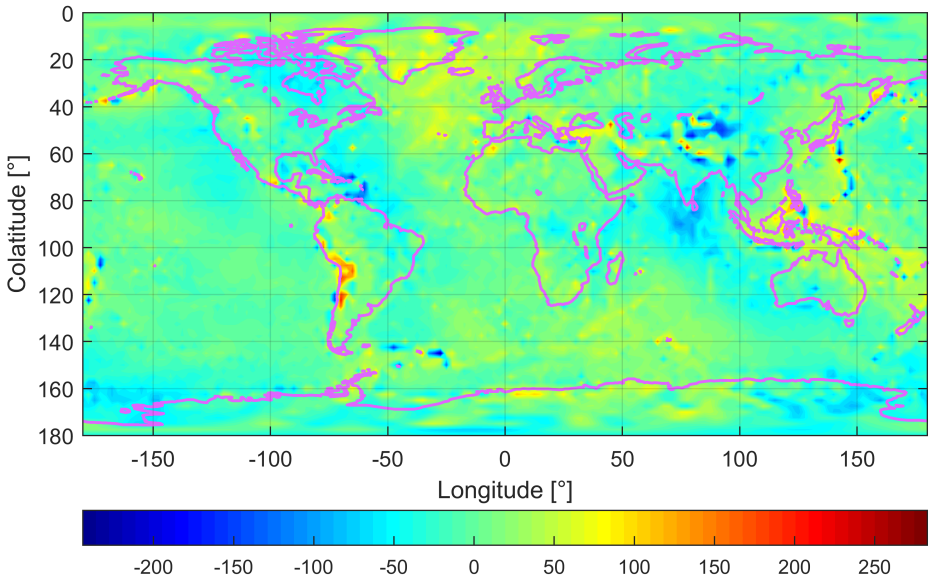


Figure 2.2: Long wavelengths of the global gravity disturbance [mGal] computed with the EGM2008 truncated at degree and order 360 at a 2.5° grid

$$V = \frac{GM}{r}\left(1 + \sum_{n=1}^{\infty}\sum_{m=0}^{n}\left(\frac{a}{r}\right)^n (C_{nm}\cos(m\lambda) + S_{nm}\sin(m\lambda))P_{nm}(\cos(\theta))\right). \tag{2.7}$$

The geocentric colatitude is obtained from the geocentric latitude $\bar{\phi}$ as $\theta = 90° - \bar{\phi}$. The coefficients C_{nm}, S_{nm} of degree n and order m are given by a gravitational model, e.g. the Earth Gravitational Model 2008 (EGM2008) (Pavlis et al., 2012). The models are truncated at a specific degree, e.g. 2160 for the EGM2008. The centrifugal potential Z and its gradient

$$\boldsymbol{z} = \boldsymbol{\nabla}(Z) = \boldsymbol{\nabla}\left(\frac{\omega_{ie}^2}{2}(x_e^2 + y_e^2)\right) = \omega_{ie}^2 \begin{pmatrix} x_e \\ y_e \\ 0 \end{pmatrix}, \tag{2.8}$$

with ω_{ie} being the Earth rotation rate and x_e, y_e being coordinates in the earth frame e (see Section 2.5), can be used to compute gravity with Equations (2.1) and (2.7). If the Earth rotation rate and the position are known, the centrifugal acceleration is computed exactly. The Euclidean norm of the gravity disturbance obtained with EGM2008 truncated at degree 360 is illustrated in Figure 2.2.

2.2 Gravimetry

The discipline of measuring gravity and the gravity gradient at the Earth and other celestial bodies is called *gravimetry* (Torge, 1989). Gravimeters (also called “gravity meters”) observe gravity; gradiometers observe gravity gradients by conducting gravity measurements simultaneously at two points with a known distance. The thesis at hand focuses on gravimetry.

The main properties of the principal observation techniques are illustrated in Figure 2.3. There are two basic approaches for conducting gravity observations:

- In **static gravimetry** (also called "terrestrial gravimetry"), a gravimeter is placed on a solid point where a single gravity observation is made. The static measurement enables the highest possible accuracy on land, but dense gravity networks in a region of interest are costly in terms of time and personnel. Furthermore, there are regions where static gravimetry is impractical or even impossible, e.g. areas covered by liquid water, remote areas like polar regions, high mountain ranges, inaccessible jungles.

- In **dynamic gravimetry**, a gravimeter is installed on a moving platform. Gravity is observed along a trajectory. The spatial resolution depends on the vehicle velocity and the length of the applied low-pass filter. The gravimeter observes the specific force

$$\boldsymbol{f}^i = \ddot{\boldsymbol{r}}^i - \boldsymbol{g}^i, \tag{2.9}$$

  which is the deviation from the acceleration that would be observed during free fall, being the difference of the kinematic acceleration $\ddot{\boldsymbol{r}}$ due to the vehicle movement and gravity $\boldsymbol{g}$, all observed in the inertial frame i (see Section 2.5). When scalar gravimeters are used, only the instantaneous vertical component in the navigation frame is observed instead of the complete specific force vector. Having computed the kinematic acceleration using GNSS observations, Equation (2.9) is solved for gravity (Kwon and Jekeli, 2001).

Dynamic gravimetry can be divided into three main categories, depending on the vehicle type:

- In **shipborne gravimetry** (also called "marine gravimetry"), gravimeters are installed on ships at sea or inland waters. Like for terrestrial measurements, the observations are made close to the geoid. Hence, the variability of the observable gravity field is maximal. The relatively low vehicle velocity allows high spatial resolutions. The combination with comparatively long low-pass filter lengths results in the best accuracy of dynamic gravimetry, with the spatial resolution still being higher than in airborne gravimetry. Since static measurements are impractical at liquid water bodies, shipborne gravimetry is the most precise gravimetric method at liquid water bodies.

- In **airborne gravimetry** (also called "aero gravimetry"), an aeroplane, a helicopter or an Unmanned Aerial Vehicle (UAV) is equipped with a gravimeter. This method can be applied everywhere on Earth, faster than with terrestrial or shipborne gravimetry. Gravity variations are damped with increasing height. Hence, small wavelengths above a specific threshold frequency depending on flight and terrain altitude as well as the vehicle velocity cannot be observed (Childers et al., 1999). Due to the higher velocities when using aeroplanes, the spatial resolution of airborne gravimetry is usually lower than in shipborne gravimetry.

- **Satellite gravimetry** enables a nearly global and repeated observation of the gravity field, except for polar gaps due to limited inclination angles of the satellite orbits. The long wavelengths of global gravity field models are almost completely based on satellite gravimetry, but even at low satellite orbits, the equipotential surface is substantially attenuated. Due to this and the high ground velocity, satellite gravimetry is limited to long wavelengths.

Further, seldom used methods are underwater gravimetry (using underwater vehicles) and car gravimetry (also called "terrestrial gravity profiling"). In both methods, the limited availability or temporary absence of GNSS signals is challenging. Further sensors like Doppler sonar velocity log, depth gauge and acoustic ranging in underwater gravimetry (Xiong et al., 2020) or map matching, Light Detection and Ranging (LIDAR)

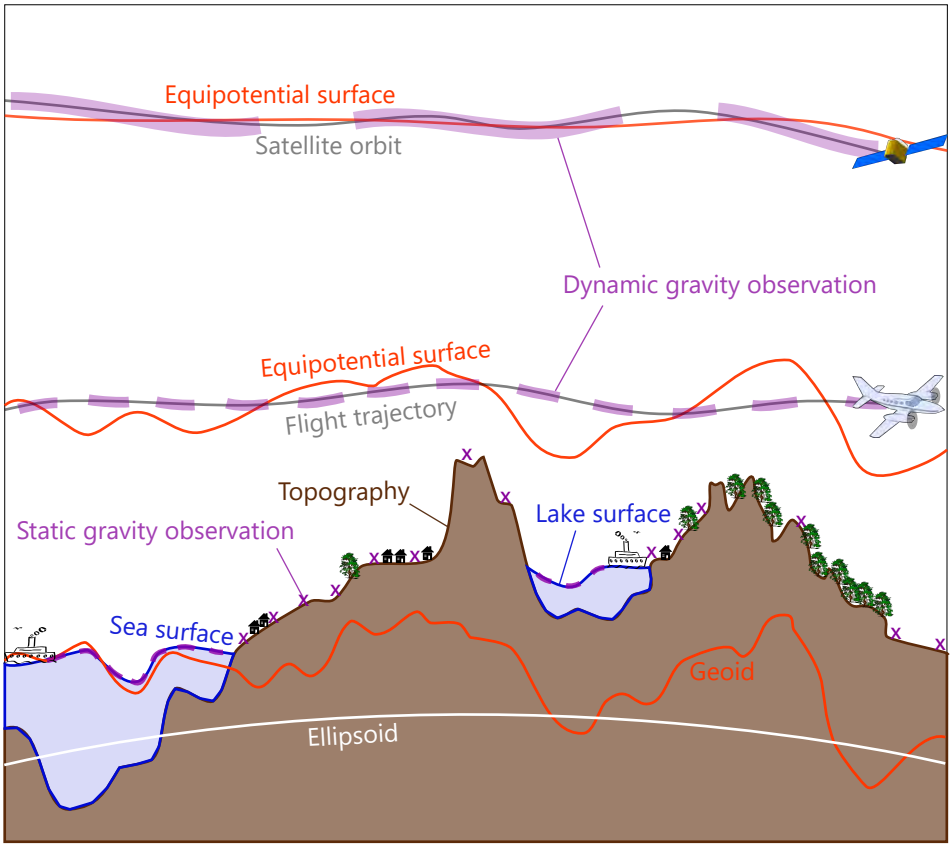


Figure 2.3: Schematic illustration of the principal gravimetric observation techniques with the equipotential surfaces of gravity near the corresponding observation heights

and image-based techniques (Groves, 2013) in car gravimetry can be used to improve the vehicle's position and attitude estimate. An advantage of car gravimetry is the possibility of point-wise 3-D gravity updates along the trajectory using terrestrial gravimeters and a zenith camera (Schack, 2021); a disadvantage is that the measurements are restricted to roads with suitable observation conditions.

Figure 2.1 summarises the resolution properties of airborne, shipborne and satellite gravimetry and possible applications. While the temporal resolution and the global coverage of recent satellite systems (see Section 2.2.1) are benefits of satellite gravimetry, the spatial resolution of airborne and even more shipborne gravimetry being well below 10 km outperforms satellite gravimetry easily.

The following Sections give an overview on the history and the state of the art of the introduced gravimetry techniques focussing on airborne and shipborne gravimetry, since the latter techniques will be analysed in detail in the work at hand.

2.2.1 Satellite gravimetry

Historically, satellites applied for gravimetry were passive. Already the first satellite, Sputnik, was used to derive the ellipsoidal shape and flattening of the Earth in the 1950s. Since the 1970s, several satellites equipped with retro-reflectors were sent to low and medium Earth orbits. The satellite positions were determined more precisely by Satellite Laser Ranging (SLR). Since their orbits are affected by gravitation, the position measurement enables the determination of the Earth's (long-wavelength) gravitational field. Examples for SLR satellites are Starlette (Satellite de Taille Adapté avec Réflecteurs Laser pour les Études de la Terre, orbit

height of 800 km) and both LAGEOS (Laser Geodynamics Satellite) satellites (launched in 1976 and 1992, orbit height of 5,900 km) (Petit and Luzum, 2010). In addition to SLR, radar and Doppler systems can be used for satellite gravimetry.

The sea surface height can be measured by satellite altimetry where a radar signal is emitted by the satellite, reflected by water surfaces and detected by the satellite. After correction for tides, sea currents and atmospheric pressure, the geoid height is obtained and can be included in the development of gravity models.

Satellite gravimetry applying laser/radar distance or Doppler measurements to the Earth is limited by inaccurate observations and atmospheric disturbances (Flechtner et al., 2021). In the 1990s, the NAVSTAR Global Positioning System (GPS) and more precise accelerometers became available enabling gravimetry with enhanced accuracy applying Satellite-to-Satellite Tracking (SST) methods. The following SST satellite gravimetry missions are of special importance. The data is taken from Flechtner et al. (2021), where the reader finds detailed information on the missions.

- **CHAMP**: In 2000, the German Research Centre for Geosciences (GFZ) and the German Aerospace Center (DLR) brought the Challenging Minisatellite Payload (CHAMP) satellite into a polar, almost circular orbit. Equipped with dual-frequency GPS receiver ("high-low SST") and precise accelerometers, CHAMP enabled the global determination of gravity with a strongly improved accuracy compared to previous satellite missions. The low initial orbit height of 454 km should allow improved observations at a spatial resolution of 800 km (half-wavelength). Until the end of operability in 2010, the satellite descended to an orbit height of 260 km before it burnt up in the atmosphere.

- **GOCE**: In the Gravity and Steady-State Ocean Circulation Explorer (GOCE) mission, a 3-D gradiometer consisting of two sets of three perpendicular accelerometers was used by the European Space Agency (ESA) to refine the global gravity field with an accuracy of 1 mGal (corresponding to a geoid height of 1...2 cm) and a spatial resolution of 100 km (half-wavelength), which was enabled by the very low, sun-synchronized orbit with an orbit height of 255 km at the launch of the mission in 2009 and 224 km at the end of operation in 2013.

- **GRACE**: The satellite mission with the longest duration of operability (2002 to 2017) was the Gravity Recovery and Climate Experiment (GRACE). The National Aeronautics and Space Administration (NASA), GFZ and DLR operated the mission based on the "tandem low-low SST" measurement principle: Two satellites were sent to the same quasi-polar, quasi-circular orbit and followed each other with a distance of 220 km at an orbit height of 500 km descending to 345 km. In addition to the satellite position determination using GPS and electrostatic accelerometers, the range between both satellites was observed using a microwave measurement system with an accuracy of a few μm. The varying gravitation field of the Earth leads to a distance variation between both satellites of up to $\pm 100\,\mu$m above the Himalayas. The main purpose of the mission was to monitor changes in the gravity field. For this, complete gravity field models were generated every 30 days with a spatial resolution of 400 km. Due to the parallel ground track of the orbits in North-South direction, erroneous striping effects occur in the results reflecting the lower sensitivity in East-West direction. The effect can be reduced in post-processing.

- **GRACE-FO**: Following a data gap of about five months, the GRACE Follow-On (GRACE-FO) mission was launched in 2018. The mission design is similar to GRACE, but the range measurements between the new satellite tandem are improved to an accuracy of 10 nm by using a Laser Ranging Interferometer. The end of operability of GRACE-FO is planned to be at the earliest in 2023.

While the GRACE-FO mission is still running, future satellite gravimetry missions are already in planning stages. A further GRACE-like mission might be supplemented by a second satellite tandem on a non-polar orbit in a constellation proposed by Bender et al. (2008) in order to remove the striping effect and improve

spatial and temporal resolution. ESA's next generation gravity mission aims to yield a geoid accuracy of 1 mm at a spatial resolution of 150 km (500 km) every 10 days (3 days) (see Figure 2.1) (Haagmans et al., 2020). In the long term, Cold Atom Interferometry (CAI) gradiometers and hybrid quantum/electrostatic accelerometers might enhance the measurement accuracy (Knabe et al., 2022).

2.2.2 Airborne gravimetry

The first airborne gravimetry flights have been conducted in the late 1950s. Thompson and LaCoste (1960) reported an accuracy of about 10 mGal for gravity readings at 5 min average. A stable platform LaCoste marine gravimeter was used and the positioning was carried out using a Doppler radar and a hypsometer (barometric elevation determination) (Nettleton et al., 1960). The positioning was verified photogrammetrically using photo-theodolites.

For some decades, the position and navigation accuracy limited the accuracy of airborne gravimetry (Nabighian et al., 2005). The advent of GPS was a push for airborne gravimetry. High-accuracy positioning became possible using precise geodetic GNSS receivers in dual frequency phase observation mode. In order to remove location-dependent errors in the GNSS observations, the position of the aircraft was computed in the (Precise) Differential GNSS ((P)DGNSS) mode requiring a base GNSS station. The first letter "P" in PDGNSS indicates that GNSS phase observations are used instead of code observations alone. When using the abbreviation "DGNSS" in the following, it is assumed that phase observations are used anyway. First airborne gravimetric flights at Greenland verified the possibility to use DGPS for horizontal and vertical positioning using stable platform LaCoste & Romberg (L&R) S-Type and Bell gravimeters. The vertical GPS accuracy was found to be at least on par with the accuracy of a radar altimeter (Brozena, 1992). Since the 1990s, airborne gravimetry campaigns using stable platform gravimeters were operated routinely using GNSS. Results have been verified by comparing them to shipborne data (Bastos et al., 1998). Forsberg et al. (2001) reported non-adjusted RMSE precision (see Section 5.5) better than 2 mGal for Arctic campaigns between 1998 and 2000. A similar accuracy was stated by Studinger et al. (2008) using stable platform IMUs as gravimeters when comparing the results with a terrestrial gravity line under the airborne line.

Alternatively to the classical approach of installing the gravimeter on a horizontally stabilised platform, IMUs can be "strapped down" to the aircraft. The theoretical feasibility of this approach was shown by K. P. Schwarz (1983). In 1995, *strapdown* gravimetry was performed successfully for the first time by Wei and K. P. Schwarz (1998). The accuracy was about 2 mGal at a spatial resolution (half wavelength) of 7 km. The IMU was a Honeywell LASEREF III with QA2000 accelerometers and GG1342 ring laser gyros. A side-by-side comparison of this IMU with a Litton 101 showed an agreement at the level of 1.6 mGal after removing a linear drift from each line (Glennie and K. P. Schwarz, 1999). Glennie et al. (2000) published a side-by-side comparison of a LASEREF III and a stable platform L&R S-type gravimeter reporting a Root Mean Square (RMS) agreement of 2...3 mGal. The operational reliability of the LASEREF was higher during the flights. The authors concluded that both systems "give the same level of gravity-field information at all but the longest wavelengths". They suggested a combination of both systems until the drift behaviour of the strapdown system is improved. An efficient method to enhance the long-wavelength behaviour of an IMU was proposed by Becker et al. (2015b). They showed that an easy-to-realise warm-up calibration of the vertical accelerometer removes the bulk of sensor drifts. Further, more elaborated calibration methods were introduced by Becker (2016). Alternatively to thermal calibration, the IMU sensors can be thermally stabilised using a designated housing. Tests with such a thermal stabilisation housing have been performed successfully at the Technical University of Darmstadt (TU Darmstadt) since 2018. Other groups with similar housings also verified their effectiveness (Jensen et al., 2019; Simav et al., 2020). Strapdown gravimeters could also be used in UAV campaigns, which might lower campaign costs and enhance safety for the personnel in future campaigns. First test flights with UAVs have already been conducted (Lin et al., 2018).

Since the early 1990s, DGNSS is typically used for GNSS positioning in airborne gravimetry. In the alternative Precise Point Positioning (PPP) approach (Zumberge et al., 1997), a GNSS base station is not needed, since the rover observations are corrected based on precise GNSS satellite and clock products provided by analysis centres. PPP proved to be a reliable positioning approach for airborne campaigns, which has been verified in multiple campaigns in Becker (2016), Jensen (2018), and Jensen et al. (2019) reaching accuracies at the 1 mGal level. Several kinematic acceleration determination methods exist that will be introduced in Section 4.

All classical stable platform and strapdown gravimeters are limited to relative gravity estimates. Typically, the absolute gravity estimates are obtained by anchoring the results to known reference values at the airports obtained by terrestrial gravimetry ("endmatching") (Kwon and Jekeli, 2001) or, seldom, by shifting the flight results to a global gravity model reference, e.g. by combining complementary high and low pass filters (Bruton, 2000). With a newly developed CAI gravimeter, Bidel et al. (2020) showed that airborne gravimetry is possible directly obtaining absolute results with a reported accuracy of less than 4 mGal in first test flights above Iceland. The results are promising and indicate that absolute gravimeters might play an important role in the future of airborne gravimetry. However, typical current relative gravity results are still of superior quality after endmatching.

2.2.3 Shipborne gravimetry

Due to the lower velocity and less high-frequency disturbing motion of the vehicle, shipborne gravimetry (also called "marine gravimetry") is easier to realise than airborne gravimetry, at least at calm sea conditions. That is why shipborne gravimetry was implemented more than 50 years before airborne gravimetry by Hecker (1903) using gas-type gravimeters where gas at a specific temperature and pressure worked like a spring element. The first actual spring type gravimeter of the manufacturer Graf enabled Worzel (1965) to obtain gravity results at the 1 mGal level (Nabighian et al., 2005), beginning from 1957. L&R spring gravimeters were first used in shipborne gravimetry in 1958 by Harrison (1959) and LaCoste (1959), who reported an agreement with submarine measurements of 5 mGal in a first test.

After the first L&R gravimeters have been gimbal supported, the successful L&R S-type gravimeter has been introduced by LaCoste et al. (1967) using a gimbaled platform. LaCoste (1967) reported that accuracies better than 1 mGal are possible with this gravimeter. S-type gravimeter have still been used in recent campaigns, e.g. Jensen et al. (2019), new gravimeters are manufactured by ZLS Corporation. Other commonly used gravimeters were manufactured by Bodenseewerke/Askania, which were also still used in the new millennium. Furthermore, there exist other stable platform gravimeter types like the Chekan-AM (Krasnov et al., 2011). In five campaigns at the Baltic Sea between 2013 and 2016, Lu et al. (2019) reported an accuracy of 0.5 mGal achieved with the Chekan-AM.

Although the long-term drift behaviour is of higher importance for marine campaigns if the cruises take more time than a typical flight, strapdown gravimeters are also suitable for shipborne gravimetry. This will be shown in the work at hand and has also been verified by Cai et al. (2017) and Wang et al. (2018), where the strapdown gravimeters SGA-WZ and SAG-2M have been used side-by-side with L&R gravimeters, respectively, indicating strapdown accuracies around the 1 mGal level. In a marine experiment presented by Yuan et al. (2020), four stable platform gravimeters (GT-2M, L&R S-type, CHZ-II and ZL11) were run side-by-side with two strapdown gravimeters (SAG-2M and SGA-WZ). A quality assessment based on crossover points indicated that the precision of all gravimeters except the L&R was better than 0.5 mGal. The best results in varying sea conditions were obtained with the GT-2M gravimeter.

2.2.4 Static terrestrial gravimetry

The first documented successful gravity measurement was done in 1656 by Huygens by measuring the oscillation period of a pendulum with known length. This absolute method was limited to the precise measurement of the pendulum length. Enhanced absolute and relative pendulum set-ups were still used until about 1940 (Nabighian et al., 2005; Marson, 2012). In the second half of the twentieth century, absolute gravity measurements were usually conducted with free-fall or rise-and-fall gravimeters where the test masses where observed by laser interferometry. At the beginning of the current century, CAI was developed where a cluster of cold Rubidium atoms are imposed to a free-fall set-up. While they fall, they are exposed to three Raman laser pulses. The subsequent phase shift of the atomic wave function depends on gravity.

Spring-type gravimeters are commonly used in *relative* gravimetry. The highest sensitivity is obtained in an astatic setup with a "zero-length" spring. The first gravimeters of this type were developed in 1934 by LaCoste. While spring-type gravimeters are subject to drifts, superconducting gravimeters are theoretically drift-free. A superconducting test mass is levitated and hold in a reference position by electromagnets. This technology was developed in the 1960s. For terrestrial reference measurements in dynamic gravimetry, spring-type gravimeters are still the most suitable gravimeters in terms of measurement mobility, weight and costs. Their accuracy is about two orders of magnitude better than the accuracy of dynamic gravimetry.

2.3 Gravimeter types of dynamic gravimetry

This work primarily analyses data of an iMAR iNAV-RQH-1003 (iNAV-RQH) strapdown gravimeter. Since 2018, this IMU is encapsulated in a thermally stabilised housing named iMAR iTempStab-AddOn (iTempStab). In some campaigns, other IMUs by iMAR (iNAT-RQH and iNAT-RQT) have been used side-by-side with TU Darmstadt's iMAR. There are only minor differences in the measurement principles of the iMAR generations. Additionally to the strapdown gravimeters, at some campaigns, the observations of two gravimeter types following the "classical" approach of horizontal stabilisation will be considered.

The main differences between TU Darmstadt's strapdown gravimeter and the stable platform gravimeters Chekan-AM owned by GFZ and L&R S-type owned by National Space Institute at the Technical University of Denmark (DTU Space) are summarised in Table 2.2. Most table information was obtained from personal experience/measurements or by the gravimeter owner. Stable platform gravimeters are limited to the vertical component of gravity. The observation accuracy depends on the quality of the automatic levelling device. Especially after turns, the platform needs some time for stabilisation. Since the levelling errors are higher during turbulence / harsh sea conditions, results of the classical gravimeters are usually omitted when obtained under such conditions. In contrast to the strapdown IMUs, an operator is required for the Chekan and the L&R during the flights/cruises, especially before and after turns. Due to the levelling platform, the classical gravimeters are heavier, need more space and the power consumption is higher. These properties limit the available flight time of stable platform gravimeters, especially in small aircraft, and make UAV flights impossible.

On the one hand, the measurement accuracy strongly improves when a strapdown IMU is encased in a thermally stabilised housing because of the elimination of thermally induced sensor drifts. On the other hand, some advantages of strapdown gravimetry are weakened: Such a housing increases the dimensions and weight of the gravimeter. Additionally, the temperature stabilisation elements (e.g. Peltier elements, fans) increase the power consumption, especially during warm-up and at very low or high environmental temperatures. However, the space, weight and power requirements are still much lower than for stable platform gravimeters (see Table 2.2).

In this section, the gravimeter types used for evaluation in this thesis will be introduced briefly. Since the focus of this work is on TU Darmstadt's strapdown gravimeter, it will be presented in more detail.

Table 2.2: Properties of gravimeters appearing in this thesis (values based on personal experience, by GFZ, DTU Space, Becker (2016), Krasnov et al. (2011) and LaCoste (1967), values include horizontal stabilisation devices)

	iNAV-RQH-1003	iNAV-RQH-1003 w. iTempStab-AddOn	Chekan-AM	L&R S-type
Installation	strapdown		stable platform	
Measurement principle	3-D quartz accelerometers and 3-D RLG		1-D double quartz elastic systen	1-D astatic zero-length spring
Temperature stabilisation	✗	✓	✓	✓
3-D results possible?	✓		✗	
Turbulence resitency	high		low	
Automatic in-flight operation?	✓		✗	
Dimensions [cm^3]	30 x 22 x 18	43 x 25 x 31	45 x 45 x 64	70 x 55 x 65
Weight [kg]	12.5	22	72	80
Power consumption [W]	< 45	200 (start-up); 30...90 after stabilisation	> 250	< 300

2.3.1 Horizontally-stabilised gravimeters: Chekan-AM and LaCoste S-Type

The *Chekan-AM* gravimeter (Figure 2.4) was developed by CSRI Elektropribor in the first decade of the current century. It was primarily designed for marine applications (Krasnov et al., 2011). The observations are based on a double quartz elastic system (DQES) with two pendulum levers (Figure 2.5). Each of the lever arms has a proof mass at its end and is installed at a quartz torsion element in an organic silicon liquid. Quartz is chosen because of its very low coefficient of thermal expansion. The liquid removes high-frequency movements of the vehicle, and reduces the influence of external temperature and pressure. The tilt angle of each lever is observed optic-electronically: A photodiode emits directed electro-optical radiation that is forwarded by a system of lenses and a mirror at the pendulum to a linear Charge-Coupled Device (CCD). The set-up with two pendulum levers strongly reduces the influence of cross-coupling effects. The temperature of the device is stabilised using Peltier elements. The position of the gimbal suspension is set based on observations of a gravity sensor, two gyroscopes and two accelerometers. The sensor drift of the Chekan-AM can reach some mGal per day, but is predominantly linear. Experiences with the sensor in measurements indicate that the non-linearity of the drift might increase with the sensor age (see Section 9.2.1).

The *L&R S-type* gravimeter by DTU Space (Figure 2.7) was already developed in the 1960's (LaCoste et al., 1967; LaCoste, 1967). Its working principle is illustrated in Figure 2.6. The core of the device is a typical L&R gravimeter: A zero-length spring is fixed to a pendulum lever arm and a non-vertical bearing (astatic set-up). In this set-up, drifts in the photoelectric measurement of the vertical beam position do not affect the gravity results adversely (LaCoste, 1967); longitudinal and transverse spring vibrations are negligible. The sensitivity is lower in comparison to terrestrial L&R gravimeters in order to resist high-frequency vehicle movements. The sensor drift observed in recent campaigns by DTU Space was lower than 0.2 mGal per day,

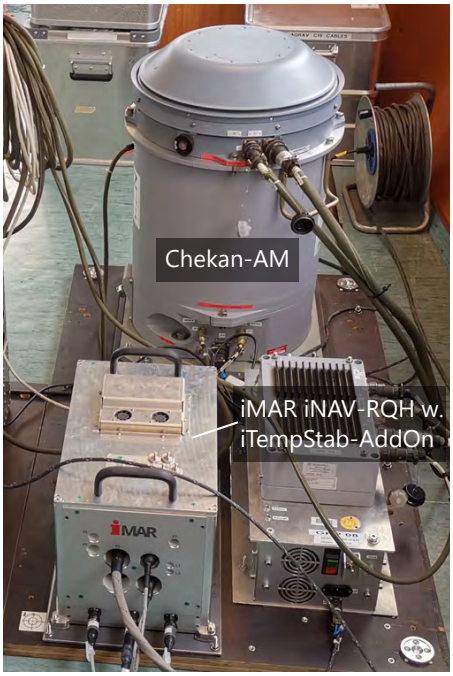


Figure 2.4: The Chekan-AM gravimeter owned by the GFZ installed next to TU Darmstadt's iMAR iNAV-RQH-1003 with iTempStab at the Müritz 2019 campaign

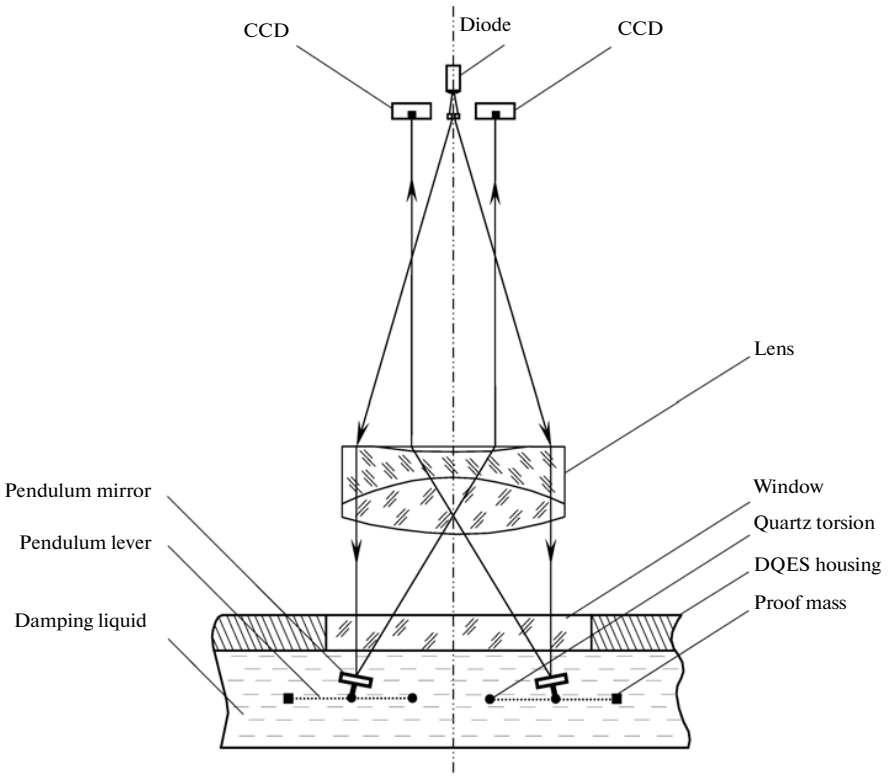


Figure 2.5: Measurement principle of the Chekan-AM gravimeter (Krasnov et al. (2011), reproduced with permission from Springer Nature)

which is almost negligible for single flights. According to LaCoste et al. (1967), cross-coupling errors are "important but correctable".

2.3.2 Strapdown gravimeter: iMAR iNAV-RQH-1003 with iTempStab-AddOn

The strapdown gravimeter owned by the chair of Physical and Satellite Geodesy at TU Darmstadt and used in all campaigns that will be presented in this work is of the type iNAV-RQH-1003 (Figure 2.8a) by the manufacturer iMAR Navigation. It is a navigation grade IMU that was originally designed for high-precision navigation purposes. In 2018, the system was extended by a thermally stabilised housing of the type iTempStab-AddOn (Figure 2.8b). There have been made some specific modifications to the IMU that are under manufacturer confidentiality.

Figure 2.9 gives an overview of the most relevant components of the combined system of the IMU and the thermal housing. The core of the system is the Internal Sensor Assembly (ISA) by the manufacturer Honeywell. The ISA is mounted to the IMU with shock mounts in order to damp exterior shocks, vibrations and the dithering of the gyroscopes (Becker, 2016). The main components of the ISA are three perpendicular QA-2000 accelerometers and GG1320AN ring-laser gyroscopes each and a clock. The manufacturer specifications can be found in Table 2.3 or in more detail in IMAR Navigation (2012).

Since the accelerometers are the main sensors for strapdown gravimetry, the working principle of the QA-2000 accelerometer based on the *Q-Flex* construction is introduced briefly. The basic construction was

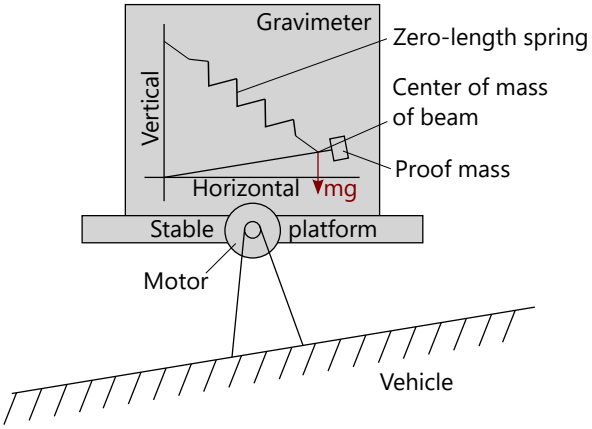


Figure 2.6: Measurement principle of the L&R S-type gravimeter including the stable platform (based on LaCoste (1967))

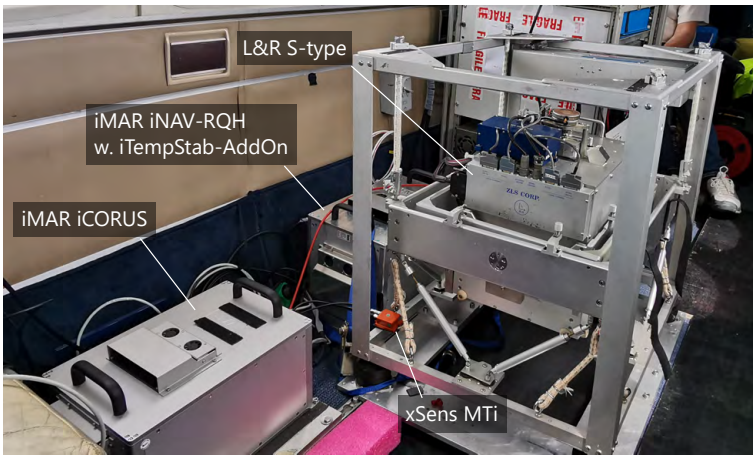
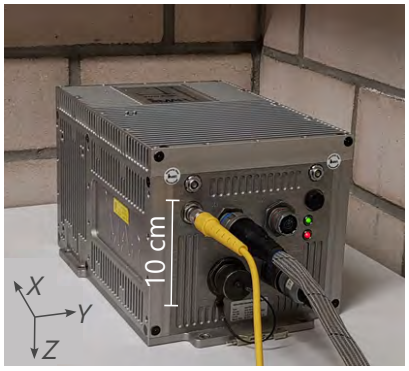


Figure 2.7: The L&R S-type gravimeter by DTU Space installed next to strapdown gravimeters and the magnetometer xSens MTi at the Malaysia 2022 campaign



(a) The IMU: iNAV-RQH-1003



(b) The IMU encased in the iTempStab-AddOn

Figure 2.8: TU Darmstadt's strapdown gravimeter by iMAR with IMU axes X, Y, Z (modified after Förste et al. (2020))

Table 2.3: Specifications of the Honeywell inertial sensors of the iNAV-RQH-1003 according to IMAR Navigation (2012)

	Accelerometers	Gyroscopes
Name	Q-Flex QA-2000	GG1320AN
Bias	$< 25\,\mu$g	$< 0.003°/$h
Bias stability	$< 10\,\mu$g	$< 0.002°/$h
Random walk	$< 8\,\mu\text{g}/\sqrt{\text{Hz}}$	$< 0.0025°/\sqrt{\text{h}}$
Linearity error	< 100 ppm	< 5 ppm
Axis misalignment	$< 25\,\mu$rad	
Data latency	< 3 ms	

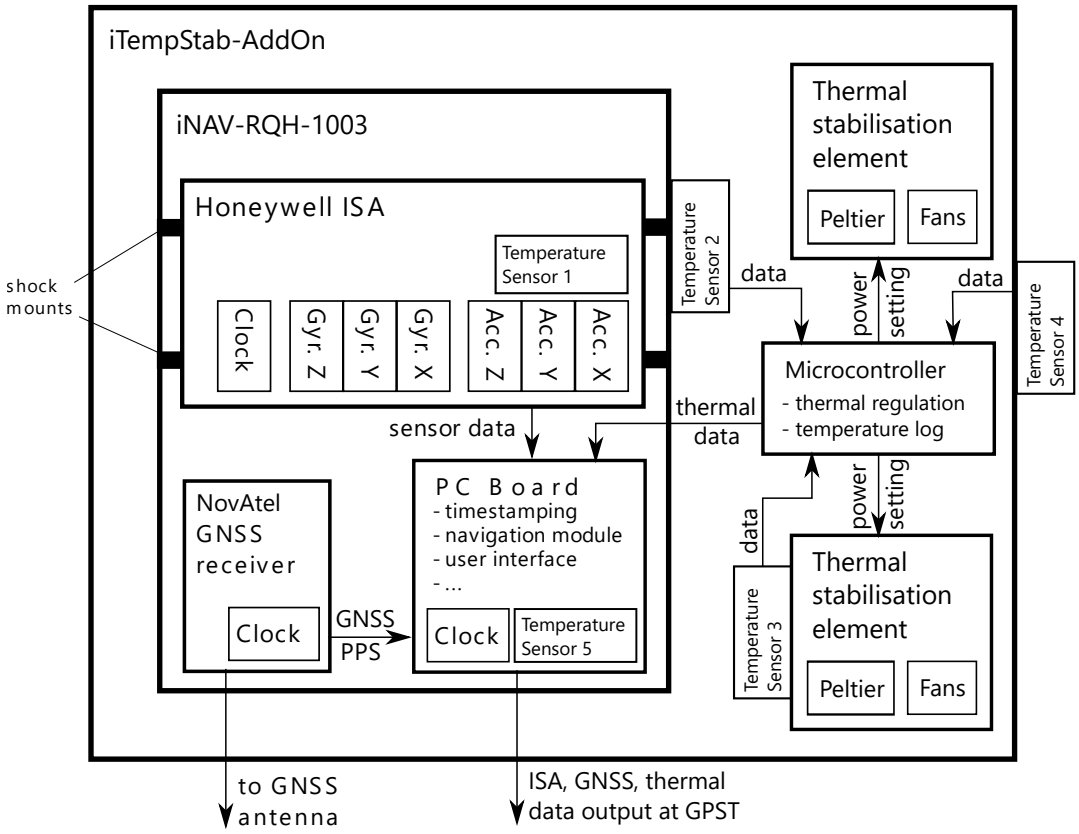


Figure 2.9: Relevant components of the system design of the iMAR iNAV-RQH-1003 with iTempStab-AddOn (modified after Becker (2016))

patented in the 1970s (Jacobs, 1972), but is still used for high-precision applications (Touboul et al., 2016). A U-shaped pendulum and the pendulum hinges ("flexures") are formed of a single fused quartz structure (Figure 2.10). The partly metallised pendulum is placed around a permanent magnet. When accelerations occur in the sensitive direction x_a of the sensor, the resulting displacement of the proof mass, the pendulum with forcer coils, is measured capacitively. A signal is sent to a servo drive which regulates the current on the forcer coils that are placed on the pendulum next to the magnet. The force is proportional to the magnetic field. The electromagnetic interaction between the magnet, the coil and the metallised pendulum lets the pendulum swing back to its centre position. More details on the Q-Flex construction can be found in Lawrence (1993).

The misalignment of the complete ISA with respect to the designated IMU axis can be up to 0.1°, but is irrelevant to the gravity results since this type of misalignment only affects the lever arm between the IMU and the GNSS antenna in an insignificant way. Becker (2016) showed that the ISA misalignment and the interior misalignment between the single accelerometers and gyroscopes depends on the temperature. The sensor data including the reading of a temperature sensor inside the ISA is transferred to a PC inside of the IMU. The location of the ISA temperature sensor is unknown due to restrictions by the manufacturer Honeywell.

Becker (2016) performed three 60 h static measurements for the IMU and analysed the noise depending on different window sizes by computing the Allan variance (Allan, 1966; El-Sheimy et al., 2008). Three different attitude settings were applied in a way that each accelerometer was vertical in one of the runs. The main results were as follows: The standard deviation of the actually vertical accelerometer was consistently lower by

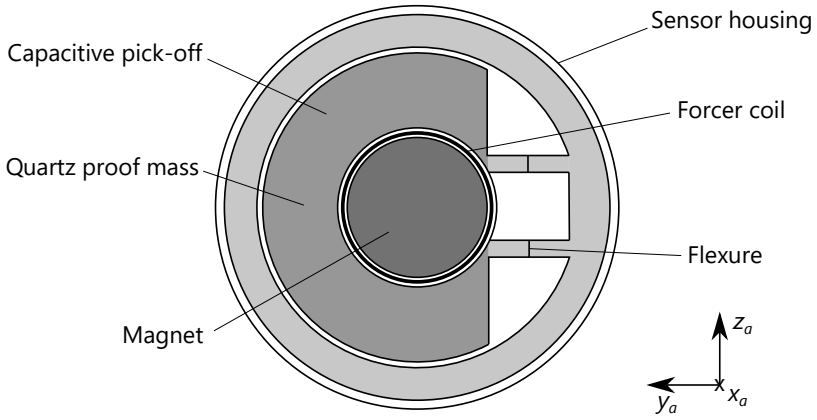


Figure 2.10: Schematic topview of the Q-Flex accelerometer construction (based on Lawrence (1993)) and single accelerometer axis directions. The sensitive axis x_a and the movement direction of the proof mass are perpendicular to the paper plane

a factor of 2.5 to 3. For small window sizes, the sensor behaviour was dominated by quantisation noise. The minimum standard deviation was about 0.07 mGal at a window size of about 42 min for the actually vertical accelerometer and more than 0.3 mGal at 15 min for the horizontal accelerometers. For longer window sizes, the increasing sensor noise could not be assigned unequivocally to a specific error category.

The IMU includes a GNSS receiver. The purpose of the original single-frequency GPS receiver by uBlox was to ensure a time synchronisation with GPS Time (GPST) using a Pulse-Per-Second (PPS) signal. By the end of 2018, the IMU received a further upgrade where the original receiver was replaced by a NovAtel OEM729 multi-frequency receiver board (NovAtel Inc., 2017). This geodetic receiver with 555 channels tracks all current GNSS frequencies. The NovAtel receiver in combination with the iNAV-RQH enables the tracking of all frequencies at a data rate of 5 Hz, which is sufficient for airborne gravimetry. Hence, an external GNSS receiver is not necessary for this gravimeter.

The ISA sensor and clock as well as the GNSS receiver observations and PPS signal are transferred to the PC board of the IMU. The board synchronizes the sensor data with the PPS signal and can be accessed via a user interface. A direct GNSS/IMU integration in order to obtain a navigation solution (i.e. position, velocity, attitude) is possible. This feature is typically not used for dynamic gravimetry since the the gravity processing can be done in post-processing.

The main elements of the iTempStab are two thermal stabilisation assemblies with Peltier elements and ventilators, a microcontroller and several temperature sensors. The thermal regulation code has been developed by iMAR and was slightly adapted by TU Darmstadt for the specific thermal properties of their strapdown gravimeter. The following temperature sensors are part of the IMU and the iTempStab (see Figure 2.9):

1. The first sensor is located inside of the ISA and is the best available information about the temperature close to the inertial sensors. It can be read out by the PC board of the IMU, but will not be used by the iTempStab controller. The data is best suited for thermal calibrations (see Section 2.4).

2. Sensor 2 is placed inside of the iTempStab housing at the cover of the IMU. This sensor is used by the controller as controlled variable with a target of 50°C. It turned out to be best practice to set the target temperature prior to a campaign, since varying target temperatures can have a huge impact to the results if the gravimeter is turned off and on again during a campaign. If the temperature is lower than the target, the Peltier elements will be set to the heating mode. If the temperature is higher, the Peltier elements will be in cooling mode. The power of the Peltier elements is set proportional to

the temperature difference to the target until a specific maximum absolute difference value is reached. Then, the Peltier elements heat/cool with 90 % power. A high target temperature was selected since heating requires less power than cooling. For most evaluated campaigns, the iTempStab was in moderate heating mode most of the time.

3. The third sensor is located inside the iTempStab as well, but close to the Peltier elements. If the sensor exceeds a specific threshold temperature, the ventilators will be activated.

4. Sensor 4 is integrated in a cable outside the iTempStab housing and is an indicator for the environment temperature. This sensor is used to examine the functionality of the iTempStab under various cabin temperature conditions.

5. Temperature sensor 5 measures at the PC board of the IMU. It is not used in the scope of this work.

The typical thermal behaviour of the strapdown gravimeter is illustrated in Figure 2.11a. In this test, the gravimeter was placed on a table at TU Darmstadt with a room temperature of about 21°C and was turned on for about 8 hours. The Peltier elements heated with full power until sensor 2 (in iTempStab on IMU) nearly reached its target temperature of 50°C after 33 min (Figure 2.11c). Afterwards, the heating reduced with some oscillations until about 5 hours after the activation of the gravimeter. The regulation stabilises with minor oscillations at a low Peltier cooling power (7...10 %). For the inertial measurements, the ISA temperature is most important. It is stable after about 4 hours. This duration was also observed at other environment temperatures between 10 and 30°C. The temperature range at the ISA sensor is typically less than 0.7 K after warm-up. During the test, the environment temperature was almost constant. Nevertheless, sensor 4 shows a slight increase in the fist 50 min, since the cable outside of the iTempStab housing where the sensor is placed is heated up by the gravimeter by some Kelvin. Typically, the actual environment temperature is about 2 to 5 K lower than the reading of sensor 4.

The low-pass filtered readings of the vertical accelerometers (up direction, mean value subtracted) are shown in Figure 2.11b. The acceleration differences of about 40 mGal are mainly due to thermal effects during warm-up. In the first 15 min after start-up, the readings are impaired by a repeatable turn-on effect. The warm-up and and turn-on behaviour of the vertical accelerometer was already described by Becker (2016). After about 4 h, the observed acceleration is approximately stable. Having removed the mean value and a linear drift of about 3 $\frac{\text{mGal}}{\text{d}}$, the RMS is about 0.2 mGal after stabilisation.

The microcontroller transmits the data of the temperature sensors 2 to 4 and the power settings of the Peltier elements and ventilators to the PC board of the IMU (see Figure 2.9). The time-stamped accelerometer, gyroscope and GNSS observations as well as the thermal data can be accessed from the IMU, e.g. via Ethernet connection.

2.4 Thermal IMU calibration

2.4.1 Possible approaches

Changes in temperature affect the readings of IMUs. For the iNAV-RQH that is used in this thesis and was presented in Section 2.3.2, several thermal calibration methods for one or more accelerometers have been applied by Becker (2016):

- **Warm-up calibration of the vertical accelerometer**: In this simple approach, the IMU is placed on a solid surface at room temperature. The readings of the vertical accelerometer are collected during the warm-up period. The procedure is repeated several times. Between the records, the IMU is turned off in order to let the IMU cool down. A calibration function of the accelerometer bias depending on the

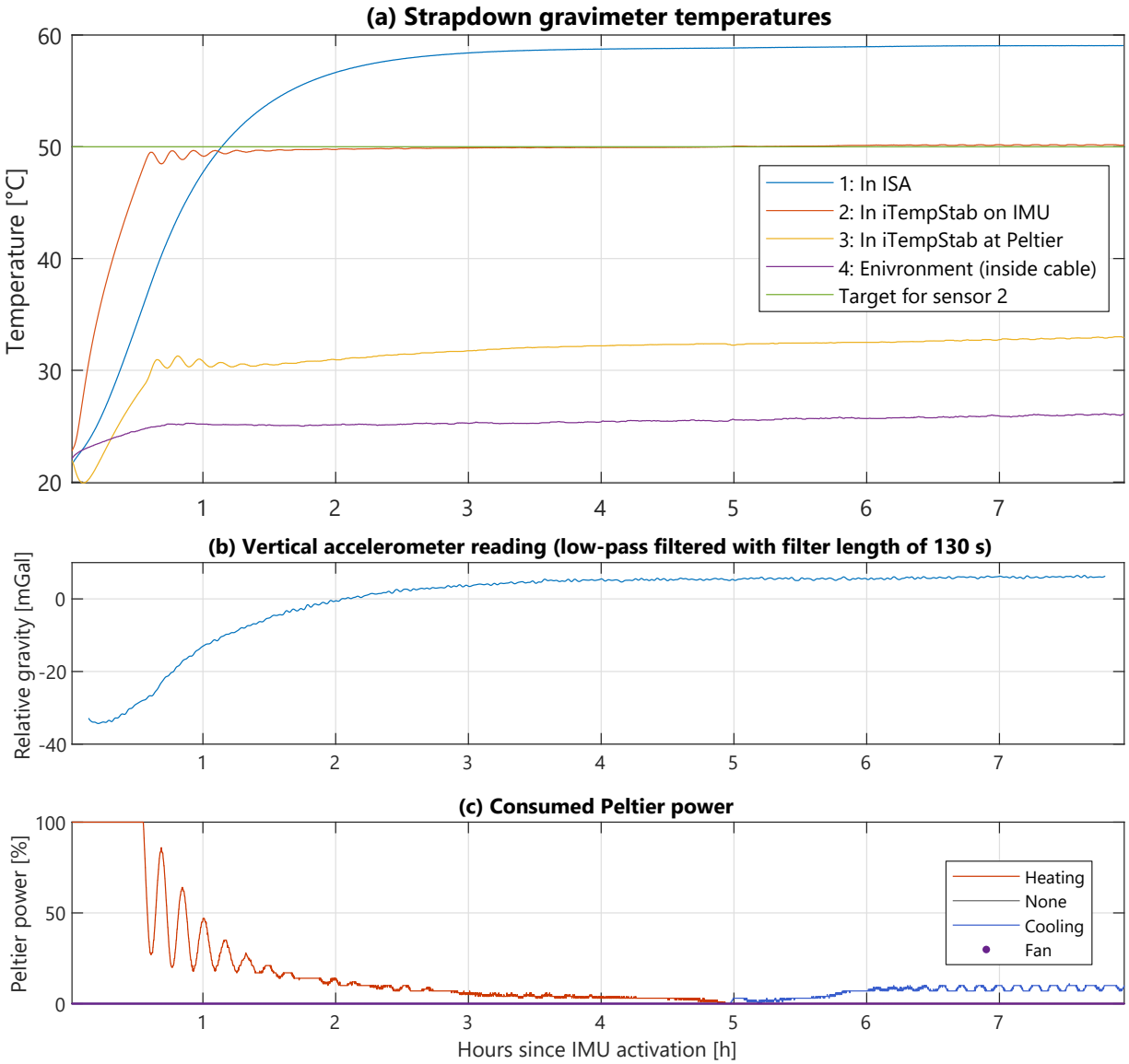


Figure 2.11: Temperatures measured by the iNAV-RQH-1003 with iTempStab-AddOn at a static measurement on May 7, 2020 with the filtered readings of the vertical accelerometer and the power settings of the Peltier elements

ISA temperature is estimated. The function is used to correct the readings of the vertical accelerometer during measurement campaigns.

- **Temperature oven calibration of the vertical accelerometer**: The approach of the warm-up calibration is slightly adapted by placing the IMU in an oven where the temperature can be set considering the IMU temperature range according to the manufacturer specifications. Each oven temperature is held for a specific time in order to enable a stabilisation of the ISA temperature.
- **Parametric calibration**: The IMU is placed on a (2-axis) turntable with a temperature oven. Gravity is used as a stimulus signal. The sensed accelerations vary since the IMU is set in various randomly chosen attitude settings. The precise gravity value is determined by terrestrial gravimetry. As for the temperature oven calibration, the selected attitude settings are repeated for various oven temperatures. For every accelerometer, a bias, one or two scale factors and a cross-coupling are estimated in least-squares adjustments.
- **Sample-based calibration**: In contrast to the previous approaches, the roll and pitch angles are assumed to influence the calibration in this approach. The accelerometer parameters are not modelled explicitly. Basically, a 3-D look-up table is generated in dependence of the roll and pitch angles as well as the environment temperature. Like in the parametric calibration, a turntable with combined oven is used to obtain results at various temperatures. Roll and pitch angles typical for airborne gravimetry campaigns are selected.

The results in Becker (2016) indicate that all mentioned thermal calibration approaches strongly improved the accuracy and precision in all evaluated airborne gravimetry campaigns. In most campaigns, the best precision was reached with the simple warm-up calibration of the vertical accelerometer. A possible reason for this might be the higher environment temperature gradient during this calibration method which is similar to the temperature gradient during flight days. In the scope of the thesis at hand, the warm-up calibration is selected since it delivers high-precision results at a low model complexity.

When Becker (2016) compared the campaign results to the combined gravity model GGM05C (Ries et al., 2016), he observed absolute differences in the mean values of more than 1 mGal for all calibration methods but the sample-based calibration. The latter is the only calibration method where the correction depends on the roll and pitch values. The systematic deviation of these Euler angles during the alignment period at the airport compared to the mean attitude during the flights might be a possible reason for in-flight biases and should be further investigated.

2.4.2 Renewed warm-up calibration

Becker (2016) performed a warm-up calibration for the vertical accelerometer of the iNAV-RQH in February 2014 covering an ISA temperature range between 23 and 44°C. After the calibration, the thermal housing iTempStab (see Section 2.3.2) was purchased in February 2018. All recent gravimetry campaigns by TU Darmstadt were conducted using the iTempStab. When the ISA temperature is stable (approximately 4 h after start-up at room temperature), a thermal correction becomes unnecessary. However, a thermal calibration will still be useful

- if measurements need to be conducted before the temperature is stable (due to a lack of time or problems with power supply during night, see Section 6.4.2) and
- if the environment temperature is out of the supported range or if there is a malfunction with the thermal housing (see Section 6.2.2).

Using the iTempStab with the settings mentioned in Section 2.3.2, the operating temperature of the ISA is almost 60°C (see Figure 2.11a) which is about 15 K higher than when the IMU is used without thermal housing. The maximum of the old warm-up calibration (44°C) is already reached less than an hour after start-up due to full power heating of the Peltier elements after activation. Poor results are expected when the old calibration is simply extrapolated to higher temperatures. Consequently, an additional warm-up calibration was conducted in June 2022.

The IMU in the iTempStab was placed on a solid surface at the TU Darmstadt facilities and was run for about 8 h. The recording was repeated four times with cool down periods of at least 15 h. The raw accelerometer outputs were low-pass filtered with a cut-off frequency of 130 s (-6 dB). Slight tilt changes of the IMU or the ISA might result in slight deterioration of the vertical (z-axis) accelerometer reading f_z^b. To avoid such effects, a tilt correction of the form

$$f_{\text{tilt},z}^n = \frac{f_z^b}{\cos(\phi_b) \cdot \cos(\theta_b)}, \tag{2.10}$$

is applied to the readings. The Euler angles roll ϕ_b and pitch θ_b are computed using the standard alignment formulas

$$\phi_b = \arctan\left(\frac{-f_y^b}{-f_z^b}\right), \quad \theta_b = \arctan\left(\frac{f_x^b}{\sqrt{{f_y^b}^2 + {f_z^b}^2}}\right), \tag{2.11}$$

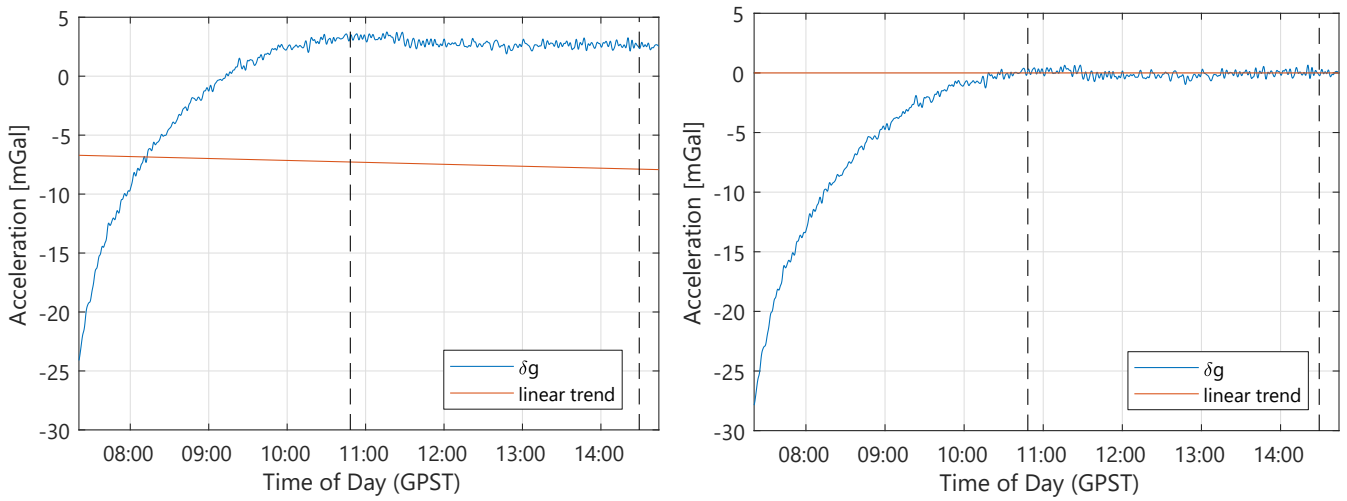
with f_x^b, f_y^b, f_z^b being the specific force observations (Groves, 2013). Basically, the tilt correction projects the observed third component f_z^b of the specific force to the local vertical by multiplying the rotation matrix $\boldsymbol{C}_b^n$ (the transposed matrix of Equation (2.21), see Section 2.5) by a reduced specific force vector $(0\ 0\ f_z^b)^{\mathrm{T}}$. Note that the four-quadrant arctangent function is required for ϕ_b. The tilt correction is only used experimentally here since the horizontal accelerometers may be significantly affected by thermal errors.

The tilt-corrected reading of the vertical accelerometer of run 3, a run with medium noise, is shown in Figure 2.12a. Note that the absolute accelerometer readings are irrelevant, since the strapdown gravimeters deliver only *relative* results. Like in dynamic gravimetry processing, the results are corrected by removing a linear trend from the data (see Section 5.4). It is assumed that the temperature is sufficiently stabilised after 3.75 h. The mean values of the 15 min after the stabilisation epoch (end illustrated by left dashed line) and at the end of the measurements (beginning after the right dashed line) are computed. For each run, a linear drift is computed using the difference between both mean values. The vertical accelerometer of run 3 shows a linear trend of about -0.1 $\frac{\text{mGal}}{\text{h}}$. The trend is illustrated by the red line in Figure 2.12a, vertically shifted for clarity. The linear trend is assumed to be consistent over the whole run and is removed along with the mean readings after stabilisation as shown in Figure 2.12b.

The standard deviation of the filtered readings of the vertical accelerometer after warm-up are 0.2...0.4 mGal at the four runs (Table 2.4). When the tilt correction is applied, the accuracy is improved by maximally 0.02 mGal. Due to the marginal changes, the tilt-corrected calibration will not be used in the dynamic campaigns.

The warm-up calibration was also applied to the horizontal accelerometers (front, left). Strong drifts after the warm-up epoch of about 5...20 $\frac{\text{mGal}}{\text{h}}$ have been observed. This is probably due to the high sensitivity of the horizontal readings to small attitude changes. An attitude error of 10″ leads to an error of less than 1 mGal in the vertical, but almost 50 mGal in the horizontal observation. Remaining thermal effects might cause slight changes in the ISA orientation. The particularly high sensor drifts of the left accelerometer should be analysed in future work.

The mean ISA temperature of the IMU with iTempStab is about 58°C. To enable a combination of the four runs, the filtered relative readings of the accelerometers are shifted to 0 at 58°C, i.e. a correction will be non-zero when the ISA temperature deviates from 58°C. The filtered, trend-free and shifted readings of the vertical accelerometer are represented as the thin lines in Figure 2.13.



(a) Zero-mean readings before drift removal

(b) Readings after drift removal (zero-mean after warm-up)

Figure 2.12: Readings of the vertical accelerometer (up, tilt correction applied) during run 3 of the warm-up calibration. The red line indicates the slope of the linear trend after warm-up

Table 2.4: Standard deviation of the accelerometer readings after warm-up, linear trend removed (all values in mGal)

	Front	Left	Up	Up (tilt cor.)
Run 1	9.11	1.51	0.39	0.37
Run 2	2.94	0.66	0.23	0.22
Run 3	4.46	4.49	0.28	0.28
Run 4	1.93	2.83	0.23	0.22

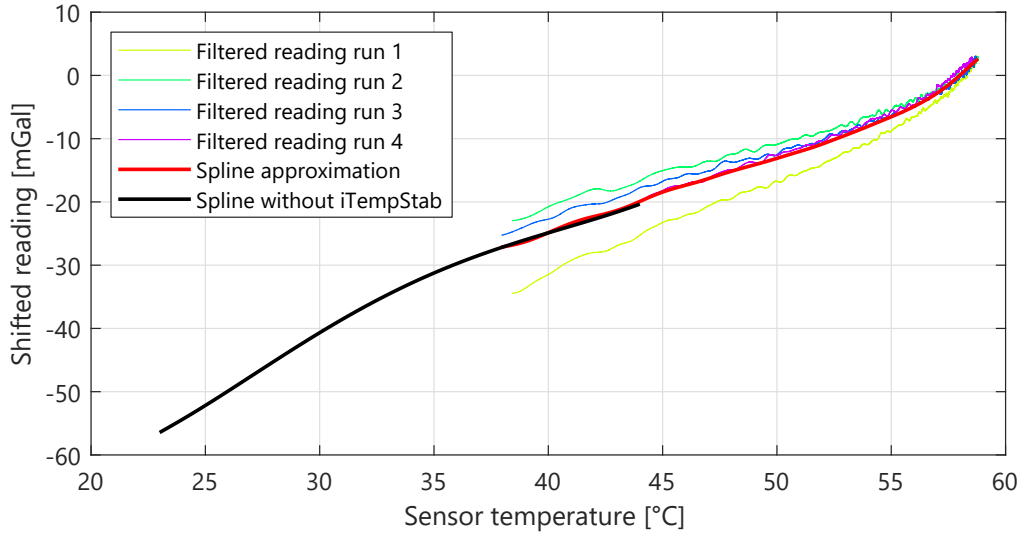


Figure 2.13: Thermal calibration of the vertical accelerometer (up, tilt correction applied)

To avoid an over-representation of the high temperatures close to the equilibrium temperature, the mean readings of the runs are computed for equally distributed bins with a width of 0.5 mK. They are used as input data to estimate a smoothing spline (red line in Figure 2.13). The new spline covers temperatures between about 38 and 58°C. In Figure 2.13, the calibration spline from 2014 (black) is added by shifting it to be equal with the new spline at 40°C. The figure indicates a good agreement between the old and the new warm-up calibration at the overlapping temperatures between 38 and 44°C suggesting the combination of both splines. However, the new spline appears sufficient since the temperature usually is high after some minutes when the iTempStab is used.

2.5 Coordinate frames

For the processing in dynamic gravimetry, several coordinate frames are required. The frames used in this work will be briefly introduced in the following and are illustrated in Figure 2.14. In-depth descriptions of the frames can be found, e.g., in Groves (2013), Wendel (2011) and Petit and Luzum (2010).

The frame, in which a coordinate vector is given, is denoted as a superscript. Transformations between coordinate frames with the same origin can be done using a 3x3 rotation matrix. In

$$\boldsymbol{r}^v = \boldsymbol{C}_u^v \cdot \boldsymbol{r}^u, \tag{2.12}$$

the coordinate vector $\boldsymbol{r}$ is transformed from the fictitious frame u to the fictitious frame v using the rotation matrix $\boldsymbol{C}_u^v$. The rotation matrix $\boldsymbol{C}_v^u$ for the reverse transformation is the inverse of $\boldsymbol{C}_u^v$. If the basis of the coordinate frame is orthogonal, the rotation matrix can be calculated as the transposed matrix of $\boldsymbol{C}_u^v$. All frames that will be presented in the following have orthogonal bases. Hence, the back transformation is given as

$$\boldsymbol{r}^u = \boldsymbol{C}_v^u \cdot \boldsymbol{r}^v = (\boldsymbol{C}_u^v)^{-1} \cdot \boldsymbol{r}^v = (\boldsymbol{C}_u^v)^{\mathrm{T}} \cdot \boldsymbol{r}^v. \tag{2.13}$$

A sequence of rotations can be fulfilled as

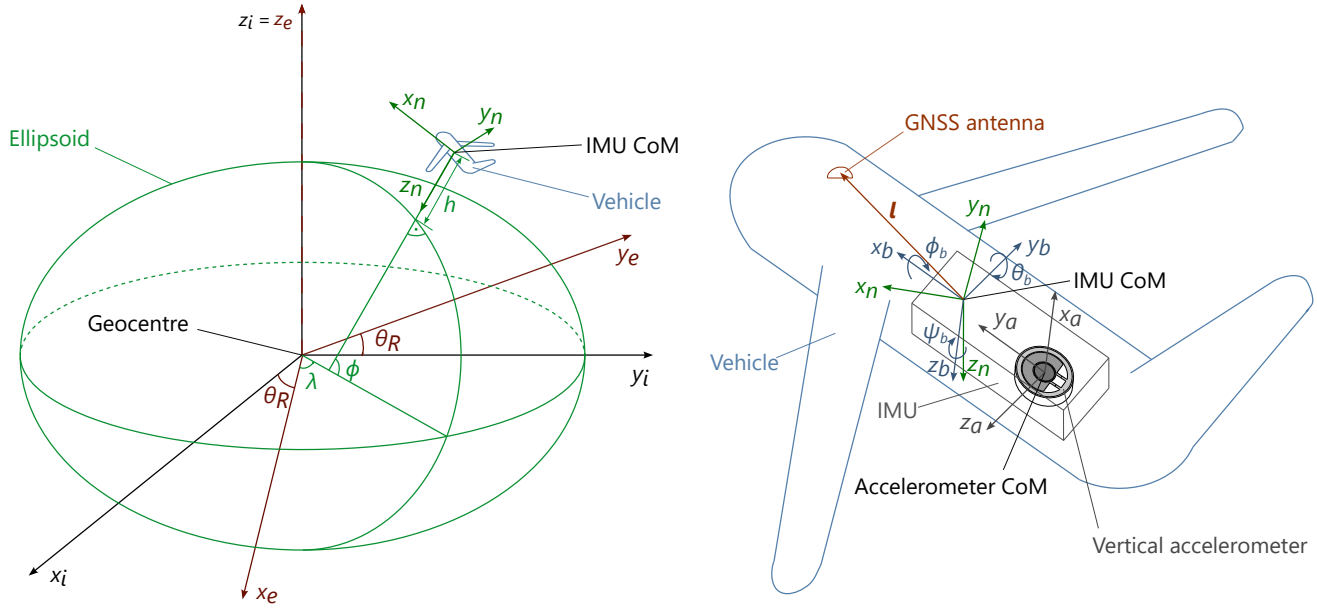
$$\boldsymbol{r}^w = \boldsymbol{C}_u^w \cdot \boldsymbol{r}^u = \boldsymbol{C}_v^w \cdot \boldsymbol{C}_u^v \cdot \boldsymbol{r}^u, \tag{2.14}$$

where a transformation of $\boldsymbol{r}^u$ to the the fictitious frame w is computed.

The *inertial frame* i is not accelerated and does not change its orientation. It might be defined with its origin in the barycentre of the solar system, but in the field of navigation close to the Earth, the origin is usually placed in the geocentre (Figure 2.14a). The z_i axis is defined to point to the celestial intermediate pole, approximates the Earth rotation axis and is perpendicular to the equatorial plane. Traditionally, the x_i axis points to the vernal equinox, i.e. the axis coincides with the line of intersection between the ecliptic and the equatorial plane. Since the vernal equinox is moving with about 50 arc-seconds per year towards West, mainly due to precession, a new, immovable celestial intermediate origin has bee introduced at the beginning of the new millennium that is currently close to the vernal equinox (Petit and Luzum, 2010). The y_i axis completes the right hand Cartesian coordinate frame and spans the equatorial plane together with the x_i axis.

Mainly due to the diurnal rotation of the Earth, inertial coordinates at the Earth change permanently. An alternative to the inertial frame is the *Earth frame* e where all coordinate axes are fixed to the Earth. The x_e axis points to an arbitrarily selected median called terrestrial intermediate origin. Traditionally, this meridian is close to the Greenwich observatory in London. The z_e axis and the origin are equal to the inertial equivalents. y_e completes the right hand frame. The rotation angle around the z axis to transform between the inertial and the Earth frame is called Earth Rotation Angle (ERA) θ_R. The Earth frame is usually used to specify coordinates of objects within the Earth's atmosphere, e.g. a moving vehicle in dynamic gravimetry. ERA can be specified in a simple way as

$$\theta_R = \omega_{ie} \cdot (t - t_0), \tag{2.15}$$



(a) Coordinate frames connected with the Earth ellipsoid: inertial coordinates x_i, y_i, z_i, earth coordinates x_e, y_e, z_e, geodetic coordinates λ, ϕ, h and navigation coordinates x_n, y_n, z_n

(b) Coordinate frames connected with the moving vehicle: navigation coordinates x_n, y_n, z_n, vehicle attitude ϕ_b, θ_b, ψ_b, body coordinates x_b, y_b, z_b and vertical accelerometer coordinates x_a, y_a, z_a

Figure 2.14: Coordinate frames in the context of dynamic gravimetry

where t is the time and t_0 is a reference epoch where both the inertial and the Earth frame coincide (Groves, 2013). A series expansion of the ERA with the International Celestial Reference Frame (ICRF) as reference system can be found in Capitaine et al. (2000). The rotation matrix

$$\boldsymbol{C}_i^e = \begin{pmatrix} \cos(\theta_R) & \sin(\theta_R) & 0 \\ -\sin(\theta_R) & \cos(\theta_R) & 0 \\ 0 & 0 & 1 \end{pmatrix} \tag{2.16}$$

is used for a coordinate transformation from the inertial to the Earth frame as a simple rotation around the z axis after Equation (2.12).

In comparison to the Cartesian Earth fixed coordinates x_e, y_e, z_e, the *geodetic (ellipsoidal) coordinates* λ, ϕ, h are more easily interpretable taking advantage of the almost ellipsoidal shape of the Earth surface. The length λ is defined as the angle in the equatorial plane between x_e and the meridian of the point of interest; the geodetic latitude ϕ is the angle between the equatorial plane and the ellipsoid normal through the point of interest. The ellipsoidal height h is the metrical distance between the ellipsoid and the point of interest along the aforementioned ellipsoid normal. The transformation between geodetic and Cartesian Earth frame coordinates can be done with

$$\begin{pmatrix} \phi \\ \lambda \\ h \end{pmatrix} = \begin{pmatrix} \arctan\left(\frac{z_e \cdot (R_E+h)}{\sqrt{x_e^2+y_e^2} \cdot ((1-e^2)R_E+h)}\right) \\ \arctan\left(\frac{y_e}{x_e}\right) \\ \frac{\sqrt{x_e^2+y_e^2}}{\cos(\phi)} - R_E \end{pmatrix} \quad \text{and} \quad \begin{pmatrix} x_e \\ y_e \\ z_e \end{pmatrix} = \begin{pmatrix} (R_E+h)\cos(\phi)\cos(\lambda) \\ (R_E+h)\cos(\phi)\sin(\lambda) \\ ((1-e^2)R_E+h)\sin(\phi) \end{pmatrix}, \tag{2.17}$$

where e is the eccentricity of the ellipsoid and R_N, R_E are the meridian and prime radii of curvature, respectively (Groves, 2013). Note that the transformation to geodetic coordinates needs to be computed

iteratively since geodetic latitude and height depend on each other as well as on the radii of curvature. R_N and R_E depend on the geodetic latitude. The four-quadrant arctangent function is required for longitude determination.

If spherical coordinates $\lambda, \bar{\phi}$ are used, the geocentric latitude is the angle between the equatorial plane and the straight through the geocentre and the point of interest. It is obtained from the geodetic latitude ϕ as

$$\bar{\phi} = \arctan((1 - e_{\text{el}}^2)\, \tan(\phi)), \quad \text{with} \quad e_{\text{el}} = \sqrt{\frac{a^2 - b^2}{a^2}} \tag{2.18}$$

being the primary eccentricity of the ellipsoid (Groves, 2013). In case of the GRS80 ellipsoid, the semi-major and semi-minor axes are $a = 6378137\,\text{m},\ b = 6356752.3141\,\text{m}$, respectively (Moritz, 1980).

The velocity and acceleration of an object relative to the Earth surface in local North x_n, East y_n and Down z_n direction can be described in the *navigation frame* n. In dynamic gravimetry, the origin of the navigation frame is fixed to the vehicle, i.e. it is equal to the origin of the vehicle body frame b. The down axis z_n is perpendicular to the ellipsoid surface (see Figure 2.14a). The rotation matrix

$$\boldsymbol{C}_e^n = \begin{pmatrix} -\sin(\phi)\cos(\lambda) & -\sin(\phi)\sin(\lambda) & \cos(\phi) \\ -\sin(\lambda) & \cos(\lambda) & 0 \\ -\cos(\phi)\cos(\lambda) & -\cos(\phi)\sin(\lambda) & -\sin(\phi) \end{pmatrix} \tag{2.19}$$

can be used to transform Earth frame coordinates to the navigation frame. When the time derivatives $\dot{\phi}, \dot{\lambda}, \dot{h}$ should be transformed to the velocity vector

$$\dot{\boldsymbol{r}}^n = \begin{pmatrix} (R_N + h)\,\dot{\phi} \\ (R_E + h)\cos(\phi)\,\dot{\lambda} \\ -\dot{h} \end{pmatrix}, \tag{2.20}$$

the radii of curvature, the scaling of the longitude and the opposite axis directions in the height must be considered (Hwang et al., 2006).

The *body frame* b (Figure 2.14b) with axes fixed to the vehicle body is mainly used for readings of sensors that are strapped-down. Furthermore, it is used to specify position differences between measurement instruments in the vehicle. The so-called lever arm $\boldsymbol{l}$, the vector from the Centre of Measurements (CoM) of the IMU and the GNSS antenna phase centre is the most important instrument coordinate difference in dynamic gravimetry. In this work, the origin of the body frame is set to the IMU CoM and is identical to the origin of the navigation frame. The x_b axis points towards the vehicle front, the z_b axis points towards the vehicle down, both depending on the current vehicle attitude. The y_b axis completes the right-hand Cartesian coordinate frame. Hence, the body frame is a front-right-down system in this definition. The rotation from the navigation to the body frame can be described using the three Euler attitude angles ϕ_b, θ_b, ψ_b fulfilling a specific order of rotations: First, a rotation is performed around the z_n axis through the yaw (heading) angle ψ_b. The second rotation is performed around the y axis of the first intermediate frame through the pitch angle θ_b. Since the x axis of the second intermediate frame is already identical to the x_b axis, a rotation around x_b through the roll angle ϕ_b finalises the transformation (Groves, 2013). The combined rotation matrix is

$$\boldsymbol{C}_n^b = \begin{pmatrix} \cos(\theta_b)\cos(\psi_b) & \cos(\theta_b)\sin(\psi_b) & -\sin(\theta_b) \\ -\cos(\phi_b)\sin(\psi_b) + \sin(\phi_b)\sin(\theta_b)\cos(\psi_b) & \cos(\phi_b)\cos(\psi_b) + \sin(\phi_b)\sin(\theta_b)\sin(\psi_b) & \sin(\phi_b)\cos(\theta_b) \\ \sin(\phi_b)\sin(\psi_b) + \cos(\phi_b)\sin(\theta_b)\cos(\psi_b) & -\sin(\phi_b)\cos(\psi_b) + \cos(\phi_b)\sin(\theta_b)\sin(\psi_b) & \cos(\phi_b)\cos(\theta_b) \end{pmatrix}. \tag{2.21}$$

In its default attitude, the IMU axes X, Y, Z are identical to the corresponding body axes (front-right-down), i.e. $X = x_b, Y = y_b, Z = z_b$. The iMAR iNAV-RQH-1003 is installed in its default attitude if its vertical axis is

perpendicular to the vehicle ground plane and if the side plate with the cable connectors points to the back of the vehicle. In practice, the vertical axis is always installed to point in its default direction but the X axis might be rotated around the Z axis by an angle β being an integer multiple of 90°.

For each sensor, a separate *sensor frame* a can be defined that can be helpful for creating or applying a sensor calibration. Figure 2.14b includes the sensor frame of the principal sensor of strapdown gravimetry, the vertical accelerometer. In this work, the x_a axis of the accelerometer sensor frame is defined to point in the positive direction of the sensitive axis of the sensor with the origin being in the accelerometer CoM. The y_a axis of the QA2000 sensor frame points in the opposite direction of the quartz flexure, perpendicular to the x_a axis; the z_a axis completes the right-hand Cartesian frame (see also Figure 2.10). In the following, each accelerometer sensor frame axis is considered parallel to a body frame axis with sufficient accuracy. In the default attitude of the iNAV-RQH, the x_a axis of the vertical accelerometer points to the up axis $-z_b$ of the vehicle, the y_a axis points to the front axis x_b and the z_a axis points to the left axis $-y_b$. Further details will be introduced in Section 3.2.2.

2.6 Processing methods of strapdown gravimetry[1]

The processing approaches in dynamic gravimetry can be divided into two basic categories: the direct and the indirect method. In the direct method, gravity is computed *directly* in the acceleration domain based on Equation (2.9). In the indirect method, the specific force observations are integrated two times. Gravity is computed *indirectly* in the position domain.

This section briefly introduces the essential properties of both methods. Figure 2.15 illustrates their main processing steps. For both approaches, alternative names exist which will be printed in italic letters in the following.

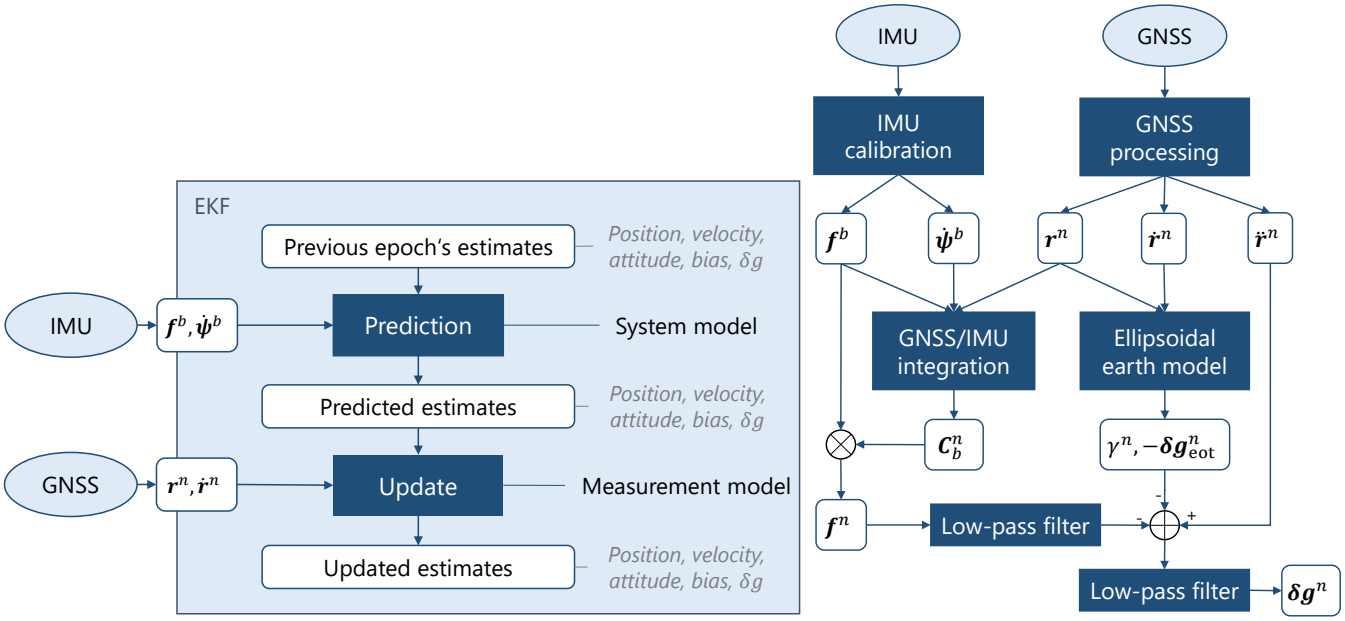
2.6.1 Indirect method

In the *indirect method* (Jekeli, 2001), the *traditional way* (Kwon and Jekeli, 2001) of strapdown gravimetry, a least-squares adjustment based on an Extended Kalman Filter (EKF) is used to estimate the vehicle position, velocity, attitude, sensor biases as well as the gravity disturbance in a *one-step approach* (Becker, 2016). Gravity determination is based on inertial positioning/navigation (Jekeli, 2001; Ayres-Sampaio et al., 2015). In the centralised approach, the aforementioned quantities form the state vector.

For every epoch with IMU observations, the Kalman filter follows the scheme of Figure 2.15a. In the first step, the “prediction”, the state estimates of the previous epoch and the current IMU observations are used to predict the current state estimates. The weighting is based on the assumed accuracy of the specific force and angluar rate measurements and the estimated accuracy of the previous state elements. If GNSS measurements are available, they are used to “update” the predicted states. In the tightly-coupled approach, GNSS processing is done within the EKF using code and phase observations. Hence, theoretically, already less than 4 satellite observations can improve the state estimates. However, a loosely-coupled approach is sufficient for dynamic gravimetry since the satellite observability is usually excellent for airborne and shipborne campaigns. In this setting, GNSS processing is done outside of the EKF. The obtained position and velocity are input to the update step.

An easy-to-realise variant of the indirect method was presented by Jensen et al. (2017). The authors take advantage of the fact that, under stable flight conditions at straight lines, the biases of the vertical accelerometer and vertical gravity are almost inseparable. They use a commercial inertial navigation software and approximate the gravity disturbance by removing a bias and a linear trend from the estimated accelerometer

[1] This section is based on Johann et al. (2019).



(a) Indirect method (b) Direct method

Figure 2.15: Schematic flow charts of processing methods in dynamic gravimetry (based on Johann et al. (2019))

bias. A drawback of this variant is that the detailed processing algorithm of the inertial navigation software remains a black box.

The indirect method might be seen as a rigorous approach since it is based on a single optimal estimator, the Kalman filter (Becker, 2016). However, since an EKF is applied due to the required linearisation of the navigation and observation equations, the EKF slightly deviates from a true optimal estimator. Results strongly depend on the careful tuning of the stochastic model (Jekeli, 1994). For a detailed introduction to inertial navigation filters, the reader is referred to Groves (2013) and Wendel (2011). Detailed descriptions of the indirect approach for airborne gravimetry can be found in Becker (2016) and Jensen (2018).

2.6.2 Direct method

While all navigation states as well as gravity are estimated all at once in the indirect method, navigational quantities and gravity are determined *cascaded* (Becker, 2016), step by step, in the *direct method*. Instead of computing gravity indirectly in the position domain, it is obtained *directly* in the acceleration domain by solving Equation (2.9) for gravity. Hence, gravity

$$\boldsymbol{g}^i = \ddot{\boldsymbol{r}}^i - \boldsymbol{f}^i \tag{2.22}$$

in the inertial frame i is the difference between the kinematic acceleration $\ddot{\boldsymbol{r}}^i$, obtained from GNSS measurements, and the specific force $\boldsymbol{f}^i$, observed by the IMU. The direct method is an *accelerometry* approach (Kwon and Jekeli, 2001; Ayres-Sampaio et al., 2015).

Typically, the results of dynamic gravimetry are expressed as the deviation of gravity from normal gravity after Equation (2.6). When the gravity disturbance is computed in the navigation frame as (Wei and K. P. Schwarz, 1998)

$$\delta\boldsymbol{g}^n = \boldsymbol{g}^n - \boldsymbol{\gamma}^n = \ddot{\boldsymbol{r}}^n - \boldsymbol{C}_b^n \boldsymbol{f}^b + \delta\boldsymbol{g}^n_{\text{eot}} - \boldsymbol{\gamma}^n, \tag{2.23}$$

which is the fundamental equation of dynamic gravimetry, two considerations must be taken: First, the specific force needs to be rotated from the body frame to the navigation frame using the rotation matrix $\boldsymbol{C}_b^n$ obtained as the transposed of Equation (2.21). Second, the rotation between the rotating Earth frame e with respect to the inertial frame and the rotation of the navigation frame with respect to the Earth frame are considered in the Eötvös correction

$$\boldsymbol{\delta g}_{\text{eot},n}^n = (2\boldsymbol{\Omega}_{ie}^n + \boldsymbol{\Omega}_{en}^n) \cdot \dot{\boldsymbol{r}}^n, \tag{2.24}$$

where $\dot{\boldsymbol{r}}^n$ is the vehicle velocity and $\boldsymbol{\Omega}_{ie}^n, \boldsymbol{\Omega}_{en}^n$ are the skew-symmetric matrices of the Earth rotation rate vector $\boldsymbol{\omega}_{ie}^n$ and the transport rate vector $\boldsymbol{\omega}_{en}^n$. Skew-symmetric matrices are used to simplify the notation and numerical computation of cross products. The cross product of a rotation rate vector $\boldsymbol{\omega} = [\omega_x\ \omega_y\ \omega_z]^{\mathrm{T}}$ with a vector $\boldsymbol{d}$ becomes

$$\boldsymbol{\Omega} \cdot \boldsymbol{d} = [\boldsymbol{\omega}\times] \cdot \boldsymbol{d} = \begin{pmatrix} 0 & -\omega_z & \omega_y \\ \omega_z & 0 & -\omega_x \\ -\omega_y & \omega_x & 0 \end{pmatrix} \cdot \boldsymbol{d} = \boldsymbol{\omega} \times \boldsymbol{d}. \tag{2.25}$$

The first term of Equation (2.24) quantifies the Coriolis acceleration. This fictitious acceleration occurs for a moving vehicle due to the rotation of the Earth frame with respect to the inertial frame. The second term corrects for the centrifugal acceleration due to the movement of the navigation frame with respect to the Earth frame during vehicle movement. The complete Eötvös correction is dependent on the vehicle movement relative to the Earth. Consequently, in static measurements, the Eötvös correction is zero. Be aware that, for a static observation, the centrifugal acceleration due to the Earth rotation is already considered in the normal gravity (Equations (2.2) and (2.3)). Also note that the Eötvös correction is only required completely if the kinematic acceleration is computed in the navigation frame. If it is computed in the Earth frame, only the first term of the Eötvös correction, i.e. the Coriolis correction, is required as

$$\boldsymbol{\delta g}_{\text{eot},e}^n = 2\boldsymbol{\Omega}_{ie}^n \cdot \dot{\boldsymbol{r}}^n. \tag{2.26}$$

If it is computed in the inertial frame, no such correction must be applied at all (Jekeli and Garcia, 1997), i.e. $\boldsymbol{\delta g}_{\text{eot},i}^n = \boldsymbol{0}$.

The processing steps of the direct method are illustrated in Figure 2.15b. There are two main data inputs. The GNSS data is processed resulting in vehicle position, velocity and kinematic acceleration $\boldsymbol{r}^n, \dot{\boldsymbol{r}}^n, \ddot{\boldsymbol{r}}^n$ in the navigation frame (see Section 4). The IMU specific force and angular rate observations $\boldsymbol{f}^b, \dot{\boldsymbol{\psi}}^b$ can be calibrated in the body frame, e.g. for thermal (see Section 2.4) or magnetic (see Section 3.3) influences. The calibrated IMU observations and the GNSS position solutions (loosely-coupled approach) are integrated in a GNSS/IMU inertial navigation algorithm (see Section 5.1) in order to obtain the vehicle attitude in shape of the rotation matrix $\boldsymbol{C}_b^n$. With this, the specific force is transformed from the body to the navigation frame as $\boldsymbol{f}^n$ and low-pass filtered afterwards. Normal gravity $\boldsymbol{\gamma}$ and the Eötvös correction $\boldsymbol{\delta g}_{\text{eot}}^n$ are computed using the GNSS position and velocity solutions after Equations (2.5) and (2.24) or (2.26), respectively. Now, all inputs for the fundamental equation of dynamic gravimetry, Equation (2.23), are prepared (see Section 5.3) and gravity disturbance is obtained after low-pass filtering followed by bias and trend removal (see Section 5.4).

The direct method is more straightforward than the indirect method since it is computed directly in the acceleration domain. A Kalman filter is typically only needed for the GNSS/IMU integration with the purpose of attitude determination. Alternatively, there also exist one-step approaches, where a Kalman filter is used for an estimation in the acceleration domain without computing the vehicle position and velocity (Jekeli, 2001). In a one-step direct method, the gravity disturbance does not necessarily need to be included in the state vector (Kwon and Jekeli, 2001). However, the direct method is usually applied in a cascaded algorithm. In another variant, scalar gravity is computed without the knowledge of the sensor attitude assuming the complete gravity vector points downwards in the navigation frame. The implementation of this “rotation

invariant" approach is easier since the IMU/GNSS integration can be omitted but this method performed consistently worse (Wei and K. P. Schwarz, 1998).

In the scope of this thesis, the direct method is applied, since it is easy to implement and less obtuse, especially if an existing commercial software is used for the GNSS/IMU integration for attitude determination. It will be shown that the precision of the direct method is on par with the indirect method (see Section 9.1). The algorithm implemented in this thesis will be described in detail in Section 5.

3 Magnetic field influences on accelerometer readings[1]

Using TU Darmstadt's IMU iNAV-RQH, a heading-dependent error in the vertical gravity disturbance estimates was observed by Becker (2016) in all evaluated campaigns. He was able to significantly improve the precision in the campaigns by applying a heading-dependent correction. The heading-dependent error

$$\varepsilon^n_{\psi_b,z} = -c\,\dot{r}^n_x \tag{3.1}$$

was based on the product of a campaign-specific constant c and the velocity $\dot{r}^n_x$ in northern direction. The constant was obtained empirically for each campaign. The results indicated that the constant is higher at low latitudes. The corrected vertical gravity disturbance $\delta g^n_{z,\text{cor}}$ was obtained from the uncorrected δg^n_z by forming the difference

$$\delta g^n_{z,\text{cor}} = \delta g^n_z - \varepsilon^n_{\psi_b,z}. \tag{3.2}$$

In the scope of the work at hand, the hypothesis is made that the heading-dependent error might be caused by the magnetic field of the Earth, which will be introduced in Section 3.1. As a first experiment, a static IMU measurement was conducted while a permanent bar magnet was placed at several positions near the IMU (Figure 3.1). The magnetic field induced at the CoM of the IMU was in the order of the Earth's field. The results showed repeatable errors in the vertical accelerometer readings in the order of several mGal that were dependent on the magnet position and attitude. However, since the accuracy of the results is low due to the inhomogeneous magnetic field around the permanent magnet, more advanced experiments have been conducted using a 3-D Helmholtz coil. The methods and results will be presented in Section 3.2. Based on the findings, a magnetic calibration approach will be developed in Section 3.3.

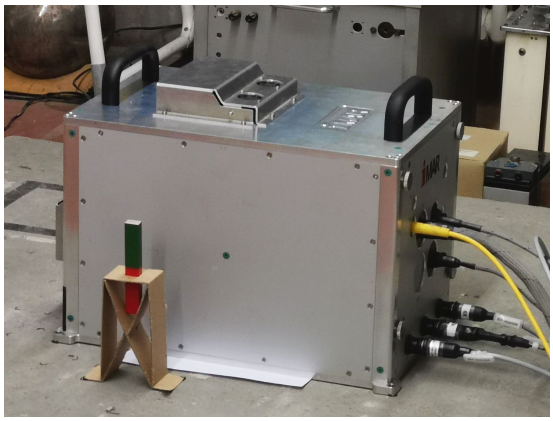


Figure 3.1: Simple static experiment with a permanent bar magnet

[1] This section is based on Johann et al. (2021).

3.1 The Earth's magnetic field

There are three main origins of the magnetic field of the Earth (Lanza and Meloni, 2006; Clauser, 2014; Oehler et al., 2018):

- The *main field* is due to a geodynamic mechanism in the fluid outer core of the Earth. It makes up approximately 95 % of the total field.
- The *crustal field* is induced by magnetised rocks in the crust of the Earth.
- Atmospheric plus interplanetary currents and magnetic fields cause the *external field*.

The magnetic field can be expressed as the magnetic field strength $\boldsymbol{H}$ or the magnetic flux density

$$\boldsymbol{B} = \mu\,\boldsymbol{H} = -\boldsymbol{\nabla}(V_{\text{mag}}), \tag{3.3}$$

which is the product of $\boldsymbol{H}$ and the magnetic permeability μ, a magnetisation measure of the material exposed to the magnetic field. For better readability, the magnetic flux density will be called "magnetic field" in the following. Similar as for the Earth's gravitational potential (see Equation 2.1), the Earth's magnetic field vector can be obtained as the gradient of the geomagnetic potential V_{mag}, but with negative sign.

Comparably to Equation 2.7, the magnetic field potential can be modelled using spherical harmonics. The International Geomagnetic Reference Frame (IGRF) is a commonly used model based on satellite observations, terrestrial surveys and observatory data. The International Association of Geomagnetism and Aeronomy released the current version, the IGRF-13 in 2019 (Alken et al., 2021). The geomagnetic potential can be approximated as

$$V_{\text{mag}}(r,\theta,\lambda,t) = R_0 \sum_{n=1}^{\infty}\sum_{m=0}^{n}\left(\frac{R_0}{r}\right)^{n+1}\left(g_n^m(t)\cos(m\lambda) + h_n^m(t)\sin(m\lambda)\right)P_n^m(\cos(\theta)), \tag{3.4}$$

with r, θ, λ being the distance to the geocentre, the geocentric colatitude and longitude, $R_0 = 6371.2\,\text{km}$ being the approximated mean Earth radius, g_n^m, h_n^m being the Gauß coefficients obtained from the IGRF up to degree and order 13 and P_n^m being the Schmidt-normed Legendre polynomials.

Note that the temporal variation of the magnetic field is much higher than that of the gravitational field. Hence, the Gauß coefficients of the IGRF are dependent on the epoch t. The IGRF-13 includes sets of Gauß coefficients with time intervals of five years between 1 January 1900 and 1 January 2020 allowing an interpolation of the coefficients between the given epochs. For epochs after 2020, a predicted rate of change for the coefficients up to degree and order 8 are part of IGRF-13, intended to cover another five years. The accuracy of the IGRF-13 is assumed sufficient for the purposes of this thesis since the Gauß coefficients higher than degree 13 are far below 1 µT (Lowes, 2000).

For the magnetic experiments and calibration in the subsequent sections, the horizontal part of the magnetic field $\boldsymbol{B}^n = (B_x^n \;\; B_y^n \;\; B_z^n)^{\text{T}}$ in the navigation frame will be of interest. Its intensity and direction can be described by the norm B_H of the horizontal field intensity and the magnetic field declination angle δ as (Lanza and Meloni, 2006)

$$B_H = \sqrt{B_x^{n\,2} + B_y^{n\,2}}, \quad \delta = \arctan\left(\frac{B_y^n}{B_x^n}\right). \tag{3.5}$$

The four-quadrant arctangent function is required to compute the declination, which is counted clockwise. The horizontal magnetic field intensity according to IGRF-13 is illustrated in Figure 3.2 with a special focus on central Europe. The horizontal field tends to be maximal with about 45 µT close to the equator and converges to zero close to the magnetic poles, where the magnetic field is almost vertical. However, the field is not

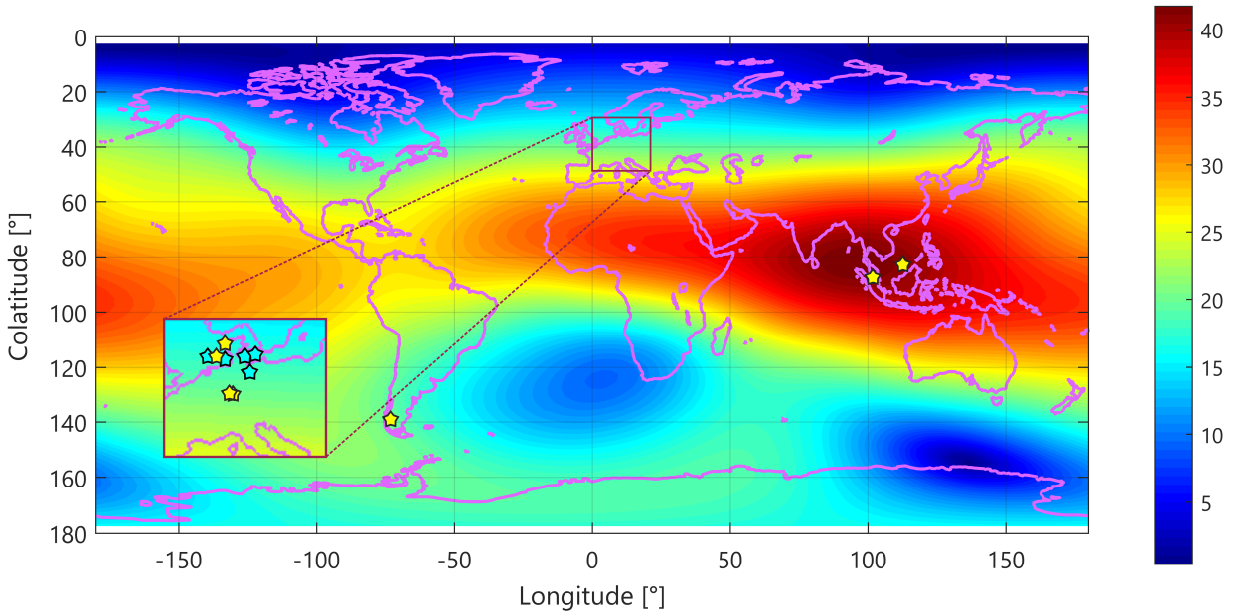


Figure 3.2: Horizontal magnetic field intensity [μT] computed with IGRF-13 for 1 January 2020 with airborne (yellow) and shipborne (cyan) campaigns evaluated in this thesis

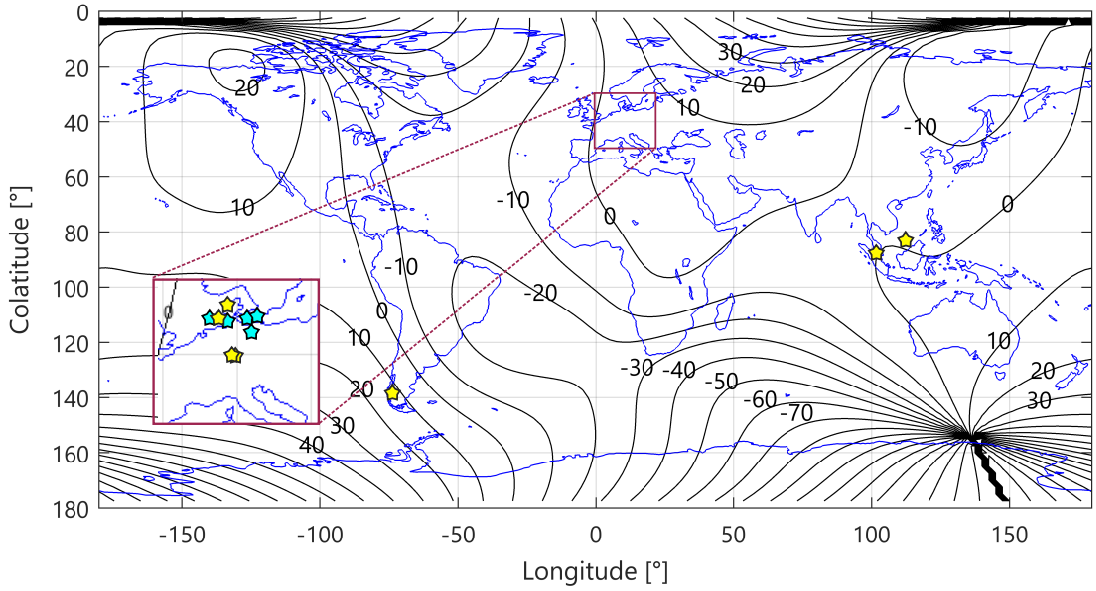


Figure 3.3: Magnetic field declination [°] computed with IGRF-13 for 1 January 2020 with airborne (yellow) and shipborne (cyan) campaigns evaluated in this thesis

distributed homogeneously with a maximum in South-East Asia and a minimum in the Atlantic Ocean close to South Africa. The magnetic field declination ranges between $\pm 30^\circ$ at the continents except for Antarctica and becomes much higher close to the magnetic poles (Figure 3.3).

There are magnetic field intensity and declination variations of up to several tens of nT per year and several arc minutes per year, respectively, and short term effects (Leitgeb, 1990; Lanza and Meloni, 2006; Clauser, 2014). Diurnal changes of 10...30 nT are mostly due to solar activity and depend on the latitude. Solar storms can cause intensity variations of up to 1 µT at the Earth's surface.

Local magnetic influences of natural origin (e.g. magnetised rocks) and artificial origin (e.g. railways, mains current) are not fully covered in the IGRF. Furthermore, the local field at buildings is disturbed by ferromagnetic construction material in floors, walls, ceilings (Vries et al., 2009) and electrical devices (Tenforde, 1995; Bachmann et al., 2004). The magnetic field during dynamic gravimetry campaigns is even more disturbed due to the moving vehicle and inconsistent electric currents. The accurate modelling of a magnetic field close to a gravimeter inside of a moving aircraft or ship is very complex and might be almost impossible. The influence of disturbing ferromagnetic objects and electric devices strongly decreases with increasing distance to the observation point.

3.2 Static experiments in a 3-D Helmholtz coil

As mentioned before, it was shown in a simple experiment using a permanent magnet (see Figure 3.1) that the accelerometer readings of the iNAV-RQH are dependent on the magnetic field outside of the IMU. This is already the case for a magnetic field in the order of the Earth's magnetic field. It might explain the heading-dependent error empirically approximated by Equation (3.1). The drawbacks of the simple experiment, the inhomogeneity and the high uncertainty in the magnetic field intensity, are resolved by using a 3-D Helmholtz coil in conjunction with a magnetometer.

A Helmholtz coil is a set of two narrow coils with the same direction of electric current. Inside of the coil, a homogeneous magnetic field is induced in the direction of the coil axis. The field intensity depends on the electric current in the coils. Using a set of three perpendicular Helmholtz coils, an almost homogenous 3-D magnetic field of user-defined intensity and direction can be generated by adjusting the currents of the three Helmholtz coils. Such a 3-D Helmholtz coil is set up in the facilities of iMAR Navigation and was used for the experiments that will be described in the following sections. The construction consists of three double-square coils with side lengths of 585 mm (blue), 610 mm (red) and 635 mm (yellow) and 84 windings per coil (Figure 3.4). The 3-D coil can be used to neutralise the magnetic field of the Earth and disturbing fields in the building of the experiment. Overlaying magnetic fields in the order of the IGRF Earth field can be induced by the coil.

In a first step, the homogeneity of the magnetic field inside the magnetic coil was inspected without IMU in June 2020. On the same day, the IMU without its thermal housing was exposed to various magnetic fields in several attitudes. In October 2020, the IMU was encased in the iTempStab and was exposed to multiple magnetic fields in its standard attitude. The results of the latter experiment have been used to develop a calibration function for the vertical accelerometer in the standard attitude (Section 3.3). The experiments are limited to the vertical accelerometer since it is considered by far most significant for dynamic gravimetry.

3.2.1 Homogeneity of the generated magnetic field

The experiments in the following sections assume that the magnetic field inside of the 3-D Helmholtz coil is homogeneous. The deviation from this assumption was measured using a solid-state 3-D magnetometer of the type iMAR iTAHS with a measurement repeatability of 10 nT according to the manufacturer (IMAR Navigation, 2016). The magnetometer was placed on non-magnetic material at points in a 3-D raster within

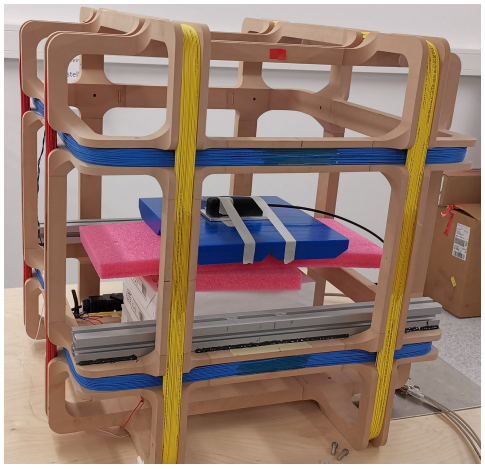


Figure 3.4: iMAR iTAHS magnetometer within the 3-D Helmholtz coil at iMAR Navigation facilities

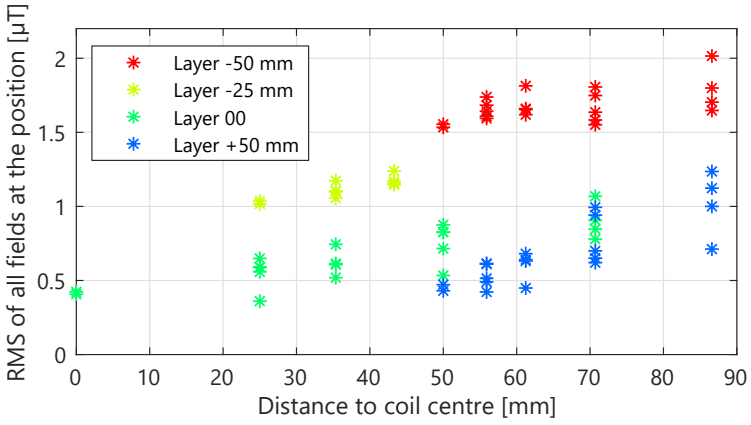


Figure 3.5: Magnetic field RMS inside the 3-D Helmholtz coil. Each point represents a grid position and is computed with all 13 magnetic field settings. The horizontal layers indicate the vertical distance from the coil centre to the grid position (Johann et al., 2021)

10 cm around the central point of the coil (see Figure 3.4). The point spacing was 25 mm. The magnetometer was exposed to a field with an intensity being approximately zero ("zero field") and fields of 32 and 65 µT in all three coil axis directions, with positive and negative sign. Hence, in total, 13 magnetic fields have been measured at all 60 grid points. The grid points were selected covering the space where the ISA of the IMU will be located in the upcoming experiments.

The magnetic fields obtained by adapting the currents of the three coils sightly deviates from the desired magnetic field intensity. This is unproblematic since the measured magnetic fields will be used in the subsequent experiments and the calibration. The fields remained approximately constant. In Figure 3.5, the RMS over the magnetic field Euclidean norm residuals are plotted as a function of the distance to coil centre. Each point is computed as the RMS of all 13 fields at a single grid position. The values range between approximately 0.4 and 2.0 µT with a slight increase with an increasing distance to the coil centre. This indicates that the deviations to the homogeneity assumption are smallest close to the coil centre. Systematic errors can be observed depending on the layer height (indicated by the different colours). This might be due to the underground material used to lift the magnetometer to the desired height. The RMS over all points is 1.1 µT which is assumed to be sufficient for calibration purposes with respect to the Earth's magnetic field. Another prerequisite is the assumption that magnetic field disturbances caused by the IMU materials and electronics are tolerable.

3.2.2 Methods

The static experiments with the iNAV-RQH in the 3-D Helmholtz coil are divided in two parts:

1. In the first part, the IMU was placed inside of the Helmholtz coil in several attitude settings at several magnetic fields. The 3-D coil generates an artificial navigation frame where the yellow coil axis defines artificial north x_n, and the red and blue axes define artificial east and down y_n, z_n, respectively (Figure 3.6). The thermal stabilising housing iTempStab was not used in this part since the temperature field inside the housing might be affected by the different heat distribution at the unusual attitude settings.

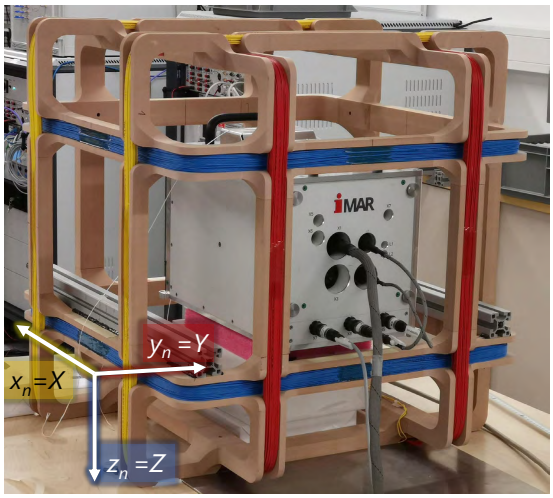


Figure 3.6: iMAR iNAV-RQH-1003 encased in the iTempStab inside of the 3-D Helmholtz coil with the IMU axes X, Y, Z in attitude 1 and the artificial navigation frame north-east-down x_n, y_n, z_n (based on Johann et al. (2021))

Table 3.1: Overview about the static magnetic field experiments (based on Johann et al. (2021))

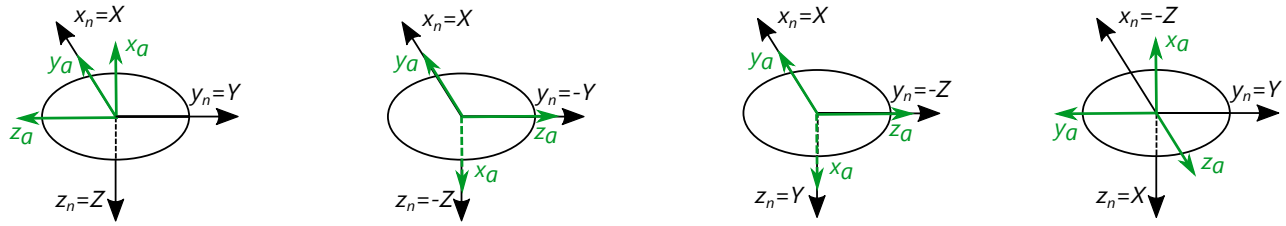
Static experiment	Part 1	Part 2
Thermal stabilisation (iTempStab)?	✗	✓
Attitudes (see Tab. 3.2, Fig. 3.7)	1,2,3,4	1
Horizontal magnetic field direction interval [°]	90	45
Horizontal magnetic field intensities [µT]	0/65	0/10/20/32/(65)
Vertical magnetic field intensities [µT]	0/65	0/32/65
Number of zero field measurements	8	7
Measurement duration per field [min]	3	5

2. About three months later, the accelerometer readings in the most relevant standard attitude were evaluated in more detail. The number of magnetic fields and the observation time per field was increased. The IMU was encased in the iTempStab in order to get similar conditions like in the recent dynamic campaigns and to evaluate possible differences to the observations without the housing.

Before the start of the experiments, the IMU was turned on for several hours to reduce thermal effects. Between some of the magnetic field settings and especially at the beginning and the end of the experiments, "zero field updates" were included where the magnetic field intensity inside the coil was set to approximately zero. The repeated observations were used to remove linear drifts from the vertical accelerometer readings. The vertical accelerometer bias was removed by shifting the readings to zero at the zero field updates. Slight tilt changes of the IMU or the ISA are considered by applying the tilt correction of Equation (2.10) to the vertical readings. After low-pass filtering and the bias/drift removal, the mean readings of the vertical accelerometer at all attitude and magnetic field settings have been analysed. In the scope of this thesis, the analysis is limited to the vertical accelerometer since it is by far most relevant for dynamic gravimetry. An overview about the set-up of both parts of the experiments is given in Table 3.1.

Table 3.2: IMU and vertical accelerometer axis directions in the four attitude settings with respect to the artificial north, east and down axes of the 3-D Helmholtz coil. For all attitudes, this thesis only analyses data of the current vertical accelerometer, i.e., the accelerometer that is oriented in up/down direction in the specific attitude setting (vertical component, bold; based on Johann et al. (2021))

Attitude	IMU axis pointing towards artificial ...			Vertical accelerometer axis pointing towards artificial ...		
	... x_n	... y_n	... z_n	... x_n	... y_n	... z_n
1 "Standard" (Fig. 3.6)	X	Y	$\boldsymbol{Z}$	y_a	$-z_a$	$-x_a$
2 "Top down"	X	$-Y$	$\boldsymbol{-Z}$	y_a	z_a	x_a
3 "Right down"	X	$-Z$	$\boldsymbol{Y}$	y_a	z_a	x_a
4 "Front down"	$-Z$	Y	$\boldsymbol{X}$	$-z_a$	$-y_a$	$-x_a$



(a) Attitude 1 (accelerometer *Z*) (b) Attitude 2 (accelerometer *-Z*) (c) Attitude 3 (accelerometer *Y*) (d) Attitude 4 (accelerometer *X*)

Figure 3.7: Mounting and axis directions X, Y, Z of the IMU (black) and axis directions x_a, y_a, z_a of the vertical accelerometers (green) in the four attitude settings with respect to artificial magnetic north, east, down x_n, y_n, z_n. The circles illustrate the shape of the accelerometer housing (based on Johann et al. (2021))

Part 1 without iTempStab

The measurements of the first part of the experiments are conducted in four attitude settings (Table 3.2, Figure 3.7). In the standard attitude 1, the IMU is based on its designated bottom plate. The Z axis of the IMU points downwards (see Figure 2.8a, but the vertical accelerometer is installed in the IMU in a way that the sensitive axis x_a of the vertical accelerometer is pointing upwards (see Figure 3.7a). The artificial z_n axis inside the coil coincides with the Z axis of the IMU. The IMU axes X, Y point towards artificial x_n, y_n, respectively, but the axes y_a, z_a of the vertical accelerometer point to artificial $x_n, -y_n$, respectively. Note that the installation of the accelerometers inside of the IMU, i.e. the sensitive direction and the rotation of the accelerometer assembly (see Figure 2.10) around the sensitive axis, is different for the three accelerometers.

In attitude 2, the IMU is rotated around its X axis by 180°. Hence, the same accelerometer like in attitude 1 (Z) is the vertical accelerometer, but with opposite sensitive axis x_a and axis z_a (Figure 3.7b). To realise attitude 3, the IMU is rotated around the X axis until the right side plate of the IMU is down. Hence, the Y accelerometer becomes the vertical accelerometer (Figure 3.7c). This accelerometer is installed in the IMU in a way that its axes x_a, y_a, z_a are pointing in the same coil directions z_n, y_n, x_n like for the Z accelerometer in attitude 2, respectively. Starting from attitude 1, attitude 4 is realised by rotating the IMU around its Y axis until the IMU is based on the front plate (Figure 3.7d). In this setting, the X accelerometer is vertical with the sensitive axis x_a pointing upwards like in attitude 1, but the internal accelerometer mounting causes the axes y_a, z_a to be rotated around x_a by 90° in comparison to attitude 1.

In each attitude, the IMU was exposed to artificial magnetic fields of 65 µT in the coil axis directions x_n, y_n, z_n as well as $-x_n, -y_n, -z_n$. Every magnetic field setting was held for three minutes allowing to compute the mean accelerometer reading with an accuracy of some tenths of mGal. In addition to the six magnetic settings per attitude, eight zero field updates were conducted in total.

Part 2 with iTempStab

In the second part of the experiments, the IMU was encased in the iTempStab and remained in the standard attitude 1 for the whole experiment (see Figures 3.6 and 3.7a). The IMU was exposed to the same magnetic fields like in the first part of the experiment and additional horizontal fields of 10, 20 and 32 µT at horizontal direction intervals of 45°. Seven zero field updates were conducted. To improve the accuracy of the mean readings per field, the observation time per field was increased to five minutes.

3.2.3 Results

In the following, only the readings of the current vertical accelerometer (depending on the attitude setting) will be analysed mainly for two reasons:

1. The vertical accelerometer is by far most relevant for dynamic gravimetry since it is roughly aligned with the local plumb line, especially during approximately straight measurement lines.

2. Small changes in the sensor orientation, e.g. due to thermal expansion or settling effects, have a much bigger impact on the horizontal accelerometers than on the vertical accelerometer. In the standard attitude, a orientation change of one arc second causes a reading shift of 4.8 mGal for the horizontal accelerometers. For the vertical accelerometer, the shift is at sub-mGal level, with the exact error being dependent on the levelling error. Hence, a precise magnetic calibration is much more difficult for the horizontal accelerometers.

In agreement with Table 3.2 and Figure 3.7, the downwards-pointing IMU axes in the four attitude settings are $Z, -Z, Y, X$, respectively.

The most obvious finding of both parts of the experiments is that all readings were significantly impaired by the magnetic fields induced by the Helmholtz coil. For the magnetic field intensity of 65 µT, maximal deviations between 3 and 6 mGal have been observed in all attitude settings. In the following, the influence of horizontal and vertical magnetic fields on the vertical accelerometer will be discussed separately.

Part 1 without iTempStab

Figure 3.8 illustrates the mean errors of the current vertical accelerometer due to *horizontal magnetic fields* in the four attitude settings. The horizontal magnetic field direction is indicated by an artificial "declination" angle. If the magnetic field direction is opposite to the x_n axis, the declination is labelled zero as it originates from artificial magnetic north; if it is opposite to the y_n axis, the angle is 90° as it comes from artificial east. The errors in all attitudes might be roughly approximated by a sine function.

In the attitudes 1 and 2, the same accelerometer (IMU axis Z) was vertical. The turnaround of the sensitive axis in attitude 2 was considered by changing the reading sign in Figure 3.8b. Both error plots might be approximated by a cosine function with its maximum close to a declination of zero and an amplitude of approximately 5 mGal. There might exist a phase shift between both attitudes of some degrees. The results suggest that the reading error does not depend on the mounting direction of the sensitive axis x_a of the accelerometer but on the mounting of the accelerometer axes y_a, z_a. The maximum error is obtained by a magnetic field acting approximately from the opposite direction of axis y_a (Figure 3.9). This hypothesis is

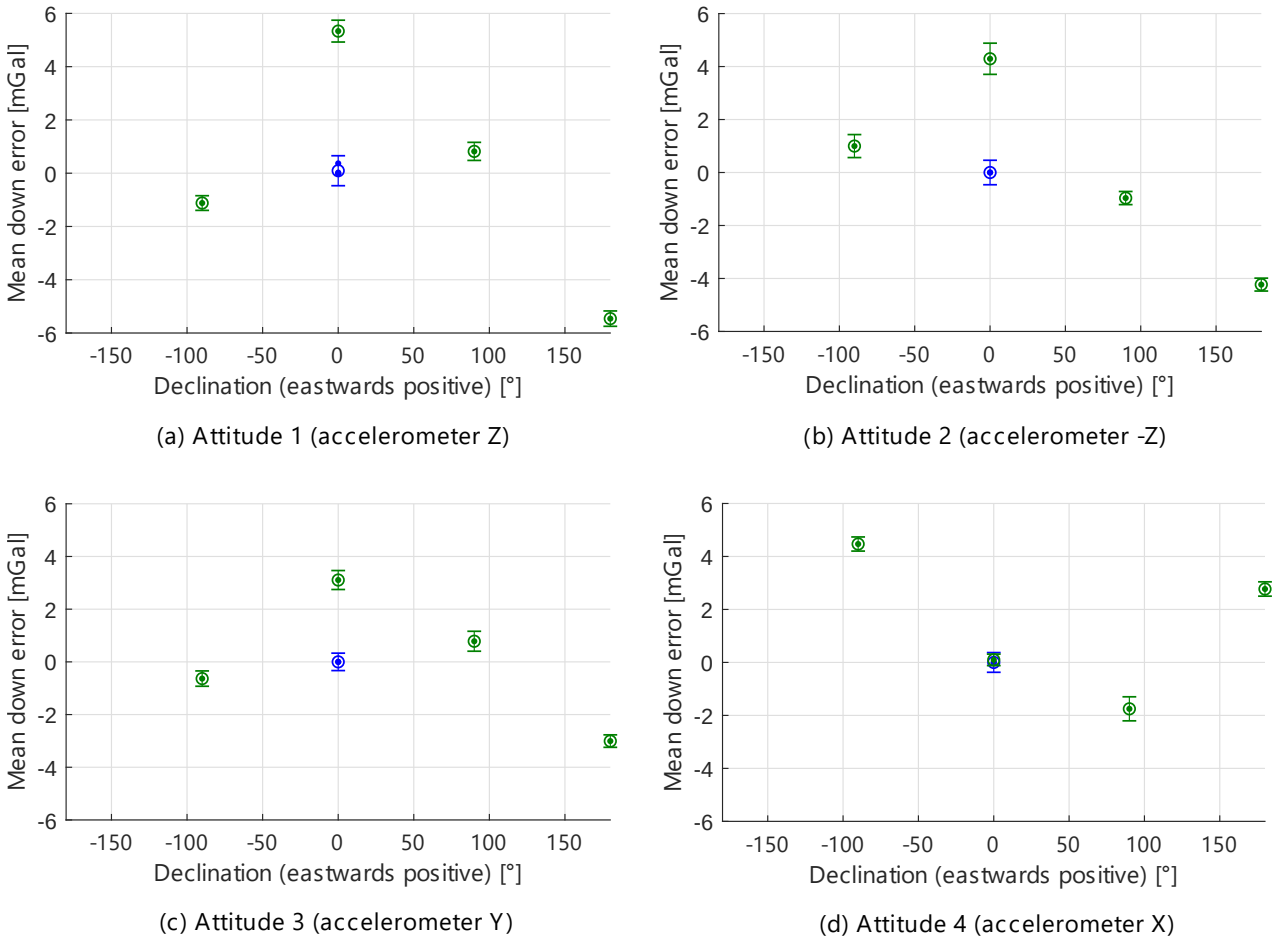
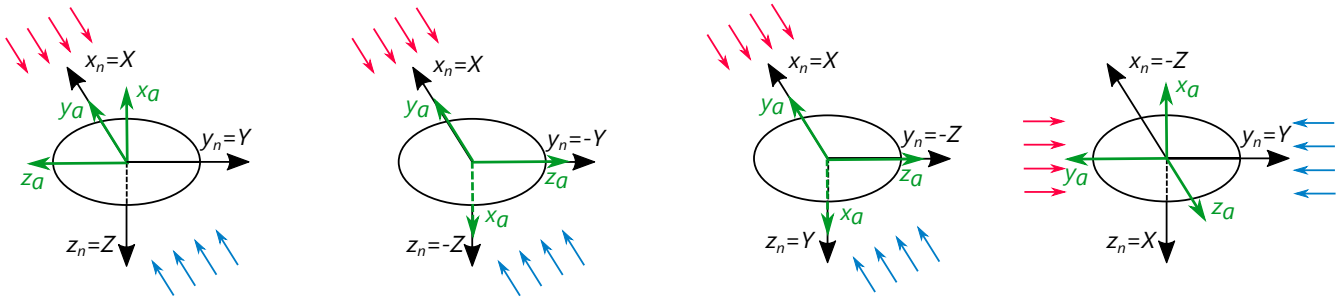


Figure 3.8: Means and standard deviations of the down component as a function of the horizontal magnetic field direction (without iTempStab; blue: zero field; green: field intensity of 65 µT) (Johann et al., 2021)

supported by the results of the attitudes 3 and 4. In attitude 3, the axes of the vertical accelerometer Y are oriented in the artificial navigation frame exactly like for the vertical accelerometer in attitude 2 (see Figures 3.7b and c). The results for both attitudes are similar with slight differences in the amplitude and the phase shift (see Figures 3.8b and c). In comparison to attitude 1, the vertical accelerometer X in attitude 4 is rotated around the sensitive axis x_a by 90° (see Figures 3.7a and d). As a result, the reading error might also be shifted by 90° (see Figures 3.8a and d). Note that the results of attitude 4 are slightly impaired due to a too short warm-up period before the start of the readings.

The vertical accelerometer reading errors due to a *vertical magnetic field* are illustrated in Figure 3.10. The absolute errors are approximately equal for the upwards and downwards pointing fields in the same attitude settings, but they are different for different attitudes. This is also the case in attitudes 1 and 2 where the same accelerometer is vertical. The error sign depends on the direction of the magnetic field with respect to the accelerometer axes. Since the vertical magnetic field is parallel to the sensitive axis x_a of the vertical accelerometer, the sign of the error solely depends on the mounting direction of x_a (Figure 3.11).

The key findings of the first part of the experiment are the following: The reading of the current vertical accelerometer is influenced by horizontal and vertical magnetic fields in the shape of a scale factor error.



(a) Attitude 1 (accelerometer *Z*) (b) Attitude 2 (accelerometer -*Z*) (c) Attitude 3 (accelerometer *Y*) (d) Attitude 4 (accelerometer *X*)

Figure 3.9: Most relevant horizontal magnetic field directions in the four attitude settings. The red (blue) arrows indicate the horizontal field direction of greatest positive (negative) influence on the down sensor reading (based on Johann et al. (2021))

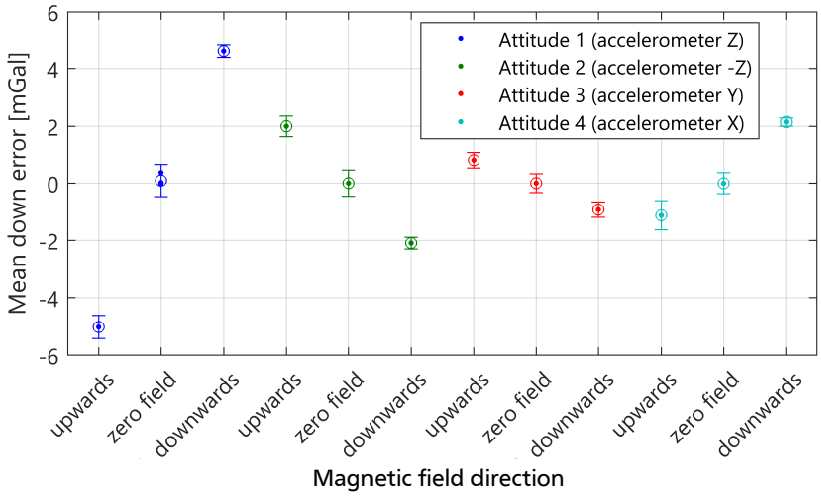
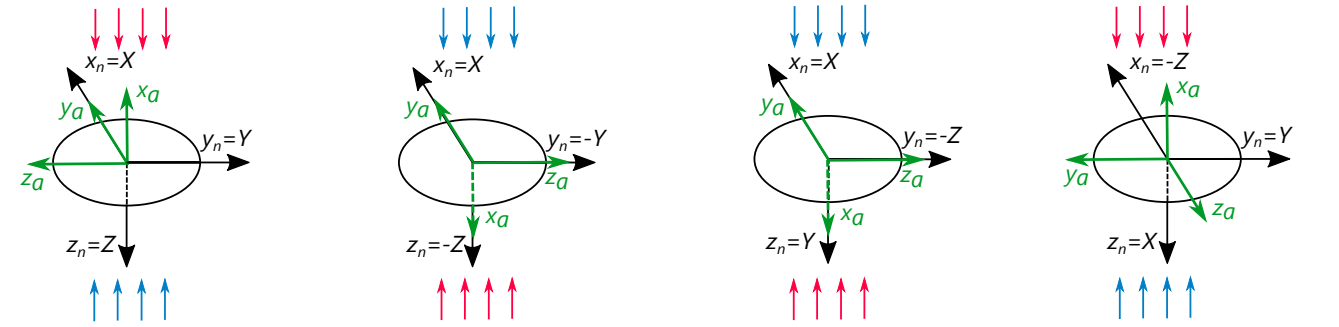
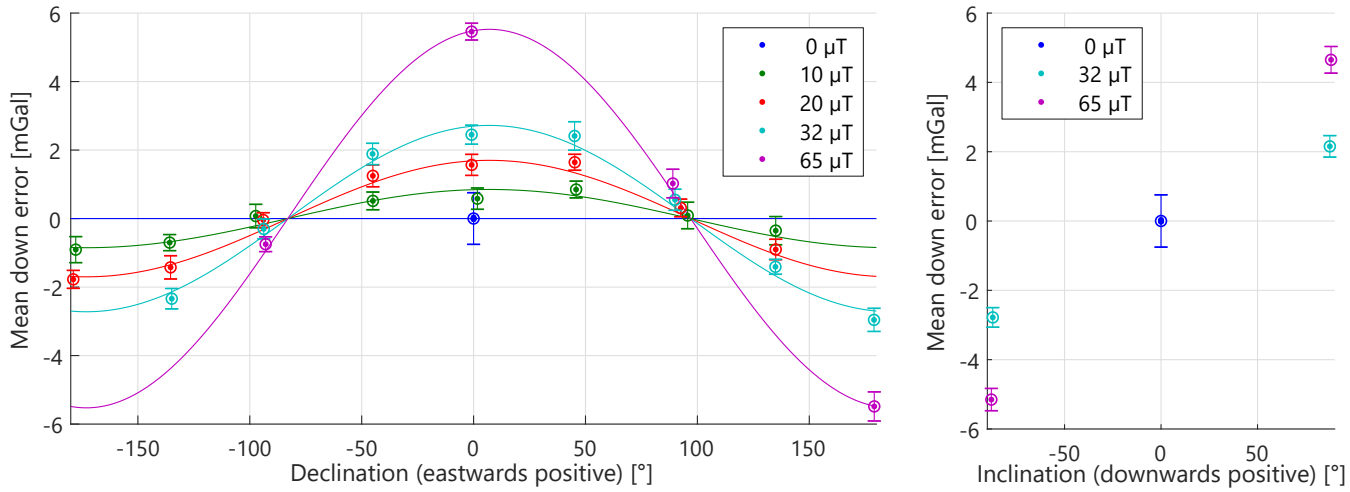


Figure 3.10: Means and standard deviations of the down component as a function of the vertical magnetic field direction in the four attitude settings (without iTempStab) (Johann et al., 2021)



(a) Attitude 1 (accelerometer *Z*) (b) Attitude 2 (accelerometer -*Z*) (c) Attitude 3 (accelerometer *Y*) (d) Attitude 4 (accelerometer *X*)

Figure 3.11: Most relevant vertical magnetic field directions in the four attitude settings. The red (blue) arrows indicate the vertical field direction of greatest positive (negative) influence on the down sensor reading (based on Johann et al. (2021))



(a) Horizontal field (b) Vertical field

Figure 3.12: Means and standard deviations of the down component as a function of the magnetic field direction and colour-coded intensity (attitude 1, accelerometer Z, with iTempStab). The solid lines illustrate the calibration function (see Section 3.3) at the evaluated magnetic field intensities (Johann et al., 2021)

The magnitude of the error depends on the direction of the magnetic field with respect to the orientation of the accelerometer inside of the IMU as defined by the accelerometer mounting. All three accelerometers have a similar error behaviour with respect to the accelerometer axes but the amplitude of the error is sensor-dependent. For vertical fields, the amplitude is additionally dependent on the mounting direction of the sensitive axis.

Part 2 with iTempStab

In the second part of the experiments, the IMU was encased in the iTempStab housing and was solely set up in attitude 1 (see Figure 2.8b). Magnetic fields with an intensity of 65 µT have been generated in both parts of the experiment in attitude 1, with and without iTempStab. All absolute differences were lower than 0.4 mGal at the same magnetic field settings with a mean of 0.01 mGal and an RMS of 0.19 mGal which is in the order of the static measurement accuracy of the IMU (see Section 2.3.2, Figure 2.11). This allows for two conclusions. Firstly, the results of the magnetic experiments are repeatable. Secondly, the thermal stabilising housing iTempStab is not reshaping the magnetic field around the vertical accelerometer significantly. Hence, the same magnetic calibration might be appropriate for the IMU with and without iTempStab. However, the most precise results are expected in part 2 of the experiment since thermally induced sensor drifts are avoided by using the iTempStab.

The number of magnetic field intensities and horizontal directions was increased in the second part of the experiments. The mean values at the individual field settings are illustrated in Figure 3.12. Higher magnetic field intensities lead to higher reading errors of the vertical accelerometer.

3.3 Calibration approach for the vertical accelerometer

In this section, a calibration approach for the vertical accelerometer for the application of dynamic gravimetry will be developed. The input data for the calibration is taken from the second part of the static experiments

within the 3-D Helmholtz coil (see Section 3.2.3) since more horizontal angles have been tested, each magnetic field was held for a longer time period and the iTempStab housing was used. In dynamic campaigns, the horizontal attitude angle (heading) covers the full range between 0 and 360°, whereas the roll and pitch angles are typically small except during flight manoeuvres. Hence, the attitude of the IMU is typically similar to attitude 1, the attitude of the second part of the experiments. The following calibration focuses on horizontal magnetic fields since the Earth's vertical magnetic field is assumed approximately constant in a campaign. A constant error is irrelevant in relative gravimetry.

The experiments in the Helmholtz coil indicated that the mean reading error of the vertical accelerometer due to a horizontal magnetic field might be approximated by a cosine function. The input for the cosine is the angle α between the geomagnetic north direction and the horizontal direction of maximal susceptibility of the IMU to a magnetic field. Furthermore, the error is dependent on the horizontal magnetic field intensity B_H of the magnetic field. The ansatz for the magnetic calibration function $\Delta f^b_{z,\text{mag}}$ is

$$\Delta f^b_{z,\text{mag}} = (c_1 B_H + c_2 B_H^2 + ... + c_k B_H^k) \cdot \cos(\alpha), \tag{3.6}$$

where the scale factor due to the horizontal field intensity is approximated by a polynomial of the order k with coefficients c_i. The polynomial does not include a constant c_0 since the calibration function is zero for a zero field.

The angle α between the local magnetic north and the direction $\Delta f_{z,\text{max}}$ of the maximal susceptibility of the vertical accelerometer to a horizontal magnetic field is dependent on several horizontal angles:

- The local magnetic field *declination* δ is the angle between the geographic x_n and magnetic N_{mag} north directions. The angle can be approximated using the IGRF (see Section 3.1, Equation (3.5)).
- *Yaw* (heading) ψ_b is the angle between the geographic north x_n and the vehicle front x_b and describes the horizontal orientation of the vehicle. Its computation will be introduced in Section 5.1.
- The *mounting direction* of the IMU in the vehicle is considered by the angle β between the vehicle front x_b and the IMU front axis X. If the IMU is mounted in its default orientation, β is zero.
- The angle κ describes the deviation of the direction $\Delta f_{z,\text{max}}$ of the *maximal susceptibility* from the IMU front axis X direction. This angle needs to be determined for the specific IMU along with the coefficients c_i.

In accordance with Figure 3.13, the input angle α for Equation (3.6) can be obtained as

$$\alpha = \psi_b - \delta + \beta + \kappa. \tag{3.7}$$

For the iNAV-RQH, attempts with polynomials of several orders indicated that the amplitude of $\Delta f_{z,\text{mag}}$ is approximately proportional to the horizontal magnetic field intensity. Hence, the non-linear terms of the polynomial in Equation 3.6 can be omitted.

If a magnetometer is used to observe the magnetic field instead of using a global model and if significant changes in the vertical field B^n_z are observed, this influence should be considered. It is assumed that the vertical field error is also proportional to the vertical field with a proportionality constant c_V. By inserting Equation (3.7) into Equation (3.6) omitting the non-linear polynomial terms and adding the vertical correction, the final calibration function for the reading of the z accelerometer is obtained as

$$\Delta f^b_{z,\text{mag}} = c_1 B_H \cos(\psi_b - \delta + \beta + \kappa) + c_V B^n_z. \tag{3.8}$$

If the magnetic field at the IMU is approximated by the Earth field using the IGRF, the vertical magnetic field is approximately constant during the dynamic campaigns and the term $c_V B^n_z$ can be neglected. If the IMU is

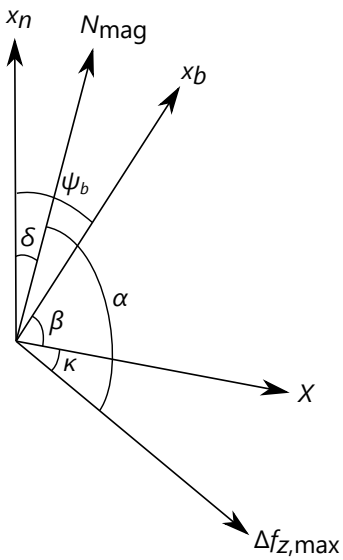


Figure 3.13: Horizontal angles relevant for the calibration approach (based on Johann et al. (2021))

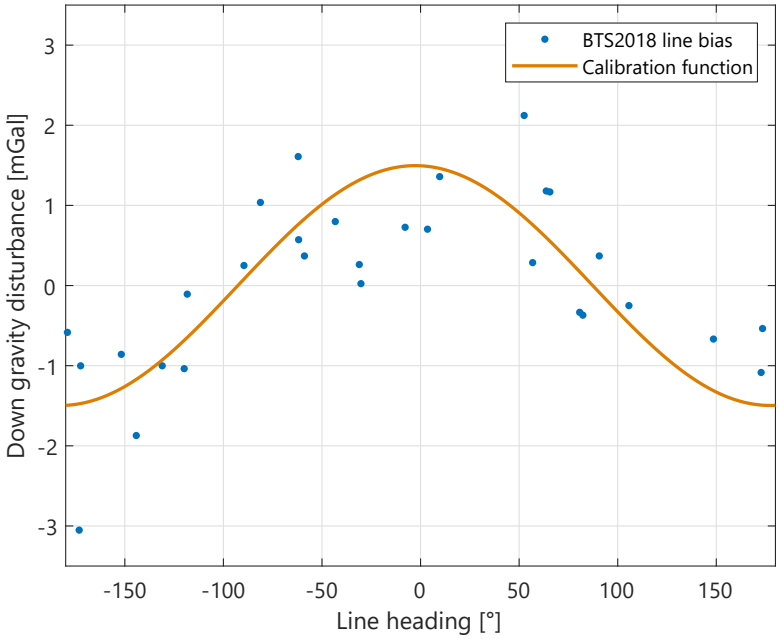


Figure 3.14: Biases of the lines of the Baltic Sea 2018 campaign with the magnetic calibration function of Equation (3.8) for a horizontal magnetic field intensity of about 17.6 µT

tilted, i.e. the roll and pitch angles ϕ_b, θ_b are non-zero, a proportion of the vertical acceleration is measured by the horizontal accelerometers. Therefore, a tilt correction similar to Equation (2.10) is considered in the corrected vertical gravity disturbance

$$\delta g^n_{z,\mathrm{cor}} = \delta g^n_z - \Delta f^b_{z,\mathrm{mag}} \cos(\phi_b) \cos(\theta_b). \tag{3.9}$$

in dynamic gravimetry. Both terms are defined positive in the down direction. If the roll and pitch angles are close to zero, the tilt correction can be neglected. A significant aircraft tilt at the airport and a small tilt during the flight or vice versa will lead to an in-flight vertical gravity bias that cannot be detected in a crossover or repeated lines analysis (see Section 5.5). For the evaluated IMU and a horizontal field intensity of 40 µT, a pitch angle of 20° and a heading angle of 0 at the airport in combination with a non-tilted flight would cause an in-flight bias of 0.2 mGal.

For the IMU at hand, the susceptibility coefficient of the vertical accelerometer to a horizontal magnetic field was estimated in a least-squares adjustment as $c_1 \approx (85.0 \pm 1.8) \frac{\mu\mathrm{Gal}}{\mu\mathrm{T}}$ along with the angle $\kappa \approx (7.0° \pm 1.1°)$ between the IMU front axis and the maximal susceptibility. The calibration function is illustrated in Figure 3.12a as solid lines with the colours representing different horizontal magnetic field intensities. The dependency of the vertical accelerometer to the vertical field is estimated as $c_V \approx (76.5 \pm 3.4) \frac{\mu\mathrm{Gal}}{\mu\mathrm{T}}$.

A first plausibility validation for the obtained calibration function is done with the shipborne gravimetry campaign Baltic Sea 2018 (see Section 7.1). Figure 3.14 shows the vertical gravity biases (blue dots) as a function of the line heading. The absolute biases are up to 3 mGal and indicate a systematic behaviour. According to the IGRF-13, the horizontal magnetic field intensity B_H at the mean campaign position and epoch was about 17.6 µT. With this, using Equation (3.8), the calibration function becomes the orange line in Figure 3.14. The function approximates the line biases well. Most remaining differences are lower than 1 mGal and are assumed to be primarily due to measurement noise. The magnetic calibration function will be applied to all campaigns of Sections 6 and 7. Results will be summarised in Section 8.3.

4 GNSS-based kinematic acceleration determination

In dynamic gravimetry, gravity is obtained as the difference of the kinematic acceleration and the specific force according to Equation (2.22). The specific force is observed by the gravimeter; the kinematic acceleration is nowadays obtained by GNSS observations. Typically, GNSS observations are used for the position determination, in navigation it is also used to estimate the receiver velocity. The determination of acceleration is a special application that is seldom used outside the field of gravimetry.

The following Section 4.1 will introduce existing strategies for acceleration determination with GNSS. If a position solution exists, the kinematic acceleration can be determined by numerical differentiation (Section 4.2) of the position (Section 4.3). Strategies that directly use GNSS phase observations will be introduced in Section 4.4. The functional model will be developed in Section 4.4.1; Sections 4.4.2 and 4.4.3 will present two corresponding algorithms. Weighting and outlier removal will be discussed in Sections 4.4.8 to 4.4.9. Section 4.5 will evaluate the proposed methods in static experiments.

In an alternative approach, the velocity can be directly obtained using the GNSS raw Doppler observable. The kinematic acceleration is then derived by numerical differentiation. This approach will not be considered in the following since the noise of the raw Doppler observable is much higher than the Doppler velocity noise that is obtained by the numerical differentiation of the phase observable (Bruton et al., 1999; Lu et al., 2017).

4.1 State of the art

The algorithms for the determination of kinematic acceleration using GNSS can be split in two basic approaches, which will be called Position Differentiation Method (PosDif) and Phase Differentiation (PhaseDif) in this thesis. In the PosDif approach, the GNSS position solution is numerically differentiated two times. This method is easy to realise if standard precise GNSS positioning software is available. The PhaseDif approach is based on the GNSS phase range observable. In two numerical differentiation steps, the phase range velocity and the phase range acceleration are obtained. There are several adaptions of the PhaseDif algorithms which will be briefly introduced in this section. The main properties of the methods are pointed out in Table 4.1. Note that reference station data is required for all methods, but in some approaches, such data has already been processed by analysis centres. Instead of setting-up own reference stations, the user can utilise the resulting precise satellite orbit and clock products. There are indications that the performance of DGNSS- and DD-based methods degrades using a far-off reference station (Li et al., 2018) even if most satellites are observered by rover and reference, but this aspect might need further investigation regarding the acceleration domain.

A successful implementation and validation of a PhaseDif method with real GNSS data was first presented by Jekeli and Garcia (1997). They used phase acceleration observations from a subset of four GPS satellites to compute the kinematic acceleration. By forming double differences between two satellites and two receivers, the influence of receiver and satellite clock errors were removed. The authors pointed out that slowly changing systematic errors are not significant in the acceleration domain. Furthermore, they claimed that cycle slips are of minor relevance for the range acceleration. The latter aspect was suggested to be the “principal advantage” of the new method. They found that errors in the satellite orbits were negligible for the processing of the range accelerations. A receiver position accuracy of about 6 m was stated to be sufficient for a kinematic acceleration

Table 4.1: Requirements for high accuracy kinematic acceleration determination approaches

	PosDif-DGNSS	PosDif-PPP	PhaseDif-DD	PhaseDif-PPP	PhaseDif-POP
Numerical differentiation of...	position solution		phase range observable		
Slowly changing effects	model/correction required		neglectable		
Reference station required?	nearby	no	nearby	no	long-distance
Satellite orbits	broadcast	final	broadcast	broadcast	broadcast
Satellite clock errors	broadcast	final	broadcast	final	estimated

determination at the 1 mGal level. With a low-pass filter length of 60 s, they obtained a standard deviation of 0.75 mGal using two static nearby receivers for PhaseDif. In dynamic experiments, the standard deviation of the difference between PhaseDif and PosDif results was between 2.2 and 5.2 mGal with mean differences up to 2.5 mGal. Bruton et al. (1999) implemented the PosDif and the PhaseDif method and evaluated several numerical differentiation strategies. They applied the methods to a gravimetric test flight. After low-pass filtering with a filter length of 90 s, RMS between 1.8 and 3.5 mGal were obtained in comparison with an upward-continued reference. Both methods performed approximately on a par.

Kennedy (2003) adapted the double difference PhaseDif approach by estimating the kinematic acceleration in a least-squares adjustment using all available satellite observations. Using a covariance model based on the satellite elevation and on the correlation between satellite observations, the errors were lowered by a factor of eight and the resistance to changes of the satellite constellation increased. In a gravimetric flight experiment with a low-pass filter length of 120 s, standard deviations of 1.2 and 1.4 mGal were obtained for the gravity disturbance in the PhaseDif method. The acceleration was also computed with the PosDif method. The results were approximately on a par or slightly worse by less than 0.2 mGal if precise receiver positions were used. If the receiver position was computed in the code mode, the PosDif results were poor with standard deviations higher than 20 mGal. Conversely, the accuracy of the PhaseDif results was not impaired showing the high resistance of the PhaseDif method to receiver position errors. Kennedy (2003) also evaluated the susceptibility of the PhaseDif method to cycle slips. Results indicated that the algorithm is robust against cycle slips. It was shown that a false cycle slip detection impairs the kinematic acceleration results. False cycle slip detection must be avoided since this was found to be more harmful than in the position domain. The author proposed to take advantage of the high sensibility of the PhaseDif method to false cycle slips by using this algorithm to identify mistaken cycle slip candidates in positioning algorithms.

Kreye and Hein (2003) also evaluated an airborne gravimetric test flight with the PosDif and PhaseDif approaches. They pointed out that changes in the satellite constellation impair the results of GNSS positioning only in the order of millimetres or a few centimetres, but the influence is amplified in the acceleration domain due to the higher noise after the numerical differentiation. Instead of directly using phase accelerations, He (2014) estimated the receiver velocity based on phase velocities. Even though the kinematic acceleration is obtained by numerical differentiation of the velocity solution, this method will be categorised as a PhaseDif method since the computation is done avoiding the position domain. He (2014) outlines the importance of proper weighting for the velocity determination. An RMS of about 1.9 mGal was obtained when the result of a test flight is compared to a global gravity model. The method was further investigated by Lu et al. (2017) who obtained a crossover point precision of about 1.0 mGal (RMSE, see Section 5.5.1). Slight differences of 0.1 mGal were obtained for the precision indicator using different GNSS sample frequencies of 1 or 10 Hz.

The PhaseDif approaches mentioned so far are based on Double Differences (DD) and are now categorised as Phase Differentiation based on DD (PhaseDif-DD) approaches. The principal drawback of this kind of PhaseDif approaches is that a reference receiver close to the rover (in the order of several tens kilometres) is required to obtain accurate kinematic accelerations or velocities (Li et al., 2018). In the method proposed by Serrano et al. (2004), a single GNSS receiver, i.e. the rover, is used to compute the acceleration in a

modified PhaseDif algorithm. Instead of double differencing, the satellite clock errors are taken from the broadcast navigation message. The receiver clock error is estimated within the approach. The purpose of the algorithm by Serrano et al. (2004) was to determine the velocity and acceleration of a moving car almost in real time independently of precise position solutions. These velocities and accelerations were fed into an EKF for navigation to enhance the position results when a single frequency GPS receiver is used. The obtained position accuracy was about 1 m which was about ten times better than using a conventional EKF with single frequency GPS data. Since no external precise data is used in this approach, the acceleration accuracy is not sufficient for airborne gravimetry. However, Serrano et al. (2004) showed that the acceleration can be computed in a PhaseDif approach without double differencing.

Xiaohong Zhang et al. (2017) also used a stand-alone receiver for the PhaseDif method. But in contrast to the aforementioned method, they used precise satellite products by the International GNSS Service (IGS) or the Center for Orbit Determination in Europe (CODE) instead of broadcast data. Since this method is similar to PPP but computed in the acceleration domain, it is categorised as Phase Differentiation based on PPP (PhaseDif-PPP). Like He (2014), the phase velocity was used to estimate the receiver velocity followed by a numerical differentiation. In static experiments using GPS data, Xiaohong Zhang et al. (2017) observed a significantly lower noise level for the kinematic acceleration when clock products with a higher data rate are used (5 s interval instead of 30 s). In an airborne gravimetry campaign with a very high number of crossover points, they obtained an RMSE precision of about 0.9 mGal which is approximately on par with PosDif reference computations based on PPP- and DGNSS-derived positions.

Based on the positioning method Precise Orbit Positioning (POP) (Salazar et al., 2010), Salazar et al. (2011) developed a PhaseDif method similar to the PhaseDif-PPP approach. The method will be called Phase Differentiation based on POP (PhaseDif-POP) in this thesis. The main innovation is that – like in the POP processing – the satellite clock errors are estimated within the approach. A network of stations is required to estimate the additional clock parameters. The results of a static experiment by Salazar et al. (2011) indicated that the accuracies of the unfiltered kinematic acceleration obtained with PhaseDif-POP, PhaseDif-DD and a PosDif solution based on Real Time Kinematic (RTK) were in the same order of magnitude. The reference station was only 13 km away from the rover. Slight advantages were reported for the PhaseDif approaches. Salazar et al. (2011) observed in another static experiment with reference stations at a distance between 1700 and 2400 km from the rover that the unfiltered acceleration computed with the PhaseDif-POP method outperformed PhaseDif-DD results by a factor of almost five. Consequently, for a typical dynamic gravimetry campaign using PhaseDif-POP, no own reference stations would be needed to be installed since IGS station data at long distance is freely available (see Section 4.5.1). The evaluation was again limited to unfiltered results.

Li et al. (2018) extended the PhaseDif-POP approach by adding the Russian GLONASS, the European Galileo and the Chinese BeiDou navigation satellite constellations to the former standard GPS computation. They down-weighted the GLONASS system in comparison to the other constellations. In static experiments at Antarctica, Li et al. (2018) reported a significant noise reduction in the unfiltered acceleration when a network of at least two static stations, i.e. a master and a reference station (see Section 4.4.3), was used. A third static station led to minor improvements. The addition of GLONASS to GPS resulted in a considerable improvement of the unfiltered results, further additions had only minor effects. The PhaseDif-POP and the PhaseDif-DD methods performed better than PhaseDif-PPP, again unfiltered. Note that filtered results should be evaluated in order to decide if a method is appropriate for the low-frequency signal of airborne gravimetry. In an extended study, Li et al. (2019) applied a low-pass filter with a filter length of 200 s to static experiments in Antarctica. In the polar regions, the GNSS visibility is limited to low-elevation satellites impairing the result quality. With a nearby reference station, the standard deviations for the PhaseDif-DD, -POP and -PPP approaches were 1.3, 1.5 and 1.9 mGal, respectively. It should be mentioned that the aforementioned references do not include any

results or precision indicators of kinematic acceleration or gravity determination with PhaseDif-POP during a flight. The author is not aware of any such publication.

In none of the publications mentioned above, the ionosphere-free linear combination was found to deliver a better kinematic acceleration than the L1 observable. In direct comparisons, the L1 observable yielded better results (Li et al., 2018) at the long wavelengths, which are of interest in airborne gravimetry. While the ionospheric change rate is considered small, the higher noise of the ionosphere-free linear combination is additionally amplified during the numerical differentiation (see Section 4.4.8). Hence, the L1 observable is preferred unless there is a particularly high ionospheric activity (Kreye and Hein, 2003).

4.2 Numerical differentiation methods

Numerical differentiations are required for the PosDif and PhaseDif approach. The first derivation $\dot{y}(t)$ of a function $y(t)$ describes the slope of the function. Numerical differentiation approximates the function slope based on the difference quotient $\frac{\Delta y}{\Delta t}$ with Δt being the time interval between two consecutive epochs and Δy being the difference of the corresponding function values. The simplest numerical differentiation method is the primary (first order) difference quotient

$$\dot{y}(t_M) = \frac{\Delta y_{0,1}}{\Delta t_{0,1}} = \frac{y_1 - y_0}{\Delta t}, \quad \text{with} \quad t_M = \frac{t_0 + t_1}{2}, \tag{4.1}$$

where the derivation is calculated at the mean epoch x_M between two consecutive epochs t_1, t_2 (Figure 4.1a). If the output epochs are preferred to be equal to the input epochs, the first order (Taylor) central difference quotient (Bruton et al., 1999) can be applied as

$$\dot{y}(t_1) = \frac{\Delta y_{0,2}}{\Delta x_{0,2}} = \frac{y_2 - y_0}{2\,\Delta t}. \tag{4.2}$$

The results of the central difference quotient (Figure 4.1b) are smoother than for Equation (4.1). Note that if the non-central quotient is applied two times to get the acceleration from the position data and if the input data rate is constant, the acceleration output epochs are the same epochs like the input epochs again. With both methods, the first and last epochs are lost. Higher order differential quotients use more epochs around the query epoch. For example, a cubic interpolation polynomial (H. R. Schwarz and Köckler, 2011) can be used as

$$\dot{y}(t_M) = \frac{y_0 - 27y_1 + 27y_2 - y_3}{24\,\Delta t}, \quad \text{with} \quad t_M = \frac{t_0 + t_3}{2} \tag{4.3}$$

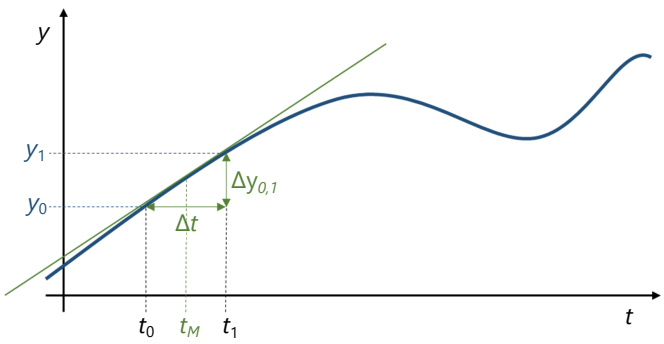
or in another formulation as

$$\dot{y}(t_1) = \frac{-2y_0 - 3y_1 + 6y_2 - y_3}{6\,\Delta t} \tag{4.4}$$

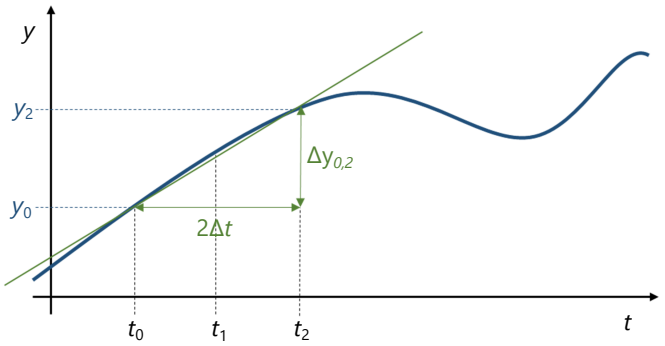
without introducing new output epochs (Figure 4.1c).

Various numerical differentiation strategies have been applied for PosDif and PhaseDif approaches. Serrano et al. (2004), He (2014), Lu et al. (2017) and Xiaohong Zhang et al. (2017) used first order (Taylor) central difference quotients. Kennedy (2003) and Salazar et al. (2011) applied fifth order Taylor filters. Previous publications used more elaborate differentiators like optimal filters based on the Remez-Exchange method (Kreye and Hein, 2003) or they approximated the original functions with B-splines followed by differentiation (Jekeli and Garcia, 1997).

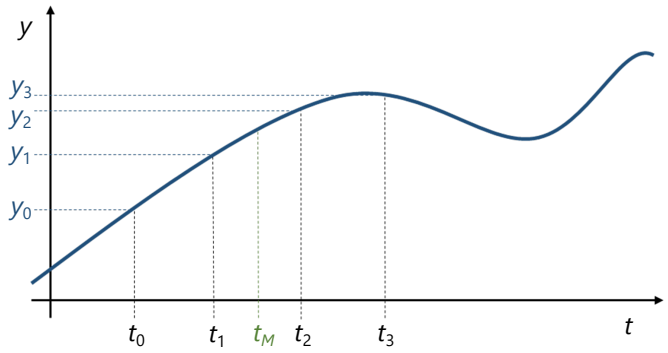
An evaluation of several differentiation methods was presented by Bruton et al. (1999). They implemented first and third order (Taylor) difference quotients, a differentiator based on Fourier series approximation and an optimal filter designed with the Remez Exchange algorithm. With increasing frequencies, the errors of



(a) First order difference quotient



(b) First order central difference quotient



(c) Epochs and function values of the cubic interpolation polynomial

Figure 4.1: Low-order numerical differentiation strategies

Taylor differentiators were found to increase. However, at frequencies under 0.05 Hz (0.15 Hz) corresponding to a signal wavelength of more than 20 s (6.7 s), Bruton et al. (1999) reported that the Taylor central difference of order 1 (3) performed very similar like an ideal differentiator. Using static data, the Taylor approximations were even performing better than the more sophisticated approaches since the latter ones caused higher noise amplification. In another study, Jekeli (2011) confirmed that optimal filter differentiators are not well suited for low frequency signals.

In the scope of this thesis, the low order difference quotients of Equations (4.1) to (4.4) were implemented. No significant differences were detected between the differentiator results in PosDif and PhaseDif modes. Hence, it is not expected that higher order Taylor approximations or more sophisticated differentiators will improve the results for the purpose of airborne gravimetry. The simple approach of Equation (4.1) is selected as numerical differentiation method in the static and dynamic experiments.

4.3 Position differentiation approach (PosDif)

In the PosDif method, the kinematic acceleration $\ddot{\boldsymbol{r}}^n$ is obtained by a two step numerical differentiation

$$\ddot{\boldsymbol{r}}^n = \frac{\delta^2 \boldsymbol{r}^n}{\delta t^2} = \frac{\delta \dot{\boldsymbol{r}}^n}{\delta t} \tag{4.5}$$

of the GNSS position solution $\boldsymbol{r}^n$ with respect to the time t, with the velocity $\dot{\boldsymbol{r}}^n$ being an intermediate solution. The position solution is typically given in the navigation frame. Hence, the complete Eötvös correction after Equation (2.24) is required in the gravimetric post-processing.

If DGNSS solutions are used, the method will be called PosDif-DGNSS in the following; if PPP solutions are used, it will be called PosDif-PPP. High accuracy results are expected for the PosDif-DGNSS approach, at least if the reference station is nearby. However, PosDif-PPP proved to consistently deliver the accuracy that is required for airborne gravimetry (Becker, 2016). Furthermore, the accuracy is not dependent from the distance to the reference station and the workload during campaigns is reduced since no reference station is required.

4.4 Phase differentiation approach (PhaseDif)

The observable of the PhaseDif approach is the phase range acceleration $\ddot{\phi}_m^p$ which is the second numerical time derivative of the phase range ϕ_m^p, obtained as

$$\ddot{\phi}_m^p = \frac{\delta^2 \phi_m^p}{\delta t^2} = \frac{\delta \dot{\phi}_m^p}{\delta t}. \tag{4.6}$$

Note that all quantities in Section 4 are given in the Earth fixed frame. The superscript e is neglected for better readability. Instead, the subscript m denotes a moving GNSS receiver, the so-called "rover"; the superscript p denotes a satellite. Hence, the notation ϕ_m^p denotes the phase range between a satellite and the rover.

The basic functional model of the PhaseDif approach will be introduced in Section 4.4.1. The specific observation equations and algorithms of the PhaseDif-PPP and PhaseDif-POP methods will be presented in Sections 4.4.2 and 4.4.3, respectively. Weighting and outlier detection strategies will be shown in Sections 4.4.8 and 4.4.9, respectively.

4.4.1 Derivation of the PhaseDif functional model

The following derivation of the functional model is closely related to the derivation of the methods by Kennedy (2003) and Salazar et al. (2011). The starting point for the derivation is the phase range observation equation

$$\phi_m^p = \rho_m^p + c(dt_m - dt^p) + \delta\phi_{\text{rel},m}^p + T_m^p - I_{f,m}^p + B_m^p + \omega_m^p + M_{\phi,m}^p + \varepsilon_{\phi,m}^p, \tag{4.7}$$

where ρ_m^p is the geometric range between the receiver and the satellite, $c = 299792458\,\frac{\text{m}}{\text{s}}$ is the velocity of light, dt_m, dt^p are the clock errors of the receiver and the satellite, respectively, $\delta\phi_{\text{rel},m}^p$ is the error due to relativistic effects, T_m^p is the tropospheric signal delay, $I_{f,m}^p$ is the ionospheric effect depending on the signal frequency f, B_m^p is a bias due to phase ambiguities and instrumental delay, ω_m^p is the phase-wind up effect, $M_{\phi,m}^p$ is the multipath effect for phase observations and $\varepsilon_{\phi,m}^p$ is measurement noise including remaining unmodelled effects.

According to Equation (4.6), the phase observation Equation (4.7) needs to be numerically differentiated two times. The quantities $\delta\phi_{\text{rel},m}^p, T_m^p, I_{f,m}^p, B_m^p, \omega_m^p, M_{\phi,m}^p$ are slowly changing or constant. Hence, their first and second time derivatives are assumed zero and the phase range acceleration becomes

$$\ddot{\phi}_m^p = \ddot{\rho}_m^p + c(\ddot{dt}_m - \ddot{dt}^p) + \ddot{\varepsilon}_{\phi,m}^p. \tag{4.8}$$

The removal of these quantities is a major benefit of the kinematic acceleration determination in the acceleration domain. Note that the noise $\ddot{\varepsilon}_{\phi,m}^p$ is amplified in the numerical differentiation process (see Section 4.4.8). However, it will be neglected in the following derivation since its expected mean value is assumed zero.

In Equation (4.8), $\ddot{\phi}_m^p$ is the observable derived from the phase range; the clock errors $\ddot{dt}^m, \ddot{dt}^p$ will be either estimated or obtained from a precise clock product; the remaining quantity, the range acceleration $\ddot{\rho}_m^p$ will be derived in the following. It will be shown that it can be computed using satellite and receiver positions and

velocities. The first step in the derivation process is the definition of the vector $\boldsymbol{x}_m^p$ as the difference between the position vectors of the satellite $\boldsymbol{x}^p$ and the receiver $\boldsymbol{x}_m$. $\boldsymbol{x}_m^p$ can also be expressed as the the unit vector $\boldsymbol{e}_m^p$ that indicates the direction from the receiver to the satellite and is scaled by the geometric range as

$$\boldsymbol{x}_m^p := \boldsymbol{x}^p - \boldsymbol{x}_m = \rho_m^p \boldsymbol{e}_m^p, \quad \text{with} \quad \rho_m^p = |\boldsymbol{x}_m^p|, \quad \boldsymbol{e}_m^p = \frac{\boldsymbol{x}_m^p}{\rho_m^p}, \tag{4.9}$$

with $a = |\boldsymbol{a}|$ being the Euclidean norm of a vector $\boldsymbol{a}$. The first derivation of the position difference vector is obtained as

$$\dot{\boldsymbol{x}}_m^p = \dot{\rho}_m^p \boldsymbol{e}_m^p + \rho_m^p \dot{\boldsymbol{e}}_m^p \quad \Longleftrightarrow \quad \dot{\boldsymbol{e}}_m^p = \frac{\dot{\boldsymbol{x}}_m^p - \dot{\rho}_m^p \boldsymbol{e}_m^p}{\rho_m^p}. \tag{4.10}$$

The velocity and acceleration difference vectors can also be written as

$$\dot{\boldsymbol{x}}_m^p = \dot{\boldsymbol{x}}^p - \dot{\boldsymbol{x}}_m, \quad \ddot{\boldsymbol{x}}_m^p = \ddot{\boldsymbol{x}}^p - \ddot{\boldsymbol{x}}_m. \tag{4.11}$$

The equation

$$\rho_m^p = \boldsymbol{e}_m^p \cdot \boldsymbol{x}_m^p \tag{4.12}$$

shows that the geometric range can be interpreted as the Euclidean norm of the projection to the line of sight of the receiver/satellite difference vector. With this and by inserting Equation (4.9), the first derivation of the geometric range, the range velocity, becomes

$$\dot{\rho}_m^p = \dot{\boldsymbol{e}}_m^p \cdot \boldsymbol{x}_m^p + \boldsymbol{e}_m^p \cdot \dot{\boldsymbol{x}}_m^p \overset{(4.9)}{=} \rho_m^p \underbrace{\dot{\boldsymbol{e}}_m^p \cdot \boldsymbol{e}_m^p}_{0} + \boldsymbol{e}_m^p \cdot \dot{\boldsymbol{x}}_m^p = \boldsymbol{e}_m^p \cdot \dot{\boldsymbol{x}}_m^p, \tag{4.13}$$

where $\boldsymbol{a} \cdot \boldsymbol{b}$ denotes the scalar product of two vectors $\boldsymbol{a}, \boldsymbol{b}$. The first term becomes zero since the scalar product of a vector and its derivative becomes zero if the Euclidean norm of the vector is constant over time. The range acceleration is obtained as the derivative of Equation (4.13) and can be modified as

$$\begin{aligned} \ddot{\rho}_m^p &= \boldsymbol{e}_m^p \cdot \ddot{\boldsymbol{x}}_m^p + \dot{\boldsymbol{e}}_m^p \cdot \dot{\boldsymbol{x}}_m^p \overset{(4.10)}{=} \boldsymbol{e}_m^p \cdot \ddot{\boldsymbol{x}}_m^p + \frac{\dot{\boldsymbol{x}}_m^p - \dot{\rho}_m^p \boldsymbol{e}_m^p}{\rho_m^p} \cdot \dot{\boldsymbol{x}}_m^p = \boldsymbol{e}_m^p \cdot \ddot{\boldsymbol{x}}_m^p + \frac{\overbrace{\dot{\boldsymbol{x}}_m^p \cdot \dot{\boldsymbol{x}}_m^p}^{|\dot{\boldsymbol{x}}_m^p|^2} - \dot{\rho}_m^p \overbrace{\boldsymbol{e}_m^p \cdot \dot{\boldsymbol{x}}_m^p}^{\dot{\rho}_m^p \ (4.13)}}{\rho_m^p} \\ &= \boldsymbol{e}_m^p \cdot \ddot{\boldsymbol{x}}_m^p + \frac{|\dot{\boldsymbol{x}}_m^p|^2 - (\dot{\rho}_m^p)^2}{\rho_m^p} \overset{(4.11)}{=} \boldsymbol{e}_m^p \cdot (\ddot{\boldsymbol{x}}^p - \ddot{\boldsymbol{x}}_m) + \frac{|\dot{\boldsymbol{x}}_m^p|^2 - (\dot{\rho}_m^p)^2}{\rho_m^p}. \end{aligned} \tag{4.14}$$

The modification is based on the insertion of Equations (4.10), (4.13) as well as (4.11) and on the fact that a scalar product of a vector with itself equals its quadratic Euclidean vector norm. The first term describes the differential acceleration along the line of sight; the second term is the centrifugal acceleration due to the rotating baseline (Jekeli and Garcia, 1997). The basic functional model is obtained by inserting the range acceleration of Equation (4.14) into the phase range acceleration of Equation (4.8) as

$$\ddot{\phi}_m^p = \boldsymbol{e}_m^p \cdot (\ddot{\boldsymbol{x}}^p - \ddot{\boldsymbol{x}}_m) + \frac{|\dot{\boldsymbol{x}}_m^p|^2 - (\dot{\rho}_m^p)^2}{\rho_m^p} + c(\ddot{dt}_m - \ddot{dt}^p). \tag{4.15}$$

In a least-squares adjustment (Gauß Markov model), the linear functional model can be expressed with linear algebra of the form

$$\boldsymbol{L} + \boldsymbol{v} = \boldsymbol{A} \cdot \hat{\boldsymbol{X}}, \tag{4.16}$$

with $\boldsymbol{L}$ being the observation vector, $\boldsymbol{v}$ being the observation residual vector, $\boldsymbol{A}$ being the design matrix and $\hat{\boldsymbol{X}}$ being the vector of the unknown parameters. Based on the functional model, the unknown parameters are estimated as

$$\hat{\boldsymbol{X}} = (\boldsymbol{A}^{\mathrm{T}} \boldsymbol{P} \boldsymbol{A})^{-1} \cdot \boldsymbol{A}^{\mathrm{T}} \boldsymbol{P} \boldsymbol{L}, \tag{4.17}$$

with $\boldsymbol{P}$ being the weight matrix based on the stochastic model. The setup of the design matrix and the observation vector will be explained separately for PhaseDif-PPP (Section 4.4.2) and PhaseDif-POP (Section 4.4.3) in conjunction with the corresponding PhaseDif algorithm. The setup of the weight matrix will be discussed in Section 4.4.8. With an appropriate stochastic model, the estimated parameter accuracies are obtained as the square root of the main diagonal elements of the variance covariance matrix

$$\boldsymbol{\Sigma}_{\hat{\boldsymbol{X}}} = \sigma_0^2 \cdot (\boldsymbol{A}^{\mathrm{T}} \boldsymbol{P} \boldsymbol{A})^{-1}, \tag{4.18}$$

where σ_0^2 is a variance factor (see Section 4.4.8).

4.4.2 Specifics of the PhaseDif-PPP functional model

In the PhaseDif method, the phase range acceleration $\ddot{\phi}_m^p$ is the observable. The geometric range ρ_m^p, the range velocity $\dot{\rho}_m^p$, the unit vector $\boldsymbol{e}_m^p$, the differential velocity $\dot{\boldsymbol{x}}_m^p$ and the kinematic acceleration $\boldsymbol{x}^p$ of the satellite can be computed using satellite and receiver positions and their numerical derivatives. Position accuracies of several meters, e.g. obtained by code positioning or broadcast orbits, are sufficient to obtain the kinematic acceleration with sub-mGal accuracy (Jekeli and Garcia, 1997). The kinematic acceleration $\ddot{\boldsymbol{x}}_m$ of the receiver, and the clock drift rates $\ddot{dt}_m, \ddot{dt}^p$ are unknown parameters. In the case of the PhaseDif-PPP method, the satellite clock drift rate $\ddot{dt}^p$ is obtained by numerical differentiation of precise satellite clock error products. The basic functional model of Equation (4.15) is reordered as

$$\ddot{\phi}_m^p \underbrace{-\boldsymbol{e}_m^p \cdot \ddot{\boldsymbol{x}}^p - \frac{|\dot{\boldsymbol{x}}_m^p|^2 - (\dot{\rho}_m^p)^2}{\rho_m^p}}_{-d_m^p} + c\ddot{dt}^p = -\boldsymbol{e}_m^p \cdot \ddot{\boldsymbol{x}}_m + c\ddot{dt}_m \tag{4.19}$$

to the form of an observation equation. The observations as well as the known quantities are put on the left and the unknown parameters on the right side of the equation. For better readability, the satellite acceleration and the centrifugal terms are merged into

$$d_m^p := \boldsymbol{e}_m^p \cdot \ddot{\boldsymbol{x}}^p + \frac{|\dot{\boldsymbol{x}}_m^p|^2 - (\dot{\rho}_m^p)^2}{\rho_m^p}. \tag{4.20}$$

In the following, the input for the epoch-wise least-squares adjustment based on Equations (4.17) and (4.18) will be prepared. The functional model of the PhaseDif approaches is linear with respect to the unknown parameters, i.e. a linearisation is not required. From now on, instead of a single observation, all observations from one receiver, i.e. the rover m, to n_{Sat} satellites at one epoch are considered. The observation vector and the vector of unknowns are

$$\boldsymbol{L} = \ddot{\boldsymbol{\phi}} - \boldsymbol{d} = \begin{pmatrix} \ddot{\phi}_m^1 - d_m^1 + c\ddot{dt}^1 \\ \ddot{\phi}_m^2 - d_m^2 + c\ddot{dt}^2 \\ \vdots \\ \ddot{\phi}_m^{n_{\mathrm{Sat}}} - d_m^{n_{\mathrm{Sat}}} + c\ddot{dt}^{n_{\mathrm{Sat}}} \end{pmatrix}, \quad \boldsymbol{X} = \begin{pmatrix} \ddot{\boldsymbol{x}}_m \\ c\ddot{dt}_m \end{pmatrix}, \tag{4.21}$$

where $\ddot{\phi}_m^j$ is the phase range acceleration between the rover m and a satellite j. The number of observations per epoch is $n_{\boldsymbol{L}} = n_{\mathrm{Sat}}$; the number of unknowns is $n_{\boldsymbol{X}} = 4$. It is recommended to select the product $c\ddot{dt}_m$ as parameter instead of $\ddot{dt}_m$ for improved numerical stability since the scale of the normal equation matrix is more uniform in this mode. The design matrix is built up as

$$\boldsymbol{A} = \begin{pmatrix} -(\boldsymbol{e}_m^1)^{\mathrm{T}} & 1 \\ -(\boldsymbol{e}_m^2)^{\mathrm{T}} & 1 \\ \vdots & \vdots \\ -(\boldsymbol{e}_m^{n_{\mathrm{Sat}}})^{\mathrm{T}} & 1 \end{pmatrix}, \tag{4.22}$$

where $\boldsymbol{e}_m^j$ is the unit vector pointing from the rover m to the satellite j.

4.4.3 Specifics of the PhaseDif-POP functional model

In the PhaseDif-POP method, the satellite clock drift rate $\ddot{dt}^p$ is estimated in addition to the kinematic acceleration of the receiver and the clock drift rate $\ddot{dt}_i$ of the receiver i. This is enabled by adding one or more static stations to the estimation process. The relative clock determination is based on the least-squares adjustment of the receiver and satellite clocks. The absolute clock drift rate cannot be estimated. However, for the purpose of kinematic acceleration determination, relative clock drift rates are sufficient. A rank defect in the adjustment is precluded by defining the clock drift rate of one static station to be the reference clock drift rate (Salazar et al., 2011). The absolute value $\ddot{dt}_0$ of this so-called master station 0 is unknown. The absolute clock drift rates $\ddot{dt}_m, \ddot{dt}_k, \ddot{dt}^p$ of the rover m, the reference station k and the satellite p are then converted to the relative clock drift rates $\ddot{d\tau}_m, \ddot{d\tau}_k, \ddot{d\tau}^p$ as

$$\ddot{d\tau}_m = \ddot{dt}_m - \ddot{dt}_0, \quad \ddot{d\tau}_k = \ddot{dt}_k - \ddot{dt}_0, \quad \ddot{d\tau}^p = \ddot{dt}^p - \ddot{dt}_0, \quad \ddot{d\tau}_0 = \ddot{dt}_0 - \ddot{dt}_0 = 0. \tag{4.23}$$

The relative clock drift rate of the master becomes zero.

There are three types of receivers in the POP-based method that observe multiple **satellites** p:

- The purpose of the method is the estimation of the kinematic acceleration $\ddot{\boldsymbol{x}}_m$ of the **rover** m. This is the only receiver that is also used in the PPP-based method.
- The **master** station 0 sets the reference clock drift rate.
- Optionally, any number of **reference** stations k can be added to improve the redundancy and the accuracy of the estimates. Note that in the following, the master station will not be considered to be part of the reference stations.

An observation from a specific reference station i to a specific satellite j will be noted as $\ddot{\phi}_i^j$ in the following. The rover and the master can be unambiguously identified by the subscripts $m, 0$, respectively.

In the PhaseDif-POP method, the absolute clock parameters in Equation (4.15) are replaced by the relative clock parameters of Equation (4.23) as

$$\ddot{\phi}_m^p = \boldsymbol{e}_m^p \cdot (\ddot{\boldsymbol{x}}^p - \ddot{\boldsymbol{x}}_m) + \frac{|\dot{\boldsymbol{x}}_m^p|^2 - (\dot{\rho}_m^p)^2}{\rho_m^p} + c(\ddot{d\tau}_m - \ddot{d\tau}^p). \tag{4.24}$$

The observation equation for the rover

$$\ddot{\phi}_m^p \underbrace{- \boldsymbol{e}_m^p \cdot \ddot{\boldsymbol{x}}^p - \frac{|\dot{\boldsymbol{x}}_m^p|^2 - (\dot{\rho}_m^p)^2}{\rho_m^p}}_{-d_m^p} = -\boldsymbol{e}_m^p \cdot \ddot{\boldsymbol{x}}_m + c\ddot{d\tau}_m - c\ddot{d\tau}^p \tag{4.25}$$

is then obtained by moving all terms that do not include unknown parameters to the left and the parameters to be estimated to the right side of the equation. The quantity d_m^p can be calculated using Equation (4.20), like in the PhaseDif-PPP approach. The main differences in comparison to the PPP-based Equation (4.19) are the relative clock parameters and the relocation of the satellite clock parameters to the estimation side.

Since there are multiple receivers in the PhaseDif-POP method, multiple observation equations are required. In the observation equation for a reference station

$$\ddot{\phi}_k^p - \boldsymbol{e}_k^p \cdot \ddot{\boldsymbol{x}}^p - \frac{|\dot{\boldsymbol{x}}_k^p|^2 - (\dot{\rho}_k^p)^2}{\rho_k^p} = c\ddot{d\tau}_k - c\ddot{d\tau}^p, \tag{4.26}$$

the kinematic acceleration of the receiver is removed since it is zero for the static station, i.e. $\ddot{\boldsymbol{x}}_k = \mathbf{0}$. The same ($\ddot{\boldsymbol{x}}_0 = \mathbf{0}$) is true for the master observation equation

$$\ddot{\phi}_0^p - \boldsymbol{e}_0^p \cdot \ddot{\boldsymbol{x}}^p - \frac{|\dot{\boldsymbol{x}}_0^p|^2 - (\dot{\rho}_0^p)^2}{\rho_0^p} = -c\ddot{d\tau}^p, \tag{4.27}$$

where the relative receiver clock drift rate is removed as well since it is zero for the master in accordance with Equation (4.23). In the following, the term “station” will be used for all static receivers, i.e. all receivers except for the rover. The term ”receiver“ will be used for all receivers, i.e. the rover, the master and all reference stations.

Since there are several receivers and the satellite clocks are estimated, the least-squares adjustment is much more complex than for the PhaseDif-PPP method. In

$$\boldsymbol{L} = \ddot{\boldsymbol{\phi}} - \boldsymbol{d} = \begin{pmatrix} \ddot{\phi}_m^1 - d_m^1 \\ \vdots \\ \ddot{\phi}_m^{n_{\text{Sat}}} - d_m^{n_{\text{Sat}}} \\ \ddot{\phi}_0^1 - d_0^1 \\ \vdots \\ \ddot{\phi}_0^{n_{\text{Sat}}} - d_0^{n_{\text{Sat}}} \\ \ddot{\phi}_{k_1}^1 - d_{k_1}^1 \\ \vdots \\ \ddot{\phi}_{k_1}^{n_{\text{Sat}}} - d_{k_1}^{n_{\text{Sat}}} \\ \vdots \\ \ddot{\phi}_{k_{n_{\text{Ref}}}}^1 - d_{k_{n_{\text{Ref}}}}^1 \\ \vdots \\ \ddot{\phi}_{k_{n_{\text{Ref}}}}^{n_{\text{Sat}}} - d_{k_{n_{\text{Ref}}}}^{n_{\text{Sat}}} \end{pmatrix}, \quad \boldsymbol{X} = \begin{pmatrix} \ddot{\boldsymbol{x}}_m \\ c\ddot{d\tau}_m \\ c\ddot{d\tau}_{k_1} \\ c\ddot{d\tau}_{k_2} \\ \vdots \\ c\ddot{d\tau}_{k_{n_{\text{Ref}}}} \\ c\ddot{d\tau}^{p_1} \\ c\ddot{d\tau}^{p_2} \\ \vdots \\ c\ddot{d\tau}^{p_{n_{\text{Sat}}}} \end{pmatrix}, \tag{4.28}$$

the number of observations and unknown parameters increases to

$$\begin{aligned} n_{\boldsymbol{L}} &= n_{\text{Sat}} \cdot (2 + n_{\text{Ref}}) = n_{\text{Sat}} \cdot n_{\text{Rec}}, \\ n_{\boldsymbol{X}} &= n_{\text{Ref}} + n_{\text{Sat}} + 4 = n_{\text{Rec}} + n_{\text{Sat}} + 2, \quad \text{with} \quad n_{\text{Rec}} = 2 + n_{\text{Ref}}, \end{aligned} \tag{4.29}$$

in the theoretical case that the same satellites are observed by all receivers. The design matrix then becomes

$$\boldsymbol{A} = \begin{pmatrix}
-(\boldsymbol{e}_m^1)^{\mathrm{T}} & 1 & 0 & 0 & 0 & \cdots & -1 & 0 & 0 & \cdots & \rightarrow \ddot{\phi}_m^1 \\
-(\boldsymbol{e}_m^1)^{\mathrm{T}} & 1 & 0 & 0 & 0 & \cdots & 0 & -1 & 0 & \cdots & \rightarrow \ddot{\phi}_m^2 \\
\vdots & \vdots & \vdots & \vdots & \vdots & \vdots & \vdots & \vdots & \vdots & \vdots & \\
\mathbf{0}^{\mathrm{T}} & 0 & 0 & 0 & 0 & \cdots & -1 & 0 & 0 & \cdots & \rightarrow \ddot{\phi}_0^1 \\
\mathbf{0}^{\mathrm{T}} & 0 & 0 & 0 & 0 & \cdots & 0 & -1 & 0 & \cdots & \rightarrow \ddot{\phi}_0^2 \\
\vdots & \vdots & \vdots & \vdots & \vdots & \vdots & \vdots & \vdots & \vdots & \vdots & \\
\mathbf{0}^{\mathrm{T}} & 0 & 1 & 0 & 0 & \cdots & -1 & 0 & 0 & \cdots & \rightarrow \ddot{\phi}_{k_1}^1 \\
\mathbf{0}^{\mathrm{T}} & 0 & 1 & 0 & 0 & \cdots & 0 & -1 & 0 & \cdots & \rightarrow \ddot{\phi}_{k_1}^2 \\
\vdots & \vdots & \vdots & \vdots & \vdots & \vdots & \vdots & \vdots & \vdots & \vdots & \\
\mathbf{0}^{\mathrm{T}} & 0 & 0 & 1 & 0 & \cdots & -1 & 0 & 0 & \cdots & \rightarrow \ddot{\phi}_{k_2}^1 \\
\mathbf{0}^{\mathrm{T}} & 0 & 0 & 1 & 0 & \cdots & 0 & -1 & 0 & \cdots & \rightarrow \ddot{\phi}_{k_2}^2 \\
\underbrace{\vdots}_{\ddot{\boldsymbol{x}}_m} & \underbrace{\vdots}_{c\ddot{d}\tau_m} & \underbrace{\vdots}_{c\ddot{d}\tau_{k_1}} & \underbrace{\vdots}_{c\ddot{d}\tau_{k_2}} & \underbrace{\vdots}_{c\ddot{d}\tau_{k_3}} & \vdots & \underbrace{\vdots}_{c\ddot{d}\tau^{p_1}} & \underbrace{\vdots}_{c\ddot{d}\tau^{p_2}} & \underbrace{\vdots}_{c\ddot{d}\tau^{p_3}} & \vdots &
\end{pmatrix}. \tag{4.30}$$

The corresponding observations and parameters are indicated at the right and bottom sides of the matrix, respectively. The vertically separated groups of the matrix represent the observation groups for the single receivers. The unknown parameters are represented by the columns. They are the kinematic acceleration of the rover as well as the clock drift errors of the rover, the reference stations and the satellites.

4.4.4 PhaseDif algorithm

The main processing steps of the PhaseDif approach are illustrated in Figure 4.2. After import and pre-processing of the input receiver and satellite data, the numerical time derivative is formed one or two times. The obtained quantities are then fed into an epoch-wise least-squares adjustment where, amongst others, the kinematic acceleration of the rover is estimated. Within the process, it needs to be checked if the observations are valid and if a sufficient number of observations is available for least-squares adjustment. In the following, the processing steps will be described in more detail. Processing steps that are specific to the PPP- or the POP-based methods will be introduced in Sections 4.4.5 and 4.4.6.

The receiver carrier phase observations are imported and specific frequencies are selected, depending on the GNSS constellation. The phase observations are typically given as cycles. They are transformed to phase ranges by multiplying the cycles by the corresponding signal wavelength (e.g. 19.05 cm for GPS L1 observations). The phase ranges ϕ_m^p can be used directly. Alternatively, two or more frequencies can be processed simultaneously by applying linear combinations. First order ionospheric errors are removed using the ionosphere-free linear combination with the drawback of noise amplification (see Section 4.4.8). An outlier test can be applied to detect and remove erroneous observations (see Section 4.4.9), e.g. due to cycle slips. The phase velocity $\dot{\phi}_m^p$ and phase acceleration $\ddot{\phi}_m^p$ are obtained by two consecutive numerical time differentiations applying methods introduced in Section 4.2. The phase accelerations are the observations for the subsequent epoch-wise least-squares adjustment.

The GNSS receiver observations are additionally used for the determination of the rover position $\boldsymbol{x}_m$. Since a rough positioning is sufficient for the acceleration determination (see Section 4.1), single point positioning (using code observations) is sufficient. However, alternatively, DGNSS, PPP or POP might be performed if the position data is required for navigation or precise localisation of the gravity results. With a single numerical differentiation, the rover velocity $\dot{\boldsymbol{x}}_m$ is obtained.

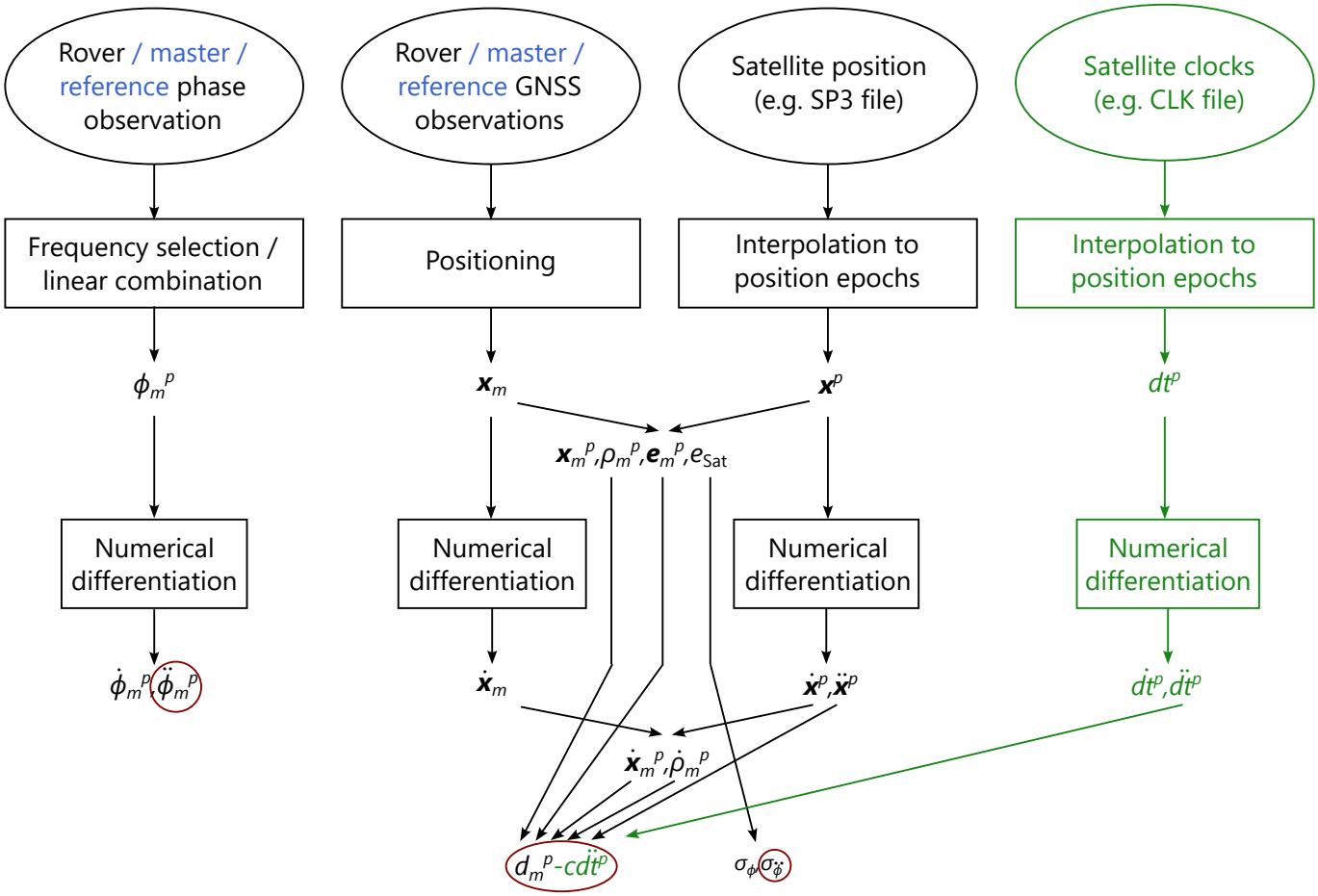


Figure 4.2: Schematic overview on the PhaseDif algorithm (green: only required for PhaseDif-PPP; blue: only required for PhaseDif-POP; red: input for least-squares adjustment)

Note that the velocity might also be determined by a variant of the PhaseDif approach, where the computation is done directly in the velocity domain using the phase velocity as observable. The functional model is

$$\dot{\phi}_m^p = \boldsymbol{e}_m^p \cdot (\dot{\boldsymbol{x}}^p - \dot{\boldsymbol{x}}_m) + c(\dot{dt}_m - \dot{dt}^p). \tag{4.31}$$

which is similar to Equation (4.15), but computed in the velocity domain and without the differential line of sight and the centrifugal term (Salazar et al., 2011). In the scope of this thesis, this direct approach was implemented in addition to the numerical differentiation of the positions, but did not result in any significant acceleration differences. Hence, the numerical differentiation of the positions was selected as default method. However, the velocity determination with Equation (4.31) might be an auspicious method for applications where precise velocity information is required. Like for the PhaseDif acceleration method, slowly changing parameters can be neglected.

The satellite position can be determined with sufficient accuracy using broadcast ephemerides or predicted satellite orbit products. The orbit positions $\boldsymbol{x}^p$ need to be interpolated to the receiver observation epochs. Using a trigonometric interpolation approach, the trigonometric shape of the satellite trajectory is considered appropriately (Schenewerk, 2003; Feng and Zheng, 2005). However, polynomial approaches might also deliver satellite positions with sufficient accuracy for the PhaseDif acceleration determination. The satellite velocities $\dot{\boldsymbol{x}}^p$ and accelerations $\ddot{\boldsymbol{x}}^p$ can be obtained by numerical differentiation or by using the orbital parameters that

were determined in the scope of the interpolation. Again, both methods are appropriate for the desired purpose.

From the receiver and satellite positions $\boldsymbol{x}_m, \boldsymbol{x}^p$, the position difference vector $\boldsymbol{x}_m^p = (x_{m,x}^p \; x_{m,y}^p \; x_{m,z}^p)^{\mathrm{T}}$, the geometric range ρ_m^p and the unit vector $\boldsymbol{e}_m^p$ are obtained using Equation (4.9). The satellite elevation angle is

$$e_{\mathrm{Sat}} = \arcsin\left(\frac{x_{m,x}^p \cos(\phi_m)\cos(\lambda_m) + x_{m,y}^p \cos(\phi_m)\sin(\lambda_m) + x_{m,z}^p \sin(\phi_m)}{\rho_m^p}\right), \tag{4.32}$$

with λ_m, ϕ_m being the geodetic longitude and latitude of the receiver. The velocity difference vector $\dot{\boldsymbol{x}}_m^p$ and the range velocity $\dot{\rho}_m^p$ are obtained from the receiver and satellite velocities $\dot{\boldsymbol{x}}_m, \dot{\boldsymbol{x}}^p$ with Equation (4.11). The quantities $\rho_m^p, \boldsymbol{e}_m^p, \dot{\boldsymbol{x}}_m^p, \dot{\rho}_m^p, \ddot{\boldsymbol{x}}^p$ are used to determine the auxiliary quantity d_m^p with Equation (4.20). The quantities $\ddot{\phi}_m^p, d_m^p$ are the input for the functional model of the least squares adjustment. e_{Sat} is required to determine the standard deviation σ_ϕ of the phase observation. This accuracy indicator will be used to determine appropriate weights for the stochastic model (see Section 4.4.8).

4.4.5 Specifics of the PhaseDif-PPP algorithm

In the PhaseDif-PPP approach, the satellite clock errors are eliminated by external satellite clock products. The satellite clock drift rate is computed in two steps: First, the satellite clock error dt^p needs to be interpolated to the position epochs. Second, the clock drift and the clock drift rate $\dot{dt}^p, \ddot{dt}^p$ are obtained by two consecutive numerical time differentiations. To avoid jumps in the derivations, the interpolation can be performed using non-linear interpolation, e.g. applying cubic or spline methods. When the PhaseDif-PPP is selected, the clock drift rates are required as additional input for the least-squares adjustment instead.

The observation vector contains all phase accelerations observed by the rover. The processing scheme that is illustrated in Figure 4.2 needs to be repeated for all satellite observations of the rover. A solution can be estimated using Equations (4.17) and (4.18) if the number of observations is at least equal to the number of unknowns, i.e. at least four rover observations are required per epoch. The length of the observation vector can vary from epoch to epoch depending on the number of observed satellites.

4.4.6 Specifics of the PhaseDif-POP algorithm

In the PhaseDif-POP method, no external clock data is needed, but a network of several GNSS receivers: the rover, the master station and optionally an arbitrary number of reference stations. Consequently, the processing scheme illustrated in Figure 4.2 needs to be followed for all receiver/satellite combinations. While the availability of four valid satellite observations is sufficient for an estimation solution in the PhaseDif-PPP method, there are several requirements for a least-squares adjustment in the PhaseDif-POP method. Generally, it is not necessary that all receivers observe the same set of satellites, but there are requirements for a shared network. The following conditions need to be met to enable an estimation without rank defect at the corresponding epoch:

- Elements of the observation vector need to be removed from the observation vector if the corresponding receiver did not observe the corresponding satellites. Clock drift rate parameters for satellites that have not been observed by any of the receivers need to be removed from the parameter vector in Equation (4.28). Both vectors need to be updated if any observations are removed in the following.
- At least four rover observations are required. Otherwise, the epoch is invalid, i.e. no solution can be estimated for the epoch.

- Master or reference stations forming a distinct network need to be removed. Those stations do not have any common satellite observations with the rover or with other reference stations that have common satellites with the rover. The removal of stations needs to be done iteratively: If a station has been removed it needs to be rechecked if the remaining stations have common satellite observations with the remaining rover network.
- Reference stations that only have common satellite observations with the rover, i.e. no common observations with other stations, also need to be removed.
- At least one satellite of a reference station needs to be observed at more than two stations if there are at least three receivers.
- If the master was removed, another remaining reference station might replace the master for the epoch. The resulting clock errors deviate from the other epochs since the absolute clock reference changes.
- The epoch becomes invalid if the number of remaining observations is smaller than the number of the remaining unknowns.
- It also is invalid if no master and reference observations are left.

If an outlier test is performed and observations are removed within a data snooping approach (see 4.4.9), the aforementioned requirements need to be re-checked. The list above makes clear that the complexity of the required pre-adjustment checks in the POP-based method is much higher than in the PPP-based method.

4.4.7 Phase observation types

For the different GNSS (GPS, Galileo, GLONASS, BeiDou) several signal frequencies exist. In the scope of this thesis, L1 will be the primary signal for GPS, Galileo and GLONASS; L2 will be used for BeiDou. The frequency identifiers correspond to the conventions of the RINEX3 format (Romero, 2020). The primary phase observation type is selected for single phase observations; the secondary phase observation type is selected as additional frequency if a Linear Combination (LC) of two frequencies is evaluated. LCs will only be computed for GPS using the L2 signal as secondary observation type.

A LC of two frequencies can be used to stress or reduce specific signal properties. In the combined signal,

$$\phi_{\text{LC}} = a_1\phi_1 + a_2\phi_2 \tag{4.33}$$

the signal frequencies are scaled by the coefficients a_1, a_2.

The *Ionosphere-Free Linear Combination (IF)* eliminates the first-order ionospheric error and preserves the geometry (Hauschild, 2017b). It is obtained by setting

$$a_1 = \frac{f_1^2}{f_1^2 - f_2^2}, \quad a_2 = -\frac{f_2^2}{f_1^2 - f_2^2} \quad \rightarrow \phi_{\text{IF}} = \frac{f_1^2\phi_1 - f_2^2\phi_2}{f_1^2 - f_2^2}, \tag{4.34}$$

where f_1, f_2 are the signal frequencies of the primary and secondary phase signal, respectively. A drawback of the IF is the noise amplification (see Section 4.4.8).

4.4.8 Weighting

Elevation-dependent weighting

The accuracy of a phase observation depends on the travel time through the Earth's atmosphere. The best accuracy is expected for a satellite at the zenith of the receiver, the worst accuracy is expected if the satellite

is located close to the horizon of the observer. Hence, the accuracy improves with the satellite elevation angle, i.e. the angle between the local horizontal plane and the satellite.

The bulk of bad observations are usually removed a priori by selecting a minimal elevation angle, the elevation cut-off, of about 5 to 20°. The varying accuracy of the remaining observations can be considered by approximating the standard deviation σ_ϕ of the phase observation based on the elevation angle e_{Sat} as obtained by equation (4.32). In a simple approach, the phase variance is approximated as

$$\sigma_\phi^2 = \frac{\sigma_{\phi,0}^2}{\sin^2(e_{\text{Sat}})}, \tag{4.35}$$

with $\sigma_{\phi,0} \approx 5$ mm being the standard deviation of a phase observation in zenith direction. The approach is called "COSZ" since the sine of the elevation angle is equal to the cosine of the zenith angle (Luo et al., 2014). More elaborated approaches are based on exponential functions where coefficients b_0, b_1 are selected based on receiver properties. In the "KING" method (King and Bock, 1999; S. Jin et al., 2005), the phase variance is approximated based on the sine as

$$\sigma_\phi^2 = b_0^2 + \frac{b_1^2}{\sin^2(e_{\text{Sat}})}, \quad \text{with} \quad b_0 = 4.3\,\text{mm}, \quad b_1 = 3\,\text{mm}. \tag{4.36}$$

In an alternative approach "JIN2" based on the cosine (X. Jin, 1996; S. Jin et al., 2005), the accuracy is given by

$$\sigma_\phi^2 = b_0^2 + b_1^2 \cos^2(e_{\text{Sat}}), \tag{4.37}$$

with the same b_0, b_1 like in Equation (4.36). Another method, "EXPZ" (Luo et al., 2014), is based on the exponential function

$$\sigma_\phi^2 = \left(b_0 + b_1 \cdot e^{-\frac{e_{\text{Sat}}}{e_0}}\right)^2, \quad \text{with} \quad b_0 = 1.7\,\text{mm}, \quad b_1 = 3.3\,\text{mm}, \quad e_0 = 40°, \tag{4.38}$$

where e_0 is an additional coefficient. Depending on the receiver type, the coefficients b_0, b_1 can be re-estimated in a least-squares adjustment (Luo et al., 2014) to improve the accuracy approximation. There exist more complex accuracy approximations considering additional parameters like signal frequencies and antenna properties. However, since relatively high efforts must be taken to compute such models or to re-estimate the coefficients at uncertain benefit, the evaluation in this thesis will be limited to the approaches of Equations (4.35) to (4.38).

Noise amplification due to linear combination

If linear combinations are computed based on Equation (4.33), the noise is amplified depending on the coefficients a_1, a_2. According to the laws of variance propagation, the variance of a linear combination is obtained as

$$\sigma_{\phi,\text{LC}}^2 = (a_1\sigma_\phi)^2 + (a_2\sigma_\phi)^2 = \sigma_\phi^2 \cdot (a_1^2 + a_2^2). \tag{4.39}$$

The accuracy of both signals is assumed to be equal. The standard deviation of the IF after Equation (4.34) becomes

$$\sigma_{\phi,\text{IF}} = \sigma_\phi \sqrt{\left(\frac{f_1^2}{f_1^2 - f_2^2}\right)^2 + \left(\frac{f_2^2}{f_1^2 - f_2^2}\right)^2} = \sigma_\phi \sqrt{\frac{f_1^4 + f_2^4}{(f_1^2 - f_2^2)^2}} = \sigma_\phi \frac{\sqrt{f_1^4 + f_2^4}}{|f_1^2 - f_2^2|}. \tag{4.40}$$

This means, the phase noise gets amplified by a factor of $\sqrt{f_1^4 + f_2^4} \cdot |f_1^2 - f_2^2|^{-1}$. For an IF of GPS L1 and L2 frequencies with $f_1 = 1575.42\,\text{MHz}, f_2 = 1227.60\,\text{MHz}$, this translates into a noise amplification by a factor of about 3.0.

Noise amplification due to numerical differentiation

In addition to the LC noise amplification, the observation noise is increased due to the numerical differentiation. The amount of the amplification depends on the time interval Δt between two consecutive epochs and the numerical differentiation method (see Section 4.2). The standard deviation σ_ϕ of the phase observation is assumed equal for consecutive epochs. The uncertainty of the epochs is assumed neglectable. The phase velocity can be determined using the primary difference quotient according to Equation (4.1) as

$$\dot{\phi}(t_M) = \frac{\Delta\phi_{0,1}}{\Delta t_{0,1}} = \frac{\phi_1 - \phi_0}{\Delta t}. \tag{4.41}$$

Applying the laws of variance propagation, the standard deviation of the phase velocity becomes

$$\sigma_{\dot{\phi}} = \sqrt{\left(\frac{\sigma_\phi}{\Delta t}\right)^2 + \left(\frac{\sigma_\phi}{\Delta t}\right)^2} = \sigma_\phi \sqrt{\frac{2}{(\Delta t)^2}} = \sigma_\phi \frac{\sqrt{2}}{\Delta t}. \tag{4.42}$$

Hence, the noise of the phase velocity is scaled by a factor of $\sqrt{2}/\Delta t$ in comparison to the noise of the phase range. The second numerical derivation causes an amplification of the same amount. Hence, the noise amplification factor of two consecutive numerical differentiations is the squared factor of a single derivation. The standard deviation of the phase acceleration becomes

$$\sigma_{\ddot{\phi}} = \sigma_{\dot{\phi}} \frac{\sqrt{2}}{\Delta t} = \sigma_\phi \frac{2}{(\Delta t)^2}. \tag{4.43}$$

The standard deviations for the phase velocity and acceleration obtained with the first order central difference quotient, Equation (4.2), are determined analogously as

$$\sigma_{\dot{\phi}} = \sqrt{\left(\frac{\sigma_\phi}{2\Delta t}\right)^2 + \left(\frac{\sigma_\phi}{2\Delta t}\right)^2} = \sigma_\phi \sqrt{\frac{2}{(2\Delta t)^2}} = \sigma_\phi \frac{1}{\Delta t\sqrt{2}} \quad \Rightarrow \quad \sigma_{\ddot{\phi}} = \sigma_{\dot{\phi}} \frac{1}{\Delta t\sqrt{2}} = \frac{\sigma_\phi}{2(\Delta t)^2}. \tag{4.44}$$

The corresponding standard deviations for the cubic interpolation polynomial according to Equations (4.3) and (4.4) are

$$\sigma_{\dot{\phi}} = \sqrt{\left(\left(\frac{\sigma_\phi}{24\Delta t}\right)^2 + \left(\frac{27\sigma_\phi}{24\Delta t}\right)^2\right) \cdot 2} = \sigma_\phi \frac{365}{12\Delta t} \quad \Rightarrow \quad \sigma_{\ddot{\phi}} = \sigma_{\dot{\phi}} \frac{365}{12\Delta t} = \sigma_\phi \frac{365}{144(\Delta t)^2} \tag{4.45}$$

and

$$\sigma_{\dot{\phi}} = \sqrt{\left(\frac{\sigma_\phi}{3\Delta t}\right)^2 + \left(\frac{\sigma_\phi}{2\Delta t}\right)^2 + \left(\frac{\sigma_\phi}{\Delta t}\right)^2 + \left(\frac{\sigma_\phi}{6\Delta t}\right)^2} = \sigma_\phi \frac{5\sqrt{2}}{6\Delta t} \quad \Rightarrow \quad \sigma_{\ddot{\phi}} = \sigma_{\dot{\phi}} \frac{5\sqrt{2}}{6\Delta t} = \sigma_\phi \frac{25}{18(\Delta t)^2}, \tag{4.46}$$

respectively. The noise amplification factors as functions of the sample interval and the numerical differentiation method are shown in Figure 4.3. The noise strongly increases with a decreasing sample interval. The noise of the derivation is starting to be higher than the undifferentiated values at a sample rate of approximately 1 s, depending on the numerical differentiation method. For higher sample intervals, the noise decreases, i.e. the derivation is smoothed. For the accelerations, the noise obtained with the first order central difference is almost one order of magnitude lower than the noise obtained with the cubic interpolation polynomial. The noise of the first order difference quotient and the cubic polynomial without introducing new epochs is only slightly lower than the noise of the cubic interpolation polynomial. At sample intervals lower than about 1 s, the noise amplification is lower for the first than for the second derivative; at higher sample intervals it is vice versa. In the case of dynamic gravimetry, the sample rate is typically higher than 1 Hz.

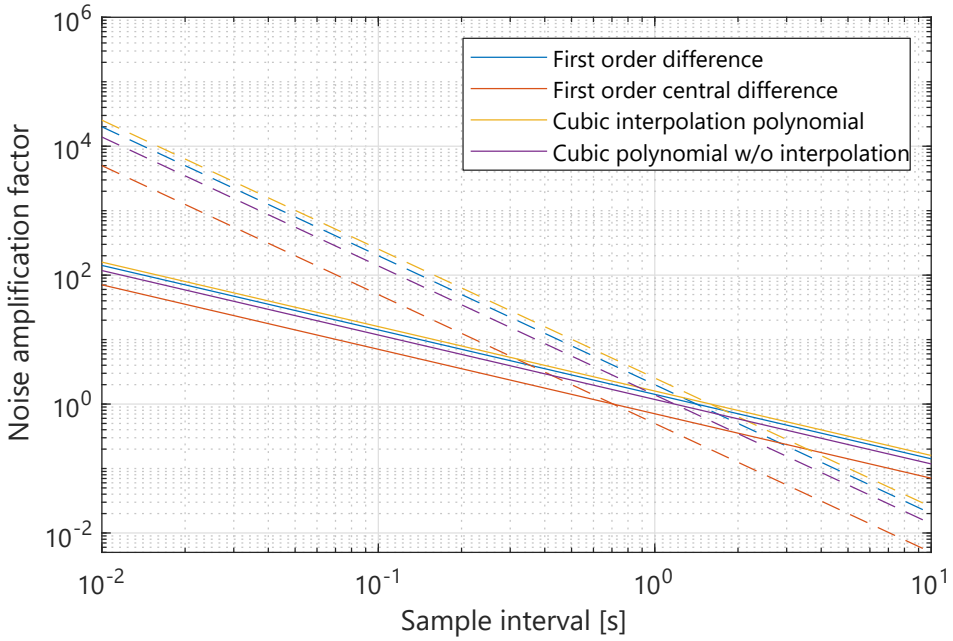


Figure 4.3: Noise amplification factors for the first (solid lines) and second (dashed lines) numerical derivative for a constant input data sample rate

Building up the weight matrix

It should be noted that the determination of the noise amplification scale factors due to numerical differentiation and linear combination do not influence the estimate of the parameters in the least-squares adjustment since all observations in the PhaseDif method are of the same type (phase accelerations). However, the estimated accuracies of the parameters are expected to be closer to reality if the noise amplification is considered in the adjustment.

Contrarily, an elevation-based weighting (Luo et al., 2014) influences the estimates for the parameters. The standard deviation of the phase acceleration can be used to weight the observations in the PhaseDif least-squares adjustment individually. The weight $w_{\ddot{\phi}}$ of a phase acceleration observation is obtained as

$$w_{\ddot{\phi}} = \frac{\sigma_0^2}{\sigma_{\ddot{\phi}}^2}, \tag{4.47}$$

where $\sigma_{\ddot{\phi}}^2$ is the variance of the phase acceleration with an elevation angle e_{Sat} and σ_0^2 is the best possible variance of a phase acceleration considering the numerical differentiation method and possible linear combinations. The a priori variance factor σ_0^2 is obtained for a satellite being in the zenith of the receiver, i.e. $e_{\text{Sat}} = 90°$. In this ideal case, the weight becomes 1. Otherwise, it decreases with decreasing elevation. Assuming uncorrelated observations, the weight matrix

$$\boldsymbol{P} = \begin{pmatrix} w_i & \varnothing \\ \varnothing & \ddots \end{pmatrix} \tag{4.48}$$

used for the least-squares estimation with Equations (4.17) and (4.18) is the diagonal matrix with the individual weights w_i.

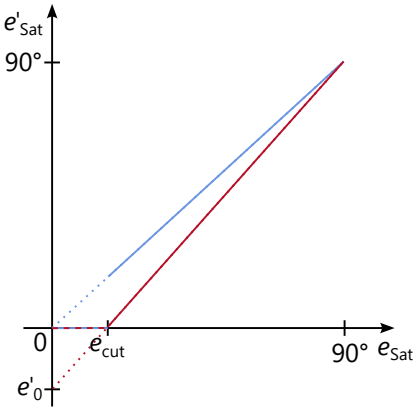


Figure 4.4: Soft elevation method (blue: standard; red: soft)

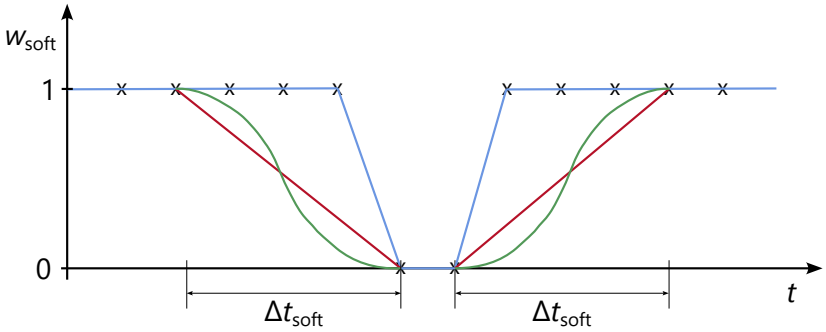


Figure 4.5: Soft loss method close to missing observations (blue: standard; red: soft linear; green: soft trigonometric)

Soft weighting approaches

Abrupt changes in the satellite configuration can impair the acceleration results of the PhaseDif approach. If the satellite signal that is fed into the estimation of the previous epoch with a high weight gets suddenly lost in the next epoch, the acceleration network geometry might be significantly altered. Such changes arise due to the appearance/disappearance of a satellite over the horizon, cut-off elevation or behind objects in the line of sight as well as temporary signal loss or removed observations after outlier detection. False positive cycle slip detection might impair the results in a much more significant way than for GNSS position estimation (Kennedy, 2003). In the scope of the thesis at hand, harmful effects due to abrupt constellation changes will be counteracted by applying “soft” weighting approaches.

With the weighting approach using the elevation-based variance estimation according to Equations (4.35) to (4.38), the weights get smaller with decreasing elevation e_{Sat}. They become minimal when the elevation is zero. For all methods, there will be a jump in the weights if a cut-off elevation angle e_{cut} is used to limit the lowest satellite observations. This effect can be reduced by setting a projected elevation $e'_{\text{Sat}}(e_{\text{Sat}})$ to zero at the cut-off angle, i.e. $e'_{\text{Sat}}(e_{\text{Sat}} = e_{\text{cut}}) = 0$. The higher projected elevation angles converge to the original angle close to the zenith where both angles are equal, i.e. $e'_{\text{Sat}}(e_{\text{Sat}} = 90°) = e_{\text{Sat}} = 90°$ (Figure 4.4).

The projected elevation is obtained as a linear function of the actual elevation,

$$e'_{\text{Sat}}(e_{\text{Sat}}) = m_e e_{\text{Sat}} - e'_0, \tag{4.49}$$

with the slope m_e and the axis intercept e'_0. The latter can be determined by applying the intercept theorem to Figure 4.4 as

$$\frac{e'_0}{e_{\text{cut}}} = \frac{90°}{90° - e_{\text{cut}}} \quad \Longleftrightarrow \quad e'_0 = e_{\text{cut}} \cdot \frac{90°}{90° - e_{\text{cut}}}. \tag{4.50}$$

The slope is obtained as

$$m_e = \frac{\Delta e'_{\text{Sat}}}{\Delta e_{\text{Sat}}} = \frac{90°}{90° - e_{\text{cut}}}. \tag{4.51}$$

By inserting Equations (4.50) and (4.51) into (4.49), the projected observation becomes

$$e'_{\text{Sat}}(e_{\text{Sat}}) = \frac{90°}{90° - e_{\text{cut}}} e_{\text{Sat}} - \frac{90°}{90° - e_{\text{cut}}} e_{\text{cut}} = \frac{90°}{90° - e_{\text{cut}}} (e_{\text{Sat}} - e_{\text{cut}}) = \frac{e_{\text{Sat}} - e_{\text{cut}}}{1 - \frac{e_{\text{cut}}}{90°}}. \tag{4.52}$$

If the projected elevation angle ("soft elevation method") of Equation (4.52) is used as input for the COSZ method of Equation (4.35), the weights will converge to zero close the cut-off elevation according to Equation (4.47). For the KING, JIN2 and EXPZ methods (Equations (4.36) to (4.38)), the influence of the constellation change will be significantly damped.

When a satellite signal is interrupted at elevations higher than the cut-off, the consequences of such geometry changes may be even more significant than at low elevations due to the higher weights put on the signal. The blue line in Figure 4.5 illustrates the standard weights that would be put on a satellite in the zenith when the signal is lost for two consecutive epochs. The weighting would be zero, i.e. removed, during the signal loss and one at the neighbouring epochs. A weighting depending on the time interval to satellite signal appearance/loss might be beneficial (Bruton et al., 2002). In the "soft loss method" introduced in the scope of the thesis at hand, the abrupt weight change is damped by linear down-weighting the epochs before the start of the signal loss in a time period Δt_{soft} (red line in Figure 4.5). The same is done after the signal regain. The soft loss weight is obtained as

$$w_{\text{soft}}(t) = \begin{cases} \frac{|t-t_{\text{loss}}|}{\Delta t_{\text{soft}}} & \forall \quad |t - t_{\text{loss}}| \leq \Delta t_{\text{soft}} \\ 1 & \text{else} \end{cases}, \tag{4.53}$$

where t_{loss} is the nearest epoch without signal before or after the query epoch t. An even smoother weighting function (green line in Figure 4.5) is obtained by applying sinusoidal weights as

$$w_{\text{soft}}(t) = \begin{cases} -\frac{1}{2}\cos\left(\frac{\pi t}{\Delta t_{\text{soft}}}\right) + \frac{1}{2} = \frac{1}{2}\left(1 - \cos\left(\frac{\pi t}{\Delta t_{\text{soft}}}\right)\right) = \sin^2\left(\frac{\pi t}{2\Delta t_{\text{soft}}}\right) & \forall \quad |t - t_{\text{loss}}| \leq \Delta t_{\text{soft}} \\ 1 & \text{else} \end{cases} \tag{4.54}$$

considering $\sin^2(\frac{x}{2}) = \frac{1}{2}(1 - \cos(x))$.

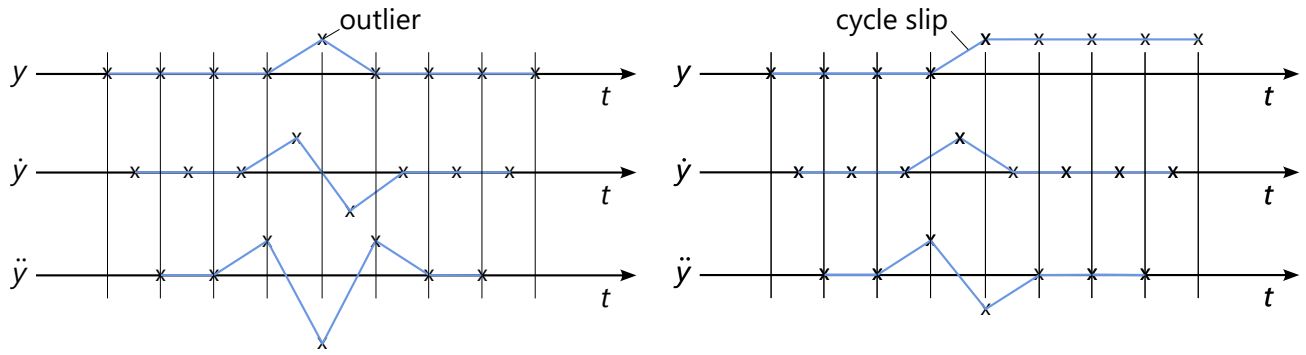
If the time period between two non-consecutive signal losses is smaller than $2\Delta t_{\text{soft}}$, the smaller weight will be selected as the weight w_{soft} for an in-between epoch. The total weight

$$w_i = \min\{w_{\ddot{\phi}}, w_{\text{soft}}\} \tag{4.55}$$

for a specific observation i that is used as input for the weight matrix in Equation (4.48) is the minimum weight of the soft elevation and the soft loss weight.

4.4.9 Outlier test

The effects of an outlier change with the numerical derivative. Resulting from two numerical time differentiations at a high sample frequency, the amplitude of a single outlier is increased as shown in Figure 4.6a. Furthermore, the outlier error smears into the neighbouring epochs. For a higher order differentiator, even more epochs are impaired. The figure also illustrates the impact of an outlier to the mean value of the data set. In the position y domain, the mean value is deteriorated by the outlier. If the outlier is removed, the mean is correct. In the velocity $\dot{y}$ and acceleration $\ddot{y}$ domain, by contrast, the mean value of the data set is correct even with the outlier. If the single outlier epoch is removed in the acceleration data, the mean is wrong. Hence, after numerical differentiation, the neighbouring epochs of an outlier need to be removed as well. If a cycle slip occurs, the mean values in the position and velocity domain are impaired, but the mean in the acceleration domain is correct again (Figure 4.6b). Less epochs around the cycle slip are impaired in comparison to a single outlier. The simple examples suggest that systematic errors due to outliers are more relevant in the position than in the acceleration domain. Due to the amplification during the numerical differentiation, outlier detection is simplified in the (phase) acceleration in comparison to the position (phase observation) (Kennedy, 2003).



(a) Single outlier (b) Cycle slip

Figure 4.6: Propagation of outliers within two numerical differentiations applying the first order difference

In the scope of this thesis, a data snooping method similar to the residual monitoring approaches presented in Reuper (2020) and Groves (2013) will be implemented. The method is based on the following steps for each epoch:

1. The PhaseDif algorithm is processed as presented in Section 4.4.4.
2. In the epoch-wise least-squares adjustment, the observation residuals are estimated in addition to the parameters and their standard deviations. The residuals indicate the differences between the actual and the expected observations.
3. If any normed residual is higher than a predefined threshold, the observation with the highest improvement is removed. Otherwise, the data snooping process is finished and the next steps are skipped.
4. The pre-processing checks, e.g. ensuring a sufficient number of observations and removing distinct networks of reference stations (see Section 4.4.6), need to be repeated.
5. If the epoch remains valid, a new least-squares adjustment is performed and the process starts again with step 1. Otherwise, the epoch becomes invalid.

The observation residuals $\boldsymbol{v}$ can be computed as

$$\boldsymbol{v} = \boldsymbol{A}\hat{\boldsymbol{X}} - \boldsymbol{L}. \tag{4.56}$$

using the estimated parameters $\boldsymbol{X}$ obtained with Equation (4.17), the observation vector $\boldsymbol{L}$ and the design matrix $\boldsymbol{A}$ obtained with Equations (4.21),(4.22) or (4.28),(4.30), respectively for PhaseDif-PPP and PhaseDif-POP. The variance covariance matrix of the observation residuals is

$$\boldsymbol{\Sigma}_{\boldsymbol{v}} = \sigma_0^2 \cdot (\boldsymbol{P}^{-1} - \boldsymbol{A}(\boldsymbol{A}^{\mathrm{T}}\boldsymbol{P}\boldsymbol{A})^{-1}\boldsymbol{A}^{\mathrm{T}}), \tag{4.57}$$

with the variance factor σ_0^2 being the standard deviation of the phase acceleration for a satellite in the zenith and the weight matrix $\boldsymbol{P}$ obtained with Equation (4.48). The standard deviation σ_v of the single observations residuals are the square root of the main diagonal of $\boldsymbol{\Sigma}_{\boldsymbol{v}}$. For each observation, the normed observation residual

$$\bar{v} = \frac{v}{\sigma_v} \tag{4.58}$$

is computed. If the maximum normed residual is greater than a certain threshold, it is removed according to the procedure described previously. The residuals are normed to allow the definition of a model-independent threshold. It should be considered that the reliability of this kind of outlier test is low for low redundancy observations.

Table 4.2: Selected IGS stations for the static GNSS experiments (data from International GNSS Service (2022))

Site	Network	Location	Receiver type	Clock type	Distance [km]
FFMJ	S1: rover	Frankfurt, Germany	Javad TRE_3 DELTA	internal	0
BRUX	S1: master	Brussels, Belgium	Sept POLARX5TR	ext. H-Maser	315
GOP6	S1: reference 1	Ondřejov, Czech Rep.	Sept POLARX5	ext. Cs	439
ONSA	S1: reference 2	Onsala, Sweden	Sept POLARX5TR	ext. H-Maser	841
LEIJ	S1: (reference 3)	Leipzig, Germany	Javad TRE_3 DELTA	internal	297
PARK	S2: rover	Parkes, Australia	Sept POLARX5TR	ext. H-Maser	0
MOBS	S2: master	Melbourne, Australia	Sept POLARX5	internal	613
MCHL	S2: reference 1	Mitchell, Australia	Trimble ALLOY	internal	736
YARR	S2: reference 2	Yarragadee, Australia	Sept POLARX5	internal	3160
LAUT	S2: reference 3	Lautoka, Fiji	Sept POLARX5	internal	3379

4.5 Static experiments in the IGS network

4.5.1 Methods

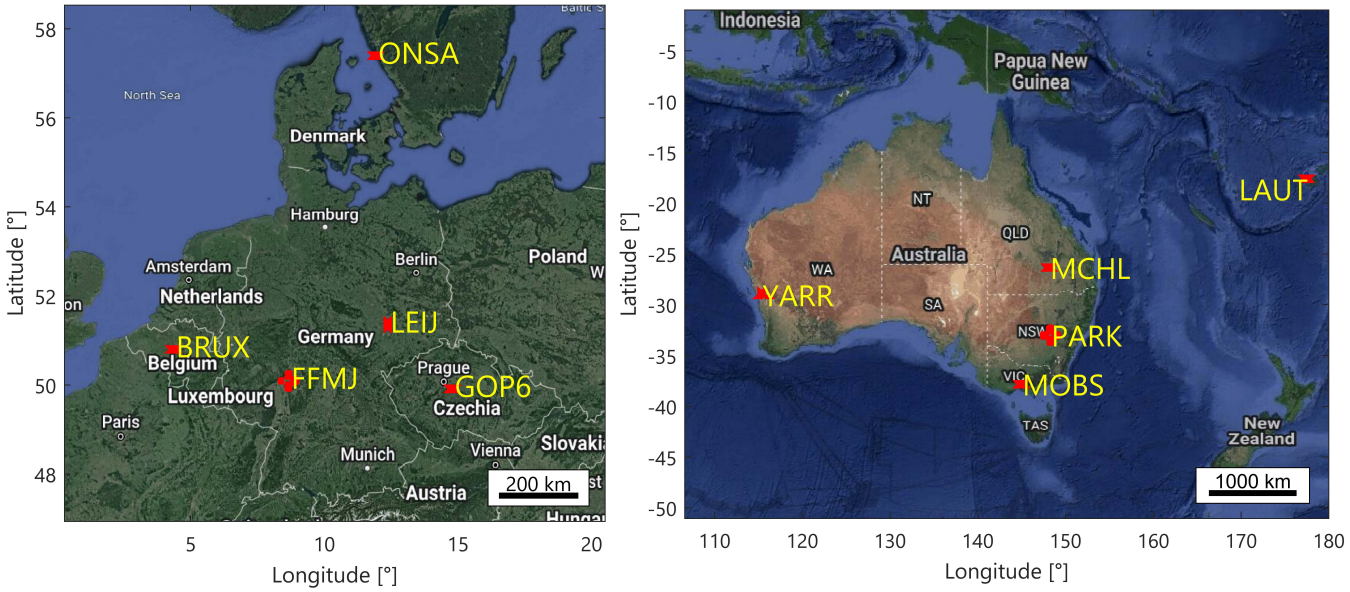
The kinematic acceleration determination approaches were evaluated in two static experiments where a static receiver was treated like a kinematic receiver, a “rover”. The mean and the standard deviation of the estimated kinematic acceleration were calculated. Theoretically, both quantities should be zero for a correct functional model and perfect observations. The acceleration determination methods are validated based on the deviation of the statistical parameters from zero.

The static GNSS observations were obtained from IGS GNSS stations. This data can be freely downloaded from IGS analysis centres (Johnston et al., 2017). In November 2022, the data of more than 500 stations was available (International GNSS Service, 2022). For the intended static experiments, stations with high-rate data frequency (1 Hz) and multiple constellations (at least GPS, Galileo, GLONASS, BeiDou) were selected (Table 4.2).

Precise satellite orbits and clock products were obtained by the CODE (Dach et al., 2020). In the final products, multi GNSS satellite orbits and clocks are available at data intervals of 5 min and 30 s, respectively. The difference in the data rate is due to the fact that interpolation errors for clock data are higher than for orbit data. CODE also offers 5 s clock data, but only for GPS and GLONASS.

For the first experiment (“Static 1”/S1), station data from Central Europe (Figure 4.7a) collected on 1 April 2021, approximately 11 am to 6 pm were used as input. The IGS site in Frankfurt, Germany (FFMJ), was selected as rover. For the PhaseDif-POP method, the master was located in Brussels, Belgium (BRUX), and two reference stations in Ondřejov, Czech Republic (GOP6) and Onsala, Sweden (ONSA) were selected (Table 4.2). The distance from rover to master was 315 km, the distance to the farthermost station ONSA was 841 km. A third reference station in Leipzig, Germany (LEIJ) was only used in a specific test concerning the number of stations for the POP-based approach (see Section 4.5.2).

The distances between the stations in the experiment S1 are several hundreds of kilometres. This might be challenging for DGNSS, but higher distances may be possible with the POP method (Salazar et al., 2011). In the second experiment (”Static 2“/S2), a network with distances to the rover of up to 3,400 km was analysed. The stations were on the opposite side of the globe, with the rover being at Parkes, Australia (PARK). The master was located at Melbourne (MOBS) in a distance of about 600 km. The IGS sites for the reference stations were Mitchell (MCHL), Yarragadee (YARR), both Australia, and Lautoka, Fiji (LAUT). Several authors reported discontinuities at the GPST day boundaries of the GNSS satellite orbit and clock products, e.g.



(a) Static 1

(b) Static 2

Figure 4.7: IGS stations selected for the static experiments (Map data: Google, Landsat/Copernicus)

Xiangbo Zhang et al. (2021), Strasser et al. (2019), and Lyu et al. (2019). Selecting an observation period over GPST midnight, from 2 October 2022, 9 pm to 3 October, 3 am, enables an evaluation in this regard.

Within the two networks, several methods and parameters will be evaluated that have been introduced before. The estimated vertical kinematic accelerations obtained with the PosDif-PPP, the PhaseDif-PPP and the PhaseDif-POP methods will be evaluated concerning their suitability for airborne gravimetry. The following aspects will be regarded:

- The *elevation-based weight methods* KING, JIN2, EXPZ and COSZ will be tested for both PhaseDif approaches and compared to unweighted processing.
- The linear and trigonometric *soft loss method* will be compared to abrupt signal appearance for the PhaseDif approaches.
- For PosDif and PhaseDif-PPP, the differences when using 30- or 5-s *precise clock products* will be evaluated.
- Possible advantages of the ionosphere-free *linear combination* will be identified in comparison to the L1 raw observations.
- The results using single *GNSS constellations* or several combinations will be compared. Only GPS results are available for the PosDif approach, PhaseDif-PPP was only computed for GPS and GLONASS combinations since 5 s clock data was not available for the other constellations.
- The results using the presented *kinematic acceleration determination methods* will be evaluated.
- For PhaseDif-POP, the *number of reference stations* will be evaluated using zero to three stations in addition to the master.
- Furthermore, the *distance from the rover to the master* without any reference station will be analysed for S2.

In the default settings, a GPS-only L1 solution using 5-s clock data is computed with an elevation cut-off of 5°, the KING elevation weighting, the trigonometric soft loss method with a down-weighting period of 1000 s and first order numerical differentiation. The standard deviation will be given for the unfiltered and low-pass filtered kinematic acceleration with filter lengths (-6 dB) of 100 s and 200 s. The low-pass filter was an Finite Impulse Response (FIR) filter designed with the window method. The PosDif solution was computed with the NovAtel Waypoint InertialExplorer 8.90 (NovAtel Inc., 2020) using the PPP method. A new software was developed for the PhaseDif approaches using MATLAB.

4.5.2 Results

With the default settings, the standard deviations of all low-pass filtered vertical kinematic accelerations were well below 1 mGal. Hence, all selected numerical differentiation methods are suited for airborne gravimetry. However, it will be shown in the following that significant differences have been obtained depending on the processing settings and the observation conditions.

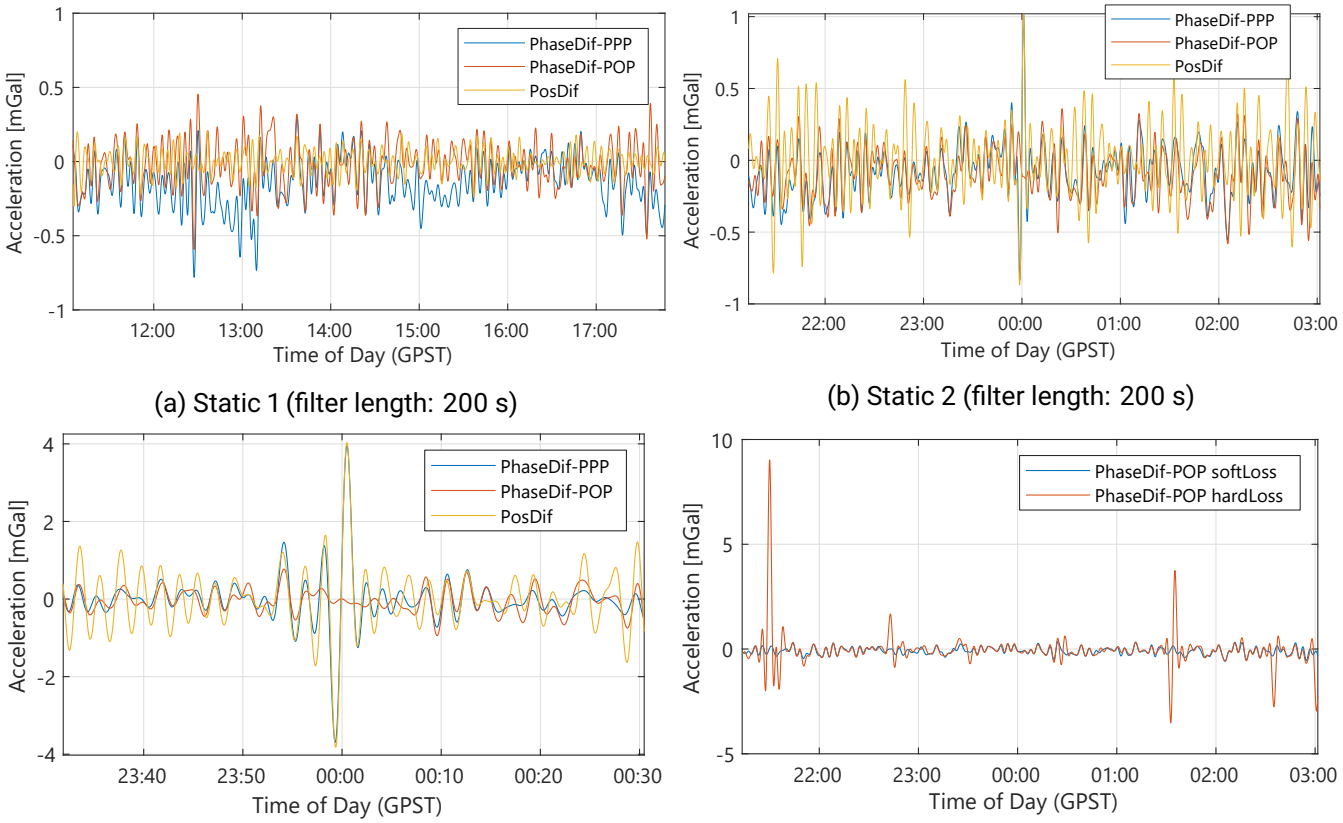
The acceleration results of the static experiments 1 and 2 (S1/S2) are shown in Figures 4.8a and 4.8b, respectively. In the S1 experiment, the standard deviation of the PosDif approach was best with 0.21 mGal (0.08 mGal) using a 100 s (200 s) low-pass filter. The PhaseDif approaches were almost on a par to each other with 0.26 mGal (0.16 mGal) for the PhaseDif-PPP and 0.28 mGal (0.15 mGal) for the PhaseDif-POP method. While the mean values of the PosDif and the PhaseDif-POP approach are neglectable, the PhaseDif-PPP shows a slight systematic error resulting in a mean of -0.14 mGal. In the S2 experiment, the noise level of all methods is generally higher. The best standard deviation was obtained with the PhaseDif-POP approach with 0.36 mGal (0.17 mGal). The standard deviation of the PhaseDif-PPP was only marginally worse being 0.41 mGal (0.18 mGal), the corresponding values of the PosDif method are significantly worse being 0.69 mGal (0.24 mGal). The mean values of the PhaseDif methods were approximately -0.09 mGal, the mean of PosDif is neglectable. The experiments indicate that there is no acceleration determination method that offers an outstanding accuracy; the accuracy might depend on the observation conditions.

In Figure 4.8b, a spike can be observed at midnight. The hour around midnight is zoomed in in Figure 4.8c applying a lower filter length. While almost the same erroneous acceleration is estimated for the PosDif and the PhaseDif-PPP methods at the minutes around midnight, the PhaseDif-POP results do not show any extraordinary behaviour. Since the former methods rely on precise satellite clock products, their results might be disturbed due to midnight discontinuities.

The amplitude spectra of the three methods are visualised in Figure 4.9 for both experiments. It is shown again that the noise level of the experiment S2 is generally higher. Furthermore, the noise level increases for the higher frequencies where the PhaseDif methods perform significantly better than the PosDif method. However, the frequencies of interest for airborne gravimetry are lower than approximately 0.01 Hz (corresponding to a signal period of 100 s). At these wavelengths, the standard deviations mentioned before are confirmed by the amplitude spectra. At S1, PosDif performs slightly better. Contrarily, the same method performs significantly worse at S2. At the very low frequencies, higher amplitudes are observed with the PhaseDif methods contributing to appreciable biases.

The results concerning several processing settings (see Section 4.5.1) are illustrated in Figures 4.10 and 4.12. The main findings will be discussed in the following. The settings have been applied for both static experiments and for the three kinematic acceleration methods if applicable.

The accuracy is significantly improved if an *elevation-based weighting* was applied (Figure 4.10a). In the case of the PhaseDif-PPP method in the experiment S1, the standard deviation improved from 0.38 mGal without elevation-based weighting to 0.26 mGal with the COSZ method. After low-pass filtering, in most cases, this weighting based on the sine of the elevation angle led to the best accuracy. Furthermore, the biases were reduced. The KING method performed approximately on a par with the COSZ method. The JIN2 and



(a) Static 1 (filter length: 200 s)

(b) Static 2 (filter length: 200 s)

(c) Static 2 around midnight (filter length: 100 s)

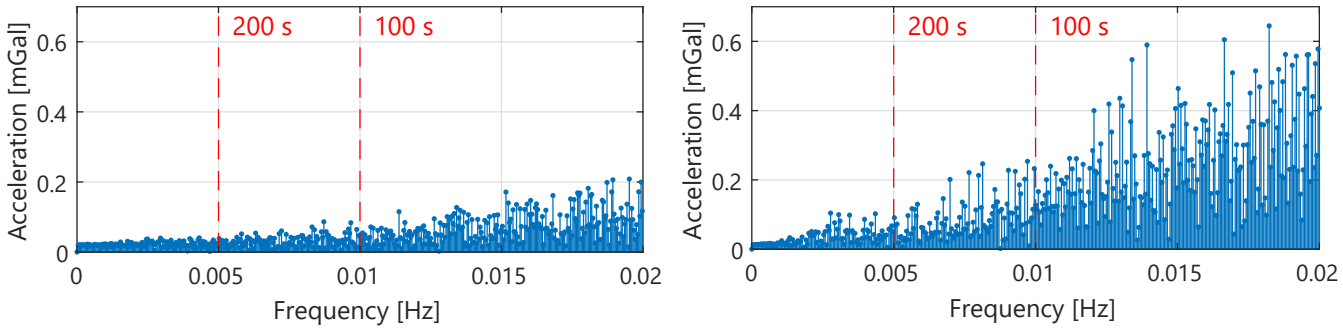
(d) Static 2 loss approaches (filter length: 200 s)

Figure 4.8: Low-pass filtered vertical kinematic acceleration

EXPZ methods were applied less successfully. The performance was at the level of the unweighted approach or even worse, especially for the EXPZ method in the experiment S1. The application of the projected elevation only resulted in significant improvements if the soft signal loss method is not applied (not included in Figure 4.10a).

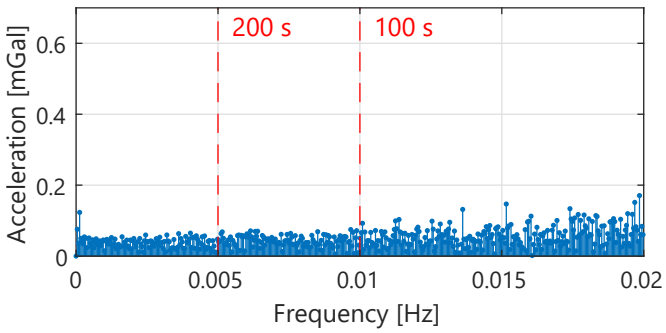
Figure 4.10b illustrates that the standard deviation was massively improved if a soft *loss approach* was applied for PhaseDif acceleration determination. This was the case in three of the four experiment/method combinations. With the PhaseDif-PPP method used in the experiment S1, the standard deviation improved from 1.93 mGal (1.29 mGal) to 0.26 mGal (0.16 mGal) using a 100 s (200 s) filter length. No significant differences were found between the linear and the trigonometric soft loss methods.

For the experiment S2, the kinematic acceleration results with and without soft loss method are visualised in Figure 4.8d. Peaks in the order of several mGal were only observed in the results without soft loss method. The peak epochs will now be compared with the satellite observability diagram in Figure 4.11 where satellite observations are displayed as five rows for each satellite corresponding to the rover, the master and the three reference stations. An observation that was used since the satellite was observed by a sufficient number of receivers is displayed green; a rejected single station observation is displayed orange; an observation that was categorised and removed as an outlier is displayed red. The first major peak appears at 21:29 (GPST) where a couple of outliers are removed for the GPS satellite with Pseudo Random Number (PRN) 5 at the MCHL reference station and the satellite G13 appears. The second peak at 22:43 coincidences with outliers for the satellites G08 and G20. At the third peak at 01:33, the master station loses the signal of satellite G30. The

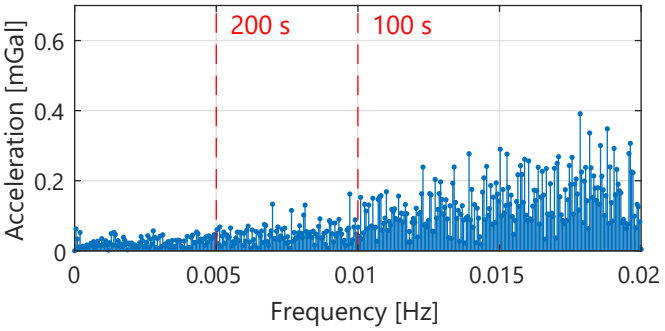


(a) PosDif (static 1)

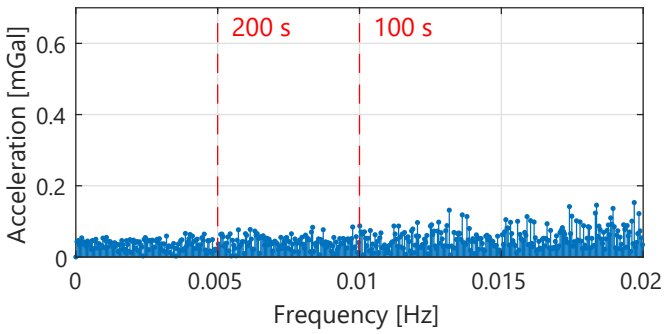
(b) PosDif (static 2)



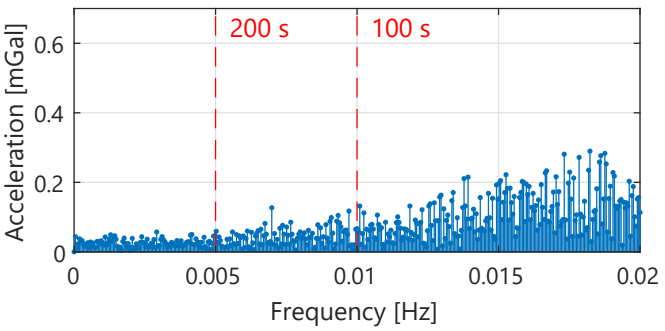
(c) PhaseDif-PPP (static 1)



(d) PhaseDif-PPP (static 2)

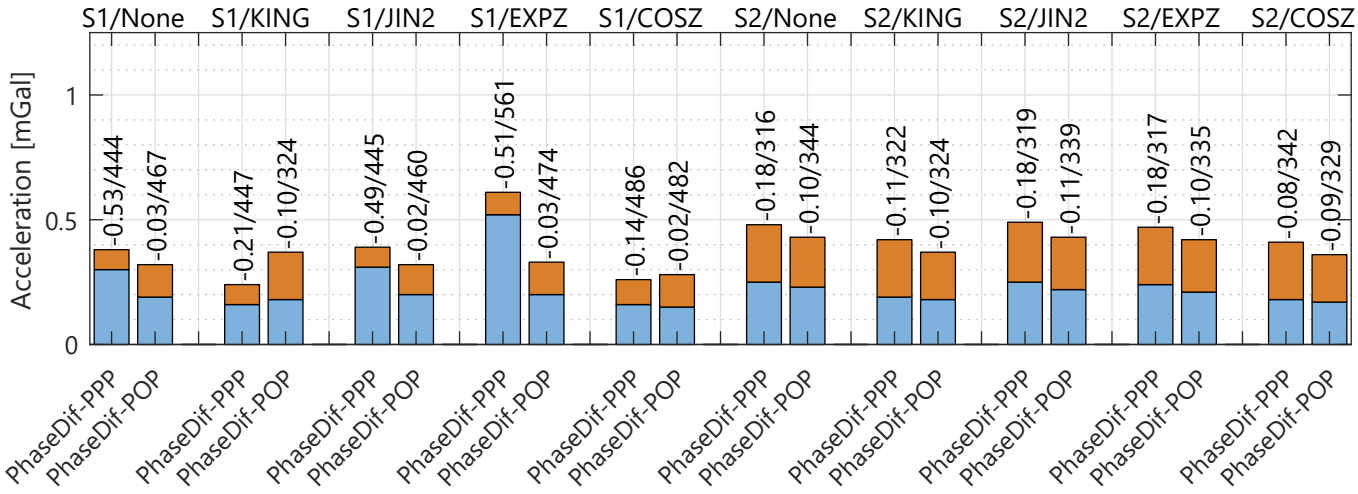


(e) PhaseDif-POP (static 1)

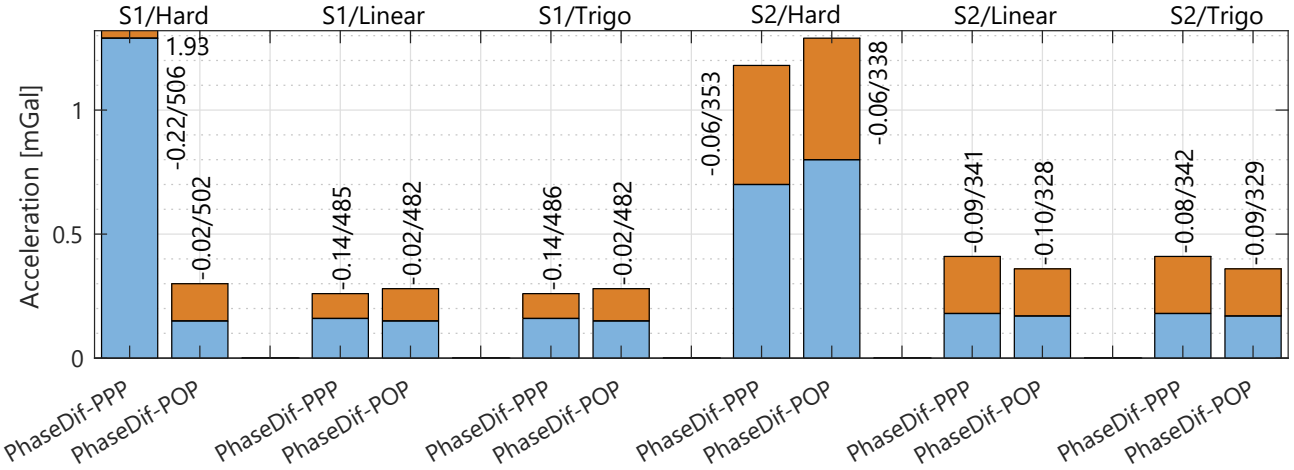


(f) PhaseDif-POP (static 2)

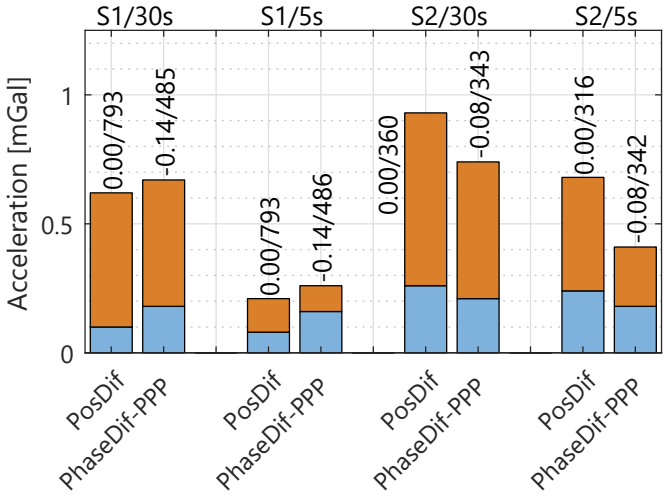
Figure 4.9: Amplitude spectra of the vertical kinematic acceleration (red: signal period)



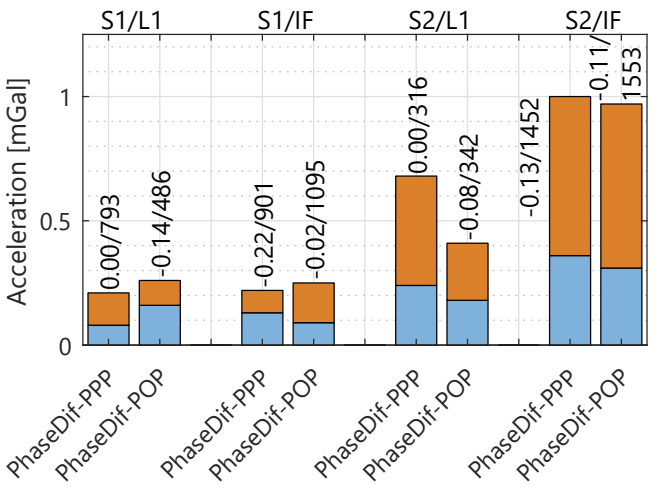
(a) Elevation-based weighting methods



(b) Signal loss approaches: hard (abrupt), linear or trigonometric



(c) Data interval of the precise clock product



(d) Observable: Raw L1 or linear combination

Figure 4.10: Standard deviations of the vertical kinematic acceleration compared for different processing approaches, part 1 (blue: 200 s filter length; blue+orange: 100 s filter length; values above bars: mean / standard deviation without low-pass filter; S1/2: static 1/2; all values in mGal)

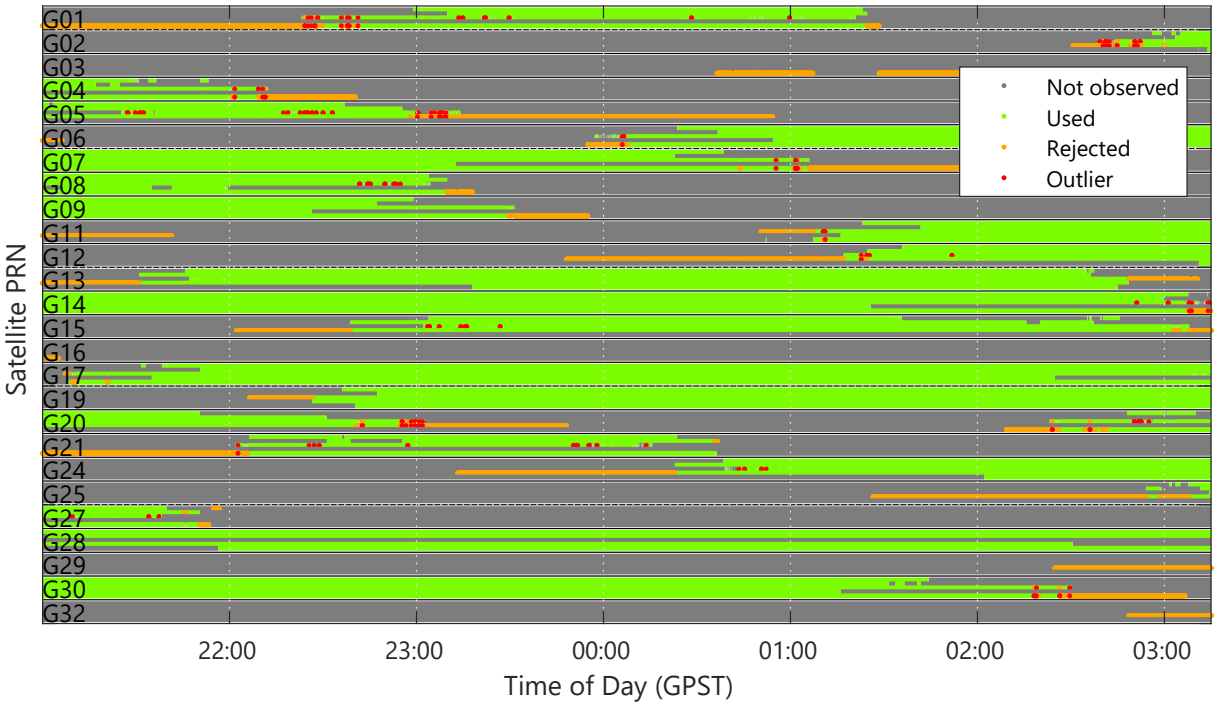


Figure 4.11: Satellite observability in the PhaseDif-POP network (static 2)

peak at 02:35 appears simultaneously with signal losses of the satellites G13 and G15. The examples indicate that abrupt constellation changes due to signal loss/appearance or outlier removal might be harmful for the PhaseDif approach, but a soft loss approach is able to solve this issue.

For the PosDif and the PhaseDif-PPP approaches, the use of 5 and 30 s *clock products* was tested (Figure 4.10c). Massive improvements were obtained for the experiment S1 with both methods when 5 s clock data was used. Especially for a lower filter length, the accuracy has improved approximately by a factor of three. In the experiment S2 using 100 s filters, the accuracy of the PosDif approach fell off to almost 1 mGal using 30 s clocks. The accuracy using 5 s data was better by a factor of 1.5 to 2.

The changes in the results using the ionosphere-free *linear combination* are illustrated in Figure 4.10d. For most experiment/method combinations, the unfiltered noise was amplified several times. While, according to Equation (4.40), a noise amplification of 3.0 was expected, the factor obtained for the unfiltered PhaseDif-POP standard deviation (labels above bars in Figure 4.10d) was lower for the experiment S1 being 2.3 and was higher for S2 being 4.5. The filtered standard deviations were on a similar level in the experiment S1 and were significantly higher for the LC in the experiment S2. Based on these findings, the ionosphere-free linear combination should not be recommended for the PhaseDif methods. The results suggest that remaining ionospheric effects are of minor relevance for the PhaseDif approach.

The next evaluation is about the *GNSS constellations*. The results for the experiments S1 and S2 are given in Figures 4.12a and 4.12b, respectively. The computation results for the PosDif approach could only be obtained for GPS-only observations. Since 5 s CODE clock products were only available for GPS (G) and GLONASS (R), the Galileo (E) or BeiDou (C) systems were only processed with the PhaseDif-POP method. Results for GPS and Galileo alone were approximately on a par being 0.28...0.29 mGal for S1 and 0.36 mGal for S2 with a 100 s filter. In both experiments, the processing using BeiDou performed best, especially for the experiment S2 (0.31 mGal). For S2, this might be due to the higher number of BeiDou satellites above Eastern Asia and Australia. The accuracy using GLONASS observations was significantly lower. At the S2 experiment, the

GLONASS accuracy was particularly poor being 1.23 mGal. However, the accuracy slightly improves for every GNSS constellation that is added, with the largest improvement using two GNSS constellations. For S2, the standard deviation improves from 0.36 mGal for GPS-only to 0.24 mGal adding Galileo, to 0.18 mGal adding BeiDou and marginally improves to 0.17 mGal adding GLONASS. For S1 (S2), the four-system multi-GNSS standard deviations are as low as 0.15 mGal (0.17 mGal) with a 100 s filter length and 0.08 mGal (0.09 mGal) with a 200 s filter length. The general down-weighting of the GLONASS observations similar as proposed by Li et al. (2018) did not lead to any significant accuracy changes.

The comparison of the *kinematic acceleration determination methods* based on the GPS-only solutions (also included in Figures 4.12a and 4.12b) shows a mixed picture: In the experiment S1, PosDif performed best with a standard deviation of 0.21 mGal (0.08 mGal) using a 100 s (200 s) low-pass filter, followed by the PhaseDif-PPP method with 0.26 mGal (0.16 mGal) and the PhaseDif-POP method with 0.28 mGal (0.15 mGal). For S2, the order is reversed: PhaseDif-POP is best with 0.36 mGal (0.17 mGal) closely followed by PhaseDif-PPP with 0.41 mGal (0.18 mGal) and, with a significant loss of accuracy, followed by PosDif with 0.69 mGal (0.24 mGal).

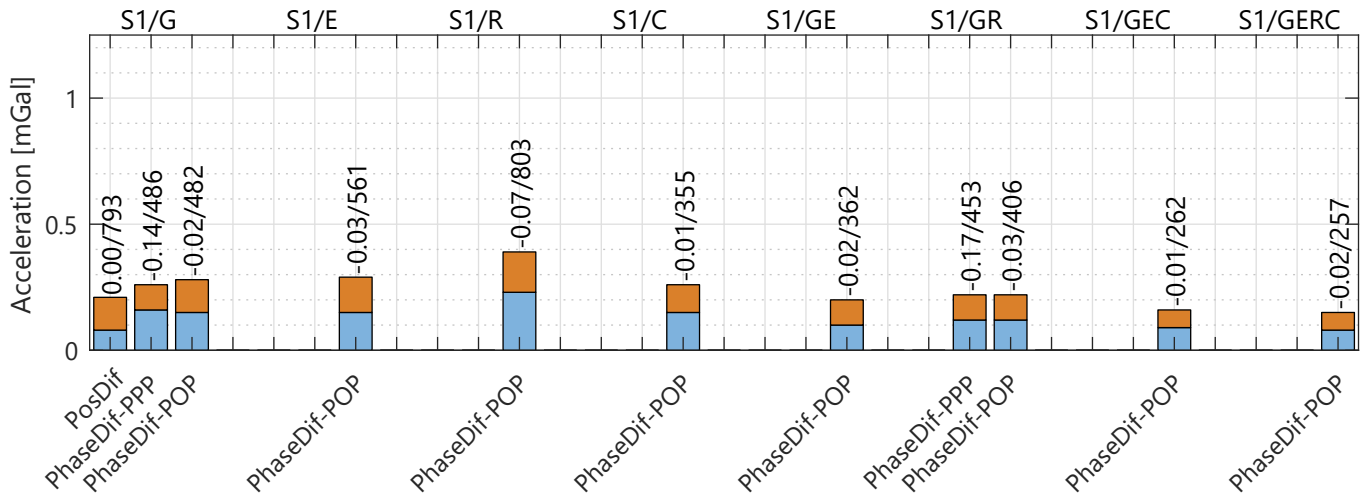
In the PhaseDif-POP method, an arbitrary *number of reference stations* can be added to the rover and the master. Figure 4.12c visualises the standard deviations based on the number of reference stations. In both experiments, the accuracy improves with the number of reference stations. In the experiment S2, the accuracy improves from 0.44 mGal (0.20 mGal) to 0.40 mGal (0.18 mGal) with one reference to 0.37 mGal (0.17 mGal) with two references using a 100 s (200 s) filter length. The amount of the improvement is lowered with a higher number of stations. The enhancement is only marginal when a third reference station is added.

The network of the experiment S2 (see Figure 4.7b, Table 4.2) is well suited to evaluate the performance of the PosDif-POP method when master stations are used that are far away from the rover. For this test, the network was reduced to the rover at PARK and a master station without any reference stations. Unlike in the previous tests, four GNSS constellations are used (GPS, Galileo, GLONASS, BeiDou). The resulting accuracy slightly degraded with increasing *distance between both receivers* (Figure 4.12d). With the station MOBS as master in a distance to the rover of 613 km, the standard deviation was 0.21 mGal (0.10 mGal) with a 100 s (200 s) filter length. For the master station LAUT in a distance of 3,379 km, the accuracy was 0.33 mGal (0.16 mGal). Although the master is far away, the accuracy would be very well suited for airborne gravimetry. This result indicates that a single Multi-GNSS master station at the same continent can be sufficient for high precision acceleration determination with the PhaseDif-POP method. Furthermore, the improvements using Multi-GNSS tend to be more significant than the improvements obtained by adding reference stations.

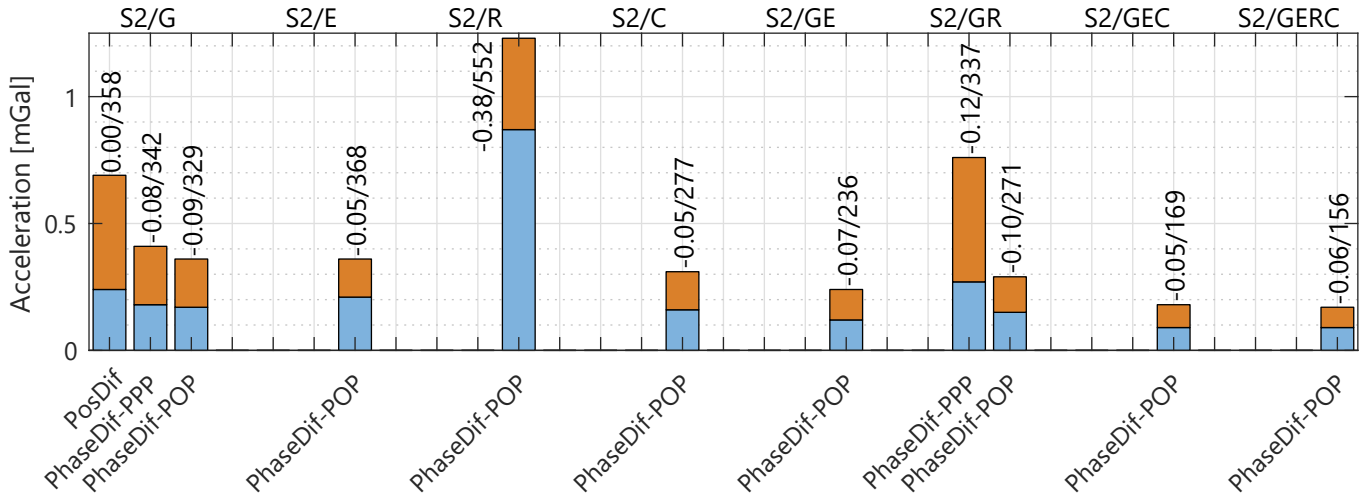
In addition to the presented parameters, several corrections have been implemented expecting to reduce further effects. The signal propagation delay causes an error in the observed range due to the relative satellite/receiver position change during signal propagation. The geometric part of this error (Beard and Senior, 2017) was corrected in an iterative approach by re-setting the satellite orbit interpolation epoch to the transmission epoch for every observation individually. The major relativistic correction, the time correction due to the orbit eccentricity (Hauschild, 2017a), was corrected in the same way. Furthermore, the carrier phase wind-up acting on circularly polarised electromagnetic waves was corrected according to Hauschild (2017a). The satellite attitude was modelled assuming a non-delayed yaw steering for all satellites. The signal propagation delay, the relativistic and the phase wind-up corrections have been found not to influence the static and dynamic acceleration results significantly. Hence, these corrections were not applied in the static experiments presented before. They will not be considered in the dynamic experiments, either.

4.5.3 Conclusions

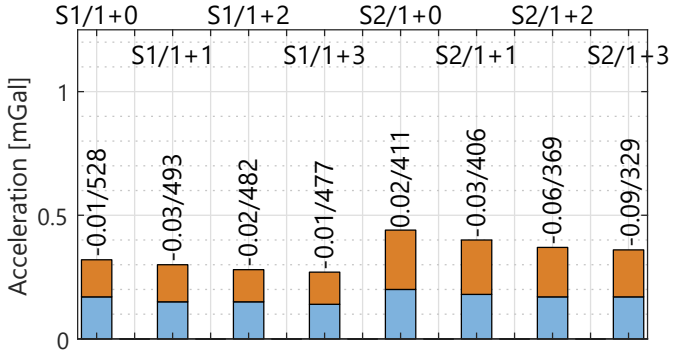
In the results of the previous section, none of the PosDif and PhaseDif approaches has outperformed the other considering different observation conditions. After the analysis of the dynamic gravimetry campaigns,



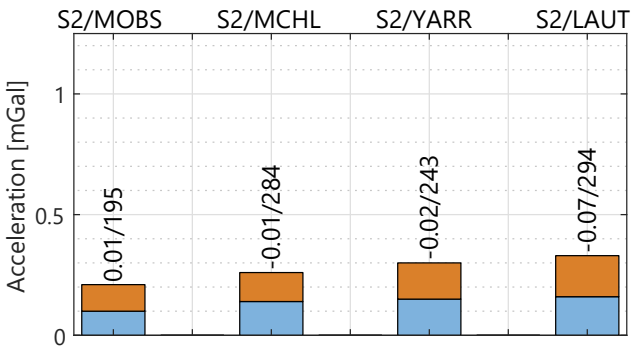
(a) Satellite constellations (static 1)



(b) Satellite constellations (static 2)



(c) Number of stations (master+reference) in the PhaseDif-POP method



(d) Master station in the PhaseDif-POP method (static 2; GERC; no reference stations)

Figure 4.12: Standard deviations of the vertical kinematic acceleration compared for different processing approaches, part 2 (blue: 200 s filter length; blue+orange: 100 s filter length; values above bars: mean / standard deviation without low-pass filter; S1/2: static 1/2; all values in mGal)

recommendations on the selection of a kinematic acceleration determination will be made in Section 8.4. Criteria will be the required accuracy, the allowed processing delay and the availability of precise satellite clock products and master/reference stations.

In the following, the main findings of the static experiments from Section 4.5.2 are summarised:

- Midnight discontinuities in precise satellite clock products may be relevant for the PosDif and PhaseDif-PPP methods, but do not influence the PhaseDif-POP results since the satellite clocks are estimated within the method.
- Biases up to approximately 0.15 mGal in the PhaseDif approach, especially in the PPP-based method need further evaluation. However, constant shifts in the vertical kinematic acceleration are of minor relevance for airborne gravimetry, since the relative results are fixed to absolute gravity values at the airport.
- There are slight improvements using elevation-based weighting. The simple COSZ method using the sine of the elevation seems sufficient. A projected “soft” elevation angle is only required if no soft loss approach is applied.
- When a signal is suddenly lost or when outliers are removed, it was found to be essential to apply a soft loss approach. The linear and trigonometric down-weighting approaches performed on a par. In the experiments, outlier removal without the signal loss approach was harmful, possibly due to the corresponding change in satellite geometry.
- In the PhaseDif-POP method, the accuracy improves with an increased number of reference stations. The amount of improvement becomes smaller in a larger network.
- However, a single master station might be sufficient for the acceleration determination for airborne gravimetry with acceptable accuracy. The accuracy is best with a reference station close to the rover. For PhaseDif-POP, a “close” station can be several hundreds of kilometres away. It was shown that an accuracy well below 0.4 mGal is even possible with a master in a distance of more than 3,000 km without any reference stations. The main requirement for master/reference stations is that many of the observed satellites match those of the rover observations.
- GPS, Galileo and BeiDou resulted in similar accuracies with slight advantages for BeiDou. Although the accuracy of the GLONASS-only results was significantly worse, the addition of every constellation resulted in an improved total accuracy. For the four-constellation solution, standard deviations of 0.15 mGal and 0.17 mGal (0.08 and 0.09 mGal) were obtained after low-pass filtering with a filter length of 100 s (200 s).
- For the methods relying on satellite clock products, major improvements were obtained using 5 s instead of 30 s clock products. Since the 5 s clock products have only been available for GNSS and GLONASS, the overall best results have been obtained for the Multi-GNSS PhaseDif-POP method where no satellite products are required.
- The ionosphere-free linear combination did not improve the accuracy in the PhaseDif approach. Especially the high-frequency noise is amplified by the linear combination. Hence, raw phase observations are recommended.
- The implemented corrections of the signal propagation delay, the relativistic effect and the carrier phase wind-up did not influence the accuracy significantly.

An essential question in dynamic gravimetry is whether the accuracy of the kinematic acceleration or of the specific force is more relevant for the overall accuracy. If the accuracy of one of the summands of Equation (2.22) was significantly worse than the other, the main potential for gravity result improvements could be seen in improving the corresponding observations or processing. Using appropriate processing settings, in both static experiments, a standard deviation between 0.1 and 0.3 mGal was obtained for the kinematic acceleration. In the warm-up calibration of the vertical accelerometer, a standard deviation of 0.2 and 0.3 mGal was observed after thermal stabilisation, low-pass filtering with a filter length of 130 s and linear trend removal (see Table 2.4). Hence, the accuracy of both components is approximately on par. Consequently, it is worth to take efforts to improve both components expecting an improved gravity accuracy. Note that this relation might differ under dynamic conditions and for other measurement systems.

5 Algorithmic design of the direct method[1]

In the scope of this thesis, the direct method of strapdown gravimetry is used for gravity disturbance determination. The approach was introduced in Section 2.6.2. The main processing steps are visualised in Figure 2.15b. In the current section, the algorithm will be elaborated. Section 5.1 will introduce the GNSS/IMU processing steps required to obtain the vehicle position, velocity, attitude and kinematic acceleration. Furthermore, some IMU pre-processing steps need to be conducted. The influence of the lever arm will be discussed in Section 5.2. Section 5.3 will be about the actual determination of gravity based on the specific force, the kinematic acceleration and the Eötvös correction and about the required low-pass filter. Section 5.4 will describe how the bias and a linear drift are removed from the results considering precise terrestrial gravimetry observations at the airport/harbour. Section 5.5 will introduce methods for quality assessment in airborne gravimetry and approaches to adjust the results based on cross-over residuals.

5.1 Basic GNSS/IMU pre-processing and integration

Both the GNSS processing (with the PosDif method) and the GNSS/IMU integration can be performed using standard navigation software. In the scope of this thesis, the NovAtel Waypoint InertialExplorer 8.90 (NovAtel Inc., 2020) is used. The PhaseDif methods and the subsequent gravity processing are performed with newly developed MATLAB software. Before the IMU accelerations can be used for gravity determination, some IMU pre-processing steps are required for high precision results.

If the IMU is not thermally stabilised or if there are significant remaining temperature changes during the observation period, a thermal correction based on a thermal calibration (see Section 2.4) should be applied. If a warm-up calibration for the vertical accelerometer was performed, the corrected vertical reading

$$f^b_{\mathrm{cor},z} = f^b_z - \Delta f^b_{z,\mathrm{therm}} \tag{5.1}$$

is obtained by subtracting the shifted reading $\Delta f^b_{z,\mathrm{therm}}$ (calibration function) from the uncorrected reading.

The GNSS and GNSS/IMU processing delivers the basic input for the subsequent steps of the direct method. The main outputs of the GNSS processing are the position of the vehicle GNSS antenna, its velocity and kinematic acceleration. A PosDif or PhaseDif approach can be implemented according to Sections 4.3 or 4.4, respectively. The positioning may be done using DGNSS or PPP methods. If a PhaseDif approach is applied for the kinematic acceleration determination, a code position solution might also be sufficient to obtain gravity. However, if the precise positions of the gravity results are needed, e.g. to determine normal gravity, a PPP approach is recommended since a reference station close to the rover is not required.

In addition to the GNSS solution, the IMU observations, i.e. the specific force observed by the accelerometers and the angular rates observed by the gyroscopes, are fused in a GNSS/IMU integration algorithm based on a Kalman filter. The resulting attitude describes the rotation from the navigation to the body frame (see Section 2.5). It can be expressed by the Euler attitude angles ϕ_b, θ_b, ψ_b (see Figure 2.14b), by a rotation matrix $\boldsymbol{C}^b_n$ or by quaternions.

[1] This section is based on Johann et al. (2019) except for Sections 5.5.2 and 5.5.3.

Typically, the IMU and GNSS epochs differ. When the GNSS epochs are selected as the processing epochs for the subsequent gravity determination, the IMU observations need to be interpolated to the GNSS epochs. The single IMU observations are affected by high frequency noise and quantisation effects. Hence, the interpolation should not be done before having applied a low-pass filter. For the implementation applied in this thesis, a filter length of about one or two seconds was found to be appropriate in combination with subsequent linear interpolation.

5.2 Lever arm

The lever arm $\boldsymbol{l}$ is the coordinate vector between the CoM of the IMU and the GNSS antenna (see Figure 2.14b). Under conditions without attitude changes, e.g. on a very stable measurement line, the lever arm does not affect the gravity determination. During attitude changes, e.g. during manoeuvres or turbulence, the accelerations at the IMU CoM and the GNSS antenna differ. Consequently, the gravity estimation needs to be adapted based on the lever arm. Furthermore, the height difference is required for normal gravity calculation and the lever arm needs to be considered for a precise localisation of the gravity results at the CoM. The lever arm $\boldsymbol{l}^b$ in the body frame can be determined by photogrammetric or tachymetric measurements. Alternatively, it can be included in a Kalman navigation filter for the GNSS/IMU integration as additional state. The accuracy of the lever arm estimate is better for flights/cruises with intense vehicle attitude changes. This is not desired during measurement lines. An analysis of the propagation of lever arm errors into gravity errors can be found in Becker (2016).

If the PosDif method is applied according to Equation (4.5), the position of the GNSS antenna $\boldsymbol{x}_m^n$ needs to be corrected for the lever arm to obtain the CoM position

$$\boldsymbol{r}^n = \boldsymbol{x}_m^n - \boldsymbol{l}^n = \boldsymbol{x}_m^n - \boldsymbol{C}_b^n \boldsymbol{l}^b \tag{5.2}$$

of the IMU. $\boldsymbol{C}_b^n$ is the rotation matrix used to transform the lever arm from the body to the navigation frame given by the transposed matrix of Equation (2.21) according to Equation (2.13). Note that no additional lever arm frame correction is required when both the antenna position and the lever arm are numerically differentiated in the navigation frame. In this case, the individual or combined derivative is equal:

$$\dot{\boldsymbol{r}}^n = \dot{\boldsymbol{x}}_m^n - \dot{\boldsymbol{l}}^n = (\boldsymbol{x}_m^n - \boldsymbol{l}^n)\dot{}, \quad \ddot{\boldsymbol{r}}^n = \ddot{\boldsymbol{x}}_m^n - \ddot{\boldsymbol{l}}^n = (\dot{\boldsymbol{x}}_m^n - \dot{\boldsymbol{l}}^n)\dot{}. \tag{5.3}$$

Recalling that all computations in the PhaseDif approach are done in the Earth frame, the numerical differentiation of the phase observations according to Equation (4.6) is done in this frame as well. To allow for a stringent Eötvös correction with the PhaseDif method, the lever arm needs to be derived in the Earth frame as well like

$$\dot{\boldsymbol{l}}^e = (\boldsymbol{C}_n^e \boldsymbol{C}_b^n \boldsymbol{l}^b)\dot{}, \quad \ddot{\boldsymbol{l}}^e = (\dot{\boldsymbol{l}}^e)\dot{} \tag{5.4}$$

using Equations (2.13), (2.14), (2.19) and (2.21). The kinematic acceleration at the IMU CoM

$$\ddot{\boldsymbol{r}}^e = \ddot{\boldsymbol{x}}_m^e - \ddot{\boldsymbol{l}}^e \tag{5.5}$$

in the Earth frame is then obtained with the antenna acceleration $\ddot{\boldsymbol{x}}_m^e$ estimated within the PhaseDif method.

5.3 Gravity disturbance determination

In preparation for the gravity disturbance determination, the skew-symmetric matrices $\boldsymbol{\Omega}_{ie}^{n}, \boldsymbol{\Omega}_{en}^{n}$ of the Earth rotation and transport rate need to be computed based on Equation (2.25) as

$$\boldsymbol{\Omega}_{ie}^{n} = \omega_{ie} \begin{pmatrix} 0 & \sin(\phi) & 0 \\ -\sin(\phi) & 0 & -\cos(\phi) \\ 0 & \cos(\phi) & 0 \end{pmatrix}, \quad \boldsymbol{\Omega}_{en}^{n} = \begin{pmatrix} 0 & \frac{\dot{r}_y^n \tan(\phi)}{R_E+h} & -\frac{\dot{r}_x^n}{R_N+h} \\ -\frac{\dot{r}_y^n \tan(\phi)}{R_E+h} & 0 & -\frac{\dot{r}_y^n}{R_E+h} \\ \frac{\dot{r}_x^n}{R_N+h} & \frac{\dot{r}_y^n}{R_E+h} & 0 \end{pmatrix}, \tag{5.6}$$

with ω_{ie} being the Earth rotation rate, ϕ being the geodetic latitude, h being the ellipsoidal height and R_N, R_E being the meridian and transverse radii of curvature (Groves, 2013). The velocity vector $\dot{\boldsymbol{r}}^n = (\dot{r}_x^n \; \dot{r}_y^n \; \dot{r}_z^n)^{\mathrm{T}}$ with its north, east, down components is obtained by numerical differentiation using Equation (2.20).

Finally, gravity disturbance can be computed based on Equation (2.23). If the PosDif approach is applied, the kinematic acceleration $\ddot{r}^n$ is typically computed in the navigation frame. The equation then becomes

$$\boldsymbol{\delta g}^n = \ddot{\boldsymbol{r}}^n - \boldsymbol{C}_b^n \boldsymbol{f}^b + (2\boldsymbol{\Omega}_{ie}^n + \boldsymbol{\Omega}_{en}^n) \cdot \dot{\boldsymbol{r}}^n - \boldsymbol{\gamma}^n \tag{5.7}$$

since the complete Eötvös correction according to Equation (2.24) is required. The kinematic acceleration $\ddot{\boldsymbol{r}}^n$ is obtained from Equation (5.3). The specific force $\boldsymbol{f}^b$ has already been corrected for thermal errors (see Section 5.1) and rotated to the navigation frame using the rotation matrix $\boldsymbol{C}_b^n$ which is obtained as the transposed matrix of Equation (2.21). Normal gravity can be calculated applying Equations (2.2) to (2.5). When the PhaseDif method is used, the kinematic acceleration $\ddot{r}^e$ is typically estimated in the Earth frame. Hence, just the first term of the Eötvös correction, the Coriolis term remains (Equation (2.26)). With the rotation matrix $\boldsymbol{C}_e^n$ from Equation (2.19), the kinematic acceleration from Equation (5.5), the gravity disturbance becomes

$$\boldsymbol{\delta g}^n = \boldsymbol{C}_e^n \ddot{\boldsymbol{r}}^e - \boldsymbol{C}_b^n \boldsymbol{f}^b + 2\boldsymbol{\Omega}_{ie}^n \dot{\boldsymbol{r}}^n - \boldsymbol{\gamma}^n \tag{5.8}$$

for the PhaseDif method. If the IMU is susceptible to a magnetic field, the magnetic field correction should be applied to the vertical gravity disturbance component according to Equation (3.9) considering the IMU tilt. If no magnetic field calibration is available, an empirical heading-dependent cosine-based correction might be applied.

Since the ranges of the kinematic acceleration and the specific force are several orders of magnitude higher than the desired gravity output, low-pass filtering is required after applying Equations (5.7) or (5.8) (Forsberg and Olesen, 2010). The filter length is selected based on the vehicle velocity, the observation height and the variability of the gravity field in the observation area. A compromise needs to be found between removing erroneous noise and maintaining the bulk of the gravity signal. Typical low-pass filters are longer than 100 s. In the scope of this thesis, FIR filters designed with the window method are used with filter lengths between about 100...200 s (equivalent to -6 dB damping) for airborne and 400 s for shipborne gravimetry. The filter lengths used in shipborne gravimetry are typically much higher than in airborne gravimetry. Due to the slower velocity, more noise can be removed without critical degradation of the spatial resolution.

The spatial resolution can be approximated as

$$R_{\lambda/2} = \frac{1}{2}\, \dot{r}\, T_{\mathrm{fil}}, \tag{5.9}$$

with T_{fil} being the filter length and $\dot{r}$ being the absolute vehicle velocity. This formulation of the spatial resolution is referred to as “geologic wavelength”. It represents the smallest wavelength of a gravitational point source that can be observed from a moving vehicle. Commonly, the geologic wavelength is alternatively called “half wavelength” since it can be approximated by the half wavelength of a sinusoid (Childers et al., 1999). Note that the comparison of spatial resolution indications is difficult since the amount of damping at the cut-off frequency (e.g. -3 or -6 dB) needs to be considered. Furthermore, the selected cut-off frequency in the filter design might differ from the actual frequency in the obtained filter.

5.4 Bias and linear drift removal using base reading data

Before and after each flight/cruise, static IMU readings need to be collected at the airport/harbour. This time period is also called “base reading” or “alignment” and has two purposes. Firstly, the alignment enables the computation of the IMU attitude. Roll and pitch are obtained using accelerometer observations by computing the tilt with respect to the local plumb line (Groves, 2013). The yaw angle is obtained from the gyroscope observation of the Earth rotation rate. The latter is only enabled with the high gyroscope precision of navigation grade IMUs. Secondly, the IMU readings enable the conjunction of the dynamic gravity results to absolute gravity (endmatching) that needs to be known for the parking position of the vehicle. This can be done by adjusting the IMU acceleration data (Glennie and K. P. Schwarz, 1999) or by adjusting the gravity disturbance approach as will be shown in the following. For both purposes of the base reading, the base reading needs to be conducted for several minutes of vehicle standstill to enable sufficient accuracy through averaging.

The gravity disturbance at the parking position is determined by a combination of high accuracy static terrestrial gravity and GNSS measurements to obtain the geodetic latitude and the ellipsoidal height. Typically, gravity points are marked at the parking position. Relative gravimeters are used to connecting measurements at reference points with known absolute gravity to the point at the parking position. If the gravity disturbance is used to tie the results, the gravity reference point at the parking position can be several tens of meters away from the aircraft since the gravity disturbance field variability is low compared to the measurement accuracy of dynamic gravimetry.

The vertical gravity biases ν_i before and after the vehicle movement can be computed as

$$\nu_i = \frac{\delta g_{z,i} - \delta g_{z,\text{ref},i}}{\cos(\phi_b)\cos(\theta_b)}, \tag{5.10}$$

with $\delta g_{z,i}$ being the (relative) gravity disturbance obtained by Equation (5.7) or (5.8) with subsequent filtering, $\delta g_{z,\text{ref},i}$ being the reference gravity disturbance at the parking position and ϕ_b, θ_b being the roll and pitch Euler attitude angles. The tilt is considered based on Equation (2.10) since the relevant bias for the vertical results is assumed to be mainly due to the vertical accelerometer.

Since no terrestrial gravity disturbance update is possible during the vehicle movement, the best reasonable assumption for the sensor drift is linearity between the vehicle parking before and after the dynamic measurements. Hence, the vertical sensor drift for any epoch t between the base reading reference epochs t_1, t_2 with the corresponding biases ν_1, ν_2 can be expressed as

$$\nu(t) = \nu_1 + \frac{t - t_1}{t_2 - t_1}(\nu_2 - \nu_1). \tag{5.11}$$

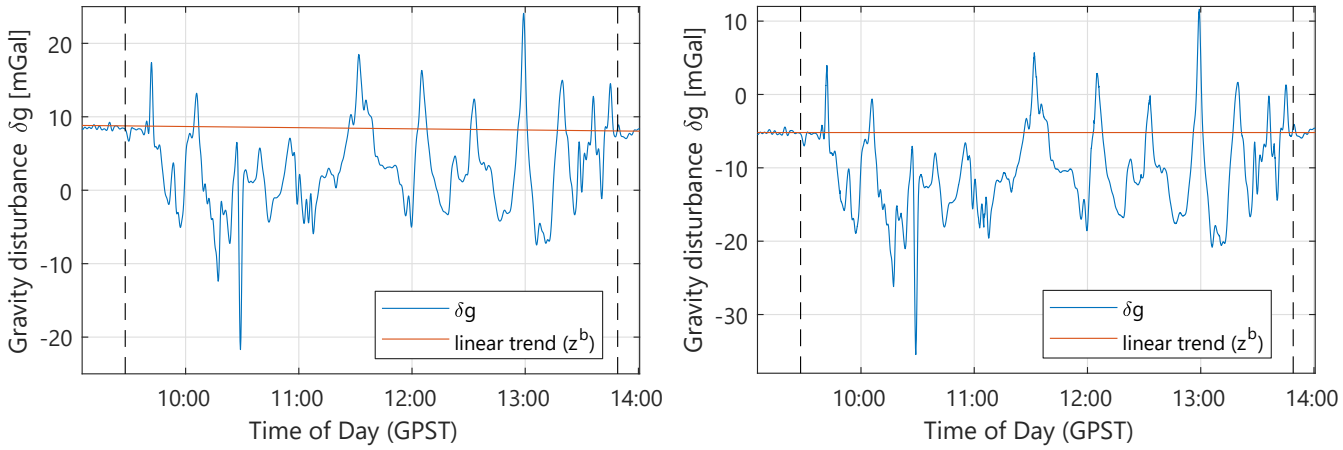
The vertical gravity disturbance $\delta g^n_{z,\text{BTfree}}$ for a specific epoch t without bias and linear drift is then obtained from the uncorrected value δg^n_z as

$$\delta g^n_{z,\text{BTfree}} = \delta g^n_z - \nu\cos(\phi_b)\cos(\theta_b) = \delta g^n_z - \left(\nu_1 + \frac{t - t_1}{t_2 - t_1}(\nu_2 - \nu_1)\right)\cos(\phi_b)\cos(\theta_b). \tag{5.12}$$

The quantities $\delta g^n_z, \nu, \phi_b, \theta_b$ depend on the epoch t. Note that the instantaneous tilt has to be considered lowering the sensor drift of Equation (5.11) in order to correctly set the absolute gravity disturbance. An example for bias and linear drift removal is shown in Figure 5.1.

5.5 Quality assessment

There are two types of quality assessment approaches in dynamic gravimetry, internal and external assessment. The internal methods rely on repeated gravity observations at the same location with the same measurement



(a) Before endmatching

(b) After endmatching

Figure 5.1: Gravity disturbance for the Bremen 2021 flight before and after bias and linear drift removal

system. Repeated measurements usually occur at trajectory intersections, the so-called crossover points (Section 5.5.1), or when trajectory segments are repeated (Section 5.5.2). Internal methods can be used to assess the precision of the gravity results, but are not suited for accuracy determination since systematic errors might remain undetected. The accuracy can be rated using external reference gravity by comparing the gravity results with global models or precise terrestrial data. A drawback of the external method is that the obtained accuracy value might be too pessimistic due to the limited accuracy of the external data. Consider that dynamic gravimetry campaigns are typically undertaken where no other precise gravity data is available.

The accuracy (precision) of n_χ differences $\chi_i = \delta g_{2,i} - \delta g_{1,i}$ of the gravity disturbance results to external (internal) gravity disturbance is usually calculated as the

$$\mathrm{RMS} = \sqrt{\frac{\sum_{i=1}^{n_\chi} \chi_i^2}{n_\chi}}, \tag{5.13}$$

e.g. in Glennie and K. P. Schwarz (1999) and Ayres-Sampaio et al. (2015). Assuming that the accuracy of both gravity disturbance results $\delta g_{j,i}$ is equal, which appears reasonable for internal quality assessment, the precision of a single gravity disturbance value is

$$\mathrm{RMSE} = \frac{\mathrm{RMS}}{\sqrt{2}} = \sqrt{\frac{\sum_{i=1}^{n_\chi} \chi_i^2}{2\, n_\chi}} \tag{5.14}$$

in accordance with variance propagation, see, e.g., Forsberg and Olesen (2010) and Becker (2016).

While with stable platform gravimeters, meaningful gravity results are typically only possible during approximately straight trajectory segments, strapdown gravimetry enables measurements during turns. However, the accuracy during turns is lowered, at least for airborne gravimetry. Becker et al. (2015b) showed that the estimability of vertical gravity is lower during flight manoeuvres since horizontal accelerations propagate into vertical gravity results if slight attitude estimation errors occur. Furthermore, some corrections like the thermal and magnetic calibration presented in this thesis focus on the vertical accelerometer.

Within quality assessment in dynamic gravimetry, the corner tightness can be considered by calculating the instantaneous radius of curvature at a discrete trajectory point P_i as illustrated in Figure 5.2. A distance Δl_{est} is set around the query point. The points within this distance are used to estimate the best fitting circle, e.g. by applying the method by Taubin (1991). The radius of the fitting circle approximates the radius of curvature

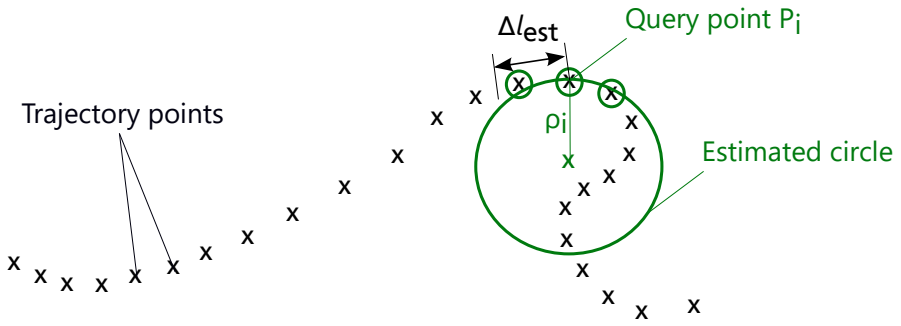


Figure 5.2: Approximation of the radius of curvature along a trajectory

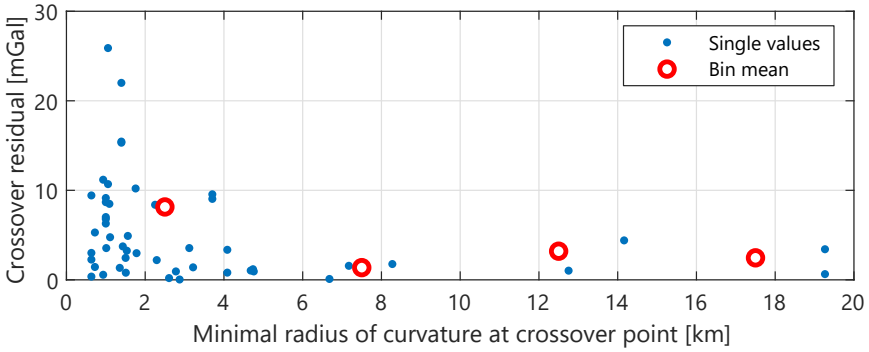


Figure 5.3: Crossover point residuals of the Chile 2021 airborne campaign with respect to the corresponding minimal radius of curvature of both adjacent trajectory segments

at the query point. The process is repeated for all trajectory points or for a reduced number of trajectory points followed by interpolation. Figure 5.3 illustrates the correlation of crossover residuals with the instantaneous radius of curvature at the example of the airborne gravimetry campaign CL2021 (see Section 6.6).

Typically, in order to obtain gravity results with the highest accuracy, the most trajectory segments are planned to be straight lines. These segments will be called in short “lines” in the following. The precision indicators are not influenced by the radii of curvature during turns if the turning including the beginning/end of lines are removed considering the low-pass filter length. Consequently, the quality assessment will be restricted to lines improving the comparability of diverse campaigns.

When comparing different publications on dynamic gravimetry, the computation of the precision/accuracy indicators needs to be studied carefully. Furthermore, comparisons are difficult since the indicators depend on many parameters like the observation conditions, the topography, the gravity field variability and the filter method.

The flight and sea conditions can be approximated by the turbulence indicator RMS-g being the moving standard deviation of the vertical kinematic acceleration (Becker, 2016).[1] Note that this indicator is influenced by the GNSS data quality, the kinematic acceleration determination approach and the data frequency. For maximum consistency, the RMS-g is computed as a 50 s moving standard deviation of 1 Hz vertical kinematic acceleration obtained with the PosDif approach in all campaigns evaluated in this thesis. Other more complex turbulence metrics like the Eddy dissipation rate which rates the atmospheric turbulence state identifying aircraft-dependent effects on the IMU are beyond the scope of the work at hand.

[1] This paragraph is based on Johann et al. (2020).

The variability of the gravity disturbance field can be evaluated by regarding the first time derivative $\dot{\delta g}_z^n$ of the vertical gravity disturbance along the trajectory. The result is the horizontal gradient of the vertical gravity disturbance. The mean absolute value indicates the general variability of the vertical gravity field of a specific campaign and will be called “mean field variability” in the following.

5.5.1 Crossover analysis

The precision of the gravity results can be estimated using residuals $\chi_i = \delta g_{2,i} - \delta g_{1,i}$ at trajectory intersections, the crossover points. The RMS and the RMSE are computed with Equations (5.13) and (5.14), representing the precision of the residual and the individual gravity value at a line, respectively. For a robust quality assessment, the number n_{CO} of crossover points needs to be high, i.e. some dozens of intersections. This should be considered in the trajectory planning of a campaign. Furthermore, the distance from the crossover points to the line ends should be higher than the expected spatial resolution according to Equation (5.9) in order to avoid low-quality gravity estimates close to turns smearing into the precision indicators. Since the gravity disturbance field varies with height, a maximum height difference for adjacent trajectory segments at the crossover point should be selected. Hence, flights at constant altitude are preferable for the quality assessment. In the scope of this work, the maximal height difference was set to 100 m by default. With larger height differences, the precision tends to be degraded significantly.

The information that the residuals should be zero at crossover points can be used to adjust the trajectory network in a so-called “crossover adjustment” or “crossover levelling”. This can be done line-wise by estimating one bias per line in a least-squares adjustment according to Equations (4.17) and (4.18). The functional model is based on the assumption that a crossover residual $\chi_{1,2}$ is equal to the biases of its adjacent lines, i.e. $\chi_{1,2} = \nu_2 - \nu_1$ plus white noise. In addition to the crossover residuals, a pseudo-observation is introduced stating that the sum of all residuals is zero, i.e. $\sum \chi_i = 0$, in order to avoid a rank defect. An adequate levelling is possible for lines with at least two valid crossover points. For a line with a single crossover point, the adjusted residual would be zero since the line bias would rely on a single residual. For valid crossover points, both adjacent lines need at least two valid crossover points. Lines and crossover points without a sufficient number of valid crossover points can be removed iteratively.

If the number of crossover points is low, the risk of over-parametrisation is high resulting in erroneously distorted line networks and too optimistic precision indicators. Hence, crossover adjustment is not recommended for networks with a low crossover/line ratio. However, precision indicators being systematically overoptimistic can be avoided by the use of correction factors that were confirmed in simulation by Becker (2016). A correction factor

$$q_j = \sqrt{\frac{n_{\mathrm{CO,j}} - 1}{2}} \cdot \frac{\Gamma\left(\frac{n_{\mathrm{CO,j}}-1}{2}\right)}{\Gamma\left(\frac{n_{\mathrm{CO,j}}}{2}\right)} \tag{5.15}$$

for a line j is determined with the number $n_{\mathrm{CO,j}}$ of valid crossover points adjacent to the line and the gamma function $\Gamma(x)$. After the crossover adjustment, the residuals should be multiplied by the mean of the correction factors q_1, q_2 of both adjacent lines as

$$\chi_{i,\mathrm{cor}} = \frac{q_1 + q_2}{2} \cdot \chi_i \tag{5.16}$$

to be used as input for the RMS/RMSE computation. For a line with 2 (3) valid crossover points, the correction factor becomes 1.25 (1.13). With a high number of crossover points, the factor converges towards 1 becoming neglectable for the precision indication. The correction factor will be applied in all crossover adjustments in the following.

If the number of crossover points is particularly high, a linear drift per line might be estimated in addition to the bias (Hwang et al., 2006). In this thesis, this approach is only applied in exceptional cases.

Instead of the previously introduced line-wise crossover adjustment, a flight/cruise-wise adjustment can be applied. The principle is the same like before, but a single bias is estimated only once per flight/cruise. In this method, only the crossover points at intersections between different flights/cruises can be considered.

5.5.2 Repeated trajectory segments

If trajectory segments, e.g. specific lines, are repeated, the residuals at the corresponding positions can be evaluated as well. In addition to the vertical position differences at crossover points, there is a horizontal position difference between both residual points due to imperfect vehicle navigation and steering. In contrast to a crossover point residual at perpendicularly intersecting lines, there is a high correlation between the repeated lines since the gravity field is traversed in the same way. With a high low-pass filter length, the residuals necessarily become small (Becker et al., 2016). Hence, an optimal filter length should be determined in a crossover analysis. It should be mentioned that lines are repeated seldom since they are particularly time-consuming and consequently expensive. However, repeated lines can be a reasonable supplement to a crossover analysis, especially if the number of crossover points is low or if the precision is of interest along a profile. For test purposes or accuracy improvement over specific areas, flight lines can be repeated multiple times.

Precision indicators that are conform with the RMS/RMSE of the crossover analysis can be obtained by applying Equations (5.13) and (5.14) on all residuals between the repetition *pairs*. In this approach, a line which is repeated three times is treated like three distinct line pairs. The RMS and RMSE are computed only once using the obtained residuals of all pairs. By doing so, the precision indicator is independent of the number of repetitions.

In an alternative approach, the standard deviation of the residual is computed with respect to the mean value of all repetitions at the comparison point. In that approach, the RMSE coincides with the RMSE of the aforementioned approach for a high number of repetitions, but in the common case of a low number of repetitions, the indicator will be too optimistic. Hence, the former approach without computing mean values is recommended. This should be remembered when results of different publications are compared.

5.5.3 Comparison to external gravity data

The accuracy of the gravity results can only be approximated by comparison with external gravity data. Global models can be used as a reference but the errors of a global model are high since such models are limited to the long wavelengths. Hence, such a comparison should be limited to the low-pass filtered results of dynamic gravimetry. Comparisons of dynamic gravimetry campaigns to global models can be found, e.g., in Jensen et al. (2019), Becker (2016), and Jensen (2018).

If a terrestrial network of gravity points exists, a gravity model can be developed based on these measurements. Before the modelled gravity can be compared to airborne results, an upward continuation is required. This process is subject to continuation errors. Hence, the accuracy indicators obtained by the comparison of airborne and upward continued data will be too pessimistic. However, such a comparison can be the best possible way to obtain an accuracy indicator and detect systematic errors in airborne results. Examples of comparisons of airborne and upward continued ground gravity can be found, e.g., in Glennie and K. P. Schwarz (1999), Jekeli and Kwon (1999), and Jensen (2018).

In the scope of this thesis, comparisons to external data are only available for selected campaigns conducted by DTU Space.

6 Airborne experiments

The algorithm of the direct method of strapdown gravimetry (see Section 5) was applied to several dynamic campaigns. The following airborne campaigns were evaluated in the scope of this thesis:

- **MY2014/MY2022**: Large-scale airborne campaigns were conducted with a medium-size aircraft above coastal and marine Malaysian areas (Sections 6.1 and 6.2).
- **ODW2017/ODW2018**: Using a motor glider and a light aircraft above the German low-mountain range Odenwald, gravimetric test flights were performed at a high resolution grid of perpendicular flight lines (Section 6.3).
- **DK2020**: Coastal areas of Denmark were covered by a one-week campaign using a light-aircraft equipped with several strapdown gravimeters (Section 6.4).
- **BRE2021**: Starting from Bremen, Germany, a test flight was conducted above German parts of the North Sea with flight lines in the shape of a triangle allowing for crossover and repeated lines analysis (Section 6.5).
- **CL2021**: A campaign with the purpose of glacier monitoring was flown above Chilean Patagonia. The project was an untypical airborne gravimetry campaign due to the absence of approximately straight flight lines (Section 6.6).

The main properties and obtained precision indicators according to Section 5.5 are summarised in Table 6.1. Details on the observation conditions and results of the airborne campaigns using the strapdown gravimeter of TU Darmstadt can be found in the current section. Shipborne campaigns will be presented in Section 7. The key findings in the scope of this work will be summarised in Section 8. The high number of campaigns allows for an evaluation of possible correlations between the varying measurement conditions and the obtained precision. This will be analysed in Section 8.2. The effect of magnetic calibration on all campaigns will be evaluated in Section 8.3. Section 8.4 will summarise the effect of different kinematic acceleration determination methods for selected campaigns.

In all campaigns, the flights/cruises are named after the day of year when their initial base reading ended. If multiple flights were started at the same day, lowercase Latin letters are added to the flight name, e.g. “32a” for the first flight on February 1. Lines are counted consecutively over the complete campaign.

6.1 MY2014: Malaysia 2014[1]

6.1.1 Campaign details

In August 2014, an airborne gravimetry campaign has been conducted by the Department of Survey and Mapping Malaysia (JUPEM) in cooperation with DTU Space. Coastal and open sea areas above the South

[1]This section is partially based on Johann et al. (2020) and Johann et al. (2021). The statistics might slightly deviate due to minor changes in the algorithm and processing settings.

Table 6.1: Airborne campaign properties and precision (campaign statistics of MY2014, ODW2017 and ODW2018 partially based on Johann et al. (2020) and Johann et al. (2021))

Campaign	MY 2014	MY 2022	ODW 2017	ODW 2018	DK 2020	BRE 2021	CL 2021
Aircraft	Beechcraft King Air 350	Beechcraft King Air 350	Grob G109B	Cessna 206 "Stationair 6"	Vul-canair P68C	Basler BT-67	Basler BT-67
Thermal stabilisation?	✗	(✓)	✗	✗	✓	✓	✓
GNSS frequency [Hz]	5	5	1...20	1	5	5	5
Number of flights	12	28	8	1	5	1	3
Total line distance [km]	9,916	17,351	1,366	1,034	4,282	595	2,316
Mean line velocity [$\frac{\mathrm{m}}{\mathrm{s}}$]	87	92	36	54	62	67	70
Ellipsoidal flight height							
mean [m]	1953	2011	655	947	471	520	1777
min [m]	1016	601	396	797	334	340	281
max [m]	4256	4890	927	980	948	839	2881
RMS-g [$\frac{\mathrm{mm}}{\mathrm{s}^2}$]							
mean	235	295	769	128	377	317	529
standard deviation	85	149	254	55	209	76	310
Filter length (-6 dB) [s]	130	120	130	120	140	170	100
Resolution $R_{\lambda/2}$ [km]	5.7	5.5	2.3	3.3	4.3	5.7	3.5
Variability $\dot{\delta g}_D$ [$\frac{\mathrm{mGal}}{\mathrm{km}}$]	1.1	0.9	2.9	2.7	0.8	0.9	3.6
IGRF magnetic field							
total intensity B [µT]	40.6	41.9	48.5	48.5	50.2	49.9	29.7
horizontal int. B_H [µT]	40.6	41.7	20.1	20.1	17.0	17.7	19.7
corr. fact. $c_1 B_H$ [mGal]	3.45	3.55	1.71	1.71	1.45	1.50	1.68
declination δ [°]	-0.2	-0.3	2.4	2.6	3.0	2.9	12.9
inclination [°]	0.1	-4.4	65.5	65.5	70.2	69.3	−48.3
Crossover analysis							
n_{CO} non-adjusted	108	98	431	222	37	10	12
n_{CO} flight-adjusted	104	-	431	-	32	-	-
n_{CO} line-adjusted	104	-	429	220	21	10	-
RMSE non-adj. [mGal]	**1.09**	**1.05**	**2.97**	**4.05**	**0.93**	**0.50**	**1.47**
RMSE flight-adj. [mGal]	0.94	-	1.82	-	0.86	-	-
RMSE line-adj. [mGal]	0.66	-	1.11	0.64	0.40	0.39	-
Repeated lines analysis							
number of pairs	5	2	-	-	1	3	-
Common distance [km]	200	52	-	-	147	131	
RMSE [mGal]	0.59	0.61	-	-	0.48	0.54	-
RMSE zero-mean [mGal]	0.47	0.51	-	-	0.39	0.48	-



Figure 6.1: Beechcraft King Air 350 at Subang used for MY2014 and MY2022

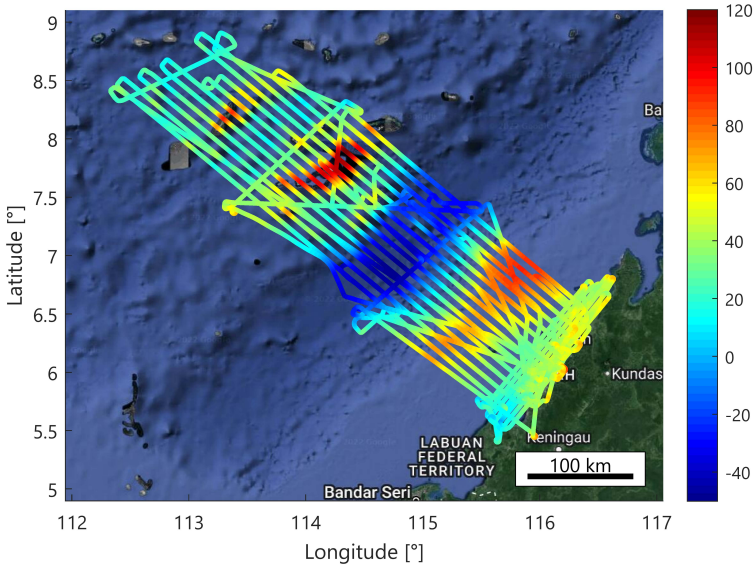


Figure 6.2: Non-adjusted gravity disturbance [mGal] MY2014 (map data: Google, Landsat/Copernicus)

China Sea north-west of Borneo were observed using a L&R S-type gravimeter (see Section 2.3.1) and the iNAV-RQH of TU Darmstadt (see Section 2.3.2). In combination with previous and subsequent campaigns, the observations were used to improve Malaysian geoid models. The line spacing at sea was 10 km. In order to obtain a consistent land/sea interface, the coastal areas were observed with a line spacing of 5 km (Jamil et al., 2017). Observations of the land area were already available from previous campaigns conducted in 2002 and 2003.

The flights were conducted with a Beechcraft King Air 350 (Figure 6.1) run by Sabah Air Aviation at a mean flight height of approximately 2 km. The total line distance of the 12 flights was almost 10,000 km (Figure 6.2). With a mean flight line velocity of 87 $\frac{\mathrm{m}}{\mathrm{s}}$ and a low-pass filter length of 130 s (-6 dB), the spatial resolution (half-wavelength) of the results becomes 5.7 km according to Equation (5.9). The magnetic field at Malaysia is almost horizontal, i.e. the inclination is approximately zero. Furthermore, the global maximum of the horizontal magnetic field is located in Southeast Asia (see Figure 3.2). The mean horizontal field intensity at the MY2014 campaign was 40.6 µT according to IGRF13. For the iNAV-RQH, the resulting amplitude for the magnetic calibration function of Equation (3.8) was $c_1 B_H \approx 3.45$ mGal. More details on the campaign and results obtained with the indirect method of strapdown gravimetry can be found in Becker (2016) who reported a crossover RMSE of 1.3 mGal.

6.1.2 Main results

The obtained gravity disturbance along the flight trajectory is illustrated in Figure 6.2. With more than 160 mGal, the range of the gravity disturbance is high. The lowest gravity disturbance is obtained at a deep sea trench with a depth of up to 3 km. However, according to Becker (2016), precision indicators do not change significantly in this campaign when a terrain reduction is applied. Except for the first flight, the gravimeter drifts vary between -10 and +15 mGal per day (Figure 6.3).

51 lines with 108 crossover points were detected with a maximal height difference of 100 m. The RMSE of the crossover points (see Section 5.5.1) was 1.09 mGal (Table 6.2). The crossover residuals sorted by flights and lines are illustrated in Figure 6.4. Every flight is represented by a specific colour. Each crossover residual

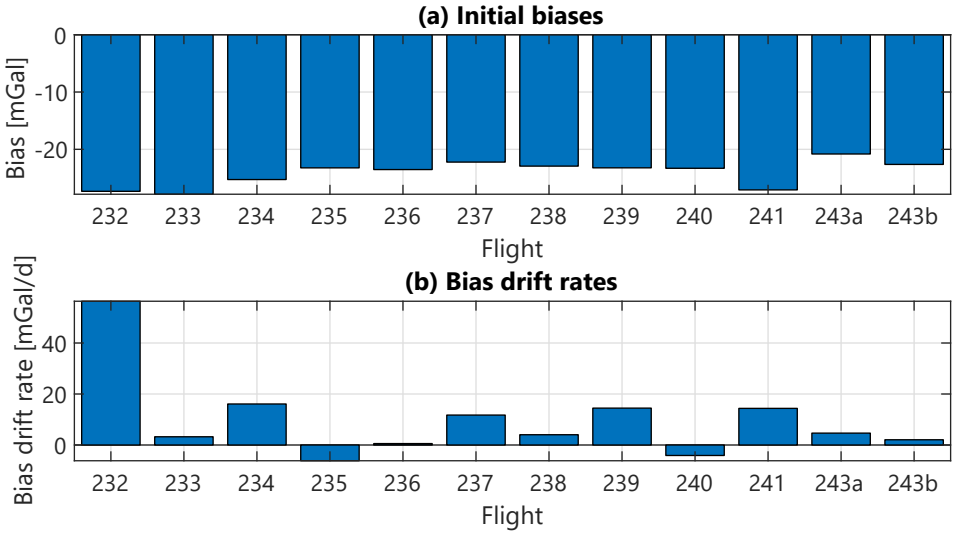


Figure 6.3: Vertical biases at the base readings before the flights of MY2014 and linear drifts between the base readings

Table 6.2: Malaysia 2014 precision

Thermal calibration?	✓	✗	✓
Magnetic calibration?	✓	✓	✗
n_{CO} non-adjusted	108	108	108
n_{CO} flight-adjusted	104	-	-
n_{CO} line-adjusted	104	-	-
CO RMSE non-adj. [mGal]	**1.09**	2.66	2.39
CO RMSE flight-adj. [mGal]	0.94	-	-
CO RMSE line-adj. [mGal]	0.66	-	-
RL distance [km]	200	-	200
RL RMSE [mGal]	0.59	-	1.77

appears in the diagram at both adjacent lines, once positive and once negative. Lines without any crossover are omitted.

Since the IMU was not thermally stabilised, the precision of the results massively degrades without a thermal calibration (see Section 2.4) to 2.66 mGal. A similar degradation (2.39 mGal) can be observed if the magnetic calibration introduced in Section 3.3 is omitted. Hence, the magnetic correction improves the precision indicator by a factor greater than 2.

Thanks to the high number of crossover points, flight-wise and line-wise crossover adjustments appear feasible. Figure 6.5a shows how the line-wise adjustment works. The absolute adjusted residuals are generally lower than in Figure 6.4 and the mean values of the adjusted lines are almost zero. Note that lines without at least two crossovers with two other adjustable lines are not shifted, i.e. no line bias is estimated. Figure 6.5b illustrates the estimated line biases which are close to the line mean values in Figure 6.4.

The MY2014 dataset includes five repeated line pairs with a total common distance of 200 km. The total RMSE of all pairs is 0.59 mGal. There are two possible reasons why the repeated lines RMSE is significantly better than the crossover RMSE: Firstly, the precision in the area of the repeated lines might be fortuitously better than the mean campaign precision. Secondly, the precision based on the repeated lines might be

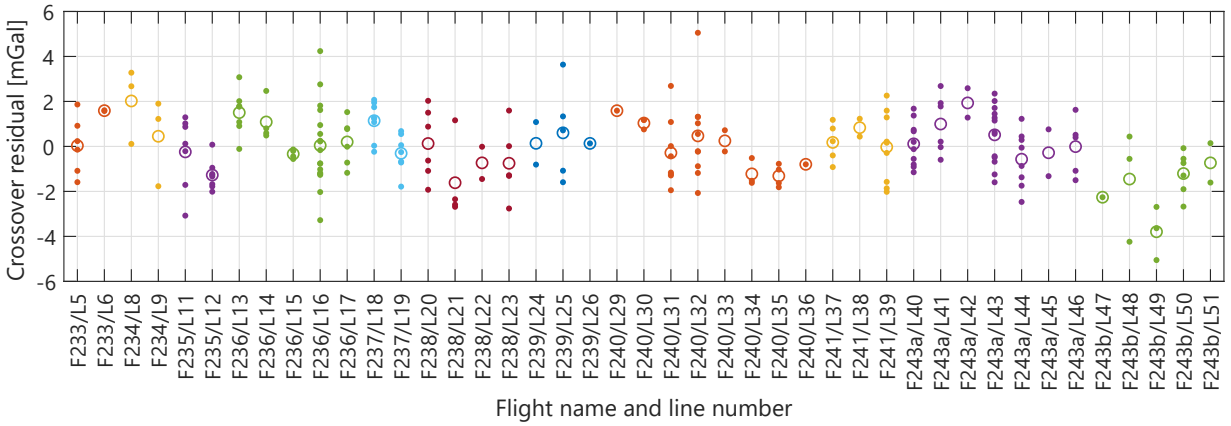


Figure 6.4: Non-adjusted crossover residuals sorted by flights (indicated by the colour) and lines of MY2014 (circles: mean values of the lines)

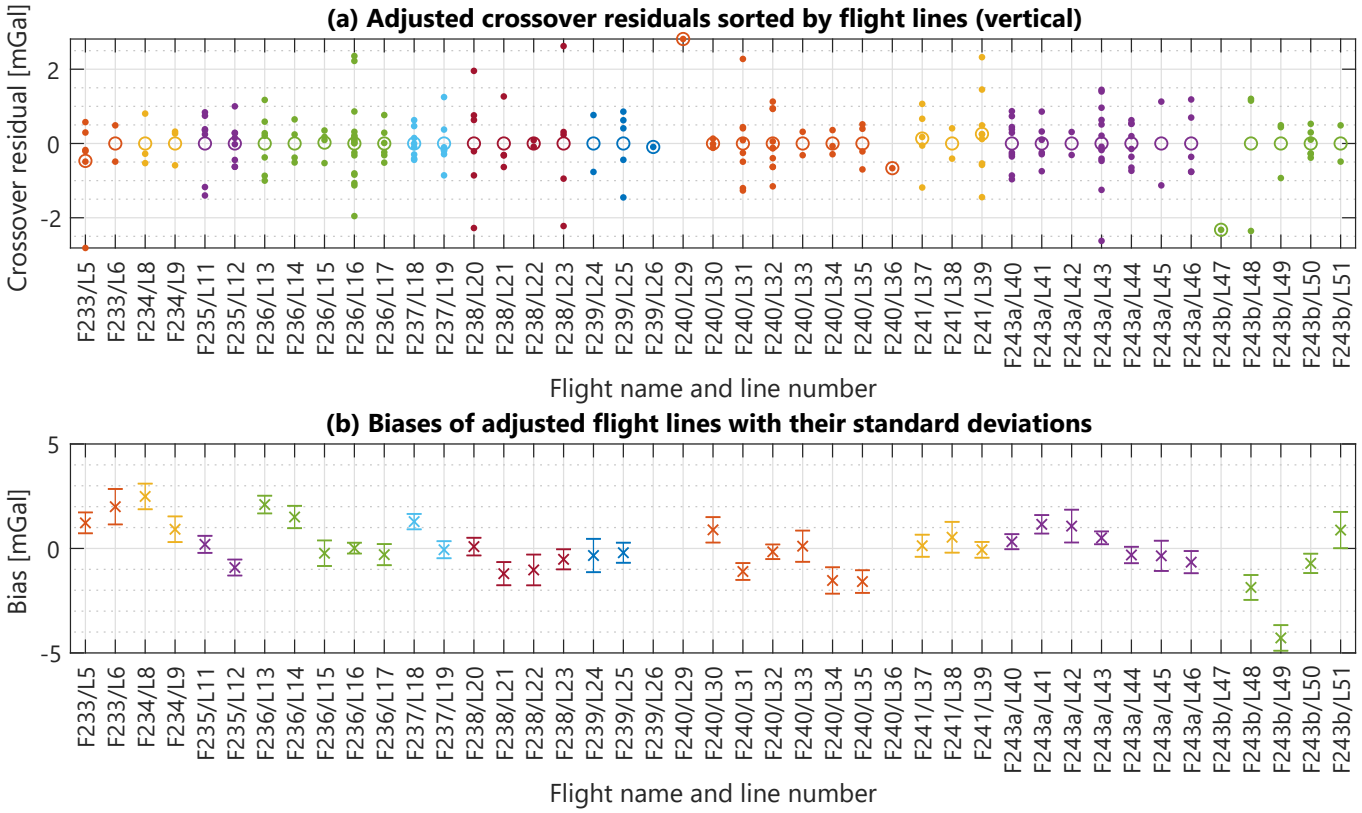


Figure 6.5: Line-wise adjusted crossover residuals sorted by flights (indicated by the colour) and lines of MY2014 (circles: mean values of the lines) and estimated line biases with their standard deviation

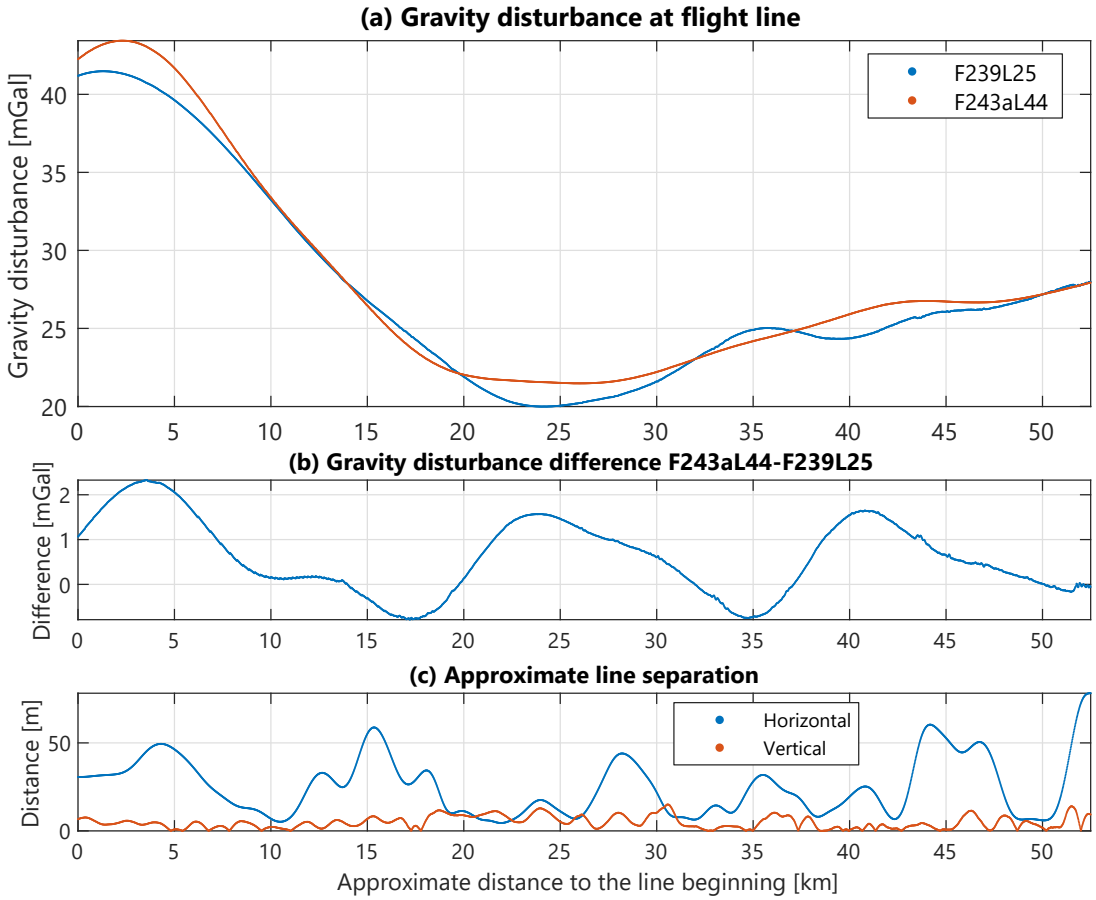


Figure 6.6: Gravity disturbance and separation of the repeated lines 25 and 44 of MY2014

overoptimistic due to the correlation of the gravity field along the repeated trajectory segments. The precision without applying the magnetic calibration is three times worse (1.77 mGal). The RMSE of the zero-mean line data is 0.47 mGal. In theory, this precision indicator is analogous to the line-wise adjusted RMSE of the crossover analysis. The slight difference between the original and zero-mean values are due to a bias of 0.19 mGal. Figure 6.6 shows the comparison of the gravity results along the pair with the worst RMSE (0.71 mGal). A precise repetition of the line trajectory, horizontally and vertically, is important to minimise the influence of variations in the gravity disturbance field.

6.2 MY2022: Malaysia 2022

6.2.1 Campaign details

In April and May 2022, the same affiliations like at the MY2014 campaign conducted a campaign covering the Malaysian coastal offshore areas western of Peninsular Malaysia, which is the western part of Malaysia, and offshore areas beyond the east coast of the peninsula close to Thailand (Figure 6.7). The results were used to establish a new height reference system, the Peninsular Malaysia Geodetic Datum 2022 (PMGVD2022) including a new geoid model (Cob et al., 2022).

With 28 flights and more than 17,000 flight line kilometres, the campaign extent was almost twice compared to MY2014. The equipment was installed in the same aircraft like at MY2014 (see Figure 6.1) at Subang

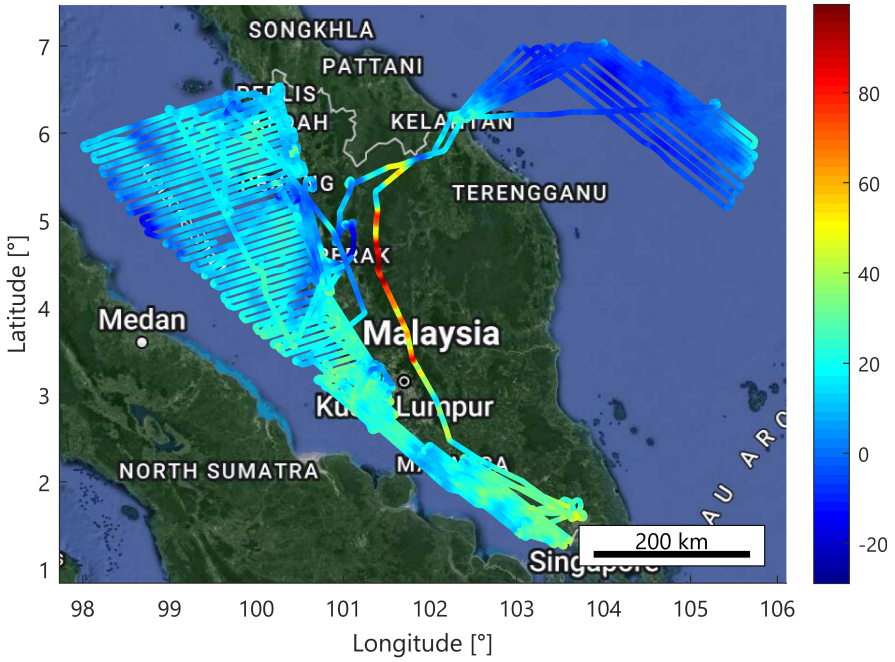


Figure 6.7: Non-adjusted gravity disturbance [mGal] MY2022 (map data: Google, Landsat/Copernicus)

near Kuala Lumpur where the first flights were based. Besides, the airports of Johor Bahru, Kota Kinabalu, Ipoh, Penang and Langkawi were part of the campaign. The terrestrial base readings were performed by DTU Space and JUPEM. The installed gravimeters are shown in Figure 2.7. TU Darmstadt's strapdown gravimeter iNAV-RQH in its thermal stabilising housing iTempStab was placed side-by-side with an iMAR iCORUS and a L&R S-type gravimeter. The flight velocity and the selected filter length were similar to the MY2014 campaign (see Table 6.1) resulting in a half-wavelength resolution of 5.5 km. The turbulence level computed as RMS-g was slightly higher than in 2014.

A low-cost IMU of the type xSens MTi-G-700 was mounted at the L&R rack close to the iNAV-RQH. Its 3-D magnetometer output can be used for the magnetic correction alternatively to the IGRF magnetic Earth field model. If the Earth's magnetic field is distorted significantly, in the order of several µT, it might be beneficial to use magnetometer data observed close to the IMU, or in an ideal case, at the ISA. When the aircraft was parked at Ipoh, static measurements were recorded with the MTi being oriented in several axis directions allowing for the removal of major magnetometer biases. The body axis mean values of the magnetometer were aligned to the corresponding IGRF mean values for the single flights to reduce the effects of flight-to-flight sensor drifts. Note that a magnetometer accuracy of a few µT is expected to be sufficient for the correction of the iNAV-RQH accelerometer observations based on the magnetic calibration function of Equation (3.8). The mean horizontal magnetic field at Peninsular Malaysia according to IGRF-13 is even slightly higher (41.7 µT) than at northern Borneo at MY2014.

6.2.2 Main results

Figure 6.8 shows the temperatures measured by the iNAV-RQH and the iTempStab, the obtained zero-mean gravity disturbance and the heating/cooling power of the Peltier elements (see Section 2.3.2) for flight 108a based at Subang. The cabin temperature during parking and base reading was continuously higher than 30°C (purple line in Figure 6.8a), sometimes higher than 40°C at other flights. It was found that the iTempStab was not able to hold the target temperature (green line in Figure 6.8a) at these conditions. Approximately

Table 6.3: Malaysia 2022 precision

Thermal calibration?	✓	✗	✓	✓	✓
Magnetic calibration?	IGRF	IGRF	✗	Magnetometer	IGRF
Included flights	all	all	all	all	east
n_{CO} non-adjusted	98	98	98	98	30
n_{CO} flight-adjusted	-	-	-	-	25
n_{CO} line-adjusted	-	-	-	-	23
CO RMSE non-adj. [mGal]	**1.05**	3.48	2.73	1.12	0.74
CO RMSE flight-adj. [mGal]	-	-	-	-	0.75
CO RMSE line-adj. [mGal]	-	-	-	-	0.34
RL distance [km]	52	-	52	-	-
RL RMSE [mGal]	0.61	-	0.76	-	-

after 5 h of flight 108a recording, during post-flight base-reading, the temperature of sensor 2 on the IMU starts to drift away. High-power cooling of the Peltier elements (blue line in Figure 6.8c) does not result in the desired cooling effect.

In order to avoid extraordinary high ISA temperatures in the absence of significant temperature reduction in the cabin during night, the iNAV-RQH was turned off after every post-flight base reading. It was turned on again in the morning when the aircraft staff arrived, but the temperature was not fully stabilised during take-off. Significant drifts in the gravity disturbance results are observed at the pre-flight base reading (Figure 6.8b) even after applying the iTempStab warm-up calibration (see Section 2.4.2). The effect was reduced by limiting the base reading period to the last minutes before the start of movement. After the flight, the obtained gravity disturbance is almost constant. Note that the newer thermal housing of the iCORUS was turned on during the whole campaign since no diverging IMU temperatures were observed.

The vertical gravity disturbance drift of the iNAV RQH was in the range of -15 to +45 $\frac{\text{mGal}}{\text{d}}$ for most flights (Figure 6.9). For most flights where the IMU temperature was already stable pre-flight, typically the second flights at a day, the drift was considerably smaller.

Without warm-up calibration, a crossover RMSE of 3.48 mGal was obtained (Table 6.3). This value was massively improved to 1.05 mGal with the iTempStab-based warm-up calibration of the vertical accelerometer (see Figure 2.13). 98 crossover points were found with a maximal height difference of 100 m.

For the mean horizontal magnetic field of MY2022, the amplitude of the magnetic field correction was 3.55 mGal, which was approximately twice the value obtained for the Central European campaigns. The crossover residuals were distributed in a range of ± 4 mGal around the calibration function (Figure 6.10) suggesting the magnetic field correction is valid in the evaluated campaign. This is also supported by the crossover RMSE degradation by a factor of 3.3 if the magnetic calibration correction based on IGRF data is not applied.

A repeated line with a length of 52 km was flown offshore between Malaysia and Indonesia. The repeated line RMSE improved from 0.76 to 0.61 mGal applying the magnetic correction. No large improvement was expected since the line was flown with a heading of approximately 75° and in opposite direction, i.e. the magnetic correction is small (see Figure 6.10).

Due to issues with the MTi data recording, the magnetometer readings could only be used for the magnetic correction in 12 of the 28 flights. If this data is used in conjunction with the IGRF data for the other flights, a crossover RMSE of 1.12 mGal is obtained. The results suggest that the Earth's magnetic field is not heavily deteriorated inside the aircraft cabin for the Malaysia campaigns. In the scope of this thesis, further magnetometer data will be analysed more elaborately for the BRE2021 and NTS2021 campaigns (see Sections 6.5, and 7.2).

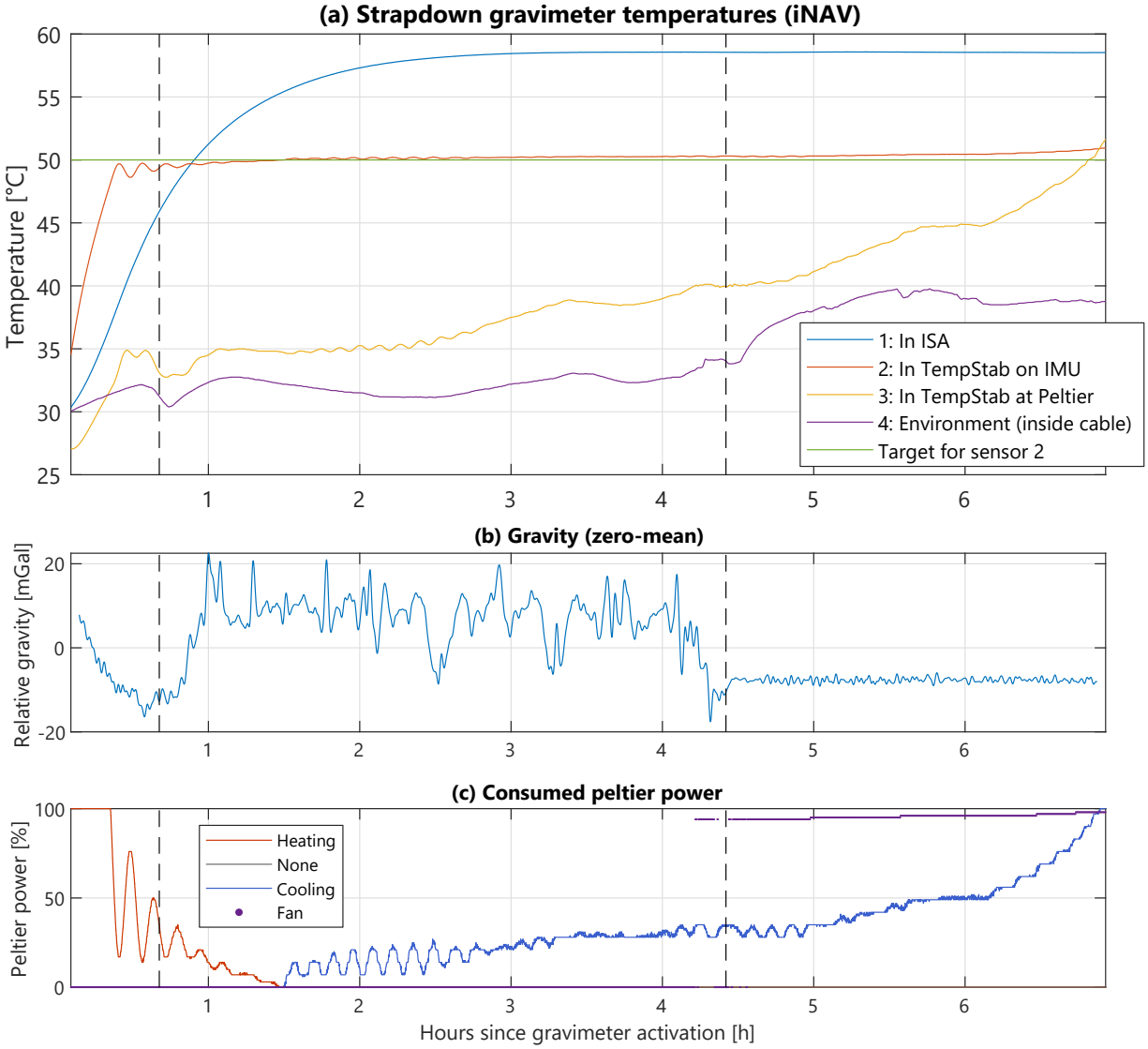


Figure 6.8: Sensor temperatures, estimated gravity and heating/cooling power of the iNAV-RQH with iTempStab-AddOn at flight 108a of MY2022

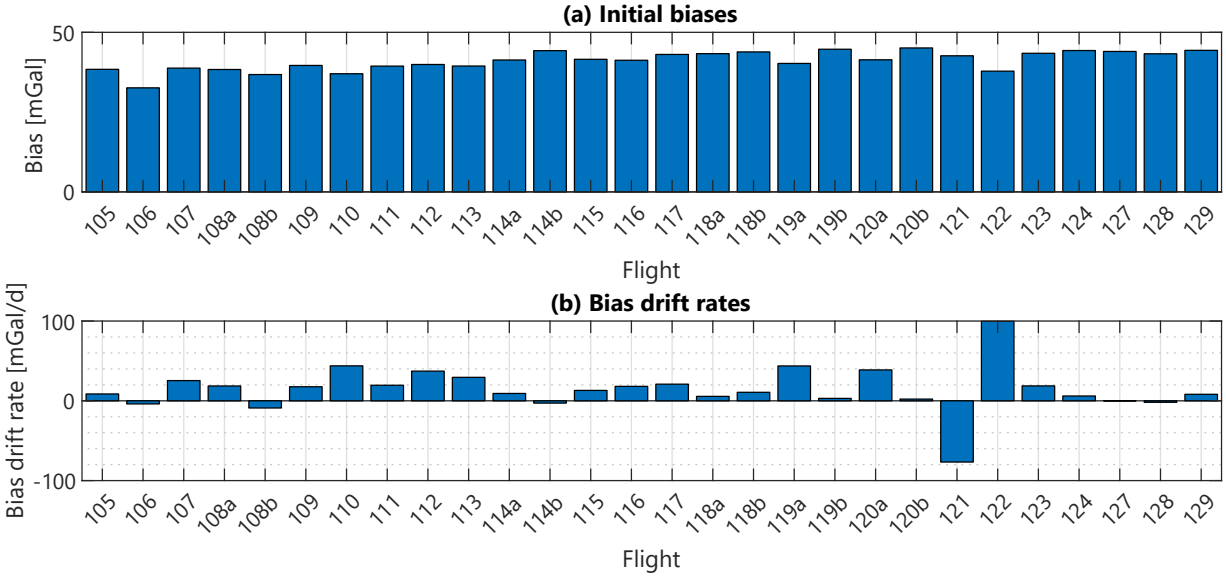


Figure 6.9: Vertical biases at the base readings before the flights of MY2022 and linear drifts between the base readings

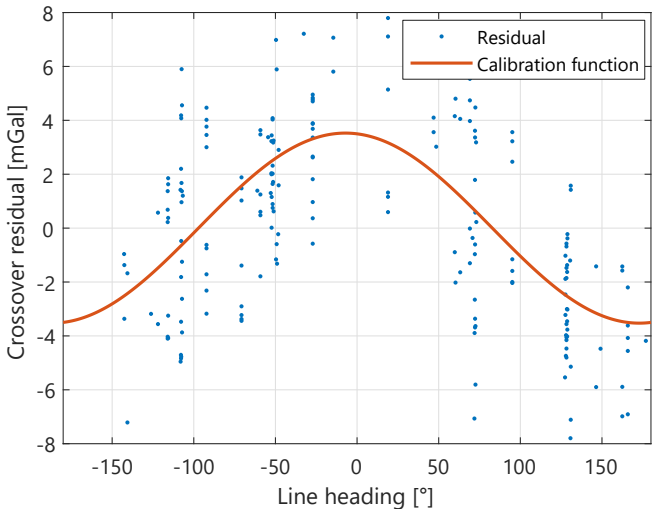


Figure 6.10: Crossover point residuals with respect to both corresponding line headings at MY2022 and magnetic calibration function of Equation (3.8)

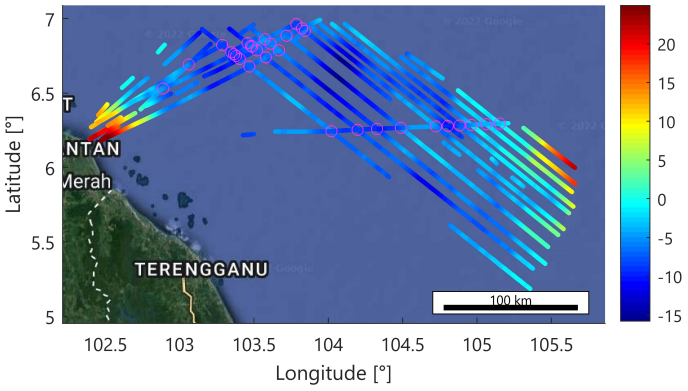


Figure 6.11: Line-wise adjusted gravity disturbance [mGal] of the eastern subnet of MY2022 with crossover points (map data: Google, Landsat/Copernicus)

The MY2022 campaign can be split in the west coast, the east coast and transit flights for airport change. While, at the west coast and the transit flights, the number of crossover points at a similar height is not sufficient for reasonable crossover adjustments, the eastern subnet was adjusted. With a line-wise adjustment (Figure 6.11), the subnet RMSE improved from 0.74 to 0.34 mGal. No significant inter-flight biases have been observed in this subnet. Consequently, the flight-wise adjusted result precision does not significantly differ from the non-adjusted. The marginally worse precision of 0.75 mGal is due to the application of correction factors according to Equation (5.15). If they would not have been applied, the flight-wise adjusted RMSE would be expected to be overoptimistic.

DTU Space compared gravity anomalies obtained from the iNAV-RQH results by TU Darmstadt with global gravity models. The mean difference between the iNAV-RQH and the XGM2019e (Zingerle et al., 2019) was -0.86 mGal. At the oceans, the XGM2019e model combines the GOCO06s model, which is based on satellite gravimetry and satellite laser ranging (Kvas et al., 2019), and the satellite altimetry based model DTU13 (Andersen et al., 2014). The accuracy of XGM2019e is improved above the oceans in comparison to the EGM2008 (Zingerle et al., 2019). With a maximal degree and order of 5399, a spatial resolution of about 4 km is theoretically enabled. The bias between the iNAV-RQH and the altimetry-based model DTU21 at the open ocean was exceptionally low being 0.12 mGal. At the Strait of Malacca, the bias was -0.91 mGal which might be due to inaccuracies in the altimetry data near the coast.

6.3 ODW2017/2018: Odenwald 2017/2018[1]

6.3.1 Campaign details

Close to Darmstadt, Germany, there is an area of high gravity field variability at the contact line between the Upper Rhine Graben and the low-mountain range Odenwald. In a sub-area of 25x10 km, two airborne gravimetry test campaigns have been organised by iMAR and TU Darmstadt in May 2017 and March 2018.

In 2017, 8 flights have been conducted from Griesheim near Darmstadt with refuelling stops at Aschaffenburg using a small motor glider of the type Grob G109B owned by TU Darmstadt (Figure 6.12a). Three strapdown IMUs, TU Darmstadt's iNAV-RQH and two other iMAR devices by DTU Space and the Technical University of Munich, were mounted in the back of the aircraft cabin (Figure 6.13). Note that horizontally stabilised gravimeters cannot be installed in this motor glider due to space requirements and operational restrictions. GNSS records were made at a sample frequency of 1...20 Hz using an antenna inside of the cabin and an antenna on a wing. The relative small test area was covered by a dense network of perpendicular flight lines with a line separation of 500 m resulting in more than 400 crossover points (Figure 6.15a). With the low mean aircraft velocity of 36 $\frac{\mathrm{m}}{\mathrm{s}}$ and a filter length of 130 s, the spatial resolution was the best of the evaluated airborne campaigns being 2.3 km. The turbulence level according to the RMS-g was 769 $\frac{\mathrm{mm}}{\mathrm{s}^2}$ being about three times higher than in the Malaysia campaigns.

In 2018, a single flight was conducted using a medium-sized light aircraft of the type Cessna 206 "Stationair 6" starting from Mainz. Again, three iMAR IMUs were installed owned by TU Darmstadt, DTU Space and the General Command of Mapping Turkey (HGK). The trajectory was similar to ODW2017 adding a few extra kilometres to the end of the lines to reduce degraded turn data smearing into the line data during low-pass filtering. GNSS data was collected at 1 Hz using an antenna installed at the aircraft roof. Due to the higher flight velocity of 54 $\frac{\mathrm{m}}{\mathrm{s}}$ and a longer flight duration, the total line length was about 1,000 km which is comparable to the 1,400 km of data collected in 2017. The spatial resolution was 3.3 km. The turbulence level was small being 128 $\frac{\mathrm{mm}}{\mathrm{s}^2}$. The terrestrial base reading was conducted by TU Darmstadt.

[1] This section is partially based on Johann et al. (2020) and Johann et al. (2021). The statistics might slightly deviate due to minor changes in the algorithm and processing settings.



(a) Grob G109B at Griesheim near Darmstadt



(b) Cessna 206 “Stationair 6” at Mainz

Figure 6.12: Aircraft used for the Odenwald campaigns (Johann et al., 2020)

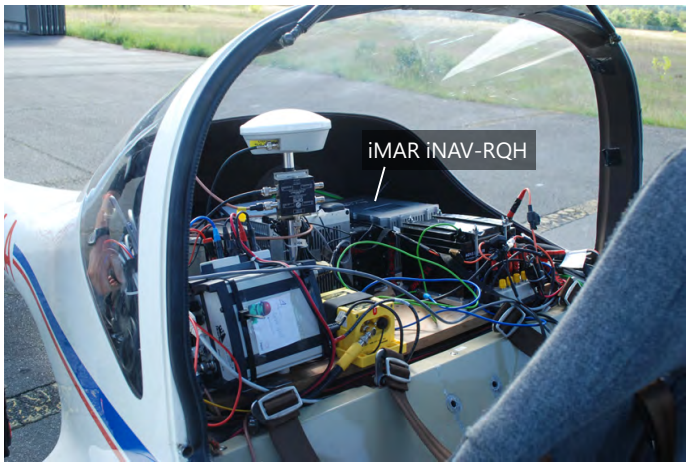


Figure 6.13: Installed gravimeters at ODW2017

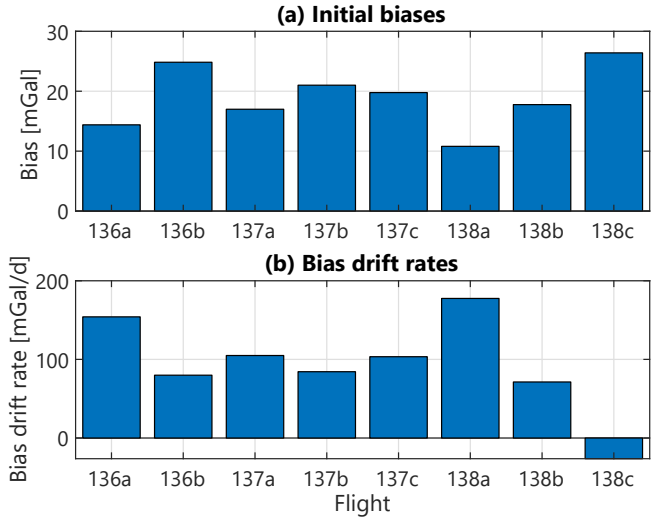
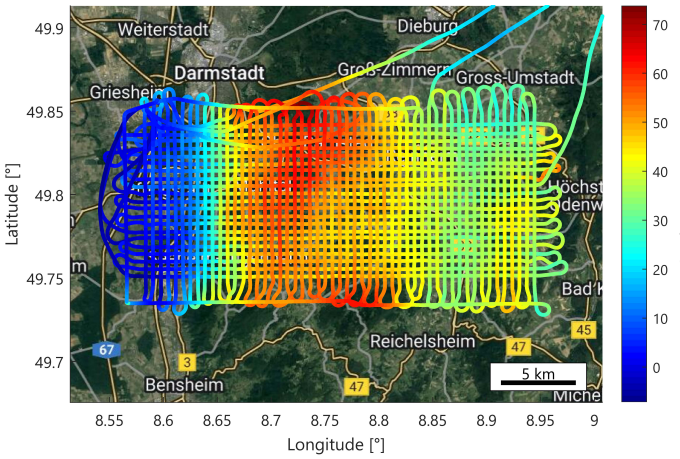
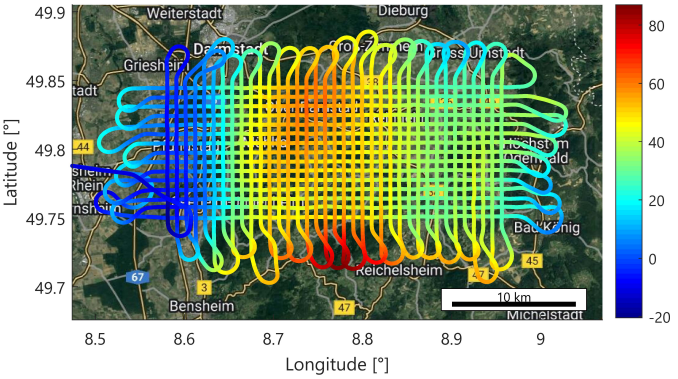


Figure 6.14: Vertical biases at the base readings before the flights of ODW2017 and linear drifts between the base readings

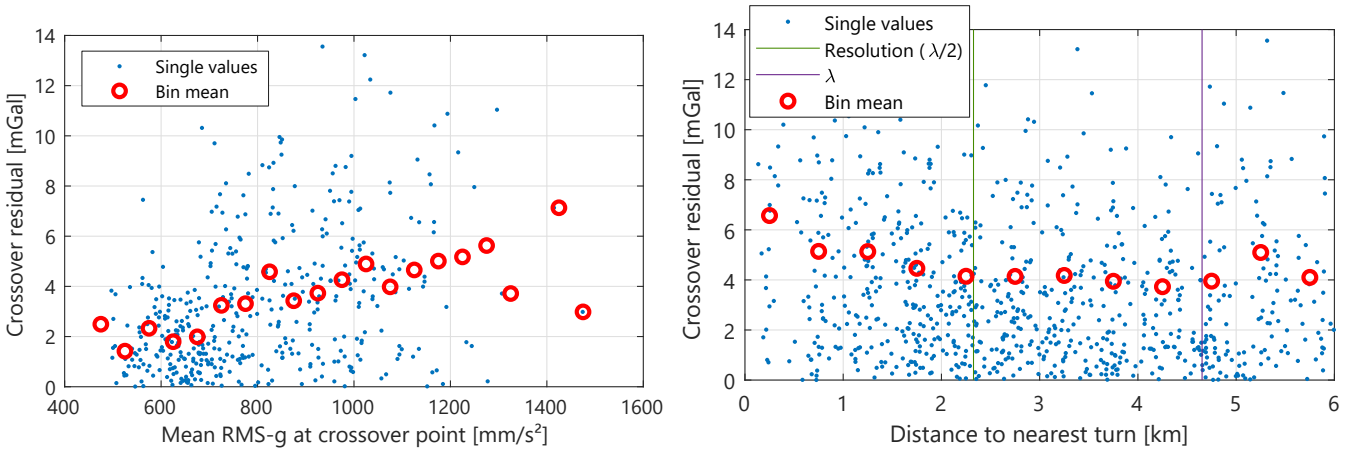


(a) ODW2017



(b) ODW2018

Figure 6.15: Non-adjusted gravity disturbance [mGal] of the Odenwald campaigns (map data: Google, Landsat/Copernicus)



(a) Turbulence level

(b) Distance to nearest turn with half- and full-wavelength resolution (vertical lines)

Figure 6.16: Crossover residuals of ODW2017 with respect to flight condition parameters (blue: single values; red: mean values of specific intervals)

6.3.2 Main results

In the ODW2017 campaign, high variations in the initial vertical gravity biases and the drift rates were observed (Figure 6.14). The linear drift varied between -30 and +180 $\frac{\text{mGal}}{\text{d}}$. Figure 6.16a indicates a possible relation between the crossover residuals and the turbulence level. The mean crossover residuals in RMS-g bins of bin size 50 $\frac{\text{mm}}{\text{s}^2}$ show a noticeable tendency to increase with increasing RMS-g. This suggests that the accuracy might degrade with higher turbulence. However, the results might be partially impaired if the GNSS antenna on the wing was exposed to wing vibrations. Another correlated parameter for the crossover residuals is illustrated in Figure 6.16b. A clear increase in the residuals can be observed if the distance of the crossover point to the nearest turn is lower than the half-wavelength resolution. Hence, crossovers within the half-wavelength distance at the line beginnings/ends are omitted in the following quality assessment. This observation should be remembered during trajectory planning. Crossover points should be placed in a sufficient distance to the line endings considering possible steering manoeuvres for attitude correction at the line beginning.

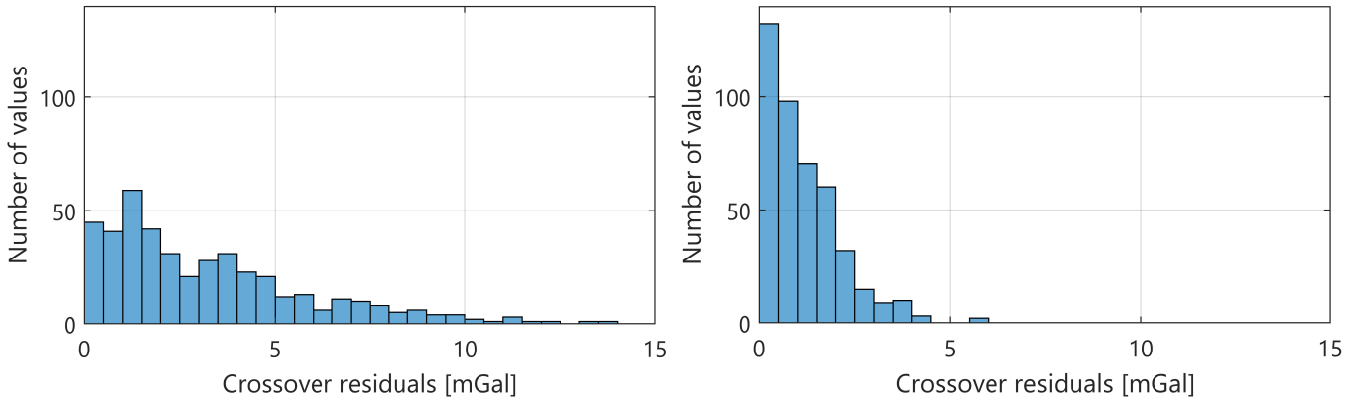
With the 431 remaining crossover points omitting the line endings, an RMSE of 2.97 mGal was obtained (Table 6.4). The comparatively poor precision might be due to the extraordinarily high turbulence level of the motor glider, possible vibrations acting on the aircraft wing antenna and distortions of the GNSS antenna under the the glass of the aircraft cabin.

A flight-wise (line-wise) adjustment improved the crossover RMSE to 1.82 mGal (1.11 mGal). Figure 6.17 shows how the residual distribution tightened after line-wise adjustment. No obvious outliers were detected. In this thesis, the standard procedure for a line-wise crossover adjustment is to estimate a bias per flight line. The extraordinarily high mean number of crossover points of about 20 per line and their homogenous distribution along the lines allows for a reasonable estimation of additional line-wise linear drift parameters. Estimating a bias and linear drift per line, the RMSE is improved further to 0.81 mGal.

222 crossover points were identified for the flight of ODW2018. The crossover RMSE was 4.05 mGal. The mean RMS-g was six times lower than for ODW2017 (see Table 6.1), but the results are suspected to be impaired by environmental temperatures near the freezing point before the start of the flight. For the iNAV-RQH without thermal stabilisation, strong sensor drifts were expected. The warm-up calibration was not

Table 6.4: Odenwald 2017/2018 precision

Campaign	2017	2017	2018	2018	2018	2017/18
CO adjustment linear trend?	✗	✓	✗	✗	✗	✗
Kinematic acceleration	PosDif-PPP	PosDif-PPP	PosDif-PPP	PhaseDif-PPP	PhaseDif-POP	PosDif-PPP
Satellite constellations	GR	GR	GR	GR	G	GR
n_{CO} non-adjusted	431	431	222	222	222	546
n_{CO} flight-adjusted	431	431	-	-	-	373
n_{CO} line-adjusted	429	429	220	220	220	540
CO RMSE non-adj. [mGal]	**2.97**	-	**4.05**	4.07	4.25	**3.37**
CO RMSE flight-adj. [mGal]	1.82	1.62	-	-	-	2.69
CO RMSE line-adj. [mGal]	1.11	0.81	0.64	0.68	0.71	1.08



(a) Before adjustment

(b) After line-wise adjustment

Figure 6.17: Histograms of the crossover residuals of ODW2017

applicable since its lowest temperatures are more than 20°C (see Figure 2.13). However, an estimation of a bias per flight line improved the precision dramatically to 0.64 mGal since temperature changes during the single flight lines were low. The estimated biases (Figure 6.18) uncover strong non-linear sensor drifts. Note that a linear drift of 1.8 $\frac{\text{mGal}}{\text{h}}$ was already eliminated before by endmatching (see Section 5.4). The adjusted RMSE was significantly better than for ODW2017 which is probably due to the lower RMS-g based on aircraft turbulence and GNSS antenna observation conditions.

Alternatively to the PosDif kinematic acceleration determination with GPS and GLONASS observations, the PhaseDif methods were applied to ODW2018. For PhaseDif-POP, the IGS stations Frankfurt/Main (FFMJ) and Hügelheim (HUEG), both in Germany, were selected. Their distances to the median line position of ODW2018 are 30 and 240 km, respectively (Figure 6.21). All methods performed on par before and after adjustment, with a marginal result degradation for the PhaseDif approaches (see Table 6.4). This suggests that all implemented methods are suited for airborne gravimetry. A more detailed analysis for different kinematic acceleration determination strategies will be done for the BRE2021 campaign (see Section 6.5.2), where the impact of the kinematic acceleration is expected to be higher due to the generally better precision level.

Since both Odenwald campaigns were conducted in the same area, both results could be combined with an overall crossover RMSE of 3.37 mGal using all 546 intra- and inter-campaign crossovers. The precision is on a medium level of both single campaigns. This suggests that no major systematic errors are apparent in the single solutions. As expected, the RMSE is closer to the value of ODW2017 due to the higher number of

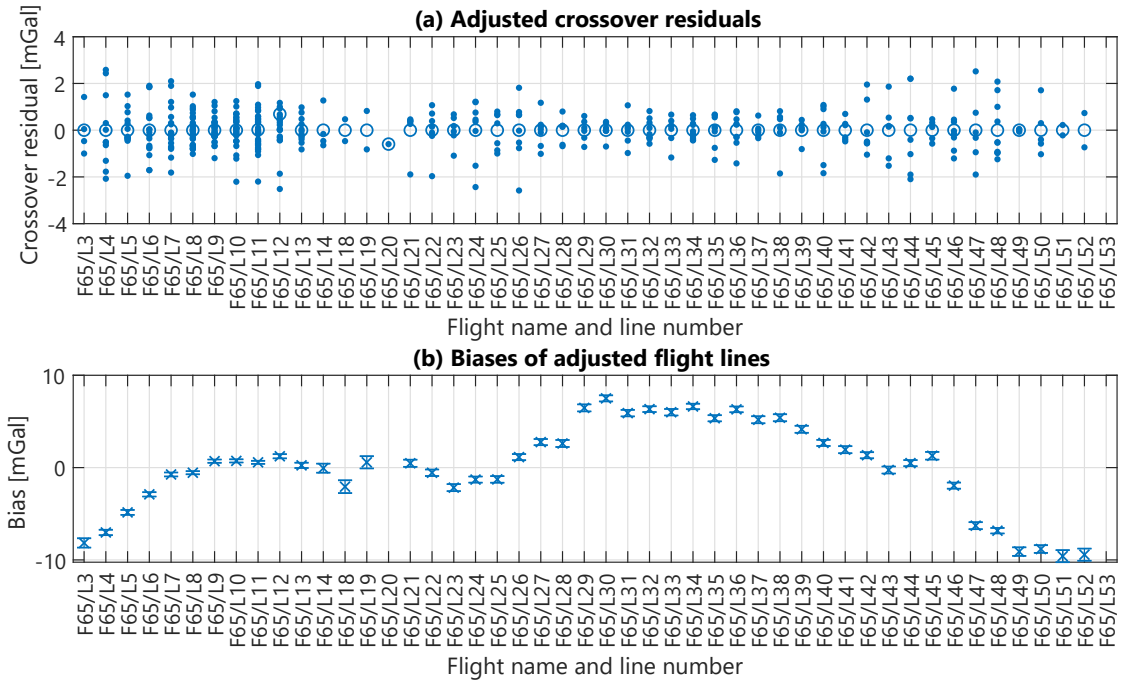


Figure 6.18: Line-wise adjusted crossover residuals sorted by flights (indicated by the colour) and lines of ODW2018 (circles: mean values of the lines) and estimated line biases with their standard deviation

crossovers for this campaign. The crossover residuals sorted by flights and lines are illustrated in Figure 6.19. Non-linear drifts are striking, especially for ODW2018. At ODW2017, the sensor drift behaviour appears to be consistent between the flights. The RMSE after line-wise adjustment becomes 1.08 mGal which is close to the ODW2017 precision. The high consistency of the adjusted results is visualised in Figure 6.20.

6.4 DK2020: Denmark 2020

6.4.1 Campaign details

In September 2020, DTU Space conducted an airborne gravimetry campaign in cooperation with TU Darmstadt using a Vulcanair P68C run by Bioflight (Figure 6.22). The purpose of the project was to cover coastal areas in the west at the North Sea and in the north at the Skagerrak strait to obtain homogenous gravity data in the transition zone of existing terrestrial and marine data (Figure 6.29). In five flights, a total line distance of about 4,300 km was surpassed. With 377 $\frac{\text{mm}}{\text{s}^2}$, the turbulence level in terms of RMS-g was slightly higher than at the Malaysia campaigns but significantly lower than at ODW2017. The mean flight height was the lowest of the airborne campaigns being less than 500 m. The magnetic field intensity was slightly lower than at the Odenwald campaigns (17.0 µT) with a resulting magnetic correction amplitude of 1.45 mGal. The flight velocity was medium being 65 $\frac{\text{m}}{\text{s}}$. With a filter length of 140 s, the corresponding spatial resolution was 4.3 km.

Three iMAR IMUs were installed as strapdown gravimeters in the aircraft: The iNAV-RQH by TU Darmstadt, an iNAT-RQH by DTU Space, both with thermal stabilisation, and a newly developed iNAT-RQT system. The results of the RQH systems will be compared in Section 9.1. The RQT results were significantly worse due to the absence of a thermally stabilising housing.

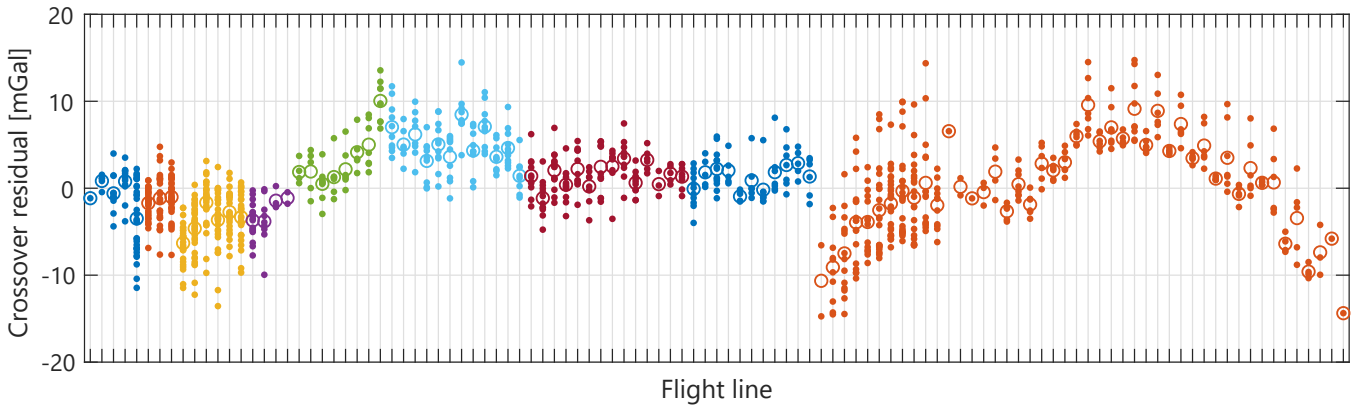


Figure 6.19: Non-adjusted crossover residuals sorted by flights (indicated by the colour) and lines of ODW2017 and ODW2018 (circles: mean values of the lines). The orange data on the right side belongs to ODW2018, the remaining data belongs to ODW2017

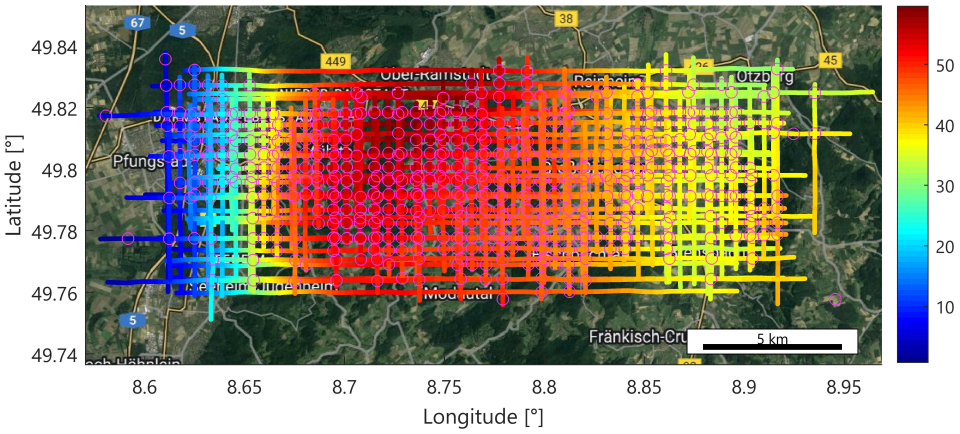


Figure 6.20: Line-wise adjusted gravity disturbance [mGal] of ODW2017 and ODW2018 with crossover points (map data: Google, Landsat/Copernicus)

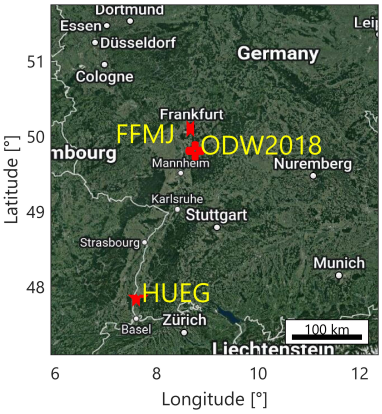
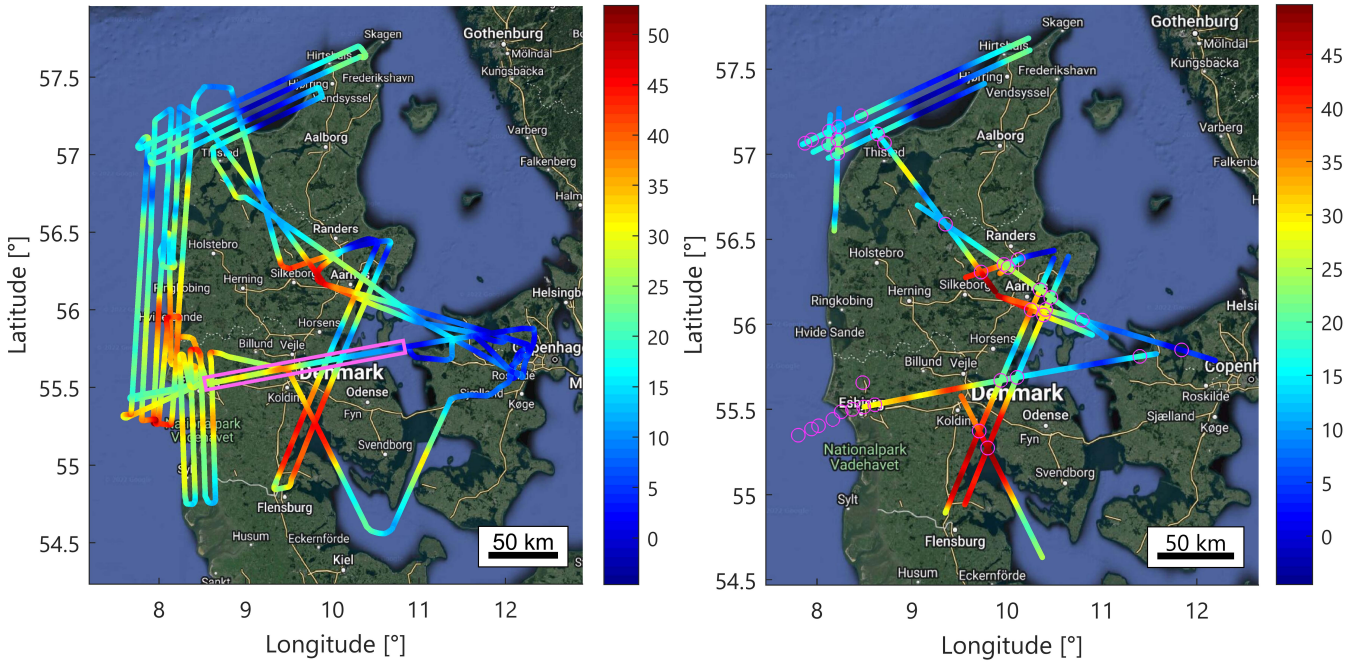


Figure 6.21: IGS stations selected for PhaseDif-POP processing of ODW2018 (Map data: Google, Landsat/Copernicus)



Figure 6.22: Vulcanair P68C at Esbjerg used for DK2020



(a) Before adjustment (magenta: repeated line)

(b) After line-wise adjustment with crossovers

Figure 6.23: Gravity disturbance [mGal] of DK2020 (map data: Google, Landsat/Copernicus)

Table 6.5: Denmark 2020 precision

Thermal calibration?	✓	✗	✓
Magnetic calibration?	✓	✓	✗
n_{CO} non-adjusted	37	37	37
CO RMSE non-adj. [mGal]	**0.93**	1.66	1.13
RL distance [km]	147	-	147
RL RMSE [mGal]	0.48	-	0.68

At the beginning of the first flight, the IMU temperatures were not fully stabilised due to a power issue in the previous night. After that, the IMUs were turned on until the end of the campaign.

6.4.2 Main results

Thanks to the continuous usage of the iTempStab, the drift rates were less than $\pm 10\ \frac{\text{mGal}}{\text{d}}$ (Figure 6.24), which is much lower than for the Malaysia and Odenwald campaigns. 37 crossover points have been identified. Figure 6.25 indicates that the residuals were generally pretty low, but there might be some flight-dependent systematic behaviour like a positive and a negative bias for flights 216b and 263, respectively. The crossover precision was 0.93 mGal (Table 6.5).

Due to the incomplete sensor heating before the start of the first flight, the precision degraded without applying the thermal calibration almost by a factor of 2 (1.66 mGal). Without magnetic calibration, the precision indicator degraded by 0.2 mGal. The influence of the magnetic field correction was expected to be lower than in Malaysia since the horizontal magnetic field intensity is lower by a factor of 2.3.

A repeated line with a total length of 147 km was obtained during the campaign. The line was surpassed across the Denish peninsula Jutland (see magenta rectangle in Figure 6.23a) in two different flights. Figure

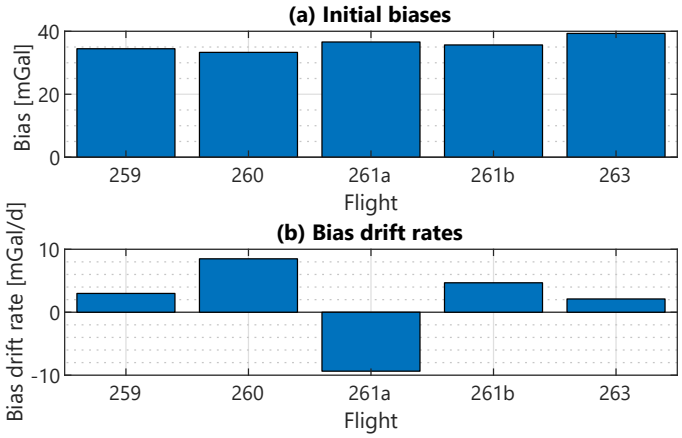


Figure 6.24: Vertical biases at the base readings before the flights of DK2020 and linear drifts between the base readings

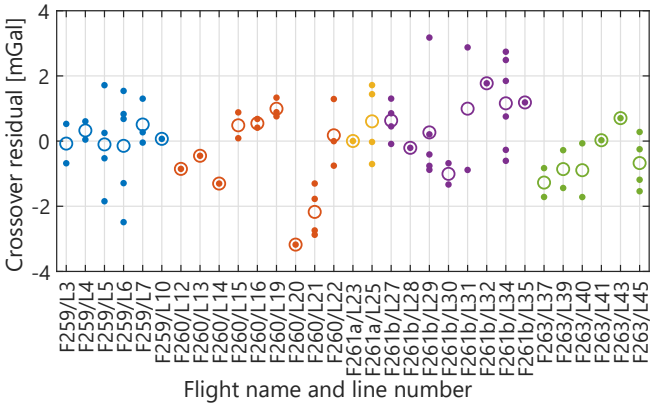


Figure 6.25: Non-adjusted crossover residuals sorted by flights (indicated by the colour) and lines of DK2020 (circles: mean values of the lines)

6.26 shows the good agreement of both repetitions in terms of gravity disturbance. The residuals were mostly lower than 1 mGal although there is a systematic trajectory separation in the height of about 80 m. The horizontal separation is predominantly less than 50 m. The RMSE of the gravity disturbance is 0.48 mGal. It was just slightly improved to 0.39 mGal when using the zero-mean gravity disturbance data. This indicates that there are only minor systematic deviations between both line repetitions.

DTU Space compared the iNAV-RQH results with upward-continued terrestrial data for accuracy evaluation. A systematic bias during the flights of 2.5 mGal was detected. The base reference gravity determination, normal gravity computation, attitude determination, IMU preprocessing, quantisation and the lever arm have been evaluated, but no reason for the systematic deviation was found. Possibly, vibrations in the IMU mounting rack might be harmful for the results. However, further evaluation of this effect is required in the future. Note that in the other campaigns, no biases in this order have been found.

6.5 BRE2021: Bremen 2021

6.5.1 Campaign details

In preparation for the CL2021 campaign (see Section 6.6), a test flight was conducted with the Polar 5 aircraft of the Alfred Wegener Institute for Polar and Marine Research (AWI) in September 2021. The Polar 5 (Figure 6.27) is a Basler BT-67, a modified Douglas DC-3 that is suited for landing and take-off in the polar regions (Wesche et al., 2016). In cooperation with Technische Universität Dresden (TU Dresden), an uninterruptible power supply assembly was developed for the iNAV-RQH with iTempStab which can be used in airborne and shipborne campaigns. The system was installed in the Polar 5 cabin between a GT-2A gravimeter and an operation rack by AWI (Figure 6.28). Unfortunately, the GT-2A data of the flight could not be used in post-processing due to technical issues.

There are three measurement lines which were flown above the North Sea. The northern and western line have been repeated within the flight. The western and eastern lines are repeated lines of the shipborne campaign NTS2021 (see Section 7.2). The results will be compared to the shipborne results in Section 9.3.2. The total line length was approximately 600 km. Within the line triangle above the North Sea, 10 crossover points and 131 km of repeated lines can be evaluated. The turbulence level was medium compared with the

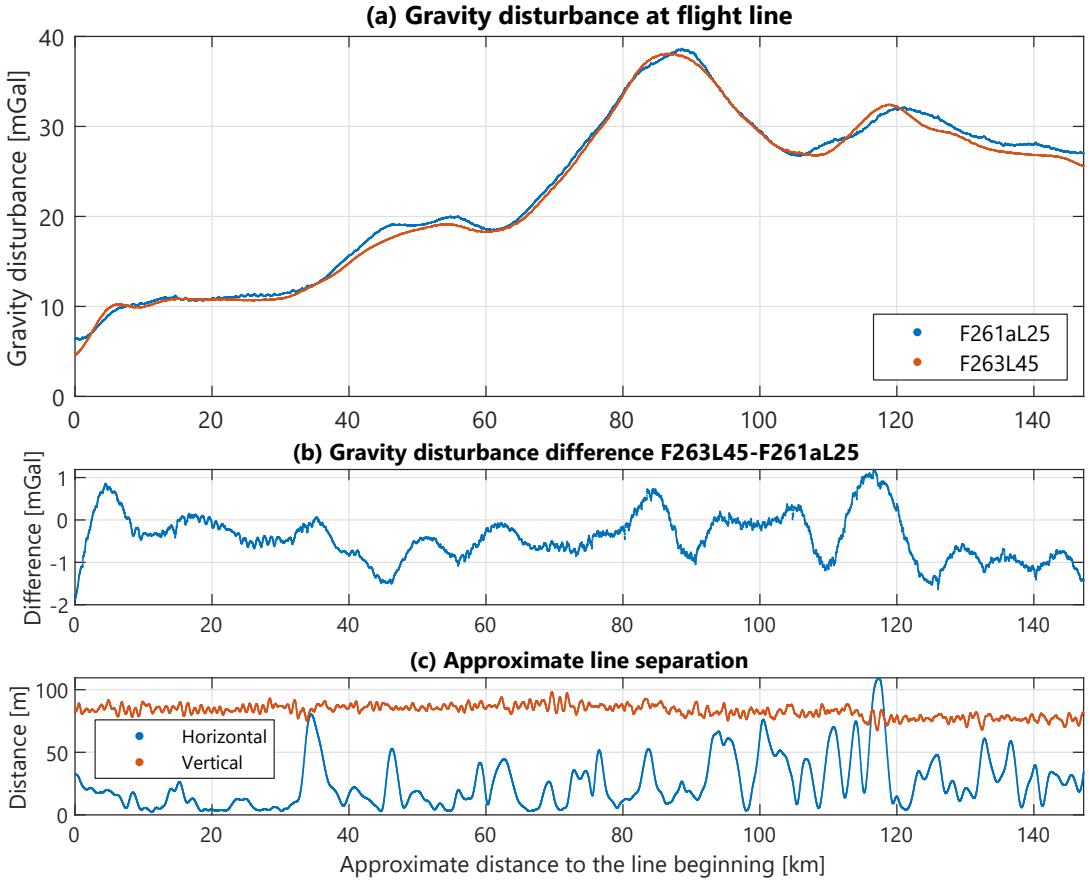


Figure 6.26: Gravity disturbance and separation of the repeated lines 25 and 45 of DK2020



Figure 6.27: Polar 5 at Bremen used for BRE2021 and CL2021

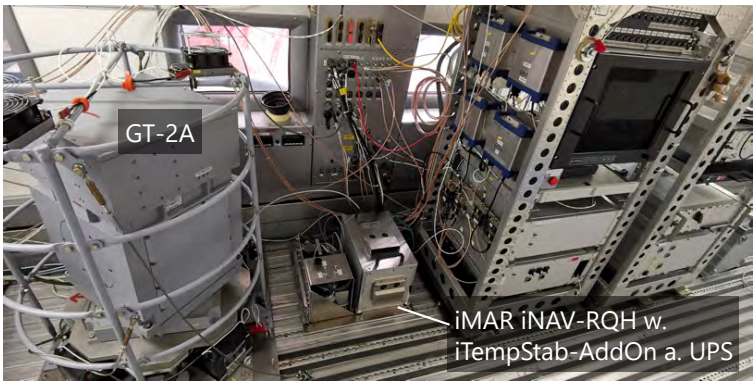


Figure 6.28: Installed gravimeters at BRE2021

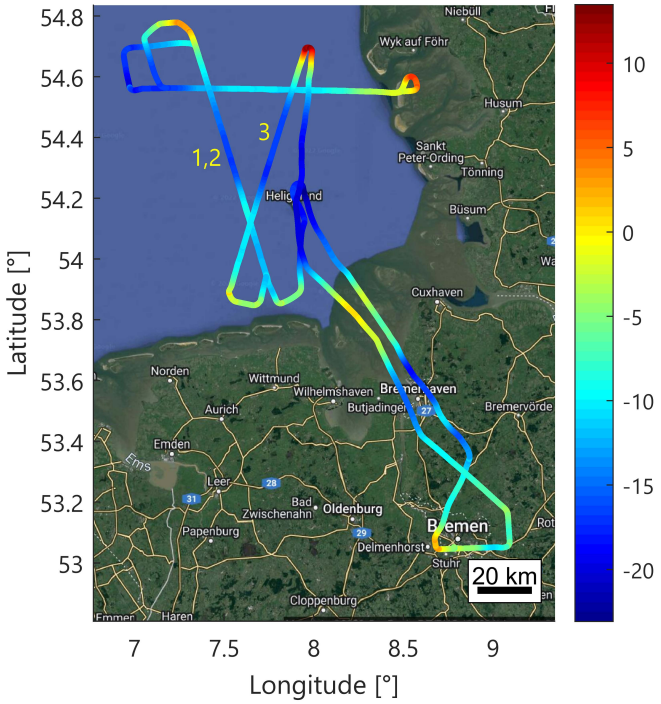


Figure 6.29: Non-adjusted gravity disturbance [mGal] BRE2021 (repeated lines of NTS2021 are labelled yellow; map data: Google, Landsat/Copernicus)

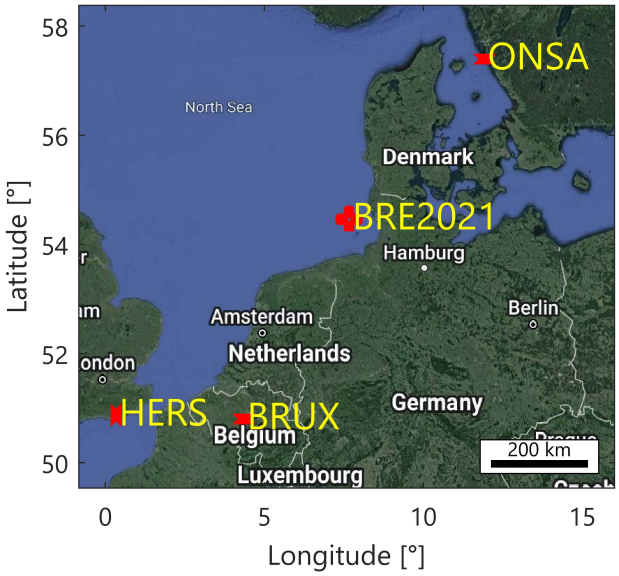


Figure 6.30: IGS stations selected for PhaseDif-POP processing of BRE2021 (Map data: Google, Landsat/Copernicus)

Table 6.6: IGS stations selected for BRE2021 (data from International GNSS Service (2022))

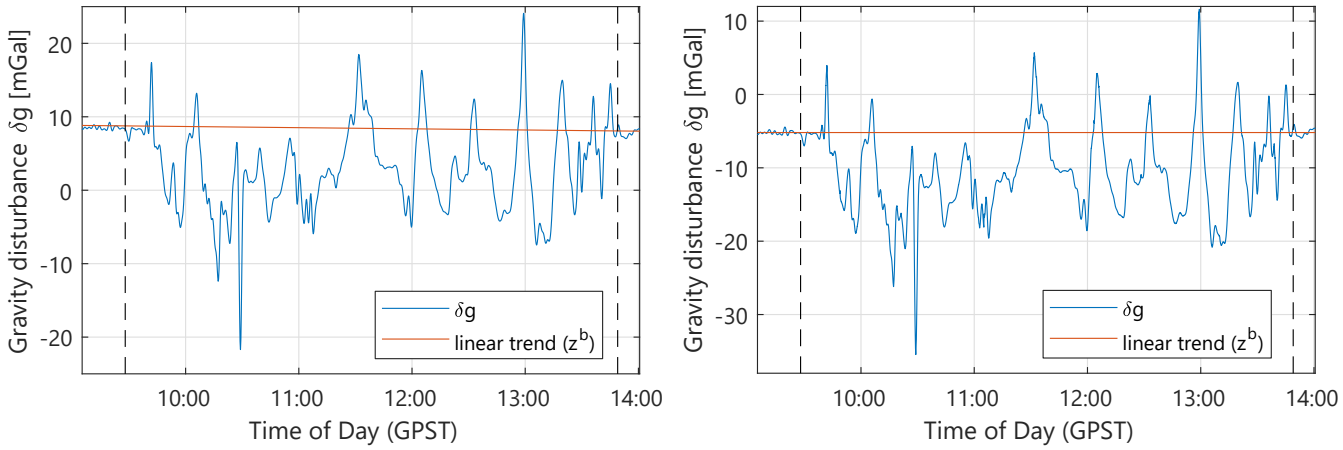
Site	Location	Receiver type	Clock type	Distance [km]
BRUX	Brussels, Belgium	Sept POLARX5TR	ext. H-Maser	470
ONSA	Onsala, Sweden	Sept POLARX5TR	ext. H-Maser	410
HERS	Hailsham, United Kingdom	Sept POLARX5TR	ext. H-Maser	640

Malaysia and the DK2020 campaigns. The mean flight height was similar like at DK2020 being about 500 m. A filter length of 170 s in conjunction with a flight velocity of 170 $\frac{\text{m}}{\text{s}}$ translates into a spatial resolution of 5.7 km. According to the IGRF, the horizontal magnetic field intensity was as low as 17.7 µT. Terrestrial base readings at Bremen were performed by TU Darmstadt.

To set up a station network for the PhaseDif-POP method, three IGS stations have been selected (Figure 6.30. The Brussels station was selected as master, the stations in Onsala, Sweden, and Hailsham, United Kingdom, were selected as reference stations. The distance between the mean campaign position and the stations was between 470 and 640 km (Table 6.6).

6.5.2 Main results

Figure 6.31 shows the gravity disturbance obtained along the flight trajectory. While the results in Figure 6.31a are subject to bias and linear drift, both were removed by endmatching at the base reading periods. The crossover residuals are shown in Figure 6.32. All absolute residuals were lower than 1.1 mGal translating into an excellent precision of 0.50 mGal without any crossover adjustment (Table 6.7). The number of crossover



(a) Before endmatching

(b) After endmatching

Figure 6.31: Gravity disturbance [mGal] referencing of BRE2021 with PhaseDif-POP results (dashed lines: end/beginning of base reading periods at airport)

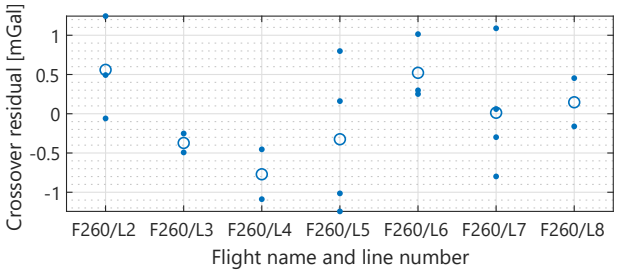


Figure 6.32: Non-adjusted crossover residuals sorted by lines of BRE2021 (circles: mean values of the lines)



Figure 6.33: Magnetometer installed in the tail rod of Polar 5

points was not very high, but the repeated lines confirmed the excellent accuracy with an RMSE of 0.54 mGal. The long low-pass filter length of 170 s might be suspected to be the reason for the good precision, but a 130 s filter leads to an only slightly worse precision of 0.57 mGal (crossovers) and 0.60 mGal (repeated lines). After a line-wise crossover adjustment or the removal of the mean values from the repeated lines, there are slight improvements in the precision to 0.39 and 0.48 mGal, respectively.

Without the IGRF-based magnetic correction, the crossover and repeated lines RMSE degraded to 1.19 and 1.72 mGal, respectively. At the tail of the aircraft, a Scintrex CS-3 caesium magnetometer was installed to observe the exterior magnetic field. The raw data of this magnetometer was pre-processed by levelling the mean observations of the three axes to the mean IGRF values. The resulting magnetic field parameters (Figure 6.34) are noisier than the IGRF results. Remaining systematic differences between the IGRF and magnetometer observations do not influence the gravity disturbance precision indicators significantly. This indicates that the monitoring of the exterior magnetic field might not be required to correct the gravimeter observations. The IGRF appears to model the exterior magnetic field with sufficient accuracy. The use of a magnetometer close to the IMU will be analysed in the North Sea 2021 shipborne campaign (see Section 7.2).

The gravity disturbance of BRE2021 has been computed using several kinematic acceleration determination approaches introduced in Section 4. With all implemented methods, a precision better than 0.75 mGal was obtained. The main results were computed using the PosDif approach where PPP position solutions obtained

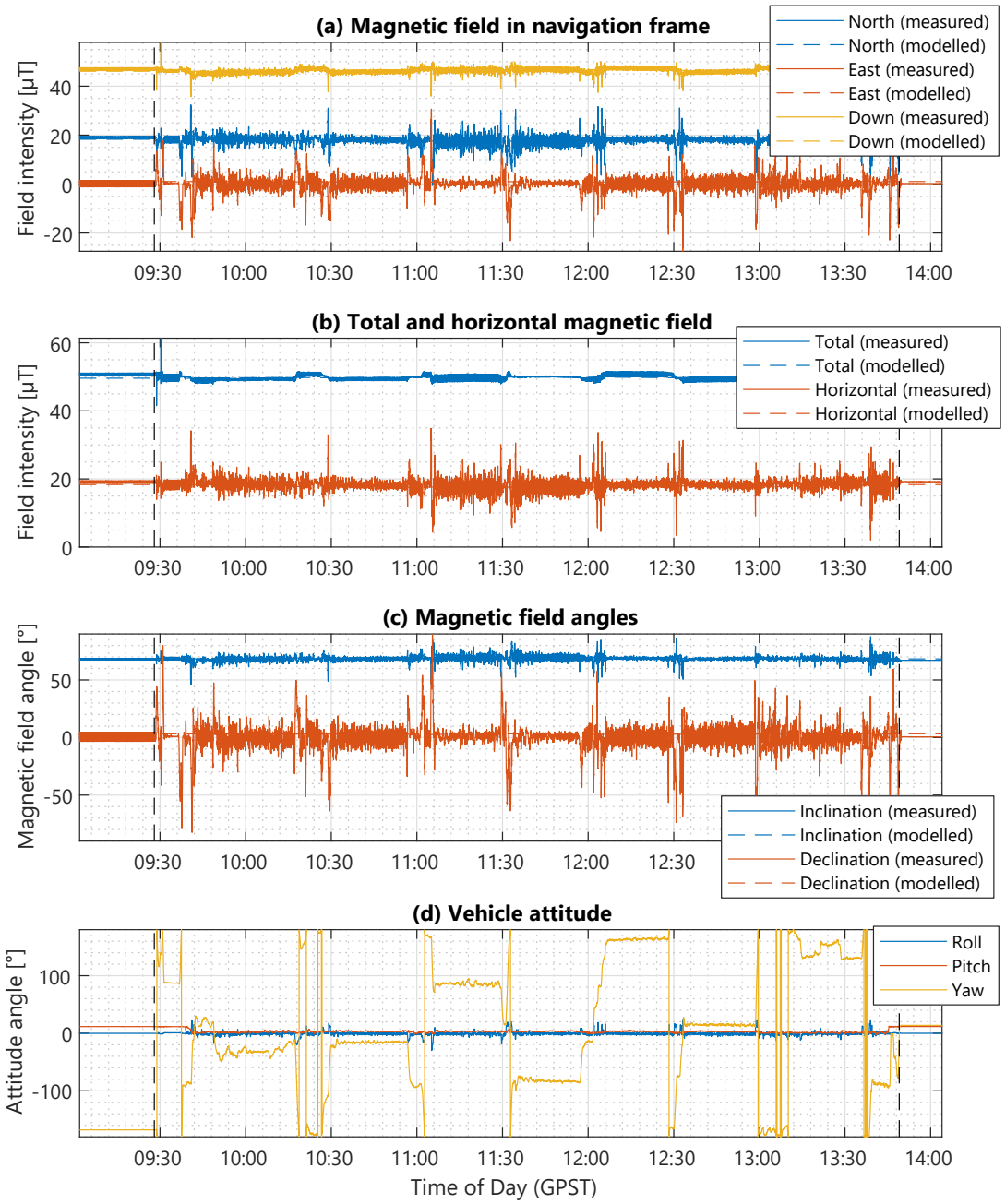


Figure 6.34: Magnetic field parameters measured with a magnetometer and modelled with IGRF13 for BRE2021 with vehicle attitude angles

Table 6.7: Bremen 2021 precision

Filter length (-6 dB) [s]	170	130	170	170	170	170	170
Kinematic acceleration	PosDif-PPP	PosDif-PPP	PhaseDif-PPP	PhaseDif-PPP	PhaseDif-POP	PhaseDif-POP	PhaseDif-POP
GNSS constellations	GR	GR	GR	GR	GR	GEC	GERC
Satellite clock interval [s]	5	5	30	5	-	-	-
n_{CO} non-adjusted	10	10	10	10	10	10	10
n_{CO} line-adjusted	10	10	10	10	10	10	10
CO RMSE non-adj. [mGal]	**0.50**	0.57	0.60	0.54	0.54	0.59	0.55
CO RMSE line-adj. [mGal]	0.39	0.48	0.42	0.30	0.31	0.44	0.41
RL distance [km]	131	131	131	131	131	131	131
RL RMSE [mGal]	0.54	0.60	0.77	0.74	0.63	0.66	0.64
RL RMSE ZM [mGal]	0.48	0.55	0.61	0.58	0.57	0.59	0.58

with 5 s satellite clock data using GPS and GLONASS observations were numerically differentiated. In contrast to the findings for the static experiments (see Section 4.5.2), no significant degradation of the gravity precision was observed using 30 s clock products for the PosDif method.

With the PhaseDif-PPP and -POP methods, the crossover RMSE marginally degraded from 0.50 mGal to 0.54 mGal. After line-wise adjustment, the PhaseDif approaches performed slightly better than PosDif. If 30 s satellite clock products were used within the PhaseDif-PPP methods, a slight degradation of 0.06 mGal was observed for the non-adjusted RMSE. Adding the BeiDou system to the PhaseDif-POP observations, the results became slightly worse. This might be due to undetected outliers. If Galileo observations were added, i.e. processing four constellations, the precision was almost on par with the GPS/GLONASS solution. Regarding the repeated lines RMSE, the findings were similar. The PhaseDif-POP method performed slightly better than the PPP-based method. Both results were slightly worse than PosDif. However, all methods proved to be suited for airborne gravimetry.

The gravity disturbance results of an exemplary trajectory segment using all three kinematic acceleration determination methods are illustrated in Figure 6.35a. All solutions are similar in most parts of the trajectory. The PosDif solution appears to be slightly smoother (Figure 6.35c). The differences between the PhaseDif results are small (Figure 6.35b). At about 10:28, an undetected outlier can be observed in the PhaseDif results. Since the error appears in both PhaseDif results, there might be an outlier in the rover observation. The error amplitude is slightly lower in the POP-based method. The figure indicates that improved outlier detection might slightly improve the PhaseDif results.

6.6 CL2021: Patagonia 2021

6.6.1 Campaign details

The Patagonia 2021 campaign was conducted by the AWI in cooperation with TU Dresden, TU Darmstadt and the University of Erlangen-Nuremberg in November 2021. Glaciers in Chilean Patagonia were surpassed and observed by the strapdown gravimeter of TU Darmstadt, laser scanners and an ice structure accumulation radar (Figure 6.36a). Future flights in the same areas are intended for glacier monitoring in the context of climate change.

All three flights were flown from Puerto Natales using AWI's Polar 5 aircraft (see Figure 6.27). The first flight took about 6.5 h and covered glaciers in the Laguna San Rafel National Park (Figure 6.36b); the

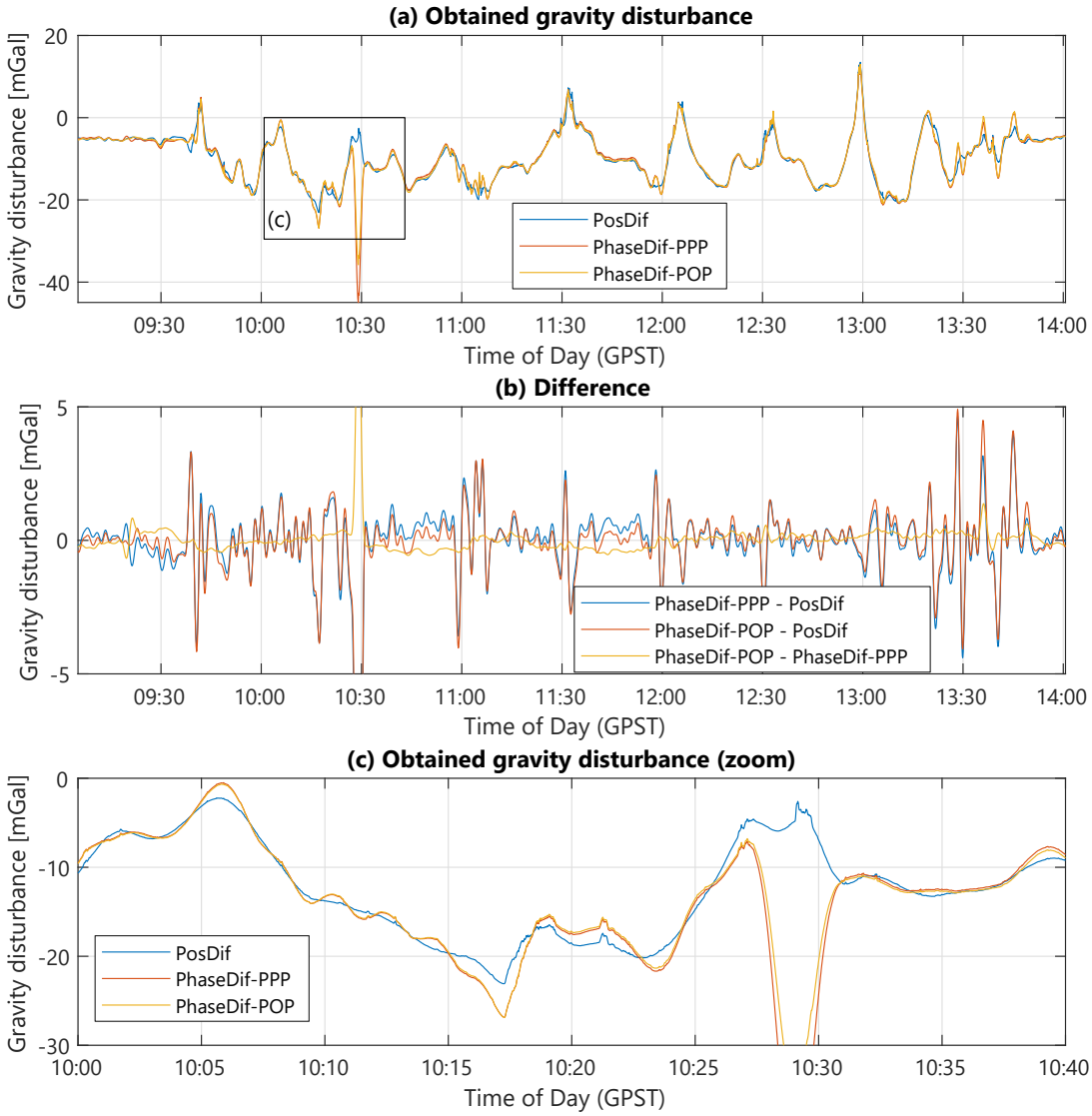
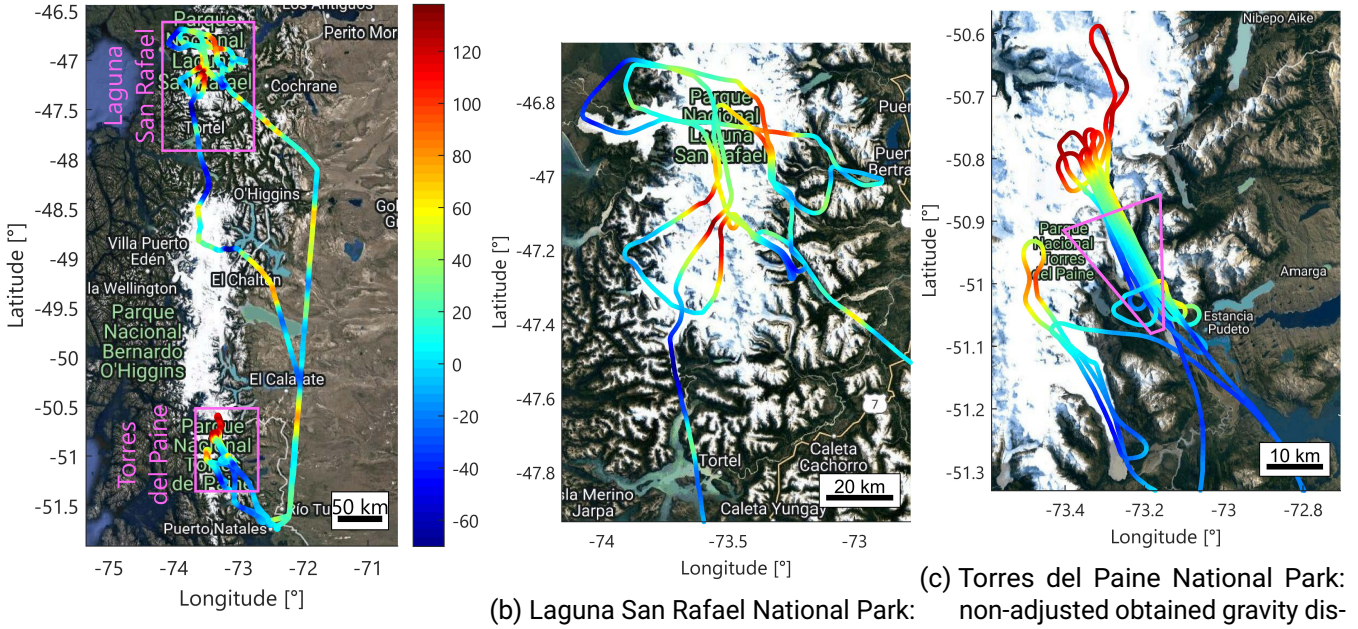


Figure 6.35: Comparison of gravity disturbance results obtained with different kinematic acceleration determination methods for BRE2021



(a) Full campaign: expected gravity disturbance

(b) Laguna San Rafael National Park: non-adjusted obtained gravity disturbance

(c) Torres del Paine National Park: non-adjusted obtained gravity disturbance (magenta: Grey glacier view of Figure 6.37)

Figure 6.36: Gravity disturbance [mGal] CL2021 (equal gravity disturbance scale; map data: Google, Landsat/Copernicus)

remaining flights took just up to 3 h covering glaciers in the Torres del Paine National Park near Puerto Natales (Figure 6.36c). Due to sensor restrictions, the flights were conducted in drape mode, i.e. the flight altitude followed the terrain height. In order to get valuable laser and radar observations, the trajectory was required to be mostly curvy. Only the transitions were flown straightly over long distance. Mainly due to a lowered estimability during flight manoeuvres, this is not ideal for gravimetry (see Section 5.5). If stable platform gravimeters like the Chekan-AM or the L&R S-type would have been used, no meaningful results could be expected. TU Darmstadt's iNAV-RQH was tested in this flight mode for the first time. The total line length was 2316 km considering lines with a minimum length of 10 km and tolerating high heading variations of 20°.

The flight trajectories at the Grey glacier are visualised in Figure 6.37. Note the narrow turns and varying flight altitudes. The terrain height around the glacier varies almost between sea level and more than 2,000 m. Along the 30 km long glacier, the gravity disturbance range is about 120 mGal translating into a mean field variability of 4 $\frac{\text{mGal}}{\text{km}}$. The variation across the glacier valley may be even higher. The mean field variability of 3.6 $\frac{\text{mGal}}{\text{km}}$ is only slightly higher than at the Odenwald campaigns (2.8 $\frac{\text{mGal}}{\text{km}}$), but much higher than in the remaining campaigns. In Denmark, the mean field variability was as low as 0.8 $\frac{\text{mGal}}{\text{km}}$. A short low-pass filter length of 100 s was found to be well-suited for the campaign. With the improved spatial resolution of 3.5 km at a mean flight velocity of 70 $\frac{\text{m}}{\text{s}}$, the high variability of the local gravity field could be well represented. At other campaigns with low field variability, the noise dampening of greater filter lengths outweighs the slight degradation of the spatial resolution.

The mean horizontal magnetic field at the survey area is similar to the Central European values being 19.7 µT according to the IGRF. The variation from the north to the south is about 0.5 µT which is barely significant for the magnetic correction of the iNAV-RQH accelerometer observations. The declination varies by about 2.5°.

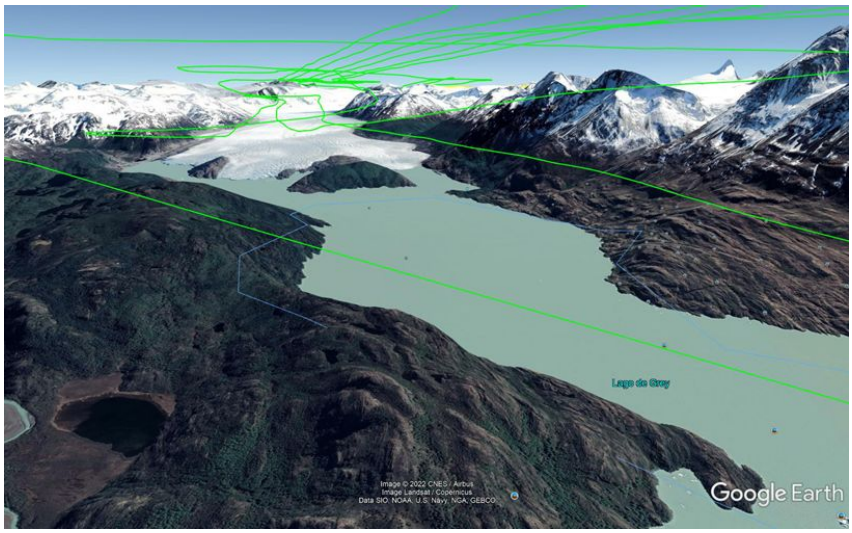


Figure 6.37: Flight trajectories at the Grey glacier (Image: Google Earth, CNES/Airbus/Landsat/Copernicus)

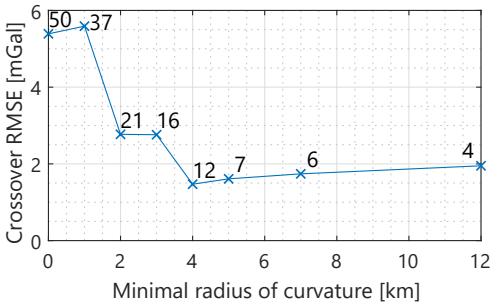


Figure 6.38: Crossover RMSE of CL2021 using points with a specific minimal radius of curvature (point labels: number of included crossover points)

Table 6.8: Chile 2021 precision

Filter length (-6 dB) [s]	100	140	100	100
Thermal calibration?	✓	✓	✗	✓
Magnetic calibration?	✓	✓	✓	✗
n_{CO} non-adjusted	12	12	12	12
CO RMSE non-adj. [mGal]	**1.47**	1.81	1.56	1.60

6.6.2 Main results

As illustrated in Figure 5.3, the crossover residuals were strongly correlated with the minimal radius of curvature of both adjacent trajectory parts (see Section 5.5). If all crossover points with a maximal vertical separation of 100 m were considered, an RMSE of 5.39 mGal was obtained. However, if a minimal radius of curvature was set, the RMSE generally improved with increasing radius (Figure 6.38). With a minimal radius of 4 km, an RMSE of 1.47 mGal was obtained. This result was better than expected since there still remained comparatively tight corners in the statistics. This result may serve as a precision indicator for the results of the campaign except for very tight corners. It should be noted that the number of remaining crossovers (12) is relatively low. Due to the lack of crossovers, no reliable precision indicator could be computed for a larger minimal radius of curvature. However, the results suggest that strapdown gravimetry is capable of gravity estimation during moderate turns and in drape mode with adequate precision. Furthermore, the results of BRE2021 and CL2021 indicate that the observation system of the iNAV-RQH with iTempStab and the Polar 5 aircraft might be especially well suited for high precision airborne gravimetry.

If a longer filter length of 140 instead of 100 s was used, the precision degraded from 1.47 to 1.81 mGal (Table 6.8). Due to a high thermal variability, the RMSE was slightly degraded to 1.56 mGal without applying the warm-up calibration. Without magnetic calibration, a similar minor degradation to 1.60 mGal was observed.

7 Shipborne experiments

Since 2017, the iNAV-RQH of TU Darmstadt has been used in several shipborne gravimetry campaigns, that will be evaluated within the scope of this thesis.

- **BTS2017/BTS2018**: The IMU was installed in two dedicated shipborne gravimetry campaigns in German and adjacent territory at the Baltic Sea using a dedicated survey vessel (Section 7.1).
- **NTS2021/NTS2022**: Having surveyed the German Baltic Sea, follow-up campaigns in the North Sea were initiated to cover the complete German sea territory (Section 7.2).
- **MRZ2019**: A dedicated test campaign was conducted at Lake Müritz, Germany. The result repeatability was evaluated by crossing the lake for many times at the same lines (Section 7.3).

The campaign statistics are summarised in Table 7.1. In the following sections, the campaigns will be analysed analogous to the airborne campaigns in Section 6. The main results concerning the magnetic field correction will be summarised in Section 8.3. Due to the long low-pass filter length of 400 s, the kinematic acceleration did not influence the precision significantly. Hence, $\ddot{\boldsymbol{r}}$ was omitted in Equation (5.7) for the shipborne campaigns.

7.1 BTS2017/2018: Baltic Sea 2017/2018[1]

7.1.1 Campaign details

In the summers of 2017 and 2018, the German Federal Agency for Cartography and Geodesy (BKG) performed two shipborne gravimetry campaigns in cooperation with GFZ and TU Darmstadt at German and neighbouring areas of the Baltic Sea. The purpose was to improve the German quasi-geoid. The campaigns were also part of the European FAMOS (Finalizing Surveys for the Baltic Motorways of the Seas) project aiming to establish a common geodetic datum for the Baltic Sea and hereby improving the shipping safety in the predominantly shallow waters (Förste et al., 2020; Schwabe et al., 2020).

In both campaigns, the survey, wreck-search and research vessel Deneb (Figure 7.1) provided by the German Federal Maritime and Hydrographic Agency (BSH) was used. With a length of about 50 m, it allowed for stable and safe measurement cruises at the open sea. Geodetic GNSS antennas were installed at the deck and the mast of the vessel. GNSS measurements were collected by the BKG and the GFZ at a sample frequency of 1 Hz. The iNAV-RQH was installed side-by-side with a Chekan-AM (see Section 2.3.1) gravimeter owned by GFZ. With a mean cruise velocity of 4.7 $\frac{\mathrm{m}}{\mathrm{s}}$, the spatial resolution (half-wavelength) was about 1.0 km.

With cruise durations of up to 60 h, the campaigns were particularly challenging for strapdown gravimetry since the influence of non-linear drifts increases with observing time. The terrestrial base readings were performed by the BKG. The RMS-g was about 50 $\frac{\mathrm{mm}}{\mathrm{s}^2}$ which is very low compared to the airborne campaigns.

[1] This section is partially based on Johann et al. (2020) and Johann et al. (2021). The statistics may slightly deviate due to minor changes in the algorithm and processing settings.

Table 7.1: Shipborne campaign properties and precision (campaign statistics of BTS2017, BTS2018 and MRZ2019 partially based on Johann et al. (2020) and Johann et al. (2021))

Campaign	BTS2017	BTS2018	NTS2021	NTS2022	MRZ2019
Vessel	Deneb	Deneb	Deneb	Wega	Klink
Thermal stabilisation?	✗	✓	✓	✓	✓
GNSS frequency [Hz]	1	1	5	5	5
Number of cruises	4	4	6	4	2
Total line distance [km]	1487	2534	2337	2194	207
Mean line velocity [$\frac{m}{s}$]	4.7	4.8	5.0	4.5	3.6
RMS-g [$\frac{mm}{s^2}$]					
mean	65	48	316	276	49
standard deviation	82	63	234	169	19
Filter length (-6 dB) [s]	400	400	400	400	400
Variability $\dot{\delta g}_D$ [$\frac{mGal}{km}$]	0.5	0.8	0.6	2.1	0.8
Resolution $R_{\lambda/2}$ [km]	0.9	1.0	1.0	0.9	0.7
IGRF magnetic field					
total intensity B [µT]	49.9	50.0	49.9	49.9	49.8
horizontal int. B_H [µT]	17.6	17.6	17.7	17.4	18.2
corr. fact. $c_1 B_H$ [mGal]	1.50	1.50	1.50	1.48	1.54
declination δ [°]	3.7	4.3	2.8	2.1	4.1
inclination [°]	69.4	69.4	69.3	69.5	68.6
Crossover analysis					
n_{CO} non-adjusted	33	70	48	20	67
n_{CO} cruise-adjusted	18	41	39	-	-
n_{CO} line-adjusted	-	-	32	-	65
RMSE non-adj. [mGal]	**1.27**	**0.82**	**1.19**	**1.60**	**0.27**
RMSE cruise-adj. [mGal]	1.08	0.57	0.88	-	-
RMSE line-adj. [mGal]	-	-	0.17	-	0.11
Repeated lines analysis					
number of pairs	-	-	-	-	24
Common distance [km]	-	-	-	-	122
RMSE [mGal]	-	-	-	-	0.41
RMSE zero-mean [mGal]	-	-	-	-	0.15



Figure 7.1: Survey, wreck-search and research vessel Deneb at Bremerhaven used for BTS2017, BTS2018 and NTS2021

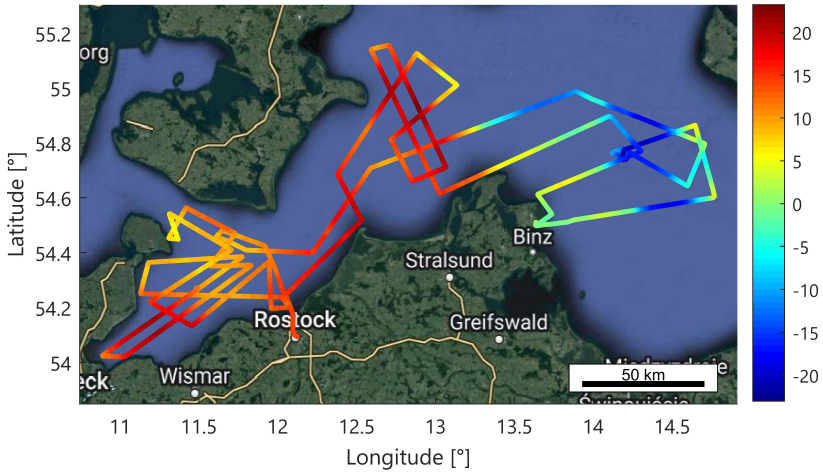


Figure 7.2: Non-adjusted gravity disturbance [mGal] BTS2017 (map data: Google, Landsat/Copernicus)

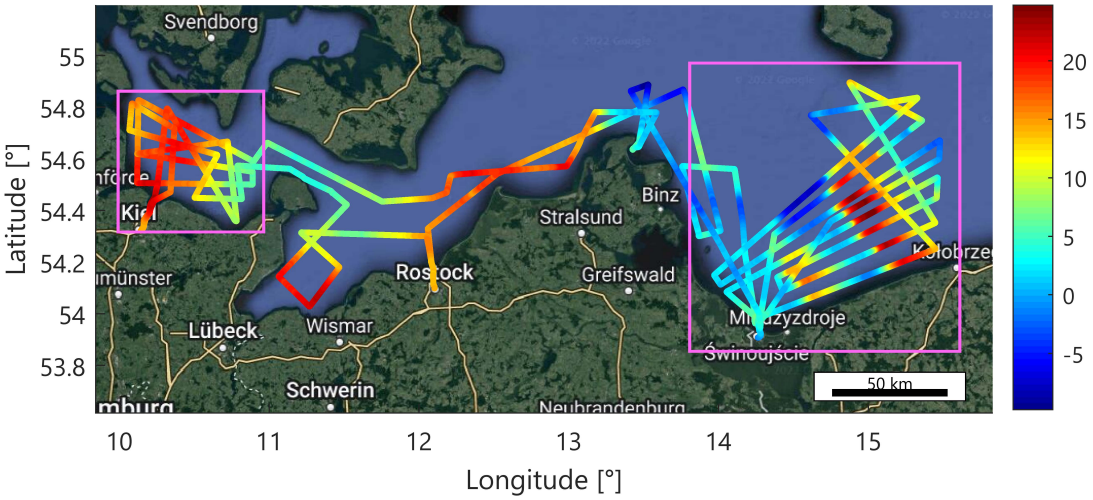


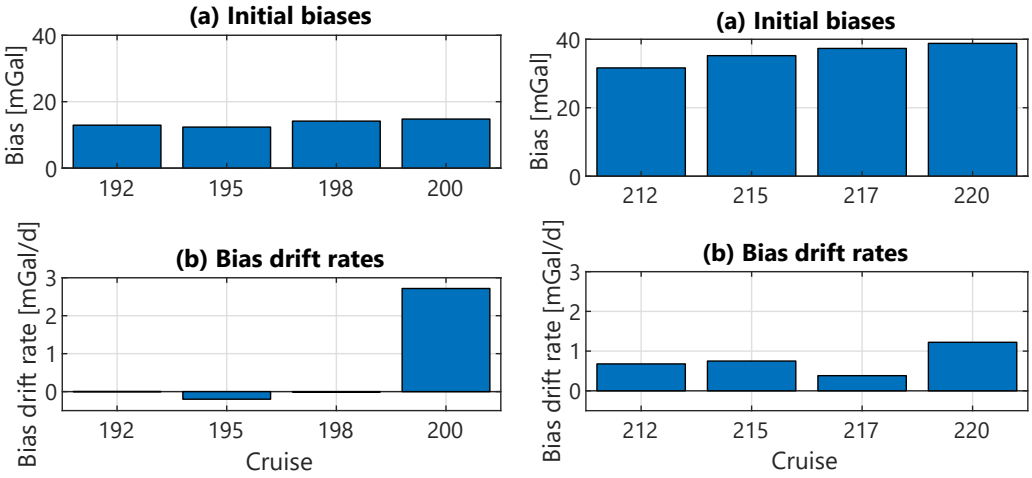
Figure 7.3: Non-adjusted gravity disturbance [mGal] BTS2018 (magenta: adjustable subnets shown in Figure 7.7; map data: Google, Landsat/Copernicus)

In 2017, the cruises were conducted from harbours at Rostock and Sassnitz and focused on the Bay of Mecklenburg which is located between the German island Rügen and the Danish islands Bornholm and Møn (Figure 7.2). The total line length of the four cruises was approximately 1,500 km.

The key areas of the 2018 campaign were the Bay of Kiel in the western North Sea and the Bay of Pomerania including Polish territory (Figure 7.3). Base readings were performed at harbours at Rostock, Kiel and Świnoujście, Poland. Four cruises with a total line length of 2,500 km were conducted. At this campaign, the iTempStab was used for dynamic gravimetry for the first time.

7.1.2 Main results

At the stable measurement conditions of the Baltic Sea campaigns, the linear drift was lower than 1 $\frac{\text{mGal}}{\text{d}}$ for all but two cruises (Figure 7.4), without and with iTempStab. At the 2017 campaign, 33 crossover points were detected with a corresponding RMSE of 1.27 mGal (Table 7.2). After estimation of a cruise-wise bias, the RMSE slightly improved to 1.08 mGal. The largest crossover residuals were observed for cruise 192. If this



(a) BTS2017 (b) BTS2018

Figure 7.4: Vertical biases at the base readings before the cruises of the Baltic Sea campaigns and linear drifts between the base readings

Table 7.2: Baltic Sea 2017/2018 precision

Campaign	2017	2017	2017	2018	2018	2018	2018	2017/18	2017/18
Cruises included (n.: not)	all	n. 192	all	all	all	west	east	all	all
Maximal RMS-g [$\frac{\text{mm}}{\text{s}^2}$]	∞	∞	100	∞	100	∞	∞	∞	100
n_{CO} non-adjusted	33	21	29	70	58	33	26	146	119
n_{CO} cruise-adjusted	18	-	-	41	32	-	-	100	79
n_{CO} line-adjusted	-	-	-	-	-	27	22	-	-
CO RMSE non-adj. [mGal]	**1.27**	0.95	1.15	**0.82**	0.61	0.60	0.69	**1.10**	0.92
CO RMSE cruise-adj. [mGal]	1.08	-	-	0.57	0.42	-	-	0.77	0.67
CO RMSE line-adj. [mGal]	-	-	-	-	-	0.32	0.32	-	-

cruise was removed, the RMSE of the remaining 21 crossover points improved to 0.95 mGal. Figure 7.5 shows that the RMS-g at the end of cruise 192 was especially high. This might indicate rough sea conditions impaired the result precision. If line segments with an RMS-g greater than 100 $\frac{\text{mm}}{\text{s}^2}$ were omitted, four crossover points were rejected and the RMSE slightly improved to 1.15 mGal.

At BTS2018, the newly developed iTempStab did not work properly. The mean sensor temperature was stable, but the control loop overshoot resulting in oscillating IMU temperatures and unnecessarily high energy consumption. As a consequence, an oscillating behaviour could be observed in the gravity disturbance results (Figure 7.6). The empirically corrected vertical gravity disturbance

$$\delta g^n_{z,\text{cor}}(t) = \delta g^n_z(t) + c_{\text{osc}} \cdot \Delta T_2(t - \Delta t_{\text{osc}}), \tag{7.1}$$

could resolve this issue, where δg^n_z is the uncorrected vertical gravity disturbance, ΔT_2 is temperature difference of IMU sensor 2 (see Section 2.3.2) to its mean temperature depending on the epoch t, c_{osc} is an amplification factor and Δt_{osc} is the time delay between temperature and gravity disturbance response. The latter two parameters were obtained in a frequency analysis as $c_{\text{osc}} \approx 2.3\ \frac{\text{mGal}}{\text{K}}, t_{\text{osc}} \approx 0$. The parameters might be dependent on the measurement conditions. Having applied this correction, the oscillation was removed (see Figure 7.6).

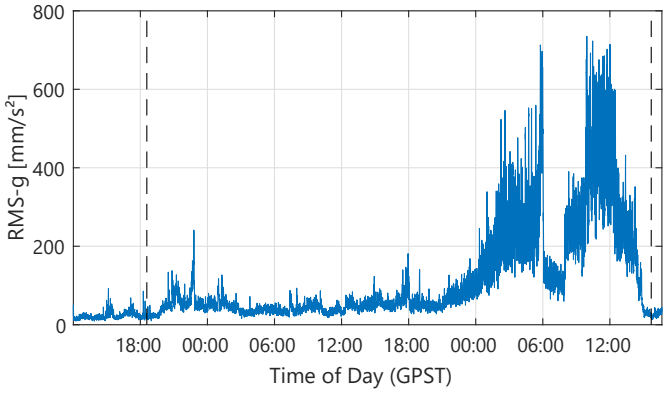


Figure 7.5: Sea conditions during the cruise 192 of BTS2017 (dashed lines: end/beginning of base reading periods at harbour)

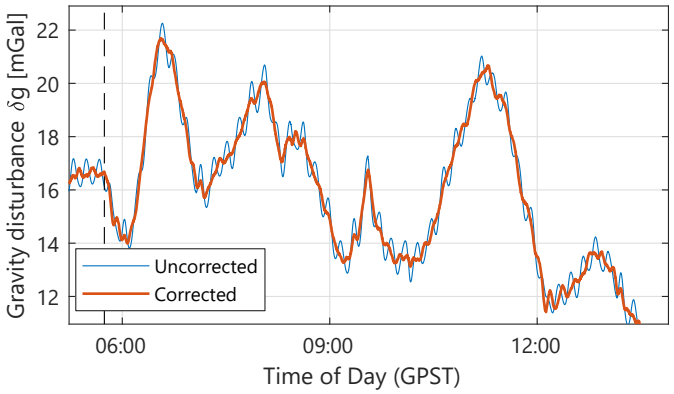


Figure 7.6: Gravity disturbance at the beginning of cruise 220 of BTS2018 before and after thermal oscillation correction

With the oscillation correction, the RMSE using all 70 crossover points became 0.82 mGal (see Table 7.2). When the RMS-g was limited, the precision improved to 0.61 mGal for the remaining 58 crossovers. After a flight-wise adjustment, the RMSE improved by about 0.2 mGal. A line-wise adjustment was not possible for the complete BTS2018 data set. When lines with less than two crossover points were removed, the network decomposed into two subnets (see Figure 7.3). Hence, the western and eastern subnets were regarded separately for the line-wise adjustment (Figure 7.7). The results for both subnets were similar. Before adjustment, the single precision was between 0.60 and 0.69 mGal calculated with about 30 crossovers each. After line-wise adjustment, 22 to 27 crossover points remained; the precision became 0.32 mGal.

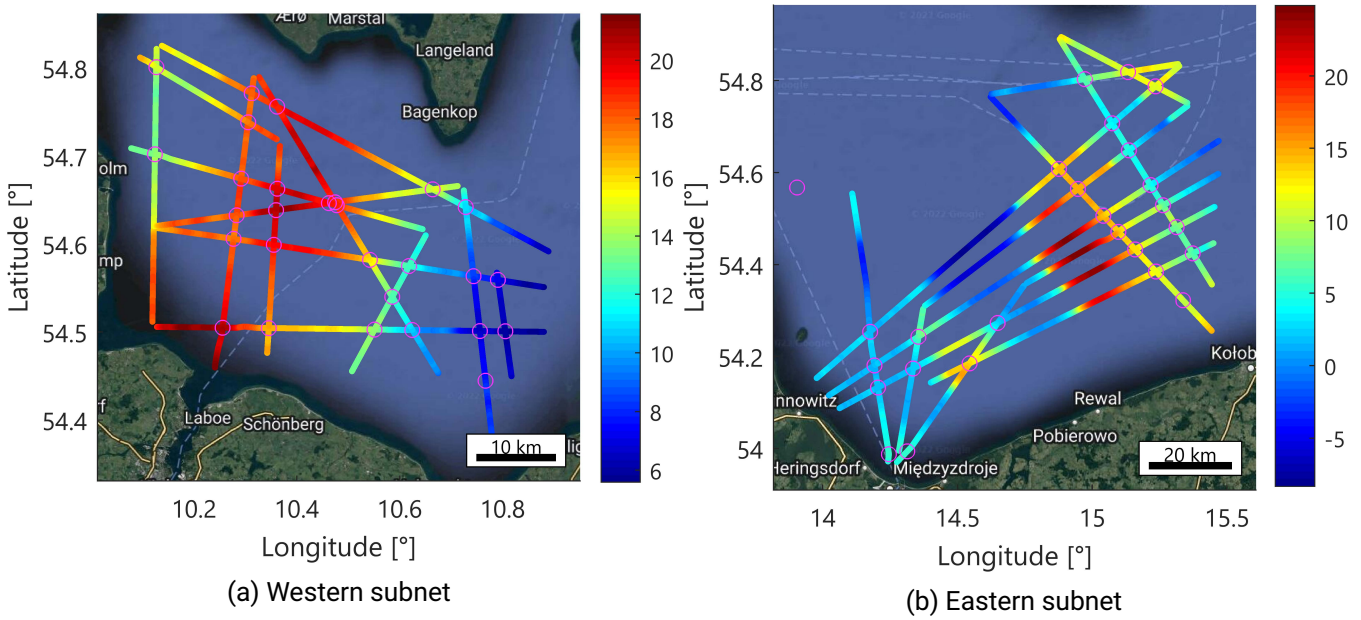
Similar to the Odenwald campaigns, both Baltic Sea campaign results can be combined since they have many intersecting lines. The gravity disturbance map in Figure 7.8 shows the high consistency of both data sets. Based on all 146 crossover points, the combined precision was 1.10 mGal being an intermediate value between both single campaigns (see Table 7.2). Figure 7.9 illustrates that remaining biases of the single cruises were at the sub-mGal level. They were removed in a cruise-wise crossover adjustment obtaining an improved RMSE of 0.77 mGal. If the RMS-g was limited, the precision became 0.92 mGal before and 0.67 mGal after crossover adjustment.

Regarding the line biases in Figure 3.14, the magnetic correction was suggested valid for the BTS2018 campaign. Regarding all crossover residuals of both Baltic Sea campaigns, a high correlation between the calibration function and the residuals can be observed as well (Figure 7.10). Note that the residuals are subject to the magnetic influence of both lines which is not considered in the latter figure.

7.2 NTS2021/2022: North Sea 2021/2022

7.2.1 Campaign details

In the summer of 2021, the same cooperation partners like at the Baltic Sea campaigns (see Section 7.1.1) conducted a similar campaign at the North Sea starting to densify available gravity observations at the German Bight. Like at BTS2018, the iNAV-RQH with iTempStab and the Chekan-AM were mounted at the Deneb. In addition, an iMAR iTAHS fluxgate 3-D magnetometer was fixed to the iTempStab handle (Figure 7.11) in order to monitor possible deterioration of the Earth's magnetic field close to the iNAV-RQH. According to the manufacturer, the raw measurement noise is 1.2 $\frac{\mathrm{nT}}{\sqrt{\mathrm{Hz}}}$ (IMAR Navigation, 2016). This is slightly better than the corresponding value of 20 $\frac{\mathrm{nT}}{\sqrt{\mathrm{Hz}}}$ that is given for the MTi used in the MY2022 campaign. However, both



(a) Western subnet

(b) Eastern subnet

Figure 7.7: Line-wise adjusted gravity disturbance [mGal] of BT2018 with crossover points (map data: Google, Landsat/Copernicus)

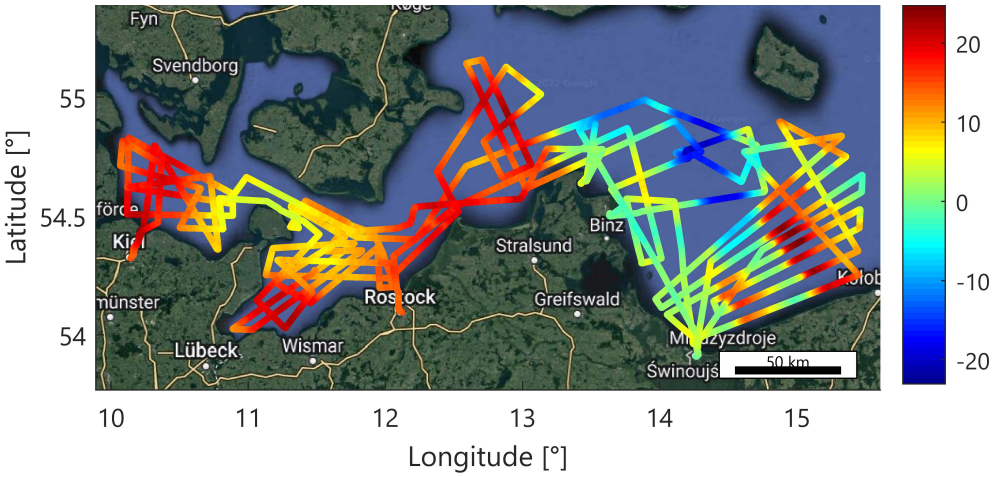


Figure 7.8: Non-adjusted gravity disturbance [mGal] of BTS2017 and BTS2018 (map data: Google, Landsat/Copernicus)

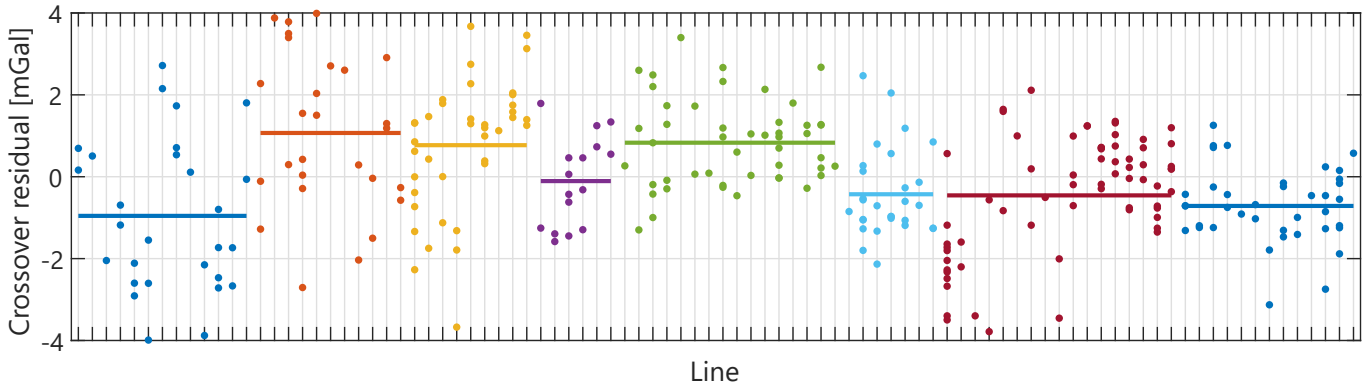


Figure 7.9: Non-adjusted crossover residuals sorted by cruises (indicated by the colour) and lines of BTS2017 and BTS2018 (horizontal bars: mean values of the cruises). The four cruises on the left side belong to BTS2017, the remaining data belongs to BTS2017

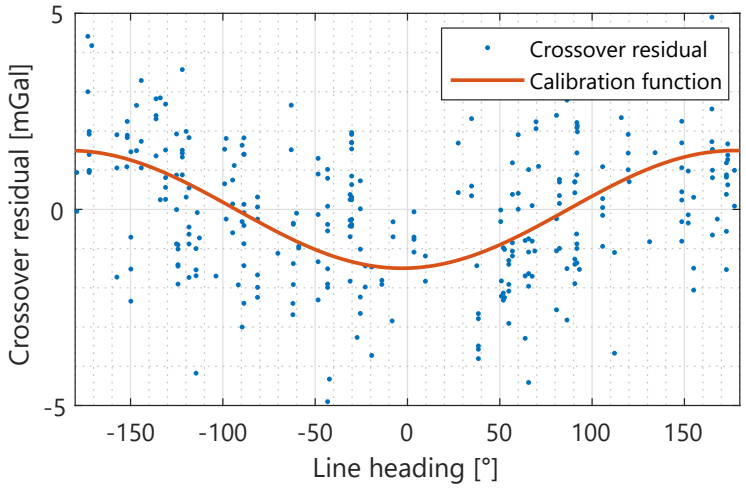


Figure 7.10: Crossover residuals of BTS2017 and BTS2018 with the magnetic calibration function of Equation (3.8)

magnetometers are expected sufficient for the purpose of the magnetic calibration of the iNAV-RQH vertical accelerometer.

In the summer of 2022, a subsequent campaign was conducted with the vessel Wega (Figure 7.12) by the BSH which is of the same design as the Deneb. In addition to the iNAV-RQH and the Chekan-AM, an iMAR iCORUS strapdown gravimeter loaned by the GFZ was installed the same cabin of the vessel. No magnetometer was used. The UPS for the iNAV-RQH with iTempStab which was originally developed for the usage in the Polar 5 aircraft (see Figure 6.28) was used in a shipborne campaign for the first time.

In both North Sea campaigns, the equipment was installed and de-installed at Bremerhaven. Six and four cruises were conducted with in-between mooring times at the island of Heligoland, respectively. The cruise durations were extremely challenging for strapdown gravimetry with a maximum of about 50 h for cruise 185 in 2021. In 2022, two of the four cruises took more than 50 h with a maximum of more than 78 h for cruise 180. Both transits from and to Bremerhaven took less than 10 h. Long cruises were required due to the lack of islands and corresponding harbours in the north-western area of the German sea territory. The total line lengths were approximately 2,300 and 2,200 km, respectively. The trajectories of NTS2021 and

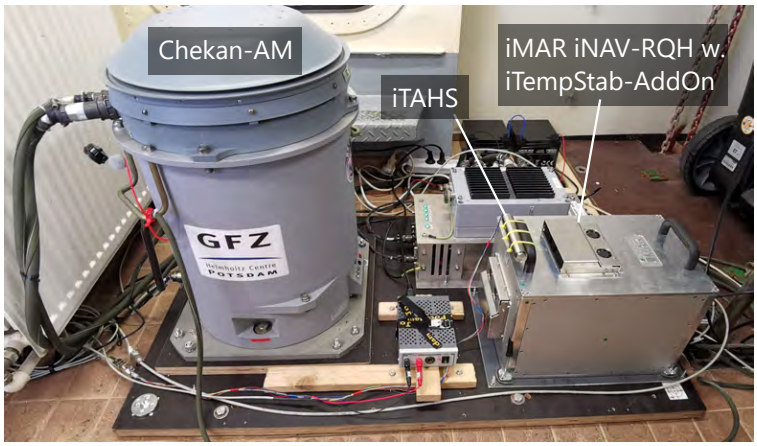


Figure 7.11: Installed gravimeters at NTS2021



Figure 7.12: Survey, wreck-search and research vessel Wega at Bremerhaven used for NTS2022

NTS2022 are shown in Figures 7.13a and 7.13b, respectively. Velocity and spatial resolution were similar for all Baltic and North Sea campaigns (see Table 7.1).

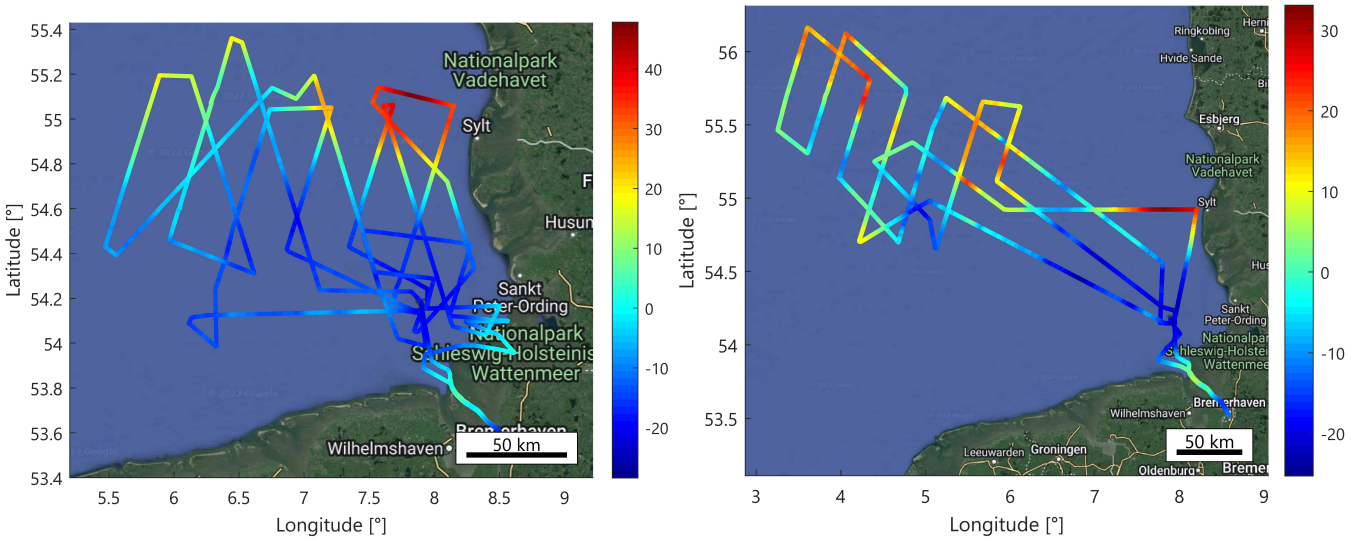
According to the RMS-g, the sea conditions at the North Sea were much harsher (295 $\frac{\text{mm}}{\text{s}^2}$) than at the Baltic Sea campaigns (55 $\frac{\text{mm}}{\text{s}^2}$). While the gravity field variation was low for the shipborne campaigns between 2017 and 2021 being between 0.5...0.8 $\frac{\text{mGal}}{\text{km}}$, it was considerably higher at NTS2022 being 2.1 $\frac{\text{mGal}}{\text{km}}$.

7.2.2 Main results

The linear gravimeter drifts of all cruises at both North Sea campaigns were lower than 3 $\frac{\text{mGal}}{\text{d}}$ with only three drifts being greater than 2 $\frac{\text{mGal}}{\text{d}}$ (Figure 7.14). In contrast to the other airborne and shipborne campaigns, the best crossover precision for both shipborne North Sea campaigns was obtained without the magnetic field correction. The reason for this is unclear. Possibly, non-linear drifts at the extraordinarily long cruises of the North Sea campaigns might cause a random RMSE degradation after applying the magnetic correction. On the one hand, another explanation might be a possible strong magnetic field deterioration in the cabins of the Deneb and the Wega. On the other hand, this seems unlikely since the Deneb was also used at the Baltic Sea campaigns, where the magnetic correction was applied successfully. A further hypothesis might be that a major change in the gravimeter behaviour with respect to the magnetic field occurred after 2020. This assumption can be excluded since the magnetic correction was applied with great success in the MY2022 campaign (see Section 6.2.2).

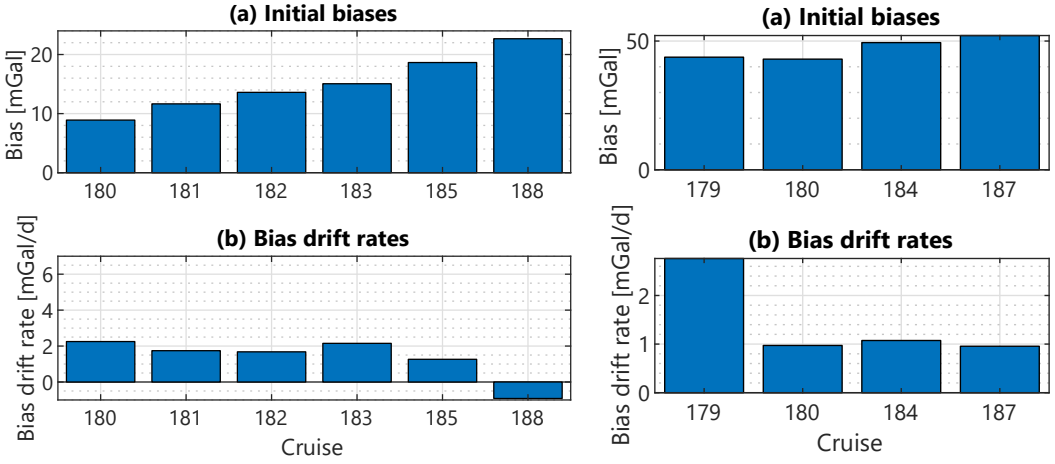
Using all 48 crossovers of the 2021 campaign, a precision of 1.19 mGal was obtained (Table 7.3). With an IGRF-based magnetic correction, the crossover precision degraded to 1.49 mGal. If the iTAHS magnetometer data was used, the precision improved to 1.28 mGal which is still slightly worse than without any magnetic correction. After cruise-wise adjustment, the precision ranking remained the same, but all indicators improved. The RMSE without correction became 0.88 mGal; 1.05 and 1.27 mGal were obtained with the magnetometer and IGRF-based corrections.

After line-wise adjustment, the RMSE without magnetic correction became 0.17 mGal with the 33 remaining crossovers. This suggests that the precision might be significantly better for shorter cruises. Remember that a too optimistic levelling precision indicator is counteracted by using correction factors according to Equation (5.15). Adjusted residuals of lines with a low number of crossovers are multiplied by a greater correction factor. When a cruise segment of about 4 h with 4 crossovers in cruise 185 was rejected as outlier, the non-adjusted precision improved to 0.84 mGal (see Table 7.3).



(a) NTS2021 (b) NTS2022

Figure 7.13: Non-adjusted gravity disturbance [mGal] of the North Sea campaigns (map data: Google, Landsat/Copernicus)



(a) NTS2021 (b) NTS2022

Figure 7.14: Vertical biases at the base readings before the cruises of the North Sea campaigns and linear drifts between the base readings (IGRF-based magnetic correction applied)

Table 7.3: North Sea 2021/2022 precision

Campaign	2021	2021	2021	2021	2022	2021/22	2021/22	2021/22
Magnetic calibration?	✗	IGRF	Magne-tometer	✗	✗	✗	✗	IGRF
Excluded segments/cruises	none	none	none	outlier segments	none	none	long cruises	none
n_{CO} non-adjusted	48	48	48	44	20	127	46	127
n_{CO} cruise-adjusted	39	39	39	35	-	110	35	110
n_{CO} line-adjusted	32	32	32	26	-	112	-	112
CO RMSE non-adj. [mGal]	**1.19**	1.49	1.28	0.84	**1.60**	2.03	0.76	**1.70**
CO RMSE cruise-adj. [mGal]	0.88	1.27	1.05	0.75	-	1.29	0.56	1.44
CO RMSE line-adj. [mGal]	0.17	-	-	0.19	-	0.80	-	0.92

The improvements when using the magnetometer data instead of the IGRF Earth field model indicates that the magnetic field close to the iNAV-RQH might be significantly deteriorated. Like in the MY2022 campaign, the magnetometer was placed in several axis directions before the start of first cruise in order to remove axis biases. No IGRF levelling of the magnetometer data was applied. Figures 7.15a-c visualise the magnetic field components according to the IGRF (dashed lines) and observed by the magnetometer (solid lines). Figure 7.15d indicates that deterioration of the cabin field depended on the vehicle yaw angle. Furthermore, electric currents close to the magnetometer might have influenced the results. Electric devices and the comparatively less stable attitude might cause the increase of noise during the cruise. Note that the magnetic field strongly depends on the exact mounting position and varies in the order of several µT if placed at the other side of the IMU. The magnetometer position was selected to be close to the ISA of the IMU (see Figure 7.11).

The number of crossover points for the NTS2022 campaign was low being 20. More crossovers or repeated lines would have ensured a more profound quality evaluation. The crossover RMSE was 1.60 mGal without magnetic correction. With an IGRF-based correction, the precision slightly degraded to 1.77 mGal.

Like for the Baltic Sea campaigns, both North Sea shipborne results were additionally evaluated in a joint analysis. The combined line network contained 127 crossover points (Figure 7.16). Figure 7.18 indicates that some cruises might be subject to systematic biases. The joint non-adjusted precision using all crossovers became 2.03 mGal without and 1.70 mGal with IGRF-based correction. In contrast to the observations at the ODW2017 (see Figure 6.16a) and the Baltic Sea campaigns, no systematic increase in the crossover residuals was observed with increasing RMS-g (Figure 7.17). However, it should be noted that almost all crossovers of the North Sea campaigns were obtained during RMS-g conditions higher than the threshold of 100 $\frac{mm}{s^2}$ which was applied at the Baltic Sea campaigns.

Figure 7.19 shows all crossover residuals of the combined North Sea results. The predominantly green colours in the south-eastern part of the map indicate that the residuals were pretty low close to Heligoland and Bremerhaven. Large residuals were mostly observed at the long cruises to the north-western part of the German Bight. If the long cruises (185 in NTS2021 and 180, 184 in NTS2022) were omitted, a hugely improved RMSE of 0.76 mGal was obtained for the remaining 46 crossovers which was better than the RMSE obtained at the Baltic Sea. Without the long cruises, the IGRF-based magnetic correction was still harmful leading to an RMSE of 1.39 mGal.

Except for the lines in the outer west, a line-wise adjustment could be performed for the combined data set. The adjusted lines are visualised in Figure 7.20. Without magnetic correction, the RMSE improved to 0.80 mGal.

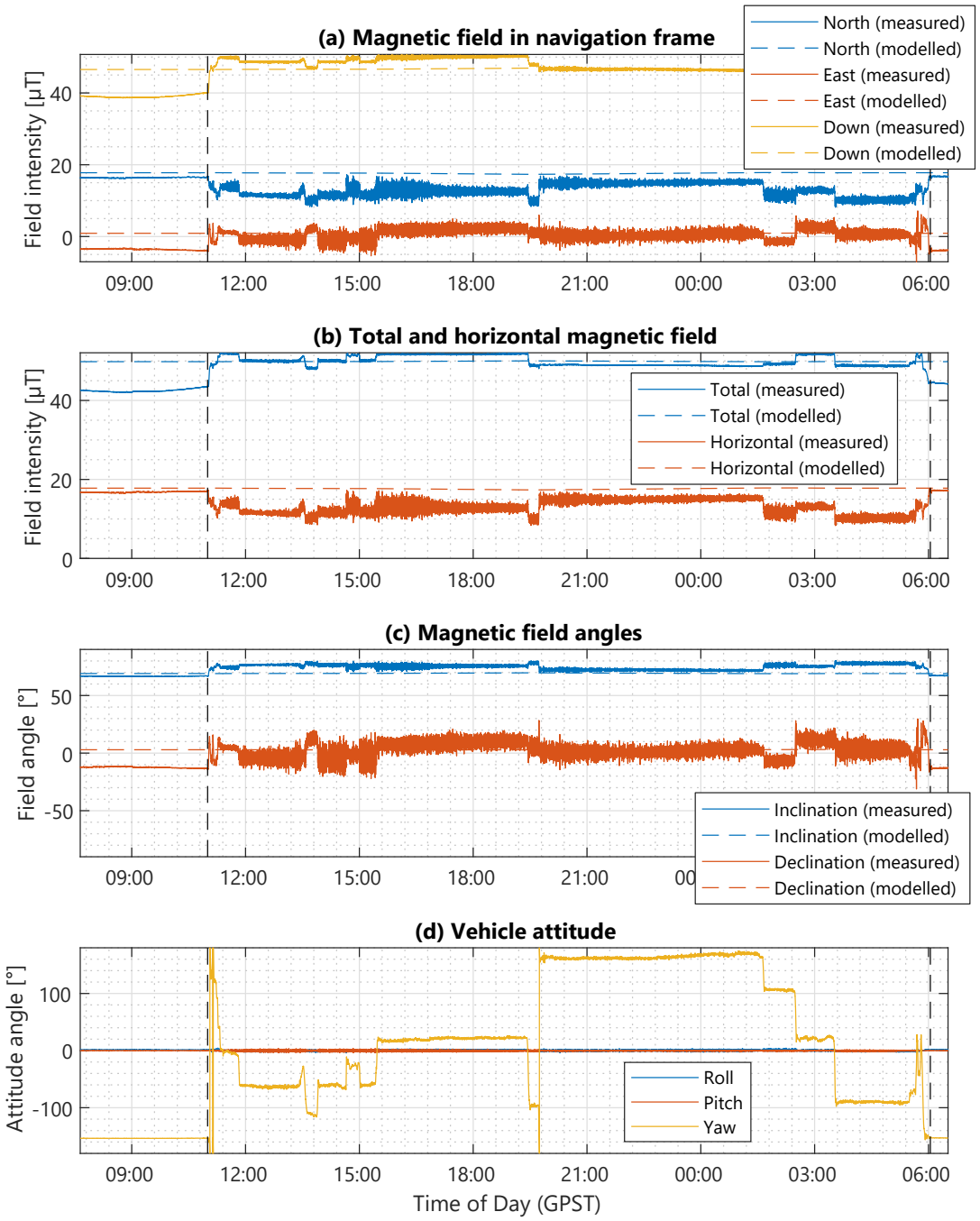


Figure 7.15: Magnetic field parameters measured with a magnetometer and modelled with IGRF13 for NTS2021 with vehicle attitude angles

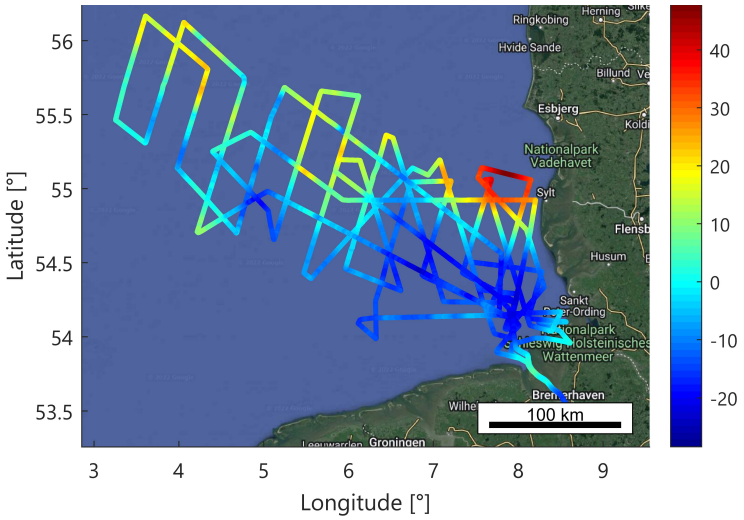


Figure 7.16: Non-adjusted gravity disturbance [mGal] of NTS2021 and NTS2022 (map data: Google, Landsat/Copernicus)

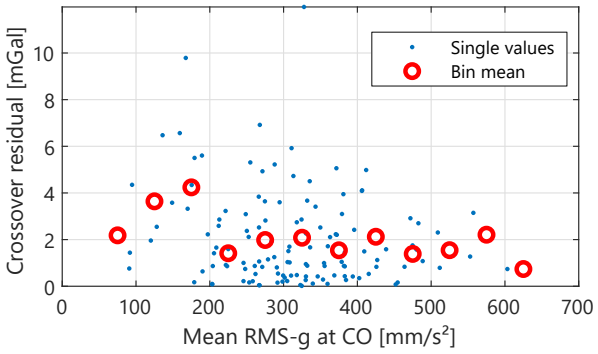


Figure 7.17: Crossover residuals and sea conditions of NTS2021 and NTS2022 (blue: single values; blue: mean values above specific intervals)

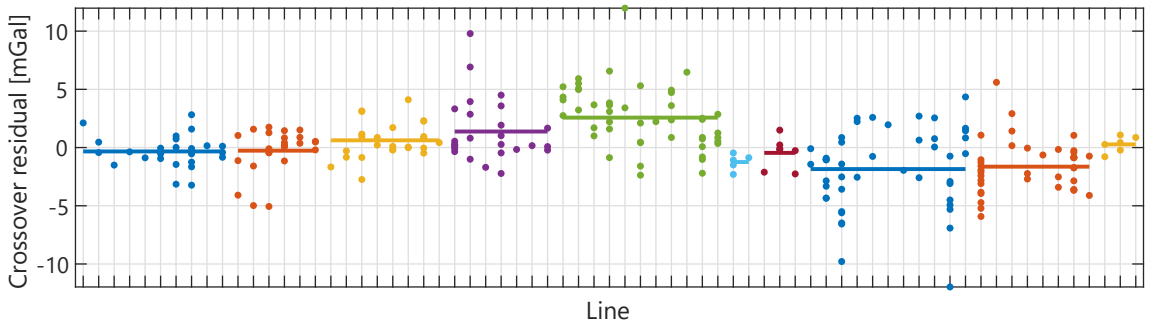


Figure 7.18: Non-adjusted crossover residuals sorted by cruises (indicated by the colour) and lines of NTS2021 and NTS2022 (horizontal bars: mean values of the cruises). The six cruises on the left side belong to NTS2021, the remaining data belongs to NTS2022

7.2.3 Influence of ocean tides

While the tidal range at the Baltic Sea is small, a tidal range of several metres is possible at the German North Sea coast. The change in gravity due to the increased distance to the geocentre at higher tides is already taken into account by considering the instantaneous ellipsoidal height when calculating the normal gravity. The attraction due to the water masses remains unconsidered so far.

Assuming a maximum tidal difference of $\Delta H = 4\,\mathrm{m}$ at the German Bight, its influence can be estimated with the gravitational constant G and the formula for the Bouguer anomaly (Torge, 1989) as

$$\delta g_{\mathrm{Pl}} = -2\pi G \rho_{\mathrm{sea}} \Delta H \approx -0.17\ \mathrm{mGal}. \tag{7.2}$$

The added water mass is approximated as a simple Bouguer plate with a water density $\rho_{\mathrm{sea}} = 1025\ \mathrm{kg/m^3}$. Thus, the effect is less than 0.2 mGal even with large tidal differences, and the tidal range also decreases with increasing distance from the German coast. Furthermore, the effect is weakened by the deformation of the elastic Earth induced by the rising water masses. The tidal effect should therefore hardly be significant for the

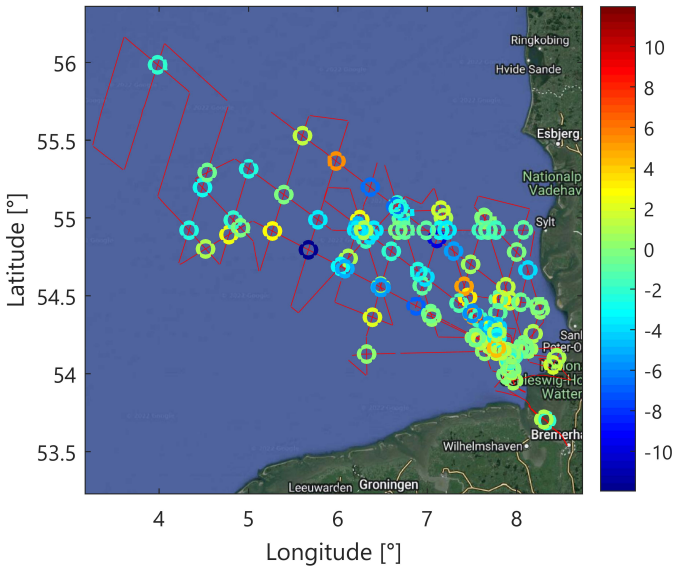


Figure 7.19: Non-adjusted crossover residuals [mGal] of NTS2021 and NTS2022 (map data: Google, Landsat/Copernicus)

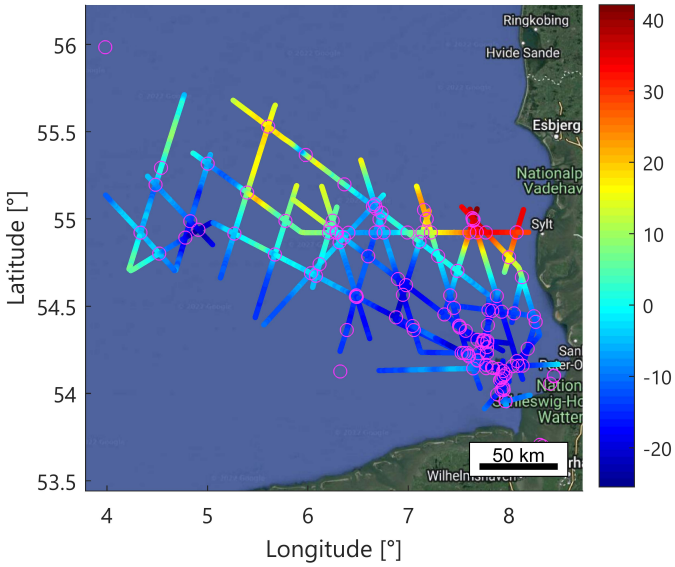


Figure 7.20: Line-wise adjusted gravity disturbance [mGal] of NTS2021 and NTS2022 with crossover points (map data: Google, Landsat/Copernicus)

presented results. However, with increased measurement accuracy in the future or at coastal areas of extreme tidal range, the effect could get more relevant.

7.3 MRZ2019: Lake Müritz 2019[1]

7.3.1 Campaign details

In November 2019, the GFZ and TU Darmstadt conducted a dedicated shipborne gravimetry test campaign at the Lake Müritz at Mecklenburg, north-east Germany. With a diameter of approximately 15 km, Lake Müritz is the second largest lake of Germany. The excursion boat Klink (Figure 7.21), owned by "Weiße Flotte Müritz" was rented to cross the lake for multiple repetitions of three lines (see Figure 7.22). Aboard of the Klink, the Chekan-AM by the GFZ and the iNAV-RQH with iTempStab were installed side-by-side.

In two cruises with a maximal duration of 9.5 h, a total line length of 207 km was covered. The mean cruise velocity of 3.6 $\frac{\mathrm{m}}{\mathrm{s}}$ was the lowest of all campaigns. With a filter length of 400 s, a half-wavelength spatial resolution of 0.7 km was obtained. The mean horizontal magnetic field was 18.2 µT according to the IGRF which is marginally higher than for the North and Baltic Sea campaigns. With 49 $\frac{\mathrm{mm}}{\mathrm{s}^2}$, the RMS-g was as low as for the Baltic Sea campaigns. The terrestrial base readings were performed by the GFZ.

7.3.2 Main results

Like in all shipborne campaigns, the linear gravimeter drift of the iNAV-RQH was lower than for the airborne campaigns ranging between -1.4 and -2.0 $\frac{\mathrm{mGal}}{\mathrm{d}}$ (Figure 7.23). Like at BTS2018, induced by a malfunction of the iTempStab, an oscillation was observed in the gravity results. Having applied the empirical correction

[1]This section is partially based on Johann et al. (2021). The statistics might slightly deviate due to minor changes in the algorithm and processing settings.



Figure 7.21: Excursion boat Klink at Waren/Müritz used for MRZ2019 (Johann et al., 2021)

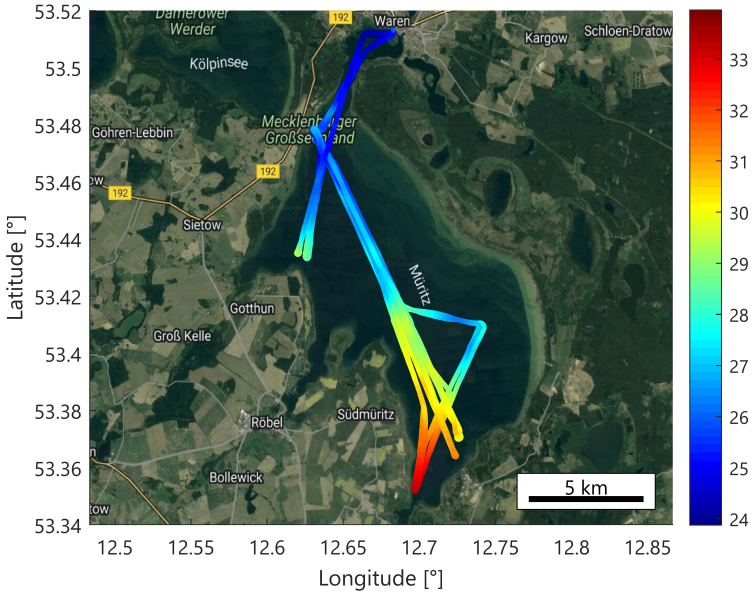


Figure 7.22: Non-adjusted gravity disturbance [mGal] MRZ2019 (map data: Google, Landsat/Copernicus)

Table 7.4: Müritz 2019 precision

Filter length (-6 dB) [s]	400	130	400
Magnetic calibration?	✓	✓	✗
n_{CO} non-adjusted	67	67	67
n_{CO} line-adjusted	65	65	65
CO RMSE non-adj. [mGal]	**0.27**	0.33	1.46
CO RMSE line-adj. [mGal]	0.11	0.21	-
RL distance [km]	122	122	122
RL RMSE [mGal]	0.41	0.55	1.67
RL RMSE ZM [mGal]	0.15	0.39	-

after Equation (7.1) with updated parameters $c_{\text{osc}} \approx 0.8\,\frac{\text{mGal}}{\text{K}}$, $t_{\text{osc}} \approx 80\,\text{s}$, the effect was successfully removed. After this campaign, the control loop of the iTempStab was adapted and the oscillation correction was no longer needed.

Due to the lack of proper navigation instruments at the Klink, the maximal horizontal line separation amounted to several hundreds of metres. To limit errors due to the gravity disturbance field variation, repeated line segments with a separation of more than 200 m were not considered in the evaluation. Note that there might still be signifiant errors due to the remaining horizontal separation. A total distance of 122 km of repeated line pairs remains. The repeated lines analysis was performed pair-wise computing a total data RMSE of 0.41 mGal afterwards as described in Section 5.5.2. Having removed the mean values of the lines before computing the RMSE which corresponds to a line-wise adjustment, the precision improved to 0.15 mGal (Table 7.4).

67 crossover points were identified. Most of them were found at repeated lines due to the poor ship navigation accuracy. With almost all residuals being lower than 1 mGal (Figure 7.25), the crossover precision became 0.27 mGal without any crossover adjustment. Figure 7.25 illustrates that the number of crossover

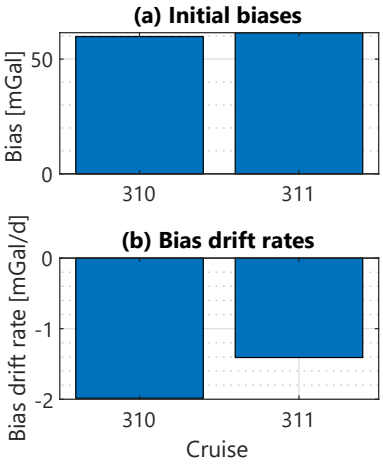


Figure 7.23: Vertical biases at the base readings before the cruises of MRZ2019 and linear drifts between the base readings

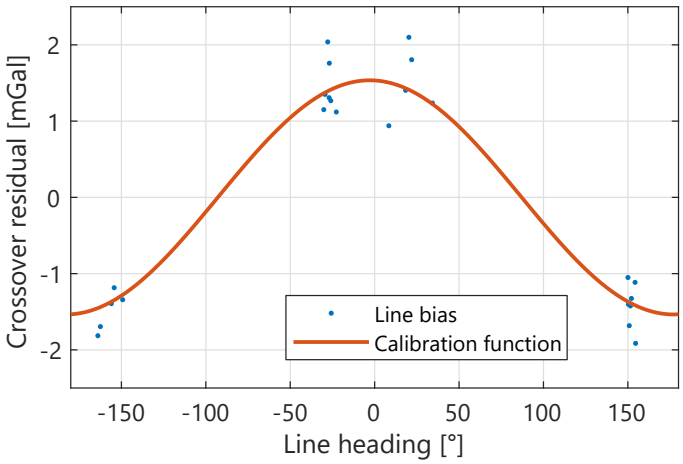


Figure 7.24: Estimated line biases of the MRZ2019 results (without magnetic calibration) plotted with the magnetic calibration function of Equation (3.8)

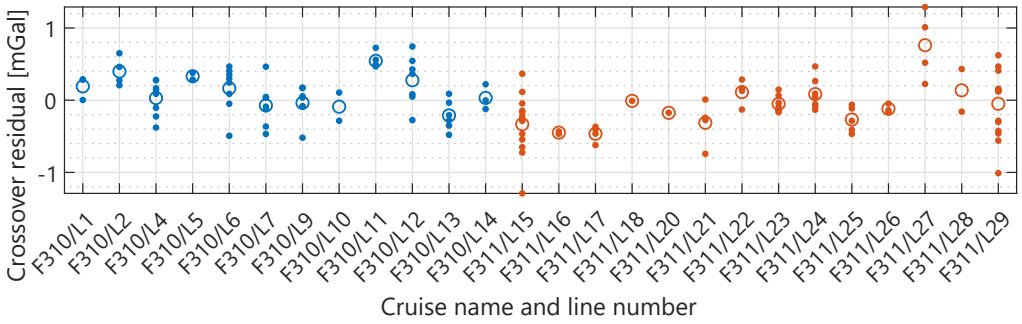


Figure 7.25: Non-adjusted crossover residuals sorted by cruises (indicated by the colour) and lines of MRZ2019 (circles: mean values of the lines)

points was sufficient for a reasonable line-wise crossover adjustment. After adjustment, all residuals were lower than 0.25 mGal and the RMSE became 0.11 mGal. Figure 7.26 visualises the estimated line biases of both cruises as a function of the time. The gravity disturbance result drift appears to be random, similar to a random walk where the linear drift was removed. Except for a line at cruise 311, no striking bias jumps are observed between consecutive lines. All absolute line biases are smaller than 1 mGal.

The high precision results of the MRZ2019 campaign are considered statistically firm due to the high consistency of the crossover and repeated lines analysis. The number of crossovers and the length of the repeated lines is considered adequate. The long filter length of 400 s which is enabled by the slow cruise velocity is not the main reason for the excellent precision indicators. If a 130 s low-pass filter was used, there were only slight degradations of the RMSE to 0.33 mGal at the crossovers and to 0.55 mGal at the repeated lines (see Table 7.4). Possible reasons for the exceptionally good precision might be the very calm sea conditions, the limited cruise time of less than 10 h and a neglectable magnetic field deterioration inside of the vessel cabin.

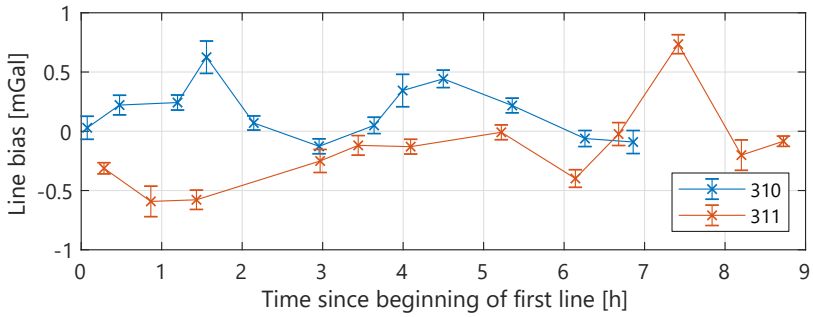


Figure 7.26: Estimated line biases of MRZ2019 with their standard deviations

If the magnetic calibration function was not applied to the results, the RMSE dramatically degraded to 1.46 mGal in the crossover and 1.67 mGal in the repeated lines analysis. The estimated line biases without correction are visualised in Figure 7.24. It can be observed that the biases were close to the calibration function. The especially large influence of the magnetic field error might be due to the fact that the line headings of the repeated lines were close to the maxima of the calibration function. Furthermore, the residuals for any heading are maximal when the heading angles are opposite at the adjacent lines. This was the case for a great proportion of the residuals in this campaign since they were located at opposing repeated lines.

8 Dynamic experiments result summary

8.1 Error sources of dynamic gravimetry

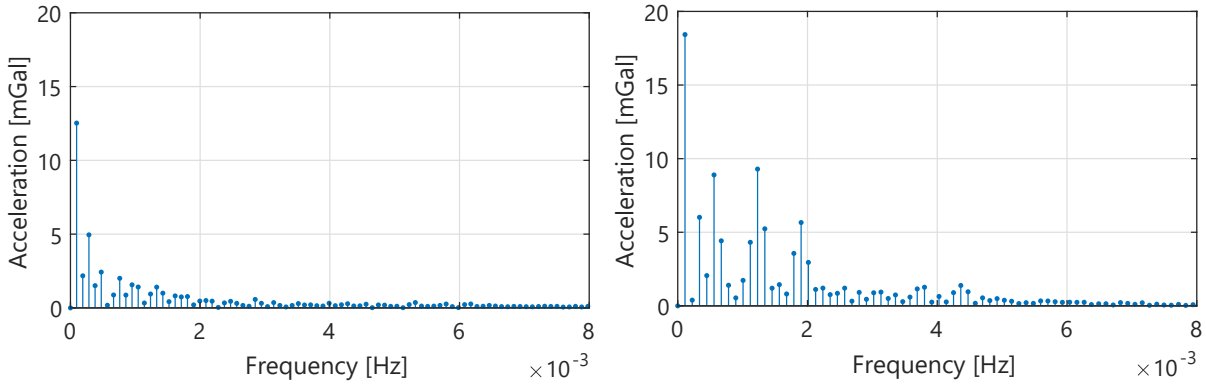
The accuracy of dynamic gravimetry is influenced by many parameters depending on the campaign location and time, the vehicle and gravimeter types and the processing algorithm. Some of them are

- instrumental effects like accelerometer, gyroscope and GNSS observation accuracy,
- the thermal and magnetic calibration or insulation quality,
- local effects like the gravity field variability and weather,
- vehicle dependent effects like the susceptibility to turbulence or sea state, the stiffness, i.e. the constancy of the lever arm (see Becker (2016)), the magnetic field distortion due to ferromagnetic material and electric devices,
- local surveying errors concerning the terrestrial reference gravity and the lever arm between gravimeter and GNSS antenna,
- processing noise due to the processing method, the exact implementation including simplifications, settings, interpolation, quantisation and
- inaccurate external reference data and up-/downward continuation errors affecting the quality assessment.

This work focuses on magnetic field induced errors, the kinematic acceleration determination approach and the analysis of the observation conditions based on the data of multiple dynamic campaigns. After the evaluation of the single airborne and shipborne campaigns in Sections 6 and 7, respectively, the main findings on the mentioned parameters will be briefly summarised in the following sections. First, the influence of the measurement conditions given by the mean gravity field variability and the mean turbulence level on the result precision will be analysed in Section 8.2. Section 8.3 summarises the effectiveness of the magnetic correction. Section 8.4 evaluates the influence of the kinematic determination method and gives recommendations for the method selection depending on campaign conditions, required observations, available data and processing delay. The ODW2018 campaign will be excluded from the evaluation since its extraordinarily bad precision is assumed being mainly due to thermal effects (see Section 6.3).

8.2 Influence of measurement conditions

The comparatively high number of airborne and shipborne campaigns discussed in Sections 6 and 7, respectively, enable the analysis of possible correlations between the campaign-specific measurement conditions and the obtained precision indicators. However, it should be noted that the following evaluation can only indicate tendencies since the campaign accuracy depends on multiple parameters (see Section 8.1). Two main



(a) DK2020, flight 261a (b) ODW2017, flight 137a

Figure 8.1: Amplitude spectrum of gravity disturbance results

Table 8.1: Correlation coefficient [%] between mean measurement condition indicators and the non-adjusted crossover precision

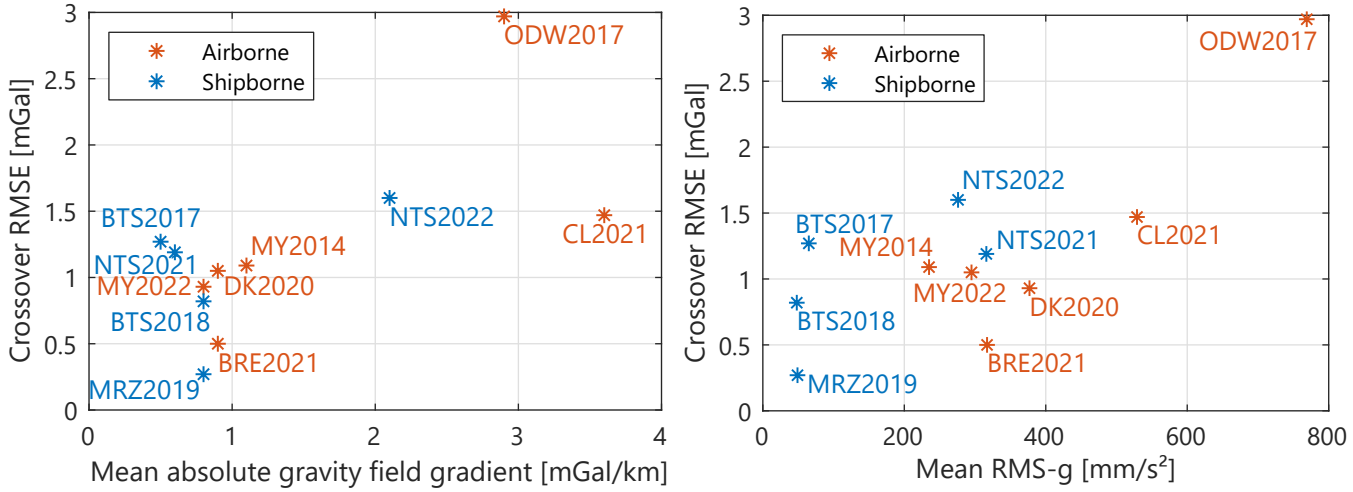
Campaign type	Gradient $\dot{\delta g}_D$	Turbulence RMS-g
Airborne	68.9	90.5
Shipborne	48.3	65.0

parameters of the measurement conditions will be regarded: the static local gravity field variability and the undesired vehicle movement due to turbulence or sea state.

The variability of the gravity disturbance field is evaluated by regarding the mean field variability of a campaign as defined in Section 5.5. In the campaigns introduced before, the mean field variability ranged between 0.8 and 3.6 $\frac{\text{mGal}}{\text{km}}$ for the airborne and between 0.5 and 2.1 $\frac{\text{mGal}}{\text{km}}$ for the shipborne campaigns (see Tables 6.1 and 7.1). For most campaigns, the mean field variability was low ranging between 0.6 and 1.1 $\frac{\text{mGal}}{\text{km}}$. High variability was observed for the NTS2022, ODW2017 and CL2021 campaigns ranging between 2.1 and 3.6 $\frac{\text{mGal}}{\text{km}}$. Examples for low and high variability conditions are DK2020 with 0.8 $\frac{\text{mGal}}{\text{km}}$ and ODW2017 with 2.9 $\frac{\text{mGal}}{\text{km}}$. The amplitude spectra of the zero-mean gravity disturbance results of two flights are visualised in Figure 8.1. The energy for the ODW2017 signal was higher at all frequencies relevant for airborne gravimetry.

In Figure 8.2a, the non-adjusted crossover precision of the campaigns are plotted above the mean field variability. A tendency is observed that the RMSE increases with increasing variability. For the airborne campaigns, a correlation coefficient of 69 % was computed for the RMSE and the mean field variability. Due to the limited spatial resolution, short signal wavelengths cannot be detected properly by airborne gravimetry. It should be noted again that the precision is affected by all error influences mentioned in Section 8.1. Furthermore, the correlation coefficient is strongly dependent on the high variability campaigns ODW2017 and CL2021. The CL2021 precision might be influenced by (remaining long radius) corner flight. The only high variability shipborne campaign NTS2022 has the highest RMSE but the correlation coefficient for the shipborne campaigns is as low as 48 % (Table 8.1) since the other campaigns have varying RMSE at similar field variability. For the shipborne campaigns, a lower correlation coefficient was expected due to the lower vehicle velocity and the corresponding higher spatial resolution of the results. More campaigns with high field variability would be required to allow for statistically firm statements on a possible correlation.

A possible relationship between the turbulence level approximated by the mean RMS-g and the crossover precision is visualised in Figure 8.2b. The correlation coefficients for airborne and shipborne campaigns are 91 and 65 %, respectively (see Table 8.1), meaning they are higher than for the field variability. The



(a) Mean gravity field variability

(b) Turbulence / sea state indicator

Figure 8.2: Possible correlations between observation conditions and the non-adjusted crossover precision

lower coefficient for the shipborne campaigns may be explained through the greater filter length. The high coefficient of the airborne data is strongly dependent on the ODW2017 result. However, the results indicate that vertical motions in the vehicle might degrade the gravity disturbance results. Shipborne gravimetry seems to be less dependent on the measurement conditions, i.e. the undesired vehicle movement and the field variability, than airborne gravimetry.

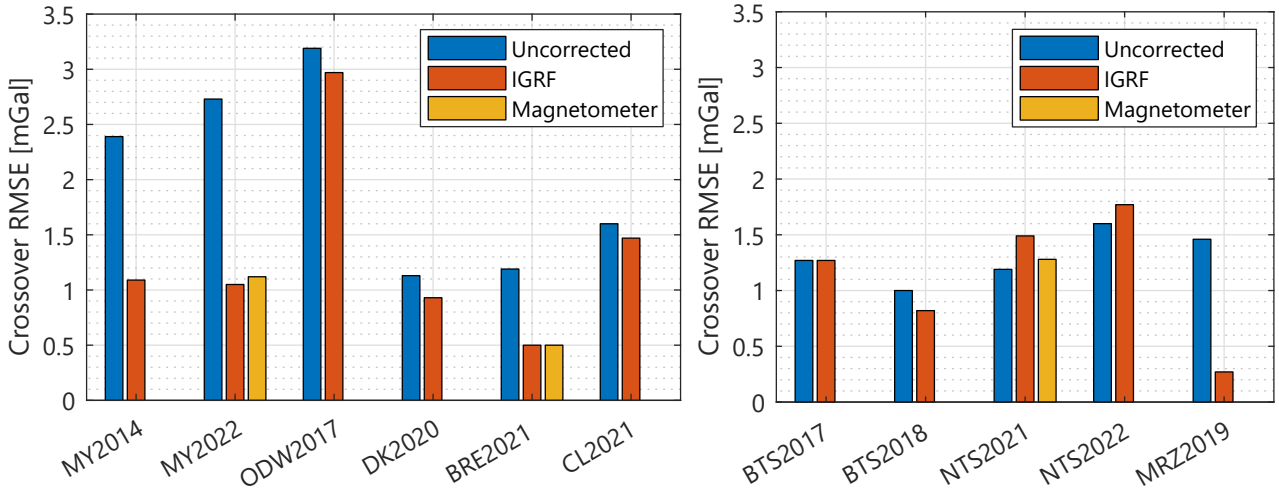
8.3 Magnetic calibration

All dynamic campaigns have been processed with and without the magnetic correction based on the magnetic field calibration for the vertical accelerometer of the iNAV-RQH. The non-adjusted crossover RMSE are visualised in Figure 8.3.

In all airborne campaigns, the RMSE improved after the magnetic correction (Figure 8.3a). The strongest improvement was observed for the Malaysia campaigns, where the RMSE decreased by a factor of 2.5. At Malaysia, the horizontal magnetic field was more than twice as intense as in the other campaigns. At BRE2021, the improvement was similar, probably due to the north-south orientation of the sensor at eight of the ten crossover points. The sensor was installed perpendicular to the aircraft front. The improvement for the ODW2017 campaign was low. The magnetic error might be small in comparison to errors induced by turbulence and GNSS antenna vibration.

The largest improvement by a factor of 4.8 was observed for the MRZ2019 shipborne campaign. The influence was presumably maximised by a large number of crossover points at almost opposite adjacent lines in combination with the orientation of all lines being close to north-south direction. However, at the shipborne campaigns conducted at the North and Baltic Sea, a significant improvement with the magnetic correction was only obtained at BTS2018. Possible explanations might be non-linear drifts at the extraordinary long cruises, especially for NTS2021 and NTS2022, and, rather likely, significant distortion of the magnetic field in the large research vessels Deneb and Wega. The latter effect might be worse than in the comparatively small aircraft and the trip boat Klink built with less ferromagnetic material.

For the magnetic correction, the magnetic field components were considered to accord to the IGRF-13. At the BRE2021 campaign, a magnetometer was installed at the aircraft exterior. Using the observations



(a) Airborne campaigns

(b) Shipborne campaigns

Figure 8.3: Influence of the magnetic field calibration correction based on IGRF-based or magnetometer data (campaigns with available magnetometer data: MY2022, NTS2021 (both close to IMU), BRE2021 (vehicle tail))

of the exterior field, the gravity disturbance precision did not change significantly. At the MY2022 and NTS2021 campaigns, magnetometers have been mounted close to the strapdown IMU. While only minor precision changes were obtained at the MY2022 campaign, the precision at NTS2021 improved by 0.2 mGal in comparison to the IGRF-based correction. Though, the precision at this campaign was still better without any magnetic correction.

The installation of magnetometers in the aircraft cabin appears more auspicious than the exterior installation. Improvements in the calibration of the magnetometer and the evaluation of the field deformation at several points around the IMU might improve the effectiveness of the magnetic correction. However, the IGRF-based magnetic correction appears to remove the bulk of the magnetic field induced error for aircraft and medium-size vessels.

Except for large research vessels, the magnetic corrections resulted in major improvements of the results obtained with the iNAV-RQH.

8.4 Selection criteria for the kinematic acceleration approach

The PosDif kinematic acceleration determination method was used in all campaigns; the PhaseDif method was tested additionally at ODW2018 and BRE2021. The general precision of both campaigns was very different being at the 4 mGal level for ODW2018 and well below 1 mGal for BRE2021. The results can be found in Tables 6.4 and 6.7 where the “main results” were computed with the PosDif method using 5 s satellite clock products. The detailed evaluation of the results was presented in Sections 6.3.2 and 6.5.2.

At the ODW2018 campaign, only minor differences were observed regarding the kinematic acceleration method. Before and after line-wise crossover adjustment, the PosDif method performed best followed by PhaseDif-PPP and PhaseDif-POP.

At BRE2021, all precision indicators of the non-adjusted results were better than 0.75 mGal. Without adjustment, all methods performed on par with the PosDif precision being just 0.04 mGal better than for PhaseDif approaches. After adjustment, a slight advantage for the PhaseDif approaches was obtained. The

use of 5 s instead of 30 s satellite clock products marginally improved the PhaseDif-PPP results. The use of more than two GNSS constellations in the PhaseDif-POP mode did not improve the results which might be due to undetected outliers. Possible improvements in the outlier detection of the PhaseDif methods might result in enhanced precision.

In summary, no major consistent result differences have been identified between the PosDif and PhaseDif approaches in the static and dynamic experiments with the implementation presented in this work. However, almost every method has specific advantages and can be recommended depending on the available hardware, software and the tolerable processing delay.

- The **PosDif-DGNSS** method is commonly used for airborne gravimetry. However, it is not further evaluated here for two practical reasons: Firstly, according to Li et al. (2018), the accuracy tends to be lowered if the aircraft moves away from the reference station by more than several dozens of kilometres. Secondly, due to the limited distance, at least one reference station needs to be set up by the user. This is not required for the other methods.

- If a commercial PPP software with a positioning accuracy of a few centimetres is available, the easiest way to determine the kinematic acceleration is the **PosDif-PPP** method. Two consecutive simple numerical differentiations can deliver high precision results when precise 5 s satellite clock products are used. All campaigns evaluated in this thesis were processed using PosDif-PPP with final satellite products.

- If a new GNSS post-processing software implementation is required, the **PhaseDif-PPP** method may be recommended. The implementation of the PhaseDif kinematic acceleration determination is simplified in comparison with the PosDif approach since slowly changing effects are neglectable in the acceleration domain. A rough position solution is sufficient for kinematic acceleration and gravity determination. However, note that the vertical position must be known with a precision of some decimetres for normal gravity and gravity disturbance determination.

- If a precise solution is required fast or even on flight day, the **PhaseDif-POP** method is recommended since there is no need to wait for precise satellite clock products. A single reference station far away can be sufficient for high precision kinematic acceleration determination. Note that the implementation of the network-based PhaseDif-POP method is more complex than the implementation of the PhaseDif-PPP method. PhaseDif-POP might also be implemented to optimise the solution using Multi-GNSS observations. As long as 5 s satellite clock products by analysis centres are not available for Galileo and BeiDou, the Multi-GNSS results of the PPP-based methods might be of worse quality since they rely on 30 s clock products. Especially in Eastern Asia and Australia, an improved accuracy is possible by adding BeiDou observations.

9 Comparison of different approaches in dynamic gravimetry

Section 8 focused on the effect of observation conditions, the magnetic correction and kinematic acceleration determination methods on the precision obtained in a crossover or repeated lines analysis. To detect systematic errors in an accuracy evaluation, an external reference is required. In the scope of this thesis, other gravimeter types, processing methods and vehicle types will be used as reference.

In Section 9.1, results taken from Sections 6 and 7 will be compared to the results obtained with other strapdown gravimeters and to results of the same dataset being processed with another processing method. Section 9.2.1 will compare iNAV-RQH results to results of the Chekan-AM stable platform gravimeter. A combination method will be implemented in Section 9.2.2. In some dedicated test campaigns, lines might be repeated at several distinct heights. In Section 9.3.1, a line-wise upward continuation method will be developed to allow for a reasonable comparison of such lines. Section 9.3.2 will apply this method to congruent lines obtained at the shipborne campaign NTS2021 and the airborne campaign BRE2021.

9.1 Strapdown gravimeter model and processing method

In some of the presented dynamic campaigns, several IMUs by iMAR were installed side-by-side as gravimeters. Exemplary, all gravimeter data of the DK2020 campaign (see Section 6.4) has been evaluated in the scope of this work. Along with the iNAV-RQH by TU Darmstadt, an iNAT-RQH by DTU Space and an early version of the iNAT-RQT without thermal stabilisation were installed in the aircraft.

The iNAT-RQT turned out to be very sensitive to temperature changes resulting in a degraded accuracy. Hence, it will not be considered in the analysis. The comparison of the gravity disturbance results obtained with both remaining gravimeters is shown in Figure 9.1. In most trajectory segments, the results agreed quite well. However, some high-frequency noise tended to impair the iNAT-RQH results. Furthermore, its results tended to be systematically higher resulting in a mean bias of 1.9 mGal. The standard deviation was 2.3 mGal. The mean bias between both results for all flights was lower being 0.45 mGal. The effect might be predominantly due to sensor drifts and errors due to a missing magnetic correction of the iNAT-RQH.

The iNAV-RQH crossover precision was 0.98 mGal, the repeated lines precision was 0.48 mGal. Without magnetic correction, these values significantly degraded to 1.11 and 0.87 mGal, respectively. Using the indirect method of strapdown gravimetry where the gravity processing is performed in the position domain (see Section 2.6.1), a slightly worse precision of 1.24 and 1.20 mGal was obtained without magnetic correction[1]. The crossover precision of the iNAT-RQH results was significantly worse being greater than 2 mGal for both processing methods with a slight advantage for the indirect method. The repeated line precision is significantly better for the indirect method. This might be due to a stronger filtering in the indirect method. The filter length cannot be easily determined in the indirect method since it depends on several Kalman filter parameters.

The example shows that dynamic gravimetry results do not only depend on the performance of the installed gravimeter, including the instantaneous sensor drift, and the observation conditions. Furthermore, the

[1] The indirect method results were obtained by David Becker on behalf of DTU Space. For line identification and quality assessment, the same algorithm like for the direct method was used.

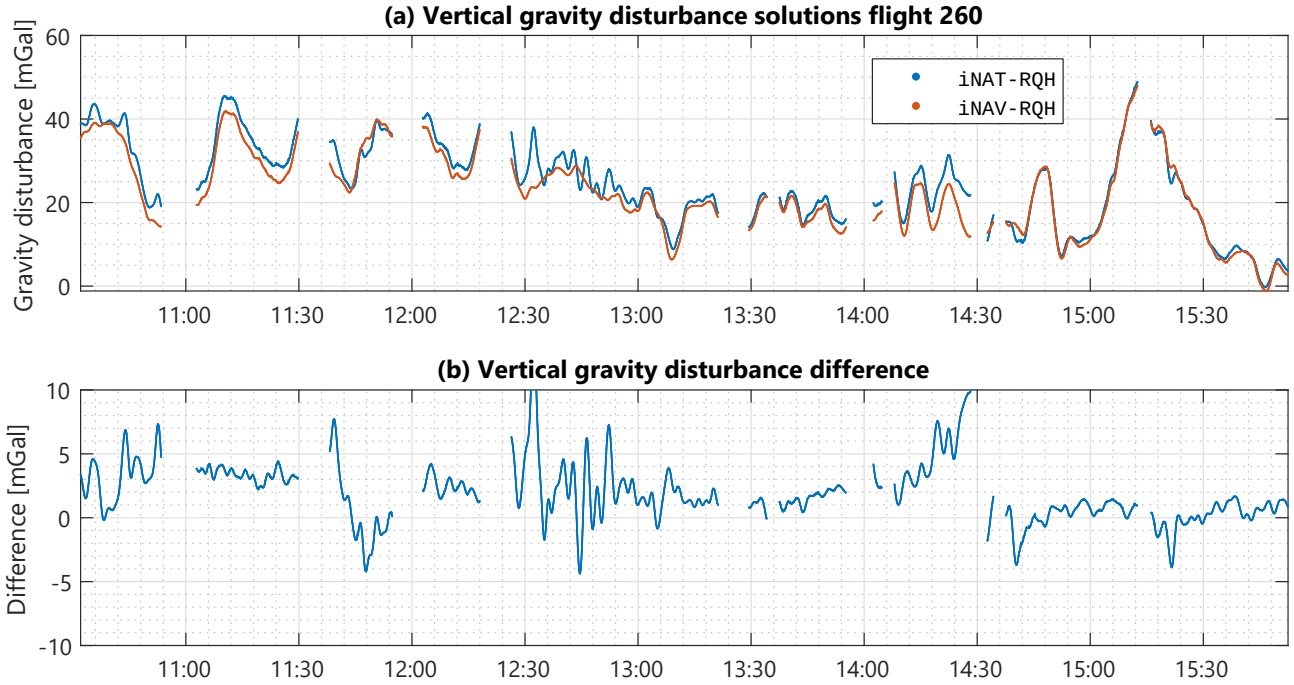


Figure 9.1: Non-adjusted gravity disturbance result comparison at flight lines of DK2020, flight 260, obtained with the direct method

Table 9.1: DK2020 precision for different strapdown gravimeters using the direct and the indirect processing method

IMU	iNAV-RQH			iNAT-RQH	
Method	direct		indirect	direct	indirect
Magnetic field correction	✓	✗	✗	✗	✗
n_{CO} non-adjusted	23	23	21	19	21
n_{CO} flight-adjusted	21	21	20	18	20
CO RMSE non-adj. [mGal]	0.98	1.11	1.24	2.51	2.17
CO RMSE flight-adj. [mGal]	0.94	1.15	0.94	2.27	2.12
RL distance [km]	147	147	142	147	142
RL RMSE [mGal]	0.48	0.87	1.20	2.56	0.33
RL RMSE ZM [mGal]	0.39	0.38	0.24	0.55	0.31

Table 9.2: Gravimeter drifts at BTS2018 and NTS2021 (all values in mGal/d)

Campaign	BTS2018				NTS2021					
Cruise	212	215	217	220	180	181	182	183	185	188
iNAV-RQH	0.68	0.75	0.38	1.22	2.25	1.75	1.68	2.15	1.26	-0.92
Chekan-AM	0.68				4.06	-1.94	0.27	-1.18	0.91	-0.50

processing method can significantly affect the results. In further evaluations, it was observed that the direct and the indirect method typically perform approximately on par. In some flights, especially for DK2020, extraordinarily high in-flight biases of up to 2.5 mGal to external reference data like upward continued terrestrial data, other gravimeter types or another processing were observed. The reason for this is unclear and should be further evaluated.

9.2 Gravimeter types: ”Classical“ and strapdown gravimeters

In addition to strapdown gravimeters, “classical”, stable platform gravimeters (see Section 2.3.1) have been installed in some airborne and shipborne campaigns. In particular, an L&R S-type gravimeter was used at the Malaysia campaigns, a Chekan-AM was used in all shipborne campaigns and a GT-2A was used at BRE2021. While the IMU observations with the iNAV-RQH were interruption-free and gravity could be determined without any gaps during all flights and cruises, malfunctions and irregular drift behaviour made a large portion of the data from the stable platform gravimeters unusable. At BRE2021, no GT-2A processing was possible. At MY2022, the L&R gravity results were very noisy and did not allow for a reasonable comparison to the strapdown results. The used S-type gravimeter might have reached the end of its lifetime. It will be shown in the following section that the results obtained with the Chekan-AM were of varying quality.

9.2.1 Comparison at several shipborne campaigns[1]

The drift behaviour of the Chekan-AM can be very homogenous. While the iNAV-RQH drifted between 0.38 and 1.22 $\frac{\text{mGal}}{\text{d}}$ at the single cruises of BTS2018, the Chekan-AM was subject to a linear drift of 0.68 $\frac{\text{mGal}}{\text{d}}$ that was almost constant during the whole campaign (Table 9.2). Contrarily, at NTS2021, the Chekan-AM showed a very unstable drift behaviour varying between -1.94 and 4.06 $\frac{\text{mGal}}{\text{d}}$ for the single cruises. For most cruises, the drift of the iNAV-RQH was comparatively homogenous. The comparison of both campaigns indicates that classical gravimeters can have superior drift behaviour but require more frequent maintenance. In the campaigns analysed in this work, the strapdown gravimeters were more reliable than the stable platform gravimeters.

Figure 9.2 visualises the gravity disturbance obtained with the iNAV-RQH and the Chekan-AM during a complete cruise of the BTS2018 campaign. In the Chekan-AM results, conspicuous peaks occurred during cornering. Furthermore, a high noise can be observed during harsh sea conditions, e.g. at about 15:00 of 5 August. Both effects originate by imperfect horizontal stabilisation during periods with relevant attitude changes. The corresponding results are usually removed in post-processing. After the removal, a precision better than 0.4 mGal was obtained with the Chekan-AM. Systematic differences during the measurement lines are suspected to be primarily due to the strapdown results. In the night between 5 and 6 August, the vessel was anchored. Hence, the gravity disturbance should be approximately constant during this period, but a slight positive drift was observed for the iNAV-RQH. The mean and RMS of the differences were -0.8 and 1.2 mGal, respectively, which was slightly worse than the total campaign values of -0.6 and 1.0 mGal

[1] This section is partially based on Förste et al. (2020). The Chekan-AM results have been obtained by the GFZ.

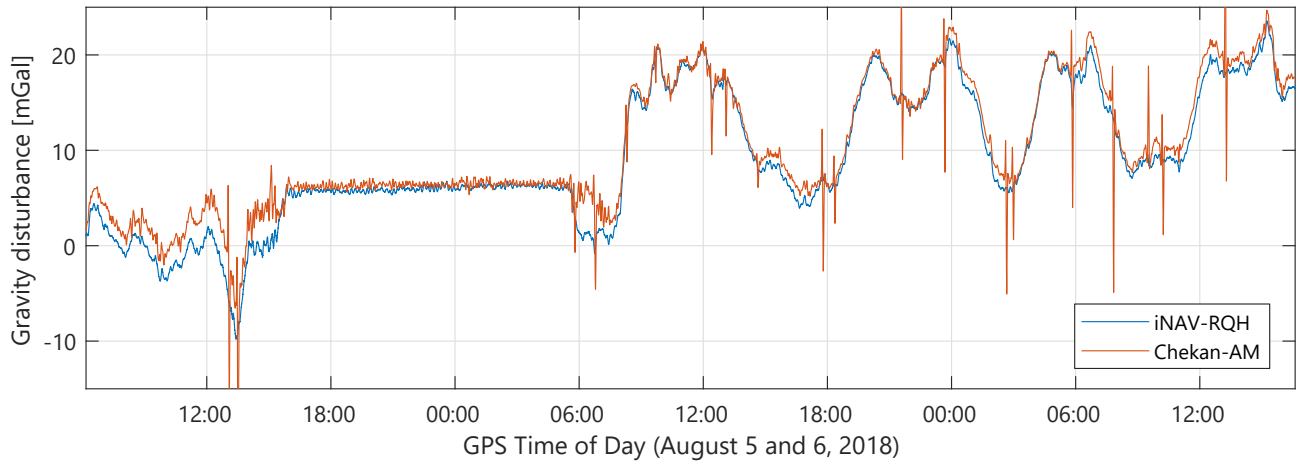


Figure 9.2: Non-adjusted gravity disturbance result comparison of BTS2018, cruise 217 (based on Förste et al. (2020))

Table 9.3: Statistics on the difference between non-adjusted iNAV-RQH and Chekan-AM results (all values in mGal, data used for Figures 9.2 and 9.3 in italic letters)

Campaign	BTS2017	BTS2018		NTS2021		MRZ2019
iTempStab?	✗	✓		✓		✓
Cruises	all	all	217	all	180	all
Mean	-0.83	-0.57	*-0.8*	-0.75	*-1.6*	-0.57
Standard deviation	1.85	0.98	*1.2*	1.66	*1.7*	1.23
RMS	2.02	1.13	*1.5*	1.82	*2.3*	1.35

(Table 9.3). The standard deviation was on a similar level like the iNAV-RQH crossover precision which was 0.82 mGal.

A second comparison was done for a cruise of NTS2021 in Figure 9.3 where the Chekan-AM results were impaired by unstable drift behaviour. While the total campaign mean difference was -0.75 mGal, it was significantly worse for the shown example being -1.6 mGal. The systematic difference might be due to non-linear drifts of the Chekan-AM and the iNAV-RQH. The Chekan-AM results are much noisier than the strapdown results. An exceptionally high deviation can be observed at about 10:00 on 29 June. The standard deviation of the difference is 1.7 mGal for both the single cruise and the total campaign which is significantly higher than the crossover precision of 1.19 mGal obtained for the iNAV-RQH. This might be due to inaccuracies of the Chekan-AM.

A higher bias and a higher standard deviation at the BTS2017 campaign (see Table 9.3) might be mainly caused by thermally induced drifts of the iNAV-RQH which was run without iTempStab. Similar to NTS2021, the Chekan-AM was subject to significantly varying drifts at the MRZ2019 campaign. This might be a reason for the comparison indicators being significantly worse than the precision of the strapdown results of less than 0.5 mGal.

9.2.2 Potential multi-instrument combinations

As Figure 9.2 showed, the results of stable-platform and strapdown gravimeters can complement each other. The strapdown results are typically of very high quality at short wavelengths. Measurements during cornering

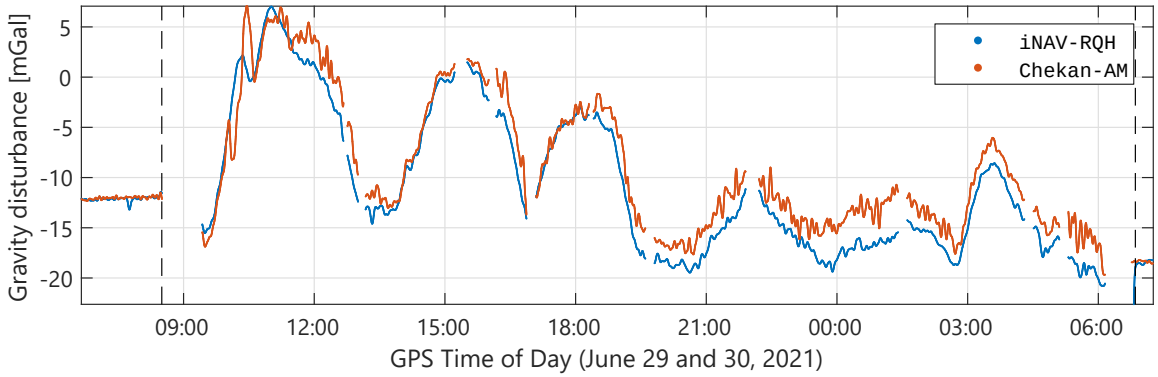


Figure 9.3: Non-adjusted gravity disturbance result comparison at harbour and cruise lines of NTS2021, cruise 180

are possible without significant accuracy degradation at shipborne campaigns. In the airborne case, there is a loss in accuracy due to the lowered estimability (Becker et al., 2015a), but the results are still much better than for the stable-platform gravimeters introduced in Section 2.3.1. Even after thermal and magnetic calibration, there may be significant sensor drifts at the long wavelengths. If the stable-platform gravimeter performs well, like at BTS2018, a combination of both results appears promising taking advantage of the benefits of each gravimeter type.

Jensen et al. (2019) implemented a “bias adjustment” method for the combination of DTU’s iNAT-RQH and a horizontally stabilised ZLS Dynamic gravimeter (D-Type). They applied the method to an airborne campaign conducted at the Kattegat strait between Denmark and Sweden. For both results, they calculated the mean values per line. Then, they removed the mean values from the strapdown results. To the result, they added the corresponding ZLS mean values. Hence, the final result took advantage of the long term stability of the ZLS as well as the high short-term accuracy and robustness against turbulence of the iNAT-RQH. Although the precision of the ZLS was significantly worse than the strapdown results, the precision after combination was improved by 20 % compared to the strapdown precision. They also investigated an approach where they estimated a bias and a linear trend per line. The method did not result in a precision improvement. Note that the bias adjustment relies on lines and may be inappropriate or would need adaption for lines with improper lengths if lines are not available.

Another approach that is independent to lines may be complementary filtering. The result of the stable-platform gravimeter is low-pass filtered and the result of the strapdown gravimeter is high-pass filtered. Then, both remaining signals are summed up. Hence, the long wavelengths of the combination originate from the stable-platform and the short wavelengths originate from the strapdown gravimeter. The filters need to be designed complementary with a narrow transition zone. An example of the magnitude responses of two complementary FIR filters designed with the window method is illustrated in Figure 9.4. A cut-off frequency of 0.185 mHz is selected corresponding to a filter length of 90 min.

These filters were applied to the shipborne gravity disturbance of BTS2018, cruise 217 that was shown in Figure 9.2. After filtering, a very smooth Chekan-AM signal and the zero-mean high frequency data of the iNAV-RQH remained (Figure 9.5). After summation, a signal with all desired properties was obtained (Figure 9.6): Non-linear drifts were small, i.e. no significant drift was observed during the anchoring period; no significant errors were apparent at the turns and the noise during harsh sea conditions before anchoring was small.

A combination of several gravimeters with similar drift behaviour and reaction to attitude changes might also be desirable. In many campaigns, at least two gravimeters are installed to avoid expensive flight/cruise

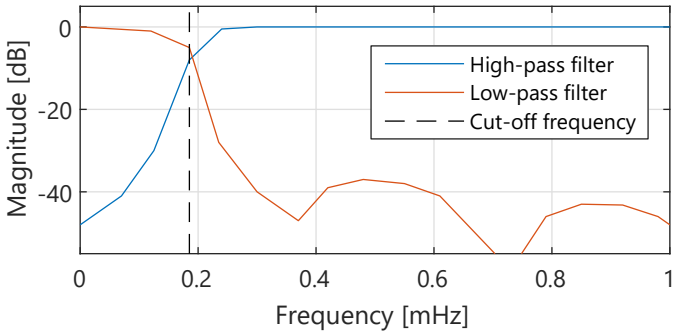


Figure 9.4: Magnitude responses of the filters designed for the combination of the iNAV-RQH and Chekan-AM results

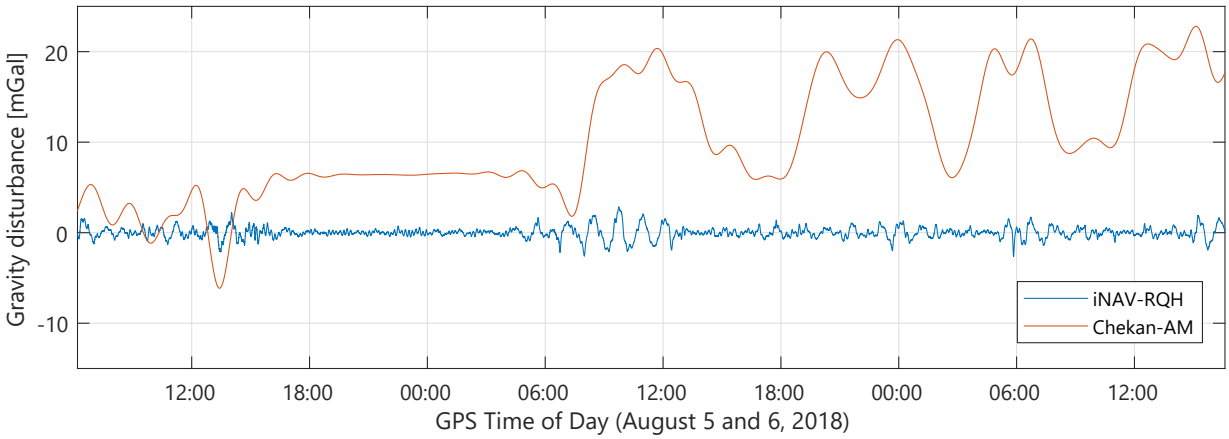


Figure 9.5: Filtered iNAV-RQH and Chekan-AM results of BTS2018, cruise 217

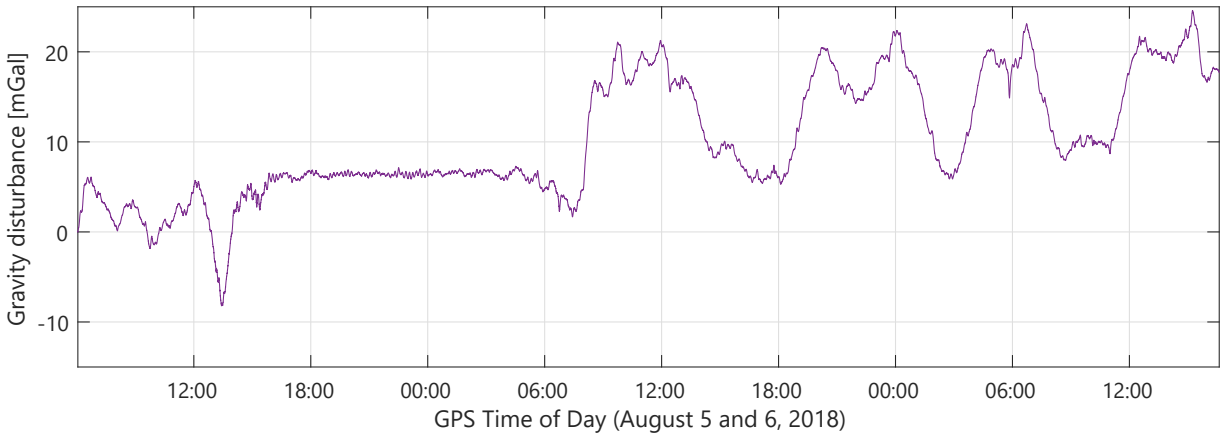


Figure 9.6: Combined gravity disturbance result using iNAV-RQH and Chekan-AM data of BTS2018, cruise 217

repetitions in case of data loss of a single gravimeter. As already proposed by K. P. Schwarz and Glennie (1998), in addition to separated processing and subsequent comparison for accuracy evaluation, a result combination might be advisable. If, for example, two strapdown gravimeters are installed, a combination on the observation or the result level might significantly reduce errors due to sensor drift. Such a combination may be an auspicious field for future research.

9.3 Comparison of congruent line results at different observation heights

As illustrated in Figure 2.3, the gravity field is damped with increasing height. The damping is stronger for shorter wavelengths. Hence, in order to compare gravity results at different heights or for geoid determination, an upward or downward continuation is required. Typically, a 2-D gravity field is modelled at a specific height and upward/downward continued afterwards, e.g. by least-squares collocation (Forsberg and Olesen, 2010).

In the following Section 9.3.1, an upward continuation procedure will be developed for the specific case that a 1-D gravity field is regarded, i.e. the results of a dynamic gravimetry line. The upward-continued lower 1-D line results can be compared to gravity line originally observed at higher altitude, but with approximately the same ground track. In Section 9.3.2, the method will be applied to repeated lines of the campaigns NTS2021 and BRE2021.

9.3.1 Line-wise upward continuation

According to Childers et al. (1999), gravity anomalies are damped by the factor $e^{-\frac{2\pi z}{\lambda_g}}$ depending on the minimal height z above terrain and the wavelength λ_g of the anomaly. The derivation of the damping factor is based on the assumption that the mass is concentrated in a surface at terrain height. The surface density varies periodically along the horizontal axis x with an amplitude σ_g (Figure 9.7). Using the Bouguer formula and considering the Laplace equation with the boundary condition that gravity converges towards zero at infinite distance, the gravity anomaly at a specific height z above the terrain is obtained as

$$g_z = 2\pi G\sigma_0 \sin\left(\frac{2\pi x}{\lambda_g}\right) e^{-\frac{2\pi z}{\lambda_g}}, \tag{9.1}$$

with G being the gravitational constant (Turcotte and Schubert, 2002). Applied to the case of two congruent dynamic gravimetry lines, the gravity disturbance signals g_f, g_m obtained at a higher height H_f and a lower height H_m become

$$g_f = 2\pi G\sigma_0 \sin\left(\frac{2\pi x}{\lambda_g}\right) e^{-\frac{2\pi H_f}{\lambda_g}}, \quad g_m = 2\pi G\sigma_0 \sin\left(\frac{2\pi x}{\lambda_g}\right) e^{-\frac{2\pi H_m}{\lambda_g}}. \tag{9.2}$$

Forming the quotient of both parts of Equation (9.2), the equal factors cancel each other assuming them being non-zero. The damping coefficient

$$\frac{g_f}{g_m} = \frac{e^{-\frac{2\pi H_f}{\lambda_g}}}{e^{-\frac{2\pi H_m}{\lambda_g}}} = e^{\frac{2\pi}{\lambda_g}(H_m - H_f)} \tag{9.3}$$

is obtained. For a specific disturbance wavelength λ_g, the gravity disturbance at the higher height H_f can then be computed from the gravity disturbance g_m at lower height by solving Equation (9.3) to

$$g_f = g_m \cdot e^{\frac{2\pi}{\lambda_g}(H_m - H_f)}. \tag{9.4}$$

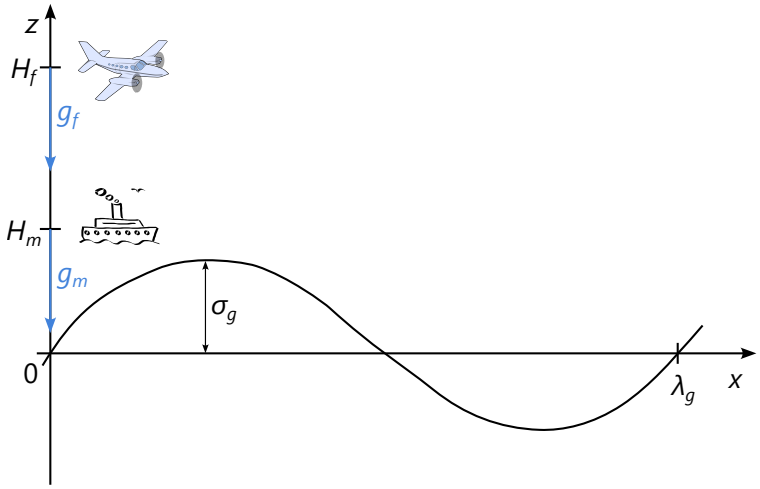


Figure 9.7: Height-dependent gravitational acceleration assuming a horizontally varying sinusoidal mass layer (based on Turcotte and Schubert (2002))

The specific disturbance wavelength can be determined as

$$\lambda_g = \frac{\dot{r}}{f_g} \tag{9.5}$$

using the norm of the vehicle velocity $\dot{r}$ and the disturbance signal frequency f_g.

Strictly speaking, the gravity disturbances g_f, g_m are gravitational disturbing accelerations $b_{S,f}, b_{S,m}$ due to a disturbing source with a specific wavelength. The damping factor can be alternatively derived from the gravitational disturbance potential

$$V_S = \sum_{n=1}^{\infty} \left(\frac{a}{r}\right)^n \underbrace{\sum_{m=0}^{n} (C_{nm}\cos(m\lambda) + S_{nm}\sin(m\lambda)) P_{nm}(\cos(\theta))}_{\Sigma_n} = \sum_{n=1}^{\infty} \left(\frac{a}{r}\right)^n \Sigma_n, \tag{9.6}$$

which is obtained from Equation (2.7) by removing the spherical potential $\frac{GM}{r}$. Regarding the field damping with increasing height, i.e. increasing the radial distance r to the centre of mass, the longitude and colatitude can be assumed constant. The inner sum then becomes a constant Σ_n per degree n which is the gravitational amplitude for a specific degree. The vertical gravitational disturbing acceleration

$$b_S = -\frac{\delta V_{S,n}}{\delta r} = n a^n r^{-n-1} \Sigma_n = \frac{n a^n}{r^{n+1}} \Sigma_n \tag{9.7}$$

due to a disturbing source of a specific wavelength is obtained as the partial derivative in down direction where only one summand of the outer sum needs to be considered. The equations

$$b_{S,f} = \frac{n a^n}{r_f^{n+1}} \Sigma_n, \quad b_{S,m} = \frac{n a^n}{r_m^{n+1}} \Sigma_n \tag{9.8}$$

for the disturbing accelerations $b_{S,f}, b_{S,m}$ at higher and lower height only differ by the radial distances r_f, r_m to the geocentre. Analogous to the derivation of Equation (9.3), the damping factor

$$\frac{b_{S,f}}{b_{S,m}} = \left(\frac{r_m}{r_f}\right)^{n+1} = \left(\frac{r_m}{r_f}\right)^{\frac{2\pi}{\lambda_g}+1} \tag{9.9}$$

is obtained by forming the quotient of both parts of Equation (9.8). Furthermore, it is considered that the degree can be expressed through the corresponding signal wavelength as $n = \frac{2\pi}{\lambda_g}$. Note that λ_g needs to be expressed in radians here by dividing Equation (9.5) through the Earth radius. A disturbance of a specific wavelength can be transformed to a higher altitude by rearranging Equation (9.9) as

$$b_{S,f} = b_{S,m} \cdot \left(\frac{r_m}{r_f}\right)^{\frac{2\pi}{\lambda_g}+1}. \tag{9.10}$$

The damping factors obtained with Equations (9.3) and (9.9) are approximately equivalent. The damping effect increases with increasing height difference and with decreasing disturbing signal wavelength. For example, for a height difference $H_f - H_m = 1\,\text{km}$ and a wavelength $\lambda_g = 5\,\text{km}$, the damping factors become $e^{\frac{2\pi}{\lambda_g}(H_m - H_f)} \approx \left(\frac{r_m}{r_f}\right)^{\frac{2\pi}{\lambda_g}+1} \approx 28.5\,\%$.

For a very large height difference, e.g. when comparing airborne and satellite results, the spherical shape of the Earth should possibly be considered in the damping factor of Equation (9.3) which is based on a flat Earth model (see Figure 9.7). For height differences of several kilometres as obtained in shipborne and airborne gravimetry, the effect is neglectable.

For the purpose of comparing two congruent lines of dynamic gravimetry at different heights, preferably, the lower signal should be upward continued since downward continuation is subject to noise amplification. To allow for proper damping, the gravity disturbance signal needs to be transformed to the frequency domain where the wavelength-specific damping factors can be applied to the corresponding amplitudes. After re-transformation to the time domain, the signal can be compared to the original high altitude signal.

The long wavelengths of the gravity disturbance signal cannot be determined from data obtained at measurement lines limited to several dozens of kilometres. To avoid over-damping, a remove-restore method may be applied. The gravity disturbance signal can be split in three components as

$$\delta g = \delta g_{\text{EGM}} + \delta g_{\text{topo}} + \delta g_{\text{resid}}, \tag{9.11}$$

where δg_{EGM} is the gravity disturbance obtained by a global gravity model, δg_{topo} is the gravity disturbance due to topography and δg_{resid} is the remaining residual signal (Forsberg and Olesen, 2010). The damping should only be applied to the residual term which consists of short wavelengths.

Considering the remove-restore method, a line-wise comparison is proposed to be applied following the procedure illustrated in Figure 9.8:

1. The gravitational acceleration is computed for the line points based on a spherical harmonic reference field, e.g. EGM2008. The corresponding gravity disturbance δg_{EGM} is obtained considering centrifugal acceleration and normal gravity using Equations (2.1) and (2.6). Optionally, the gravity disturbance g_{topo} due to terrain heights can be added.

2. In the “remove” step, δg_{EGM} and δg_{topo} are removed from the gravity disturbance δg_m observed at low altitude.

3. The resulting residual signal δg_{resid} is transformed to the frequency domain, e.g. by applying a Fast Fourier Transform (FFT).

4. For each frequency of the amplitude spectrum, a damping factor is calculated with Equation (9.3) or (9.9). The line heights H_f, H_m and line velocities can be assumed constant for lines with moderate height variations. The same applies for the vehicle velocity of a line. The relationship between the disturbing signal wavelength and the corresponding frequency is given by Equation (9.5).

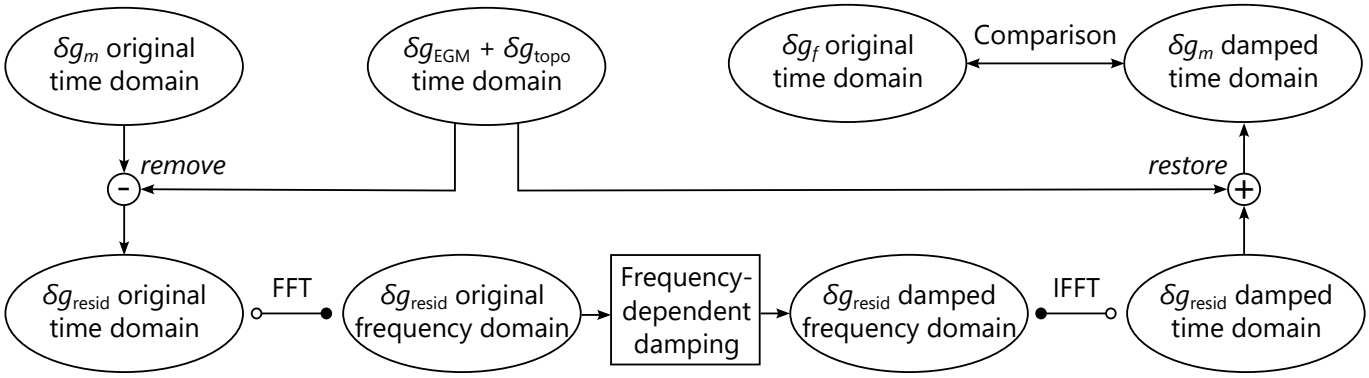


Figure 9.8: Line-wise dynamic gravimetry comparison process based on height- and frequency-dependent damping and the remove-restore method

5. The resulting damped residual signal is re-transformed to the time domain, e.g. by applying an Inverse FFT (IFFT).

6. In the "restore" step, δg_{EGM} and δg_{topo} are re-added.

7. The resulting signal is the upward continued gravity disturbance. After interpolation, it can be compared to the original gravity disturbance δg_f observed at higher altitude.

9.3.2 Application to NTS2021/BRE2021

The upward continuation introduced in Section 9.3.1 was applied to lines that have been observed shipborne at the NTS2021 and airborne at the BRE2021 campaigns. The lines 1 and 2 cover the same shipborne data, but were flown two times; line 3 is a distinct line observed once shipborne and once airborne (see Figure 6.29). The height difference was about 500 m. Hence, the height-dependent gravity field damping is comparatively small. The damping factors for the specific disturbing signal wavelengths at this height difference are illustrated in Figure 9.9. Very short sub-km signals would be removed almost completely. Beginning with wavelengths of about 20 km, the damping factor tend to converge towards 1. Consider the limited spatial resolution of gravity disturbance signals obtained with dynamic gravimetry based on vehicle velocity and filter length (see Equation (5.9)).

The experimental gravity field model XGM2019e (Zingerle et al., 2019) was selected as long wavelength reference field for the remove-restore method (see Section 6.2.2). The gravitational acceleration based on XGM2019e was accessed from the International Centre for Global Earth Models (ICGEM) (Ince et al., 2019). The amplitude spectrum of the XGM2019e along repeated line 1 is illustrated in Figure 9.10 showing that the amplitudes fall off at wavelengths greater than 6.7 km (corresponding to a frequency of 0.01 Hz). For the frequency plots in this section, the lines are assumed to be passed with a flight velocity of 67 $\frac{\text{m}}{\text{s}}$. The frequency can be translated to the corresponding wavelength by applying Equation (9.5).

Figure 9.11 shows the amplitude spectra of the dynamic gravity processing results of repeated line 1 with a focus on frequencies between 0.004 and 0.05 Hz corresponding to signal wavelengths of 16.7 and 1.3 km. The amplitude spectrum of the airborne results (Figure 9.11a) is similar to the XGM2019e showing that the spatial resolution is comparable to the global model resolution. However, a significant bias can be observed between the flight and XGM2019e data (Figure 9.12a). At line 3, the deviation of the global model behaviour from the airborne and shipborne results is larger. The local gravimetry results tend to be more consistent.

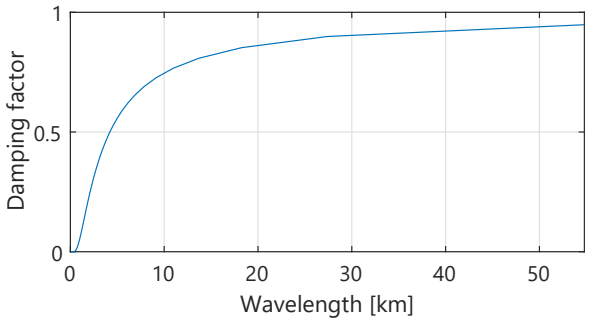


Figure 9.9: Damping coefficients for a height difference of approximately 500 m

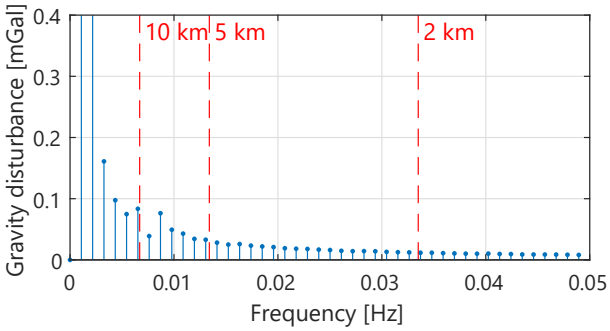
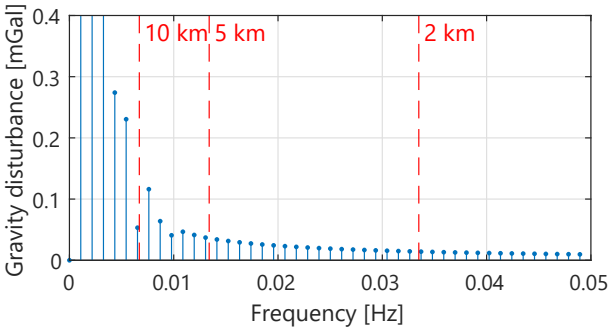
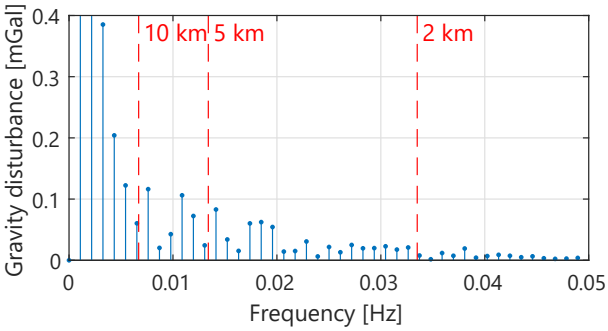


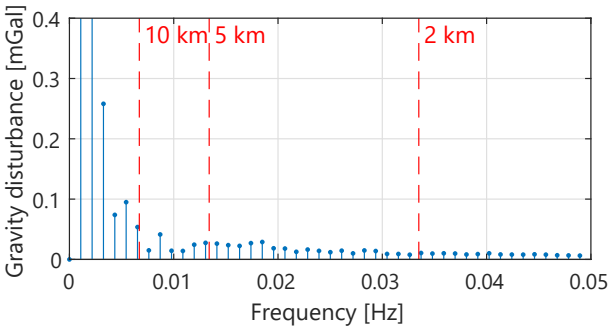
Figure 9.10: Amplitude spectrum of gravity disturbance obtained with XGM2019e along repeated line 1 (red: signal wavelength)



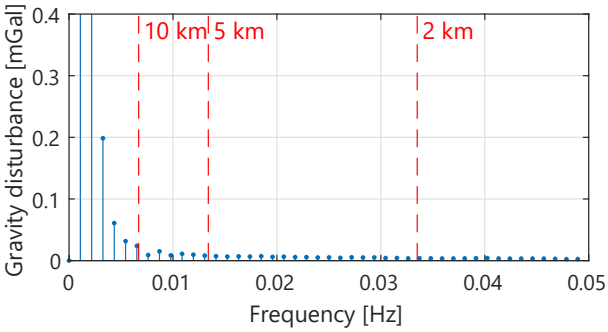
(a) Flight results



(b) Original iNAV-RQH ship results

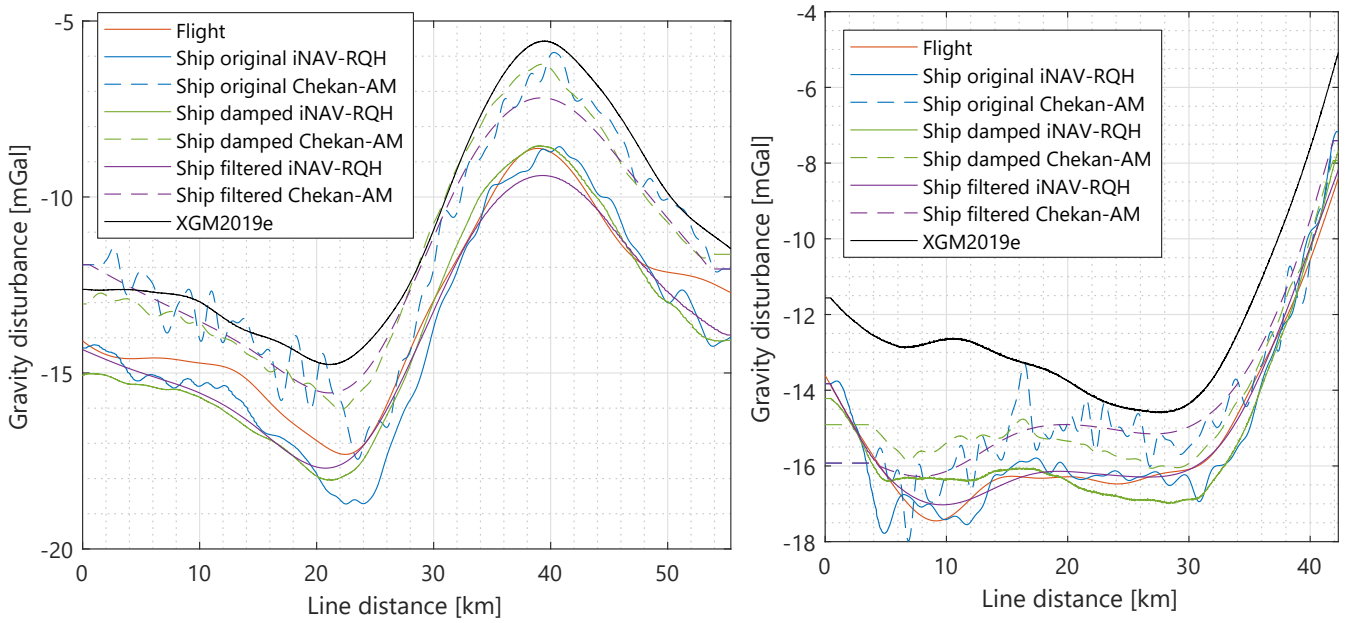


(c) iNAV-RQH ship results after upward continuation



(d) iNAV-RQH ship results after low-pass filtering

Figure 9.11: Amplitude spectra of gravity disturbance obtained with dynamic gravimetry using the iNAV-RQH along repeated line 1 (red: signal wavelength)



(a) Line 1

(b) Line 3

Figure 9.12: Gravity disturbance results along repeated lines at the North Sea. The crossover precision of the original campaigns without outlier removal was 0.50 mGal (flight), 1.19 mGal (ship iNAV-RQH) and 1.01 mGal (ship Chekan-AM)

More energy at higher frequencies can be identified in the original shipborne results (Figure 9.11b) that were generated in Section 7.2.2. This becomes apparent in higher variation during the repeated lines (Figure 9.12). After application of the wavelength-dependent damping factors in the remove-restore method, the amplitude spectrum of the shipborne result loses energy especially at the higher frequencies (Figure 9.11c). However, there is still remaining variation in the amplitudes at frequencies higher than 0.01 Hz where the airborne signal might already been dominated by noise (see Figure 9.11a). The shipborne results generally become smoother after damping (see Figure 9.12). The damped signal mostly shows a higher level of agreement to the airborne results than the original shipborne results.

So far, considering the height- and wavelength-dependent damping, the comparison was performed using the best available airborne and shipborne results. Furthermore, the different vehicle velocities and corresponding spatial resolutions of the airborne and shipborne data should also be taken into account. In addition to the height dependent damping, the airborne results are smoother since the spatial resolution at BRE2021 is only 5.7 km compared with 1.0 km at NTS2021 (see Tables 6.1 and 7.1). For an accuracy evaluation, both data sets should also be compared with the same spatial resolution. For this, a low-pass filter should be applied to the unfiltered shipborne gravity disturbance with an appropriate filter length, which is 38 min for the evaluated dataset. The filtered shipborne results do not have significant energy above 0.01 Hz (Figure 9.11d). The filtered signal (without upward continuation) agrees well with the airborne results for most line segments (see Figure 9.12).

The statistics on the difference between the airborne and the original, the upward-continued (damped) and the extensively low-pass filtered shipborne results are given in Table 9.4. As shipborne data, the Chekan-AM results can be used instead of the iNAV-RQH alternatively. At most lines, the mean values do not change significantly after damping and filtering. Except for the iNAV-RQH results at line 3, the standard deviation

Table 9.4: Statistics on the differences between adapted shipborne and original airborne gravity disturbance results (all values in mGal)

Gravimeter		iNAV-RQH			Chekan-AM		
Line		1	2	3	1	2	3
Mean	original	-0.55	-0.45	-0.08	1.62	1.71	0.65
	damped	-0.55	-0.46	-0.07	1.65	1.70	0.74
	filtered	-0.51	-0.45	0.08	1.62	1.68	0.84
Standard deviation	original	0.64	0.79	0.52	0.87	0.91	0.90
	damped	0.60	0.66	0.54	0.59	0.64	0.62
	filtered	0.40	0.45	0.17	0.48	0.51	0.75

significantly improves when comparing the damped or filtered shipborne data to the airborne results. At most lines, the standard deviation is better for the filtered results.

The spatial resolution based on the vehicle velocity and the low-pass filter length appears to be the main cause for differences between the airborne and shipborne original results. However, this does not necessarily mean that the filter approach is better suited for comparison since high-frequency data available at the shipborne results get lost during the extensive low-pass filtering. Furthermore, it should be noted that the height difference of 500 m is relatively small. The effectiveness of the presented line-wise upward continuation method is expected to increase if data is observed at a vertical distance of several kilometres, preferably collected with the same aircraft velocity. Further experiments considering the topographic reduction are required for a sound evaluation of the question whether the 1-D approach is well-suited for the 3-D gravity field.

Again, the analysis uncovers noticeable biases between different results. While the biases between the iNAV-RQH airborne and shipborne results are comparatively small, the Chekan-AM shows biases of up to 1.7 mGal in comparison to the flight results, especially on lines 1 and 2 (see Table 9.4). On the one hand, an auspicious non-linear drift behaviour has been observed for the Chekan-AM at the NTS2021 campaign (see Table 9.2). On the other hand, the difference between the Chekan-AM and the XGM2019e are lower for these two lines (see Figure 9.12a). However, the data of the three lines with a total length of about 150 km do not enable general conclusions on systematic errors in dynamic gravimetry using both gravimeter types since the mean differences are not far beyond the precision indicators of both campaigns (see Tables 6.7 and 7.3).

10 Conclusions and outlook

10.1 Conclusions

In strapdown gravimetry, gravity is obtained as the difference of the kinematic acceleration obtained by GNSS observations and the specific force obtained by IMU observations. In the scope of this thesis, both summands were analysed in order to enable improvements in their determination accuracy. Furthermore, the algorithm used for gravity disturbance computation, the direct method, was described in detail allowing for re-implementation. The influence of processing settings and observation conditions on the obtained precision was analysed by evaluating multiple airborne and shipborne campaigns.

It was shown in static experiments that the accelerometers of the analysed IMU, the iMAR iNAV-RQH-1003, are significantly impaired by magnetic fields in the order of the Earth's field. This may be due to the magnetically controlled position reset of the pendulum inside of the Q-Flex QA-2000 accelerometers. This accelerometer type is still commonly used for gravimetry and navigation. The findings might help to improve the output precision in all fields where this sensor type is used.

A calibration method was developed for the vertical accelerometer based on the horizontal field intensity and input direction. The magnetic calibration was applied to eleven dynamic gravimetry surveys. In almost all campaigns, considerable precision improvements were observed between 8 % and 82 %. Only at the campaigns conducted with the comparatively large research vessels Deneb and Wega, results of mixed quality were obtained after applying the calibration. This might be due to strong magnetic field distortions inside of the vessel. Furthermore, significant non-linear drifts at the extraordinarily long cruises of up to 78 h might have impaired the results.

In addition to the specific force determination which can be improved using thermal and magnetic calibration, existing approaches for kinematic acceleration determination were evaluated. If a GNSS positioning algorithm or a commercial navigation software is available, the PosDif method might be recommended where the acceleration is obtained as the second numerical derivative of the position result. In the more direct PhaseDif approach, the GNSS phase observable is numerically differentiated two times. The resulting phase range acceleration is used to estimate the kinematic acceleration of the rover. The processing is simplified since slowly changing parameters are neglectable in the acceleration domain. Using the PhaseDif-POP method, no precise reference clock data is required. Solutions can be precisely computed at the measurement day using GNSS observations of a static station that can be thousands of kilometres away.

The PosDif and PhaseDif methods were applied in two static and two dynamic experiments. The results did not indicate consistent accuracy and precision differences between the methods. All implemented methods have been shown to be well-suited for airborne gravimetry and confirm each other. To obtain high quality results, 5 s final satellite clock products should be used or, alternatively, the clock parameters can be estimated within a network-based least-squares adjustment. The PhaseDif approach might be especially useful if a new GNSS processing implementation or a fast solution is required at high precision. The PosDif approach is not recommended in conjunction with DGNSS since the positioning accuracy is expected to degrade with increasing distance of the rover to the reference station. The PosDif-PPP method proved to reliably deliver satisfactory kinematic acceleration and subsequent gravity results.

If working properly, the long-term drift behaviour of the “classical” stable-platform gravimeters is superior to the used strapdown IMUs. Though, a comparison of iNAV-RQH and Chekan-AM results demonstrated that only the strapdown gravimeter delivered reliable observations at cornering during the shipborne campaigns. A combination proved to be able to extract the respective advantageous properties of each gravimeter type. However, while the iNAV-RQH reliably delivered observations that could be used for stand-alone gravity determination, this was not the case for the stable-platform gravimeters in several campaigns.

An approach for line-wise upward continuation was introduced. Using this approach, the differences between airborne and shipborne results were significantly lower than when comparing the original data. However, a simple low-pass filtering of the shipborne data also proved to be suited for the comparison. The approach is expected to be more effective for flight lines with a large height difference flown at similar velocity.

Multiple dynamic gravimetry campaigns have been analysed. The results demonstrated that high precision gravity disturbance can be obtained under a wide range of observation conditions using the direct method of strapdown gravimetry. Furthermore, the evaluation supports the expectation that there might be a tendency for worse precision under high turbulence, harsh sea conditions and for a gravity field of high variability. The effect of the latter condition might be primarily due to the limited spatial resolution of dynamic gravimetry and may be reduced using a topographic reduction.

The thesis pointed out that both the specific force and the kinematic acceleration are key to high accuracy dynamic gravimetry results. At least in static experiments, their noise behaviour was shown to be approximately on par. With proper calibration and processing methods for both components and under appropriate observation conditions, the processing can be optimised to obtain a precision being as low as a few tenths of mGal, especially for shipborne campaigns.

10.2 Outlook

The multi-campaign analysis indicated correlations between the gravity precision and the local gravity field variability in addition to the turbulence level. The evaluation of more campaigns with higher turbulence level or field variability might be desirable to support or refine the interpretations made concerning the influence of the observation conditions on the result quality. If more campaigns were available, a combined analysis of environmental parameters might enable conclusions on the possible precision depending on the observation conditions if the error behaviour turns out not to be predominantly random. Such findings might be considered in the planning stage of future campaigns.

The results obtained with the Polar 5 aircraft at BRE2021 have been of superior precision compared to the other airborne campaigns. The precision of CL2021 was also unexpectedly good considering the absence of crossover points at approximately straight measurement lines. In future, it might be analysed why this measurement system, the Polar 5 in combination with the iNAV-RQH, delivered such high quality results. Parameters like aircraft flight behaviour or the gravimeter mounting stiffness might be taken into account.

In some campaigns, systematic biases between different gravimeter solutions, processing methods and to external references have been found being at the low mGal level. No implementation issues were identified regarding linear drift removal, normal gravity computation, attitude determination, interpolation and quantisation. The evaluation of such biases was outside the scope of this thesis, but should be further assessed in the future in order to ensure high accuracy along with the already available high precision for strapdown gravimetry.

The scope of this thesis was limited to the evaluation of scalar gravity disturbance results, i.e. the vertical component of the gravity disturbance vector. While a precision of 8 mGal was obtained for the horizontal components of the Malaysia 2014 campaign (Johann et al., 2019), particularly high linear drift behaviour was observed for a horizontal accelerometer of the iNAV-RQH in recent campaigns. Strategies for drift removal

in the horizontal accelerometers using high accuracy attitude angles should be developed to enable the computation of deflections of the vertical in all campaigns.

Becker (2016) found that the sensor attitude might affect the thermal calibration results. The accuracy of the magnetic calibration of the iNAV-RQH with iTempStab might be improved considering the roll and pitch angle. In a first experiment using a turntable, measurements might be collected at a single temperature being the typical working temperature with the iTempStab.

The magnetic field in the vehicle cabins used for dynamic gravimetry should be regarded in more detail using magnetometers, especially in large vehicles containing much ferromagnetic and electric components. Cabin magnetometer observations may be required if the magnetic field is strongly distorted close to the IMU. The modelling is intricate since indoor magnetic fields can strongly vary in intensity and direction depending on the exact sensor position. A magnetometer inside of the IMU might be an auspicious alternative. However, assuming the magnetic field being confirm with the IGRF proved to be sufficient for strong result improvements at most evaluated campaigns.

While the magnetic calibration was demonstrated to considerably improve the readings of the accelerometer of the iNAV-RQH, it is unclear if other sensors are impaired by an exterior magnetic field as well. Consequently, it is recommended to analyse the results of other IMUs, especially if the working principle of their sensors is based on magnetic feedback. Heading-dependent biases may be an indication for influences of the magnetic field of the Earth. If systematic heading-dependent behaviour is observed, a sensor-specific precise magnetic calibration can be performed using a Helmholtz coil. If this is not feasible, an empirical sinusoidal approximation of the error may be used alternatively to counteract the effect.

The kinematic acceleration methods performed approximately on par. However, improvements in the related processing might still be possible. At the airborne experiments, undetected outliers or their improper removal seemed to impair some of the PhaseDif results. Hence, improved outlier detection and removal strategies or parameter tuning in the data snooping algorithm in addition to the soft removal strategy might further enhance the PhaseDif results. Furthermore, experimental application of atmospheric corrections might result in improving accuracies, although this is deemed unlikely since the atmospheric parameters are changing very slowly.

The interpretation of the introduced upward continuation method for repeated lines was complicated by the fact that the regarded line data were collected at very different vehicle velocities. The line-wise upward continuation method should be further evaluated with airborne data flown at similar velocity. A height difference of several kilometres is desirable for this purpose.

In the scope of this work, it was demonstrated that a precision around the 1 mGal level was possible in almost all evaluated strapdown dynamic gravimetry campaigns. In most surveys, at least two gravimeters were installed side-by-side for redundancy. Methods to combine different gravimeter types with advantages at specific wavelengths were presented in this thesis. The combination of gravimeter data with similar properties might also be eligible for significant improvements in the accuracy. The influence of sensor drifts of strapdown IMUs might be reduced by a combination on observation or result level.

Bibliography

Alken, P et al. (2021). “International Geomagnetic Reference Field: the thirteenth generation”. In: *Earth, Planets and Space* 73.49, pp. 1–25. DOI: https://doi.org/10.1186/s40623-020-01288-x.

Allan, David W. (1966). “Statistics of Atomic Frequency Standards”. In: *Proceedings of the IEEE* 54.2, pp. 221–230. ISSN: 15582256. DOI: 10.1109/PROC.1966.4634.

Andersen, Ole B., Per Knudsen, Steve C. Kenyon, and Simon A. Holmes (2014). “Global and Arctic Marine Gravity Field From Recent Satellite Altimetry (DTU13)”. In: *76th EAGE Conference and Exhibition 2014*. Vol. 2014. 1. European Association of Geoscientists & Engineers, pp. 1–5. DOI: 10.3997/2214-4609.20140897.

Anselmi, Alberto, Stefano Cesare, Sabrina Dionisio, Giorgio Fasano, and Luca Massotti (2019). “Control Propellant Minimization for the Next Generation Gravity Mission”. In: *Springer Optimization and Its Applications*. Vol. 144. Springer, pp. 1–32. ISBN: 9783030105013. DOI: 10.1007/978-3-030-10501-3_1.

Ayres-Sampaio, Diogo, Richard Deurloo, Machiel Bos, Américo Magalhães, and Luísa Bastos (2015). *A Comparison Between Three IMUs for Strapdown Airborne Gravimetry*. DOI: 10.1007/s10712-015-9323-5.

Bachmann, Eric R., Xiaoping Yun, and Christopher W. Peterson (2004). “An investigation of the effects of magnetic variations on inertial/magnetic orientation sensors”. In: *Proceedings - IEEE International Conference on Robotics and Automation* 2004.2, pp. 1115–1122. ISSN: 10504729. DOI: 10.1109/robot.2004.1307974.

Bastos, Luísa, S Cunha, René Forsberg, Arne Vestergaard Olesen, Arne Gidskehaug, U Meyer, T Boebel, Ludger Timmen, G Xu, M Nesemann, and Klaus Hehl (1998). “An Airborne Geoid Mapping System for regional sea-surface topography: application to the Skagerrak and Azores areas”. In: *Geodesy on the Move. In: International Association of Geodesy Symposia*. Berlin, Heidelberg: Springer, pp. 30–36. DOI: 10.1007/978-3-642-72245-5_5.

Beard, Ron and Ken Senior (2017). “Clocks”. In: *Springer Handbook of Global Navigation Satellite Systems*. Ed. by P. J.G. Teunissen and Oliver Montenbruck. Cham: Springer. Chap. 5, pp. 121–164. DOI: 10.1007/978-3-319-42928-1_5.

Becker, David (2016). “Advanced Calibration Methods for Strapdown Airborne Gravimetry”. PhD Thesis. Darmstadt: Technische Universität Darmstadt. ISBN: 9783935631402. URL: http://tuprints.ulb.tu-darmstadt.de/5691/.

Becker, David, Matthias Becker, Stefan Leinen, and Yingwei Zhao (2015a). “Estimability in strapdown airborne vector gravimetry”. In: *International Association of Geodesy Symposia*. ISBN: 9783319398198. DOI: 10.1007/1345_2015_209.

Becker, David, Matthias Becker, Arne Vestergaard Olesen, J. Emil Nielsen, and René Forsberg (2016). “Latest results in strapdown airborne gravimetry using an iMAR RQH unit”. In: *4th IAG symposium on Terrestrial Gravimetry*. State Research Center of the Russian Federation, pp. 19–25.

Becker, David, J. Emil Nielsen, Diogo Ayres-Sampaio, René Forsberg, Matthias Becker, and Luísa Bastos (2015b). “Drift reduction in strapdown airborne gravimetry using a simple thermal correction”. In: *Journal of Geodesy* 89.11, pp. 1133–1144. ISSN: 14321394. DOI: 10.1007/s00190-015-0839-8.

Bender, P L, D N Wiese, and R S Nerem (2008). “A possible dual-GRACE mission with 90 degree and 63 degree inclination orbits”. In: *Proceedings of the 3rd International Symposium on Formation Flying, Missions and Technologies. European Space Agency Symposium Proceedings, SP-654 jILA Pub*. Vol. 8161, pp. 1665–1669.

Bidel, Yannick, Nassim Zahzam, Alexandre Bresson, Cédric Blanchard, Malo Cadoret, Arne V. Olesen, and René Forsberg (2020). “Absolute airborne gravimetry with a cold atom sensor”. In: *Journal of Geodesy* 94.2. ISSN: 14321394. DOI: 10.1007/s00190-020-01350-2. arXiv: 1910.06666.

Brozena, John M. (1992). “The Greenland Aerogeophysics Project: Airborne Gravity, Topographic and Magnetic Mapping of an Entire Continent”. In: *From Mars to Greenland: Charting Gravity With Space and Airborne Instruments. In: International Association of Geodesy Symposia*. New York, NY: Springer, pp. 203–214. DOI: 10.1007/978-1-4613-9255-2_19.

Bruton, Alexander Mark (2000). “Improving the Accuracy and Resolution of SINS/DGPS Airborne Gravimetry”. PhD thesis. University of Calgary. ISBN: 0612648036.

Bruton, Alexander Mark, C. L. Glennie, and K. P. Schwarz (1999). “Differentiation for High-Precision GPS Velocity and Acceleration Determination”. In: *GPS Solutions* 2.4, pp. 7–21. ISSN: 15211886. DOI: 10.1007/PL00012771.

Bruton, Alexander Mark, K. P. Schwarz, S. Ferguson, M. Kern, and Ming Wei (2002). “Deriving Acceleration from DGPS: Toward Higher Resolution Applications of Airborne Gravimetry”. In: *GPS Solutions* 5.3, pp. 1–14. ISSN: 15211886. DOI: 10.1007/PL00012894.

Cai, Shaokun, Junbo Tie, Kaidong Zhang, Juliang Cao, and Meiping Wu (2017). “Marine gravimetry using the strapdown gravimeter SGA-WZ”. In: *Marine Geophysical Research* 38.4, pp. 325–340. ISSN: 15730581. DOI: 10.1007/s11001-017-9312-9.

Capitaine, N, B Guinot, and D D McCarthy (2000). “Definition of the Celestial Ephemeris Origin and of UT1 in the International Celestial Reference Frame”. In: *Astronomy and Astrophysics* 355, pp. 398–405.

Childers, Vicki A., Robin E. Bell, and John M. Brozena (1999). “Airborne gravimetry: An investigation of filtering”. In: *Geophysics* 64.1, pp. 61–69. ISSN: 0016-8033. DOI: 10.1190/1.1444530.

Clauser, Christoph (2014). *Einführung in die Geophysik: Globale physikalische Felder und Prozesse in der Erde*. Berlin, Heidelberg: Springer. DOI: 10.1007/978-3-642-04496-0.

Dach, Rolf, Stefan Schaer, Daniel Arnold, Maciej Sebastian Kalarus, Lars Prange, Pascal Stebler, Arturo Villiger, and Adrian Jäggi (2020). *CODE final product series for the IGS*. Tech. rep. Bern: Astronomical Insitute, University of Bern. DOI: 10.7892/boris.75876.4. URL: http://www.aiub.unibe.ch/download/CODE.

Feng, Yanming and Yi Zheng (2005). “Efficient interpolations to GPS orbits for precise wide area applications”. In: *GPS Solutions* 9.4, pp. 273–282. ISSN: 10805370. DOI: 10.1007/s10291-005-0133-y.

Flechtner, Frank, Christoph Reigber, Reiner Rummel, and Georges Balmino (2021). “Satellite Gravimetry: A Review of Its Realization”. In: *Surveys in Geophysics* 42.5, pp. 1029–1074. ISSN: 15730956. DOI: 10.1007/s10712-021-09658-0.

Forsberg, René and Arne V. Olesen (2010). “Airborne gravity field determination”. In: *Sciences of Geodesy - I: Advances and Future Directions*. Ed. by Guochang Xu. Berlin: Springer. Chap. 3, pp. 83–104. ISBN: 9783642117404. DOI: 10.1007/978-3-642-11741-1_3.

Forsberg, René, Arne Vestergaard Olesen, K. Keller, M. Møller, and Arne Gidskehaug (2001). “Airborne Gravity and Geoid Surveys in the Arctic and Baltic Seas”. In: *Proceedings of international symposium on kinematic systems in geodesy, geomatics and navigation (KIS-2001)*, pp. 586–593.

Glennie, C. L. and K. P. Schwarz (1999). “A comparison and analysis of airborne gravimetry results from two strapdown inertial/DGPS systems”. In: *Journal of Geodesy* 73, pp. 311–321. ISSN: 09497714. DOI: 10.1007/s001900050248.

Glennie, C. L., K. P. Schwarz, Alexander Mark Bruton, René Forsberg, Arne Vestergaard Olesen, and K. Keller (2000). “A comparison of stable platform and strapdown airborne gravity”. In: *Journal of Geodesy* 74.5, pp. 383–389. ISSN: 09497714. DOI: 10.1007/s001900000082.

Groves, Paul D. (2013). *Principles of GNSS, inertial and multisensor integrated navigation systems*. 2nd ed. Boston; London: Artech House. ISBN: 9781608070053.

Haagmans, Roger, Christian Siemes, Luca Massotti, Olivier Carraz, and Pierluigi Silvestrin (2020). “ESA’s next-generation gravity mission concepts”. In: *Rendiconti Lincei* 31.s1, pp. 15–25. ISSN: 17200776. DOI: 10.1007/s12210-020-00875-0.

Harrison, J. C. (1959). “Tests of the LaCoste-Romberg surface-ship gravity meter I”. In: *Journal of Geophysical Research* 64.11, pp. 1875–1881. DOI: 10.1029/JZ064i011p01875.

Hauschild, André (2017a). “Basic Observation Equations”. In: *Springer Handbook of Global Navigation Satellite Systems*. Ed. by P. J.G. Teunissen and Oliver Montenbruck. Cham: Springer. Chap. 19, pp. 561–582. DOI: 10.1007/978-3-319-42928-1_19.

– (2017b). “Combinations of Observations”. In: *Springer Handbook of Global Navigation Satellite Systems*. Ed. by Peter J.G. Teunissen and Oliver Montenbruck. Cham: Springer. Chap. 20, pp. 583–604. DOI: 10.1007/978-3-319-42928-1_20.

He, Kaifei (2014). “GNSS Kinematic Position and Velocity Determination for Airborne Gravimetry”. PhD Thesis. Technische Universität Berlin.

Hecker, Oskar (1903). “Bestimmung der Schwerkraft auf dem atlantischen Ozean sowie in Rio de Janeiro, Lissabon und Madrid”. In: *Veröffentlichung königlich Preußisches Geodätisches Institut* III.

Hwang, Cheinway, Yu Shen Hsiao, and Hsuan Chang Shih (2006). “Data reduction in scalar airborne gravimetry: Theory, software and case study in Taiwan”. In: *Computers and Geosciences* 32, pp. 1573–1584. ISSN: 00983004. DOI: 10.1016/j.cageo.2006.02.015.

IMAR Navigation (2012). *iNAV-RQH-1003: Inertial Measurement System for Advanced Applications*. St. Ingbert. URL: https://www.imar-navigation.de/downloads/NAV_RQH_1003_en.pdf (visited on 11/25/2022).

– (2016). *iTAHS: Tactical Alignment & Heading Sensor: 3D Magnetometer with integrated Inertial Sensors*. St. Ingbert. URL: https://www.imar-navigation.de/downloads/TAHS_Magnetometer.pdf (visited on 11/25/2022).

Ince, E. Sinem, Franz Barthelmes, Sven Reißland, Kirsten Elger, Christoph Förste, Frank Flechtner, and Harald Schuh (2019). “ICGEM – 15 years of successful collection and distribution of global gravitational models, associated services, and future plans”. In: *Earth System Science Data* 11.2, pp. 647–674. ISSN: 18663516. DOI: 10.5194/essd-11-647-2019.

International GNSS Service (2022). *Network*. URL: www.igs.org/network (visited on 11/18/2022).

Jacobs, Earl D (1972). *Accelerometer*.

Jamil, H., Majid Kadir, René Forsberg, Arne Vestergaard Olesen, M. N. Isa, S. Rasidi, A. Mohamed, Z. Chihat, J. Emil Nielsen, Fadhil Majid, K. Talib, and S. Aman (2017). “Airborne geoid mapping of land and sea areas of East Malaysia”. In: *Journal of Geodetic Science* 7.1, pp. 84–93. ISSN: 2081-9943. DOI: 10.1515/jogs-2017-0010.

Jekeli, Christopher (1994). “Airborne vector gravimetry using precise, position-aided inertial measurement units”. In: *Bulletin Géodésique* 69.1, pp. 1–11. ISSN: 00074632. DOI: 10.1007/BF00807986.

– (2001). *Inertial Navigation Systems with Geodetic Applications*. Berlin: de Gruyter. ISBN: 3-11-015903-1.

– (2011). “On Precision Kinematic Accelerations for Airborne Gravimetry”. In: *Journal of Geodetic Science* 1.4. ISSN: 2081-9943. DOI: 10.2478/v10156-011-0016-9.

Jekeli, Christopher and R. Garcia (1997). “GPS phase accelerations for moving-base vector gravimetry”. In: *Journal of Geodesy* 71.10, pp. 630–639. ISSN: 09497714. DOI: 10.1007/s001900050130.

Jekeli, Christopher and Jay H. Kwon (1999). “Results of airborne vector (3-D) gravimetry”. In: *Geophysical Research Letters* 26.23, pp. 3533–3536. ISSN: 00948276. DOI: 10.1029/1999GL010830.
Jensen, Tim Enzlberger (2018). “Airborne Strapdown Gravity Measurements for Geodesy and Geophysics”. PhD Thesis. Technical University of Denmark.
Jensen, Tim Enzlberger, J. Emil Nielsen, Arne Vestergaard Olesen, and René Forsberg (2017). “Strapdown Airborne Gravimetry Using a Combination of Commercial Software and Stable-Platform Gravity Estimates”. In: *International Symposium on Gravity, Geoid and Height Systems 2016*. Ed. by G. Vergos, Roland Pail, and R. Barzaghi. May. Cham: Springer. ISBN: 978-3-319-95318-2. DOI: 10.1007/1345_2017_9. URL: http://link.springer.com/chapter/10.1007/1345%7B%5C_%7D2015%7B%5C_%7D50.
Jensen, Tim Enzlberger, Arne V. Olesen, Rene Forsberg, Per Anders Olsson, and Örjan Josefsson (2019). “New results from strapdown airborne gravimetry using temperature stabilisation”. In: *Remote Sensing* 11.22, pp. 1–19. ISSN: 20724292. DOI: 10.3390/rs11222682.
Jin, Shuanggen, J. Wang, and Pil Ho Park (2005). “An improvement of GPS height estimations: Stochastic modeling”. In: *Earth, Planets and Space* 57.4, pp. 253–259. ISSN: 18805981. DOI: 10.1186/BF03352561.
Jin, Xinxiang (1996). “Theory of Carrier Adjusted DGPS Positioning Approach and Some Experimental Results”. PhD Thesis. Technische Universiteit Delft, p. 178.
Johnston, Gary, Anna Riddell, and Grant Hausler (2017). “The International GNSS Service”. In: *Springer Handbook of Global Navigation Satellite Systems2*. Ed. by P. J.G. Teunissen and Oliver Montenbruck. Cham: Springer, pp. 967–982. DOI: 10.1007/978-3-319-42928-1_33.
Kennedy, S. L. (2003). “Precise acceleration determination from carrier-phase measurements”. In: *Navigation, Journal of the Institute of Navigation* 50.1, pp. 9–19. ISSN: 00281522. DOI: 10.1002/j.2161-4296.2003.tb00314.x.
King, R W and Y Bock (1999). “Documentation for the GAMIT GPS software analysis version 9.9”. In.
Knabe, Annike, Manuel Schilling, Hu Wu, Alireza HosseiniArani, Jürgen Müller, Quentin Beaufils, and Franck Pereira dos Santos (2022). “The Benefit of Accelerometers Based on Cold Atom Interferometry for Future Satellite Gravity Missions”. In: *International Association of Geodesy Symposia*, pp. 1–8. DOI: 10.1007/1345_2022_151.
Krasnov, A. A., L. P. Nesenyuk, V. G. Peshekhonov, A. V. Sokolov, and L. S. Elinson (2011). “Integrated marine gravimetric system. Development and operation results”. In: *Gyroscopy and Navigation* 2.2, pp. 75–81. ISSN: 20751087. DOI: 10.1134/S2075108711020052.
Kreye, Christian and Guenter W Hein (2003). “GNSS Based Kinematic Acceleration Determination for Airborne Vector Gravimetry: Methods and Results”. In: *Proceedings of the ION GPS/GNSS 2003 Meeting*.
Kvas, Andreas, Torsten Mayer-Gürr, Sandro Krauss, Jan Martin Brockmann, Till Schubert, Wolf-Dieter Schuh, Roland Pail, Thomas Gruber, and Adrian Jäggi (2019). *The satellite-only gravity field model GOCO06s*. Tech. rep. GFZ Data Services. DOI: 10.5880/ICGEM.2019.002.
Kwon, Jay H. and Christopher Jekeli (2001). “A new approach for airborne vector gravimetry using GPS/INS”. In: *Journal of Geodesy* 74, pp. 690–700. ISSN: 09497714. DOI: 10.1007/s001900000130.
LaCoste, Lucien (1959). “Surface Ship Gravity Measurements on the Texas A. and M. College Ship, the Hidalgo”. In: *Geophysics* XXIV.2, pp. 309–322.
– (1967). “Measurement of Gravity at Sea and in the Air”. In: *Reviews of Geophysics1* 5.4, pp. 477–526. ISSN: 23249250. DOI: 10.1029/TR002i001p00003.
LaCoste, Lucien, Neal Clarkson, and George Hamilton (1967). “LaCoste and Romberg Stabilized Platform Shipboard Gravity Meter”. In: *Geophysics* XXXII.1, pp. 99–109.
Lanza, Roberto and Antonio Meloni (2006). *The Earth’s Magnetism*. Berlin: Springer, p. 278. ISBN: 9783540279792.
Lawrence, Anthony (1993). “The Pendulous Accelerometer”. In: *Modern Inertial Technology*. 1st ed. New York, NY: Springer US, pp. 57–71. ISBN: 978-1-4684-0446-3. DOI: 10.1007/978-1-4684-0444-9_5.
Leitgeb, Norbert (1990). *Strahlen, Wellen, Felder*. Stuttgart: Thieme, p. 310. ISBN: 3-13-750601-8.

Li, Min, Karl Hans Neumayer, Frank Flechtner, Biao Lu, Christoph Förste, Kaifei He, and Tianhe Xu (2018). "Performance Assessment of Multi-GNSS Precise Velocity and Acceleration Determination over Antarctica". In: *Journal of Navigation*, pp. 1–18. ISSN: 14697785. DOI: 10.1017/S0373463318000656.

Li, Min, Tianhe Xu, Biao Lu, and Kaifei He (2019). "Multi-GNSS precise orbit positioning for airborne gravimetry over Antarctica". In: *GPS Solutions* 23.2, p. 53. ISSN: 1080-5370. DOI: 10.1007/s10291-019-0848-9.

Lin, C A, K W Chiang, and C Y Kuo (2018). "Integration of INS and GNSS for Gravimetric Application with UAS". In: *Innovative Sensing - From Sensors to Methods and Applications*. Vol. XLII. October, pp. 10–12.

Lowes, F. J. (2000). "An estimate of the errors of the IGRF/DGRF fields 1945-2000". In: *Earth, Planets and Space* 52.12, pp. 1207–1211. ISSN: 18805981. DOI: 10.1186/BF03352353.

Lu, Biao, Franz Barthelmes, Min Li, Christoph Förste, Elmas Sinem Ince, Svetozar Petrovic, Frank Flechtner, Joachim Schwabe, Zhicai Luo, Bo Zhong, and Kaifei He (2019). "Shipborne gravimetry in the Baltic Sea: data processing strategies, crucial findings and preliminary geoid determination tests". In: *Journal of Geodesy*. ISSN: 0949-7714. DOI: 10.1007/s00190-018-01225-7.

Lu, Biao, Franz Barthelmes, Svetozar Petrovic, Christoph Förste, Frank Flechtner, Zhicai Luo, Kaifei He, and Min Li (2017). "Airborne Gravimetry of GEOHALO Mission: Data Processing and Gravity Field Modeling". In: *Journal of Geophysical Research: Solid Earth* 122.12, pp. 10, 586–10, 604. ISSN: 21699356. DOI: 10.1002/2017JB014425.

Luo, Xiaoguang, Michael Mayer, Bernhard Heck, and Joseph L. Awange (2014). "A realistic and easy-to-implement weighting model for GPS phase observations". In: *IEEE Transactions on Geoscience and Remote Sensing* 52.10, pp. 6110–6118. ISSN: 01962892. DOI: 10.1109/TGRS.2013.2294946.

Lyu, Daqian, Fangling Zeng, Xiaofeng Ouyang, and Heli Yu (2019). "Enhancing multi-GNSS time and frequency transfer using a refined stochastic model of a receiver clock". In: *Measurement Science and Technology* 30, pp. 1–12. ISSN: 13616501. DOI: 10.1088/1361-6501/ab2419.

Marson, Iginio (2012). "A short walk along the gravimeters path". In: *International Journal of Geophysics* 2012. ISSN: 1687885X. DOI: 10.1155/2012/687813.

Moritz, H. (1980). "Geodetic reference system 1980". In: *Bulletin Géodésique*. ISSN: 00074632. DOI: 10.1007/BF02521480.

Nabighian, M. N., M. E. Ander, V. J. S. Grauch, R. O. Hansen, T. R. LaFehr, Y. Li, W. C. Pearson, J. W. Peirce, J. D. Phillips, and M. E. Ruder (2005). "Historical development of the gravity method in exploration". In: *Geophysics* 70.6, 63ND–89ND. ISSN: 0016-8033. DOI: 10.1190/1.2133785. URL: http://library.seg.org/doi/10.1190/1.2133785.

Nettleton, L. L., Lucien LaCoste, and J. C. Harrison (1960). "Tests of an Airborne Gravity Meter". In: *Geophysics* 25.1. ISSN: 0016-8033. DOI: 10.1190/1.1438685.

NovAtel Inc. (2017). *Receivers OEM729: Multi-frequency, backward compatible GNSS receiver includes all modern signals (version 2)*. URL: https://hexagondownloads.blob.core.windows.net/public/Novatel/assets/Documents/Papers/OEM729-Product-Sheet/OEM729-Product-Sheet.pdf (visited on 09/14/2022).

– (2020). *Waypoint Software 8.90 User Manual*. URL: https://hexagondownloads.blob.core.windows.net/public/Novatel/assets/Documents/Manuals/Waypoint-Software-User-Manual-OM-20000166/Waypoint_8.90_Software_User_Manual.pdf (visited on 12/06/2022).

Oehler, Jean François, Didier Rouxel, and Marie Françoise Lequentrec-Lalancette (2018). "Comparison of global geomagnetic field models and evaluation using marine datasets in the north-eastern atlantic ocean and western mediterranean sea". In: *Earth, Planets and Space* 70.1. ISSN: 18805981. DOI: 10.1186/s40623-018-0872-y.

Pavlis, Nikolaos K., Simon A. Holmes, Steve C. Kenyon, and John K. Factor (2012). "The development and evaluation of the Earth Gravitational Model 2008 (EGM2008)". In: *Journal of Geophysical Research: Solid Earth* 117.4, pp. 1–38. ISSN: 21699356. DOI: 10.1029/2011JB008916.

Petit, Gérard and Brian Luzum (2010). *IERS Conventions (2010)*. Tech. rep. Frankfurt am Main: Federal Agency for Cartography and Geodesy, Germany, pp. 1–179. URL: https://www.iers.org/IERS/EN/Publications/TechnicalNotes/tn36.html.

Reuper, Björn Friedrich (2020). "Multi-Frequency GNSS Sensor Fusion With Quality Assessment for Automotive Applications". Ph.D. Thesis. Technical University of Darmstadt. ISBN: 9783935631464. URL: https://tuprints.ulb.tu-darmstadt.de/11655/.

Ries, J, S Bettadpur, R Eanes, Z Kang, U Ko, C McCullough, P Nagel, N Pie, S Poole, T Richter, H. Save, and B. Tapley (2016). *The Combination Global Gravity Model GGM05C*. Tech. rep. GFZ Data Services. DOI: 10.5880/icgem.2016.002.

Romero, Ignacio (2020). *The Receiver Independent Exchange Format Version 3.05*. Tech. rep. December. Darmstadt: ESA/ESOC/Navigation Support Office.

Salazar, Dagoberto, M. Hernandez-Pajares, J. M. Juan-Zornoza, and J. Sanz (2010). "Network-based high accuracy positioning with the GPSTk". In: *5th ESA Workshop on Satellite Navigation Technologies and European Workshop on GNSS Signals and Signal Processing, NAVITEC 2010*. IEEE, pp. 1–6. ISBN: 9781424487417. DOI: 10.1109/NAVITEC.2010.5708030.

Salazar, Dagoberto, Manuel Hernandez-Pajares, Jose Miguel Juan-Zornoza, Jaume Sanz-Subirana, and Angela Aragon-Angel (2011). "EVA: GPS-based extended velocity and acceleration determination". In: *Journal of Geodesy* 85.6, pp. 329–340. ISSN: 09497714. DOI: 10.1007/s00190-010-0439-6.

Schack, Peter Wolfgang (2021). "Multi-sensor data fusion for terrestrial 3D-gravity profiling". PhD thesis. Technical University of Munich. ISBN: 9783769652925.

Schenewerk, Mark (2003). "A brief review of basic GPS orbit interpolation strategies". In: *GPS Solutions* 6.4, pp. 265–267. ISSN: 15211886. DOI: 10.1007/s10291-002-0036-0.

Schwabe, Joachim, Gunther Liebsch, Patrick Westfeld, T Hammarklint, J Mononen, and Ole B. Andersen (2020). "The Baltic Sea Chart Datum 2000 (BSCD2000)". In: *International Hydrographic Review* 23.May, pp. 63–83.

Schwarz, Hans Rudolf and Norbert Köckler (2011). *Numerische Mathematik*. 8th ed. Wiesbaden: Vieweg+Teubner. ISBN: 978-3-8348-1551-4. DOI: 10.1007/978-3-8348-8166-3.

Schwarz, K. P. (1983). "Inertial surveying and geodesy". In: *Reviews of Geophysics* 21.4, pp. 878–890. DOI: 10.1029/RG021i004p00878.

Schwarz, K. P. and C. L. Glennie (1998). "Improving Accuracy Reliability airborne gravimetry multiple sensor configurations". In: *Geodesy on the Move. In: International Association of Geodesy Symposia*. Berlin, Heidelberg: Springer, pp. 11–17.

Serrano, Luis, Don Kim, and Richard B. Langley (2004). "A single GPS receiver as a real-time, accurate velocity and acceleration sensor". In: *Proceedings of the 17th International Technical Meeting of the Satellite Division of the Institute of Navigation, ION GNSS 2004*, pp. 2021–2034.

El-Sheimy, Naser, Haiying Hou, and Xiaoji Niu (2008). "Analysis and Modeling of Inertial Sensors Using Allan Variance". In: *IEEE Transactions in Instrumentation and Measurements* 57.1, pp. 140–149. DOI: 10.1109/TIM.2007.908635.

Simav, Mehmet, David Becker, Hasan Yildiz, and Matthias Hoß (2020). "Impact of temperature stabilization on the strapdown airborne gravimetry: a case study in Central Turkey". In: *Journal of Geodesy* 94.4. ISSN: 14321394. DOI: 10.1007/s00190-020-01369-5.

Strasser, Sebastian, Torsten Mayer-Gürr, and Norbert Zehentner (2019). "Processing of GNSS constellations and ground station networks using the raw observation approach". In: *Journal of Geodesy* 93.7, pp. 1045–1057. ISSN: 14321394. DOI: 10.1007/s00190-018-1223-2.

Studinger, Michael, Robin Bell, and Nick Frearson (2008). "Comparison of AIRGrav and GT-1A airborne gravimeters for research applications". In: *Geophysics* 73.6. ISSN: 00168033. DOI: 10.1190/1.2969664.

Taubin, Gabriel (1991). “Estimation of Planar Curves, Surfaces,and Nonplanar Space Curves Defined by Implicit Equations with Applications to Edge and Range Image Segmentation”. In: *IEEE Transactions on Pattern Analysis and Machine Intelligence* 13.11, pp. 1115–1138.

Tenforde, T. S. (1995). “Spectrum and intensity of environmental electromagnetic fields from natural and man-made sources”. In: *Advances in Chemistry Series* 250, pp. 37–56. ISSN: 00652393. DOI: 10.1021/ba-1995-0250.ch002.

Thompson, Lloyd G D and Lucien LaCoste (1960). “Aerial gravity measurements”. In: *Journal of Geophysical Research1* 65.1, pp. 305–322. DOI: 10.1029/JZ065i001p00305.

Torge, Wolfgang (1989). *Gravimetry*. Berlin: de Gruyter. ISBN: 0-89925-561-2.

Torge, Wolfgang and Jürgen Müller (2012). *Geodesy*. 4th ed. Berlin; Boston: de Gruyter. ISBN: 978-3-11-020718-7.

Touboul, P., G. Métris, H. Sélig, O. Le Traon, Alexandre Bresson, Nassim Zahzam, Bruno Christophe, and M Rodrigues (2016). “Gravitation and Geodesy with Inertial Sensors , from Ground to Space”. In: *Aerospace Lab Journal* 12, pp. 1–16. DOI: 10.12762/2016.AL12-11.

Turcotte, Donald L. and Gerald Schubert (2002). *Geodynamics*. 2nd ed. Cambridge: Cambridge Univ. Pr., p. 456. ISBN: 0521666244.

Vries, W. H.K. de, H. E.J. Veeger, C. T.M. Baten, and F. C.T. van der Helm (2009). “Magnetic distortion in motion labs, implications for validating inertial magnetic sensors”. In: *Gait and Posture* 29.4, pp. 535–541. ISSN: 09666362. DOI: 10.1016/j.gaitpost.2008.12.004.

Wang, Wei, Jinyao Gao, Dongming Li, Tao Zhang, Xiaowen Luo, and Jinling Wang (2018). “Measurements and accuracy evaluation of a strapdown marine gravimeter based on inertial navigation”. In: *Sensors* 18.11, pp. 1–13. ISSN: 14248220. DOI: 10.3390/s18113902.

Wei, M. and K. P. Schwarz (1998). “Flight test results from a strapdown airborne gravity system”. In: *Journal of Geodesy* 72, pp. 323–332. ISSN: 09497714. DOI: 10.1007/s001900050171.

Wendel, Jan (2011). *Integrierte Navigationssysteme: Sensordatenfusion, GPS und Inertiale Navigation*. 2nd ed. München: Oldenbourg. ISBN: 9783486704396.

Wesche, Christine, Daniel Steinhage, and Uwe Nixdorf (2016). “Polar aircraft Polar5 and Polar6 operated by the Alfred Wegener Institute”. In: *Journal of large-scale research facilities JLSRF* 2, pp. 1–7. DOI: 10.17815/jlsrf-2-153.

Worzel, John Lamar (1965). *Pendulum gravity measurements at sea, 1936-59*. Wiley.

Xiong, Zhiming, Juliang Cao, Meiping Wu, Shaokun Cai, Ruihang Yu, and Minghao Wang (2020). “A Method for Underwater Dynamic Gravimetry Combining Inertial Navigation System, Doppler Velocity Log, and Depth Gauge”. In: *IEEE Geoscience and Remote Sensing Letters* 17.8, pp. 1294–1298. ISSN: 1545-598X. DOI: 10.1109/LGRS.2019.2945628.

Yuan, Yuan, Jinyao Gao, Zhaocai Wu, Zhongyan Shen, and Guochao Wu (2020). “Performance estimate of some prototypes of inertial platform and strapdown marine gravimeters”. In: *Earth, Planets and Space* 72.1. ISSN: 18805981. DOI: 10.1186/s40623-020-01219-w.

Zhang, Xiangbo, Ji Guo, Yonghui Hu, Baoqi Sun, Jianfeng Wu, Dangli Zhao, and Zaimin He (2021). “Influence of Precise Products on the Day-Boundary Discontinuities in GNSS Carrier Phase Time Transfer”. In: *Sensors* 21.4, pp. 1–24. ISSN: 14248220. DOI: 10.3390/s21041156.

Zhang, Xiaohong, Kai Zheng, Cuixian Lu, Jiakuan Wan, Zhanke Liu, and Xiaodong Ren (2017). “Acceleration estimation using a single GPS receiver for airborne scalar gravimetry”. In: *Advances in Space Research* 60.60, pp. 2277–2288. ISSN: 18791948. DOI: 10.1016/j.asr.2017.08.038.

Zingerle, Philipp, Roland Pail, Thomas Gruber, and Xanthi Oikonomidou (2019). *The experimental gravity field model XGM2019e*. Tech. rep. GFZ Data Services. DOI: 10.5880/ICGEM.2019.007.

Zumberge, J. F., M. B. Heflin, D. C. Jefferson, M. M. Watkins, and F. H. Webb (1997). “Precise point positioning for the efficient and robust analysis of GPS data from large networks”. In: *Journal of Geophysical Research: Solid Earth* 102.B3, pp. 5005–5017. ISSN: 01480227. DOI: 10.1029/96JB03860.

Own publications

Cob, Sanusi, Majid Kadir, René Forsberg, Wim Simons, Marc Naeije, Ami Hassan Din, Husaini Yacob, Asyran Amat, Daud Mahdzur, Zuhairy Ibrahim, Kenidi Aziz, Norehan Yaacob, Felix Johann, Tim Enzlberger Jensen, Hergeir Teitsson, Shahrum Ses, Anim Yahaya, Soeb Nordin, and Fadhil Majid (2022). "Epoch-Based Height Reference System for Sea Level Rise Impact Assessment on the Coast of Peninsular Malaysia". In: *Remote Sensing* 14.23, pp. 1–34. DOI: 10.3390/rs14236179.

Förste, Christoph, E Sinem Ince, Felix Johann, Joachim Schwabe, and Gunter Liebsch (2020). "Marine Gravimetry Activities on the Baltic Sea in the Framework of the EU Project FAMOS". In: *Zeitschrift für Geodäsie, Geoinformation und Landmanagement* 145.5, pp. 287–294. DOI: 10.12902/zfv-0317-2020. URL: https://geodaesie.info/zfv/heftbeitrag/8609.

Johann, Felix, David Becker, Matthias Becker, René Forsberg, and Majid Kadir (2019). "The Direct Method in Strapdown Airborne Gravimetry - a Review". In: *Zeitschrift für Geodäsie, Geoinformation und Landmanagement* 144.5, pp. 323–333. DOI: 10.12902/zfv-0263-2019. URL: https://geodaesie.info/zfv/heftbeitrag/8493.

Johann, Felix, David Becker, Matthias Becker, Matthias Hoss, Alexander Löwer, and Christoph Förste (2021). "The influence of the Earth's magnetic field on strapdown inertial gravimetry using Q-Flex accelerometers: static and dynamic experiments". In: *Journal of Geodesy* 95.9, pp. 1–15. ISSN: 14321394. DOI: 10.1007/s00190-021-01553-1.

Johann, Felix, David Becker, Matthias Becker, and E. Sinem Ince (2020). "Multi-Scenario Evaluation of the Direct Method in Strapdown Airborne and Shipborne Gravimetry". In: *International Association of Geodesy Symposia*. Berlin, Heidelberg: Springer, pp. 1–8. DOI: 10.1007/1345_2020_127.

List of acronyms

(P)DGNSS (Precise) Differential GNSS

AWI Alfred Wegener Institute for Polar and Marine Research

BKG German Federal Agency for Cartography and Geodesy

BRE2021 Bremen / North Sea 2021 airborne gravimetry campaign

BSH German Federal Maritime and Hydrographic Agency

BTS2017 Baltic Sea 2017 shipborne gravimetry campaign

BTS2018 Baltic Sea 2018 shipborne gravimetry campaign

CAI Cold Atom Interferometry

CCD Charge-Coupled Device

CHAMP Challenging Minisatellite Payload

CL2021 Chile/Patagonia 2021 airborne gravimetry campaign

CO Crossover Point

CODE Center for Orbit Determination in Europe

CoM Centre of Measurements

DD Double Differences

DK2020 Denmark 2020 westcoast airborne gravimetry campaign

DLR German Aerospace Center

DTU Space National Space Institute at the Technical University of Denmark

EGM2008 Earth Gravitational Model 2008

EKF Extended Kalman Filter

ERA Earth Rotation Angle

ESA European Space Agency

FFT Fast Fourier Transform

FIR Finite Impulse Response

GFZ German Research Centre for Geosciences

GNSS Global Navigation Satellite Systems

GOCE Gravity and Steady-State Ocean Circulation Explorer

GPS NAVSTAR Global Positioning System

GPST GPS Time

GRACE Gravity Recovery and Climate Experiment

GRACE-FO GRACE Follow-On

GRS80 Geodetic Reference System 1980

ICGEM International Centre for Global Earth Models

ICRF International Celestial Reference Frame

IF Ionosphere-Free Linear Combination

IFFT Inverse FFT

IGRF International Geomagnetic Reference Frame

IGS International GNSS Service

IMU Inertial Measurement Unit

ISA Internal Sensor Assembly

iTempStab iMAR iTempStab-AddOn

JUPEM Department of Survey and Mapping Malaysia

L&R LaCoste & Romberg

LC Linear Combination

LIDAR Light Detection and Ranging

MRZ2019 Lake Müritz 2019 shipborne gravimetry campaign

MY2014 Malaysia 2014 airborne gravimetry campaign

MY2022 Malaysia 2022 airborne gravimetry campaign

NASA National Aeronautics and Space Administration

NTS2021 North Sea 2021 shipborne gravimetry campaign

NTS2022 North Sea 2022 shipborne gravimetry campaign

ODW2017 Odenwald 2017 airborne gravimetry campaign

ODW2018 Odenwald 2018 airborne gravimetry campaign

PhaseDif Phase Differentiation

PhaseDif-DD Phase Differentiation based on DD

PhaseDif-POP Phase Differentiation based on POP

PhaseDif-PPP Phase Differentiation based on PPP

POP Precise Orbit Positioning

PosDif Position Differentiation Method

PosDif-DGNSS Position Differentiation based on DGNSS

PosDif-PPP Position Differentiation based on PPP

PPP Precise Point Positioning

PPS Pulse-Per-Second

PRN Pseudo Random Number

RL Repeated lines

RLG Ring Laser Gyrosocope

RMS Root Mean Square

RMSE Root Mean Square Error

RTK Real Time Kinematic

SLR Satellite Laser Ranging

SST Satellite-to-Satellite Tracking

TU Darmstadt Technical University of Darmstadt

TU Dresden Technische Universität Dresden

UAV Unmanned Aerial Vehicle

ZM Zero-Mean

List of Figures

2.1 Spatial and temporal resolution of Earth system processes and gravimetric measurement methods 5
2.2 Long wavelengths of the global gravity disturbance computed with the EGM2008 6
2.3 Schematic illustration of the principal gravimetric observation techniques 8
2.4 The Chekan-AM gravimeter owned by the GFZ installed next to TU Darmstadt's iMAR iNAV-RQH-1003 with iTempStab at the Müritz 2019 campaign 14
2.5 Measurement principle of the Chekan-AM gravimeter 14
2.6 Measurement principle of the L&R S-type gravimeter including the stable platform 15
2.7 The L&R S-type gravimeter by DTU Space installed next to strapdown gravimeters and the magnetometer xSens MTi at the Malaysia 2022 campaign 15
2.8 TU Darmstadt's strapdown gravimeter by iMAR 15
2.9 Relevant components of the system design of the iMAR iNAV-RQH-1003 with iTempStab-AddOn 16
2.10 Schematic topview of the Q-Flex accelerometer construction 17
2.11 Temperatures measured by the iNAV-RQH-1003 with iTempStab-AddOn at a static measurement on 7 May 2020 19
2.12 Readings of the vertical accelerometer during run 3 of the warm-up calibration 22
2.13 Thermal calibration of the vertical accelerometer 22
2.14 Coordinate frames in the context of dynamic gravimetry 24
2.15 Schematic flow charts of processing methods in dynamic gravimetry 27

3.1 Simple static experiment with a permanent bar magnet 30
3.2 Horizontal magnetic field intensity with airborne and shipborne campaigns 32
3.3 Magnetic field declination with airborne and shipborne campaigns 32
3.4 iMAR iTAHS magnetometer within the 3-D Helmholtz coil at iMAR Navigation facilities 34
3.5 Magnetic field RMS inside the 3-D Helmholtz coil 34
3.6 iMAR iNAV-RQH-1003 encased in the iTempStab inside of the 3-D Helmholtz coil 35
3.7 Mounting and axis directions of the IMU and the vertical accelerometers in the four attitude settings 36
3.8 Means and standard deviations of the down component as a function of the horizontal magnetic field direction (without iTempStab) 38
3.9 Most relevant horizontal magnetic field directions in the four attitude settings 39
3.10 Means and standard deviations of the down component as a function of the vertical magnetic field direction in the four attitude settings (without iTempStab) 39
3.11 Most relevant vertical magnetic field directions in the four attitude settings 39
3.12 Means and standard deviations of the down component as a function of the magnetic field direction and intensity (with iTempStab) 40
3.13 Horizontal angles relevant for the calibration approach 42
3.14 Biases of the lines of the BTS2018 campaign with the corresponding magnetic calibration function 42

4.1 Low-order numerical differentiation strategies 47
4.2 Schematic overview on the PhaseDif algorithm 54

4.3 Noise amplification factors for the first and second numerical derivative . . . 59
4.4 Soft elevation method . . . 60
4.5 Soft loss method close to missing observations . . . 60
4.6 Propagation of outliers within two numerical differentiations . . . 62
4.7 IGS stations selected for the static experiments . . . 64
4.8 Low-pass filtered vertical kinematic acceleration . . . 66
4.9 Amplitude spectra of the vertical kinematic acceleration . . . 67
4.10 Standard deviations of the vertical kinematic acceleration compared for different processing approaches, part 1 . . . 68
4.11 Satellite observability in the PhaseDif-POP network (static 2) . . . 69
4.12 Standard deviations of the vertical kinematic acceleration compared for different processing approaches, part 2 . . . 71

5.1 Gravity disturbance for the Bremen 2021 flight before and after bias and linear drift removal . 78
5.2 Approximation of the radius of curvature along a trajectory . . . 79
5.3 Crossover point residuals of the Chile 2021 campaign with respect to the radius of curvature . 79

6.1 Beechcraft King Air 350 at Subang used for MY2014 and MY2022 . . . 84
6.2 Non-adjusted gravity disturbance MY2014 . . . 84
6.3 Vertical biases at MY2014 and linear drifts . . . 85
6.4 Non-adjusted crossover residuals sorted by flights and lines of MY2014 . . . 86
6.5 Line-wise adjusted crossover residuals sorted by flights and lines of MY2014 and estimated line biases . . . 86
6.6 Gravity disturbance and separation of repeated lines of MY2014 . . . 87
6.7 Non-adjusted gravity disturbance MY2022 . . . 88
6.8 Sensor temperatures, estimated gravity and heating/cooling power at MY2022 . . . 90
6.9 Vertical biases at MY2022 and linear drifts . . . 91
6.10 Crossover point residuals with respect to line headings at MY2022 and magnetic calibration function . . . 91
6.11 Line-wise adjusted gravity disturbance of the eastern subnet of MY2022 . . . 91
6.12 Aircraft used for the Odenwald campaigns . . . 93
6.13 Installed gravimeters at ODW2017 . . . 93
6.14 Vertical biases at ODW2017 and linear drifts . . . 93
6.15 Non-adjusted gravity disturbance of the Odenwald campaigns . . . 93
6.16 Crossover residuals of ODW2017 with respect to flight condition parameters . . . 94
6.17 Histograms of the crossover residuals of ODW2017 . . . 95
6.18 Line-wise adjusted crossover residuals sorted by flights and lines of ODW2018 and estimated line biases . . . 96
6.19 Non-adjusted crossover residuals sorted by flights and lines of ODW2017 and ODW2018 . . . 97
6.20 Line-wise adjusted gravity disturbance of ODW2017 and ODW2018 . . . 97
6.21 IGS stations selected for PhaseDif-POP processing of ODW2018 . . . 97
6.22 Vulcanair P68C at Esbjerg used for DK2020 . . . 97
6.23 Gravity disturbance of DK2020 . . . 98
6.24 Vertical biases at DK2020 and linear drifts . . . 99
6.25 Non-adjusted crossover residuals sorted by flights and lines of DK2020 . . . 99
6.26 Gravity disturbance and separation of the repeated lines of DK2020 . . . 100
6.27 Polar 5 at Bremen used for BRE2021 and CL2021 . . . 100
6.28 Installed gravimeters at BRE2021 . . . 100

6.29 Non-adjusted gravity disturbance BRE2021 . . . 101
6.30 IGS stations selected for PhaseDif-POP processing of BRE2021 . . . 101
6.31 Gravity disturbance referencing of BRE2021 with PhaseDif-POP results . . . 102
6.32 Non-adjusted crossover residuals sorted by lines of BRE2021 . . . 102
6.33 Magnetometer installed in the tail rod of Polar 5 . . . 102
6.34 Magnetic field parameters for BRE2021 with vehicle attitude angles . . . 103
6.35 Comparison of gravity disturbance results obtained with different kinematic acceleration determination methods for BRE2021 . . . 105
6.36 Gravity disturbance CL2021 . . . 106
6.37 Flight trajectories at the Grey glacier . . . 107
6.38 Crossover RMSE of CL2021 using points with a specific minimal radius of curvature . . . 107

7.1 Survey, wreck-search and research vessel Deneb at Bremerhaven used for BTS2017, BTS2018 and NTS2021 . . . 109
7.2 Non-adjusted gravity disturbance BTS2017 . . . 110
7.3 Non-adjusted gravity disturbance BTS2018 . . . 110
7.4 Vertical biases at the Baltic Sea campaigns and linear drifts . . . 111
7.5 Sea conditions during a cruise of BTS2017 . . . 112
7.6 Gravity disturbance at BTS2018 before and after thermal oscillation correction . . . 112
7.7 Line-wise adjusted gravity disturbance of BT2018 . . . 113
7.8 Non-adjusted gravity disturbance of BTS2017 and BTS2018 . . . 113
7.9 Non-adjusted crossover residuals sorted by cruises and lines of BTS2017 and BTS2018 . . . 114
7.10 Crossover residuals of BTS2017 and BTS2018 with the magnetic calibration function . . . 114
7.11 Installed gravimeters at NTS2021 . . . 115
7.12 Survey, wreck-search and research vessel Wega at Bremerhaven used for NTS2022 . . . 115
7.13 Non-adjusted gravity disturbance of the North Sea campaigns . . . 116
7.14 Vertical biases at the North Sea campaigns and linear drifts . . . 116
7.15 Magnetic field parameters for NTS2021 with vehicle attitude angles . . . 118
7.16 Non-adjusted gravity disturbance of NTS2021 and NTS2022 . . . 119
7.17 Crossover residuals and sea conditions of NTS2021 and NTS2022 . . . 119
7.18 Non-adjusted crossover residuals sorted by cruises and lines of NTS2021 and NTS2022 . . . 119
7.19 Non-adjusted crossover residuals of NTS2021 and NTS2022 . . . 120
7.20 Line-wise adjusted gravity disturbance of NTS2021 and NTS2022 . . . 120
7.21 Excursion boat Klink at Waren/Müritz used for MRZ2019 . . . 121
7.22 Non-adjusted gravity disturbance MRZ2019 . . . 121
7.23 Vertical biases at MRZ2019 and linear drifts . . . 122
7.24 Estimated line biases of the MRZ2019 results plotted with the magnetic calibration function . 122
7.25 Non-adjusted crossover residuals sorted by cruises and lines of MRZ2019 . . . 122
7.26 Estimated line biases of MRZ2019 . . . 123

8.1 Amplitude spectrum of gravity disturbance results . . . 125
8.2 Possible correlations between observation conditions and the non-adjusted crossover precision 126
8.3 Influence of the magnetic field calibration correction based on IGRF-based or magnetometer data 127

9.1 Non-adjusted gravity disturbance result comparison at DK2020 . . . 130
9.2 Non-adjusted gravity disturbance result comparison of BTS2018 . . . 132
9.3 Non-adjusted gravity disturbance result comparison of NTS2021 . . . 133

9.4 Magnitude responses of the filters designed for the combination of the iNAV-RQH and Chekan-AM results . . . 134
9.5 Filtered iNAV-RQH and Chekan-AM results of BTS2018, cruise 217 . . . 134
9.6 Combined gravity disturbance result using iNAV-RQH and Chekan-AM data of BTS2018, cruise 217 . . . 134
9.7 Height-dependent gravitational acceleration assuming a horizontally varying sinusoidal mass layer . . . 136
9.8 Line-wise dynamic gravimetry comparison process . . . 138
9.9 Damping coefficients for a height difference of approximately 500 m . . . 139
9.10 Amplitude spectrum of gravity disturbance obtained with XGM2019e . . . 139
9.11 Amplitude spectra of gravity disturbance obtained with dynamic gravimetry . . . 139
9.12 Gravity disturbance results along repeated lines at the North Sea . . . 140

List of Tables

2.1 Main influencing factors on gravity observations at the Earth's surface . . . 4
2.2 Properties of gravimeters appearing in this thesis . . . 13
2.3 Specifications of the Honeywell inertial sensors of the iNAV-RQH-1003 . . . 15
2.4 Standard deviation of the accelerometer readings after warm-up . . . 22

3.1 Overview about the static magnetic field experiments . . . 35
3.2 IMU and vertical accelerometer axis directions in the four attitude settings . . . 36

4.1 Requirements for high accuracy kinematic acceleration determination approaches . . . 44
4.2 Selected IGS stations for the static experiments . . . 63

6.1 Airborne campaign properties and precision . . . 83
6.2 Malaysia 2014 precision . . . 85
6.3 Malaysia 2022 precision . . . 89
6.4 Odenwald 2017/2018 precision . . . 95
6.5 Denmark 2020 precision . . . 98
6.6 IGS stations selected for BRE2021 . . . 101
6.7 Bremen 2021 precision . . . 104
6.8 Chile 2021 precision . . . 107

7.1 Shipborne campaign properties and precision . . . 109
7.2 Baltic Sea 2017/2018 precision . . . 111
7.3 North Sea 2021/2022 precision . . . 117
7.4 Müritz 2019 precision . . . 121

8.1 Correlation coefficient between the mean measurement condition the and crossover precision 125

9.1 DK2020 precision for different strapdown gravimeters using the direct and the indirect processing method . . . 130
9.2 Gravimeter drifts at BTS2018 . . . 131
9.3 Statistics on the difference between non-adjusted iNAV-RQH and Chekan-AM results . . . 132
9.4 Statistics on the differences between shipborne and airborne gravity disturbance results . . . 141